Development of a novel sorption-based dehumidification system

by

Amin Elsafi

MSc., King Fahd University of Petroleum and Minerals, 2014

BSc., University of Khartoum, 2009

Thesis Submitted in Partial Fulfillment of the
Requirements for the Degree of
Doctor of Philosophy

in the
School of Mechatronic Systems Engineering
Faculty of Applied Sciences

SIMON FRASER UNIVERSITY

Fall 2022

Declaration of Committee

Name:	**Amin Elsafi**
Degree:	**Doctor of Philosophy**
Title:	**Development of a novel sorption-based dehumidification system**
Committee:	**Chair:** **Amr Marzouk** Senior Lecturer, Mechatronic Systems Engineering
	Majid Bahrami Supervisor Professor, Mechatronic Systems Engineering
	Bonnie Gray Committee Member Professor, Engineering Science
	Sami Khan Committee Member Assistant Professor, Sustainable Energy Engineering
	Gordon McTaggart-Cowan Examiner Associate Professor, Sustainable Energy Engineering
	David Sinton External Examiner Professor, Mechanical Engineering University of Toronto

Abstract

The required energy to control the temperature and humidity for human comfort is estimated as 50% of the building's total energy consumption. Several serious health problems which are caused by mildew, viruses, and reduction of air quality in buildings are all associated with excessive humidity. Humidity control also plays a vital role in greenhouse food production. Developing a compact and efficient dehumidification system for buildings and greenhouses is a necessity in order to reduce the energy consumption and greenhouse gas (GHG) emissions.

Despite the advantages of "thermally-driven" liquid desiccant absorption systems over the other dehumidification systems, the research on them is still limited to laboratory-scale experiments rather than practical applications. The conventional packed-column absorbers in liquid desiccant dehumidification systems have fundamental limitations (a slow absorption process) and practical challenges (solution carryover, crystallization, and corrosion) that hinder their utilization in real dehumidification applications.

In this research, a new design concept for absorption reactors is proposed for the dehumidification applications. The proposed reactor concept provides compactness (i.e high moisture removal rates per volume), permits working in the crystallization region, and eliminates the metal corrosion which is associated with the hygroscopic salts. This was achieved by creating spherical microreactors (i.e., microcapsules) that encapsulates the aqueous hygroscopic salt (such as LiBr) solution inside an elastic spherical semi-permeable membrane shell using a custom-built microfluidic device.

A compact "packed-sheet" absorber that houses packed spherical microcapsules was designed, built, and tested for dehumidification applications. The results showed that the developed absorber had moisture removal rates per volume (of 75 g/s-$m^{3)}$ that were two folds higher than the conventional packed-column absorbers (35 g/s-m^3).

In addition, fundamental studies were presented to study the heat transfer from/to spherical particles. Moreover, a one-dimensional model that considers the coupled heat and mass transfer was developed to simulate the transient behaviour of the proposed packed-sheet reactor. The validated model was used to conduct a parametric study to reveal the impact of the various design and operating conditions, and to optimize the design. The results from the optimization study showed that the performance of the proposed design can be maximized to realize moisture removal rates of up to 135 g/s-m^3 with a coefficient of performance of 0.25.

Keywords: dehumidification, liquid absorption, microfluidics, encapsulation, and moisture removal rate.

Dedication

This thesis is dedicated to my family for the endless love, support, and encouragement.

Acknowledgements

I would like to thank the following people, without whom I would not have been able to complete this research. First, I would like to express my gratitude to my supervisor, Dr. Majid Bahrami, for his invaluable supervision, support, and patience during my graduate studies at Simon Fraser University. His immense knowledge and plentiful experience were really influential in shaping my experiment methods, critiquing my results, and polishing my presentation skills.

My gratitude extends to my supervisory committee members, Dr. Bonnie Gray and Dr. Sami Kahn, for their time and valuable feedback throughout my PhD proposal and defense. I am also thankful to my examining committee members, Dr. David Sinton and Dr. Gordon McTaggart-Cowan for their valuable time, reading the thesis and giving their feedback.

I would like to thank my friends, lab mates, colleagues and research team at the Laboratory for Alternative Energy Conversion at Simon Fraser University for a cherished time spent together in the lab, and in social settings.

I would like to thank 4D LABS at Simon Fraser University for providing access to the scanning electron microscopy and X ray diffraction spectroscopy facilities. I am also thankful to Dr. Paul Li for providing me with syringe pumps and a UV light source to complete my microfluidics experimental setup. I would also like to thank Dr. Tom Claydon from the Department of Biomedical Physiology and Kinesiology for giving me the access to the micropipette puller in his research lab.

I gratefully acknowledge the financial support of the Natural Sciences and Engineering Research Council of Canada (NSERC) through the Automotive Partnership Canada Grants No. APCPJ 401826-10 and ACCPJ 536076-18.

Special thank is due to my family for their enormous love, support. Without their tremendous understanding and encouragement in the past few years, it would be impossible for me to complete my study.

Table of Contents

List of Tables

List of Figures

Nomenclature

Roman letters

a	inner radius of a sphere, *m*
A	surface area of a sphere, m^2
A_c	contact area, m^2
b	outer radius of a sphere, *m*
Bi	Biot number, -
c	chord, circular source radius, *m*
D	diameter of a sphere, *m*
h	convective heat transfer coefficient, W/m^2-K
H	channel height, *m*
k	thermal conductivity, *W/m-K*
L	sorption bed length, *m*
Nu	Nusselt number, -
P	pressure, *kPa*
Pr	Prandtl number, -
Q	wall heat flux, *W*
$\dot{q}''_w$	wall heat flux, W/m^2
r	radial direction, *m*
R	thermal resistance, *K/W*
R^*	non-dimensional thermal resistance, -
Re	Reynolds number, -
RH	relative humidity, %
t	thickness, *K*
t_{deh}	dehumidification process (i.e., half-cycle) time, *min*
T	temperature, *K*
u	air velocity, *m/s*
V	velocity, *m/s*
$\overline{V}_e$	surface averaged-effective velocity, *m/s*
X	sorbent water uptake, g_w/g_{dry}

Greek symbols

α	thermal diffusivity, m^2/s | half-contact angle, *rad*
β	thermal expansion coefficient, *1/K*
ε	radii ratio, -
ρ	density, kg/m^3
ω	humidity ratio, g_w/g_{air}
θ	polar angle, *rad*
ϑ	non-dimensional temperature, - | non-dimensional half contact angle, -
η	similarity variable, -
δ_T	thermal boundary layer thickness, *m*
δ_H	hydrodynamic boundary layer thickness, *m*
Φ	viscous dissipation, m^2/s^2
χ	relative disk thickness, -

Subscripts

a	related to air
s	related to sorbent
w	related to wall
∞	related to ambient fluid

Abbreviations

MRR	moisture removal rate, $g/s\text{-}m^3$
DCOP	dehumidification coefficient of performance, -

Executive summary

The required energy to control the temperature and humidity for human comfort is estimated as 50% of the building's total energy consumption. Several serious health problems which are caused by mildew, viruses, and reduction of air quality in buildings are all associated with excessive humidity. Humidity control also plays a vital role in greenhouse food production. Low humidity leads to reduced stem lengths and leaf sizes, while excessive humidity along with condensation can lead to fungal diseases, leaf necrosis, and soft and thin leaves. Data collected in France and the United Kingdom shows that the current dehumidification methods (i.e., venting) used to reduce the moisture content in greenhouses can account for 20% of the overall yearly energy consumption. Developing an efficient dehumidification system for buildings and greenhouses is a necessity in order to reduce energy consumption and greenhouse gas (GHG) emissions.

Air dehumidification can be achieved using heat pumps (cooling-condensation), a membrane-based heat/enthalpy exchanger, and sorption (solid or liquid desiccant) desiccant dehumidification systems. Despite their high efficiency, using heat pumps for dehumidification comes with challenges, such as high initial and operating cost, maintenance issues, ozone depletion potential, and global warming potential. On the other hand, membrane-based heat/enthalpy exchangers are simple, inexpensive, and have an overall efficiency of 60-90%, but they are prone to frost formation in cold climates and are less effective during the summer periods. Utilizing thermally-driven sorption systems can significantly reduce the emissions associated with ventilation and air conditioning systems, particularly, when waste-heat is used. Waste-heat (temperature <100 ^{o}C) is abundant energy that can harvested from various sources, such as industrial facilities, data centers, fuel cells, to name a few.

Hygroscopic liquid desiccants have a higher sorption capacity than solid adsorbents and a lower regeneration temperature (60-90 ^{o}C). Another advantage of using an inorganic salt solution in dehumidification is that it can improve the indoor air quality as these salts act as disinfectants. Nevertheless, the research on liquid salt solution dehumidification systems is limited to laboratory-scale experiments rather than practical applications in buildings. The absorber (or the reactor) is the most critical component of the system, and has a significant impact on their size, cost, and efficiency. A packed-column absorber that operates in the falling film mode is the most popular design used in liquid desiccant dehumidifiers due to its high effectiveness and low pressure drop. In this design, the humid air is brought into "direct" contact with a concentrated salt solution to absorb the moisture. Due to this, there is a high risk of solution carryover into the air stream. Inhaling air contaminated with salt particles can cause problems in the human respiratory system. Other issues, such as salt crystallization and corrosion, should also be addressed for practical applications.

Crystallization imposes a limit on the operational range, and it is a major operation and maintenance issue that can lead to significant down-time and service costs.

The main mechanism for the mass transfer in such conventional packed-column absorbers is the diffusion through the liquid solution film, which is a rather slow process and presents a fundamental limitation on the maximum performance that can be achieved. A compact absorber design requires high absorption rates. One way to enhance the absorption rate is to increase the surface-to-volume ratio for the reaction.

In this PhD program, an innovative reactor concept was proposed to address the central challenge in utilizing high-capacity absorbent hygroscopic salts in liquid absorption systems, where absorption kinetics and crystallization are resolved through encapsulation. In the proposed approach, a custom-built microfluidic device was used to encapsulate the aqueous salt solution inside a spherical semi-permeable polymeric membrane shell that is highly permeable to sorbate but impermeable to the salt and its solution. The produced microcapsules (i.e., microreactors) provide the large reaction surface area per-volume that would result in a more compact design than the conventional absorber. The uniformity of the produced microreactors enables fundamental studies to able applied on a single spherical particle to investigate the heat and mass transfer and predict the performance with high certainty.

Research Objectives

The main objective of this research is to develop a new concept for compact absorbers and to provide fundamental understanding of the heat and mass transfer inside the proposed absorber. The milestones of the present work are summarized as follows:

- to develop a novel design concept for efficient and compact absorption reactors with a large surface-to-volume ratio and high moisture removal rates;

- to eliminate practical challenges, such as solution carryover, crystallization, and corrosion that are associated with the liquid absorption system and hinder its utilization in dehumidification applications; and

- to build a bench-scale demonstration as a proof-of-concept and evaluate its performance for dehumidification applications under typical working conditions.

Research Methodology

To achieve the objectives of this research, the following methodology and step-by-step procedures have been followed, Fig. 1 shows the research roadmap:

i. Produce spherical microreactors (i.e., microcapsules) using microfluidic encapsulation:
   - Identify a shell material (UV-curable resin) with proper water vapor permeability;
   - Verify the material compatibility between the hygroscopic salt solutions, namely, LiBr, LiCl, and $CaCl_2$ and the shell (UV-curable resin) for creating core-shell emulsion by conducting interfacial, crosslinking, and degradation studies; and
   - Design and fabricate a microfluidic device to encapsulate aqueous salt solutions inside the polymeric shell and produce spherical microreactors that are uniform in size.

ii. Material characterization:
   - Measure the sorption capacity of microcapsules;
   - Perform microscopic and scanning electron microscope imaging to measure and verify the size uniformity of the produced microcapsules;
   - Perform X-ray diffraction testing to verify the salt encapsulation;
   - Test the mechanical strength of the microcapsules by performing expansion and compression tests; and
   - Investigate the longevity and performance degradation by running multiple cycles to ensure insignificant reduction in absorption capacity of the microcapsules.

iii. Build and test a proof-of-concept reactor:
   - Design and build a bench-scale proof-of-concept reactor with the proposed design; and
   - Test and evaluate the performance of the reactor for dehumidification under applicable conditions.

iv. Mathematical modeling and optimization:
   - Develop an analytical model to predict the forced-convection heat and mass transfer coefficients for the encapsulated spherical particle;
   - Develop a coupled heat and mass transfer model to simulate the transient performance of the proposed reactor packed with spherical microreactors; and
   - Perform multi-objective optimization using the above model to find an optimum trade-off between the energy efficiency and moisture removal capacity rates.

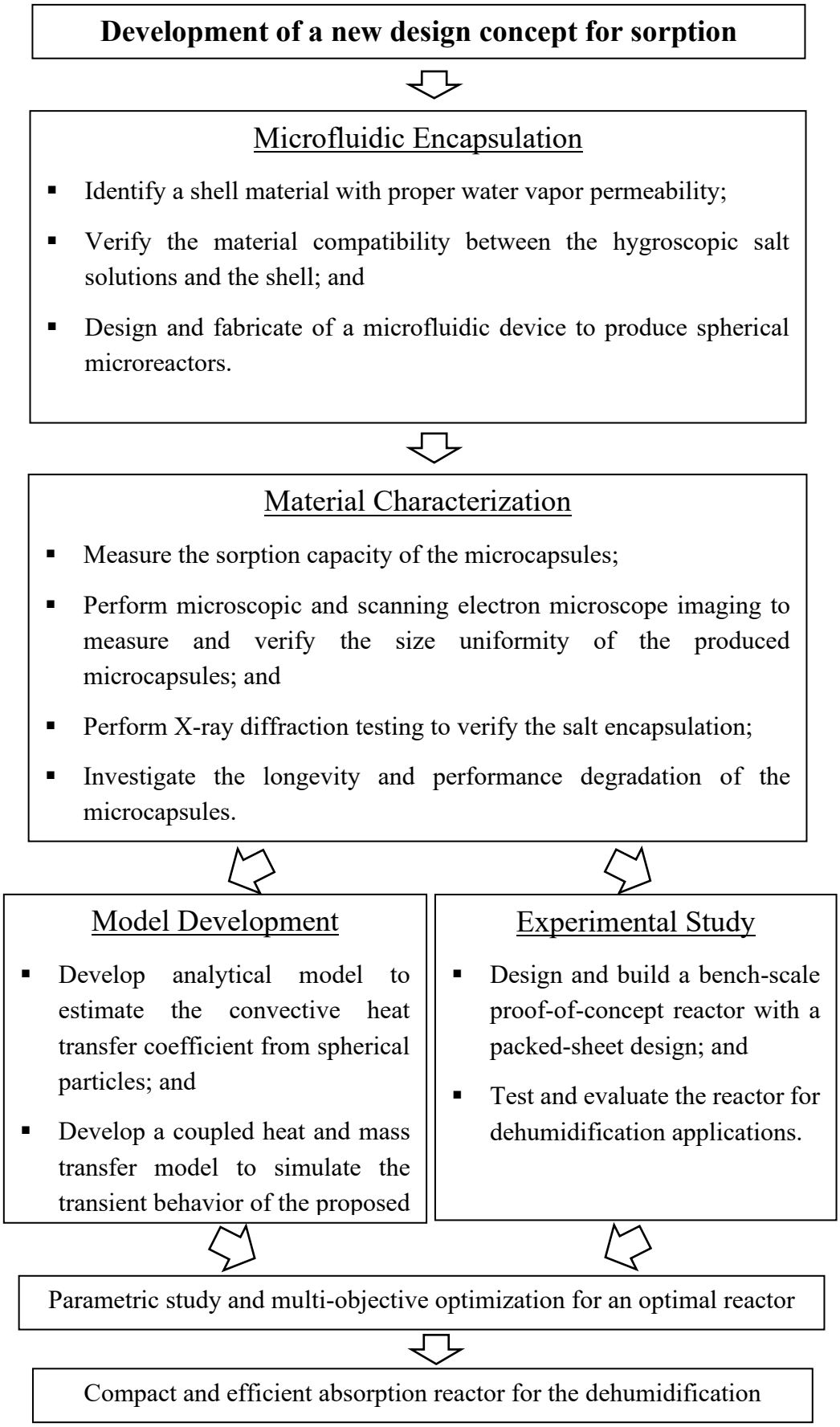

Fig. 1: Research Roadmap.

Contributions

The contributions of this research project are listed as follows:

- For the first time, highly uniform spherical microcapsules that contain highly moisture absorbent hygroscopic salts (LiBr, LiCl, and $CaCl_2$) were produced for dehumidification applications using a custom-built microfluidic device. The microreactors (i.e., microcapsules):
    - provide a high surface-to-volume ratio of up to 6000-12000 m^2/m^3 (compared to a 200-600 m^2/m^3 for the conventional absorbers), which is crucial to achieve high absorption rates;
    - eliminate the corrosion problems associated with hygroscopic salts;
    - allow working in the crystallization region for increased absorption capacities;
    - can withstand a force up to 2 X 10^5 their weight, and expand (elastically) during the absorption process without rupture; and
    - have a sorption capacity that does not deteriorate even after an accelerated test of 200 sorption-desorption cycles.

- A novel compact absorber that houses packed spherical microcapsules was designed, built, and tested for dehumidification applications under typical operating conditions. The developed absorber provides moisture removal rates per volume of 75 g/s-m^3 that are two-folds higher than the conventional packed-column absorbers (35 g/s-m^3);

- Fundamental study was presented to study the heat transfer from/to spherical particles. An expression for the convective heat transfer coefficient was derived using analytical modeling;

- An analytical model was developed to estimate the thermal resistance of the spherical microreactors to consider designs in which the microreactors are attached to a metal heat exchanger;

- A mathematical model, that considers the coupled heat and mass transfer was developed to simulate the transient behaviour of the proposed packed-sheet reactor. The model was validated with the collected experimental data under various operating conditions;

- A parametric study, based on the developed model, was conducted to investigate the impact of the key design parameters and operating conditions, as well as to serve as a guideline for designing the future prototypes; and

- A multi-objective optimization (using the validated developed model) was conducted to find the optimal design variables that offer a proper trade-off between the energy efficiency and moisture removal rates. The study showed that proposed absorber can maximize the performance and achieve moisture removal rates up to 135 g/s-m^3 (270% higher than the conventional liquid desiccant systems) with a coefficient of performance of 0.25.

Publications

1) Elsafi, A. M., Ashouri, M., and Bahrami, M. (2023). A similarity solution for laminar forced convection heat transfer from solid spheres. *International Journal of Heat and Mass Transfer*, *196, 123310*.
2) Elsafi, A. M., and Bahrami, M. (2021). Thermal spreading resistance of hollow hemi-sphere with internal convective cooling. *International Journal of Heat and Mass Transfer*, *170*, 120959.
3) Elsafi, A. M., and Bahrami, M. (2019). Sorption-based desalination systems: A comparison. *The Fifth International Symposium on Innovative Materials and Processes in Energy Systems, IMPRES2019.*
4) Elsafi, A. M., and Bahrami, M. (2022). A novel liquid desiccant absorber for dehumidification systems. *Applied Energy Journal.* (in progress)

Patents

5) Elsafi, A. M., and Bahrami, M. (2022). Microencapsulated liquid sorbents for dehumidification applications (in progress)

1. Introduction

1.1. Motivation

The building sector (residential and commercial) is the largest energy consumer, consisting of approximately 40% of the global energy consumption as of 2019 [1]. The required energy to control the temperature and humidity for human comfort is estimated as 50% of the building's total energy consumption [2]. Several serious health problems which are caused by mildew, viruses, reduction of air quality, and the occupants' discomfort in buildings are all associated with excessive humidity [3].

Humidity control also plays a vital role in greenhouse food production. Low humidity leads to reduced stem lengths and leaf sizes [4], while excessive humidity along with condensation can lead to fungal diseases, leaf necrosis, and soft and thin leaves. A considerable part of the Canadian economy is from the agriculture and food sectors , i.e., they are almost 5% of the total Canadian Gross Domestic Product [5]. In 2005, the Canadian greenhouse industry energy costs were approximately $260 million, which was 12% of their total revenue [6]. In Canada, the temperature and humidity in greenhouses are controlled by systems that run on fossil fuels and have significant operating costs. Developing an efficient dehumidification system for buildings and greenhouses is a necessity in order to reduce its energy consumption and their greenhouse gas (GHG) emissions.

Air dehumidification can be achieved using cooling-condensation and membrane-based heat/enthalpy exchanger, solid desiccant, and liquid desiccant dehumidification systems. Cooling-condensation dehumidification is achieved by using a mechanical refrigeration system such as a heat pump, as illustrated in **Fig. 2**. These systems rely on cooling the humid air below its dew point until condensation occurs. This is an energy intensive process that consumes a significant amount of "high-quality" electrical energy. Heat pump-based dehumidification systems offer high efficiency, for example, their coefficient of performance (COP), defined as the ratio between the latent heat removed to the energy input, is around 10 [7]. However, using heat pumps for dehumidification comes with challenges, such as a high initial and operating cost, maintenance issues, an ozone depletion potential, and a global warming potential [8]. The condensed water can also cause bacterial growth on the cooling coil surface [9].

Membrane-based dehumidifiers (see **Fig. 3**) are classified as air-to-air heat exchangers with a vapor-permeable membrane core that allows heat and moisture transfer between the supply (outdoor air) and exhaust (indoor air) airstreams through the membranes. They are simple, inexpensive, and have an overall efficiency of 60-90% [10,11], but they are prone to frost formation in cold climates [12] and are less effective during the summer periods [12].

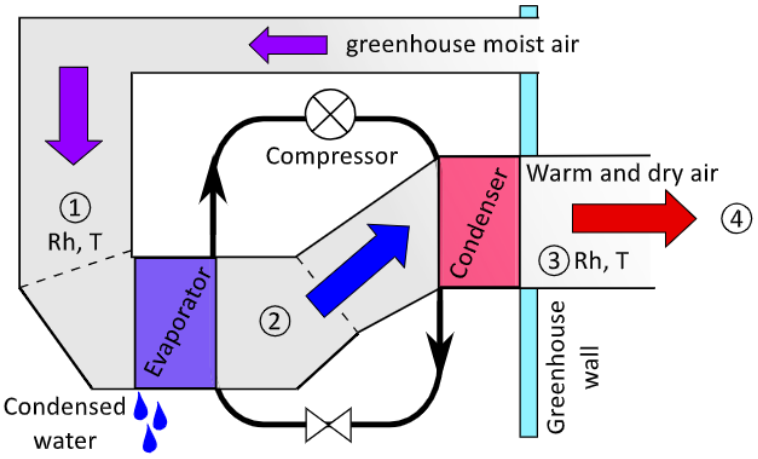

Fig. 2: Air flow in a dehumidifying heat pump [13].

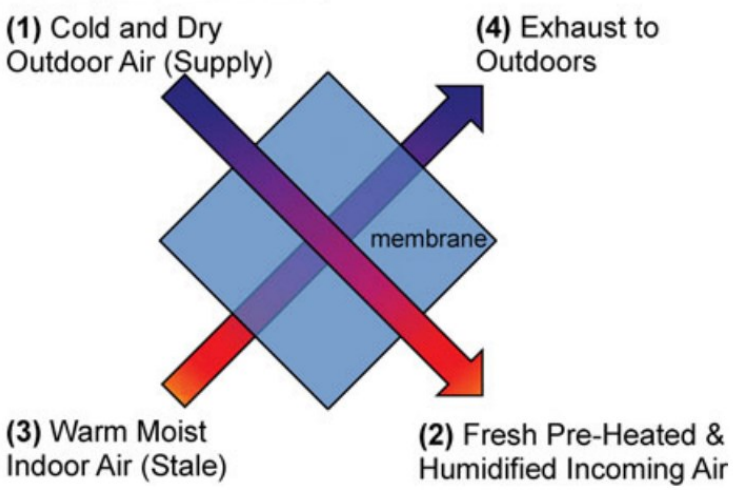

Fig. 3: A cross-flow membrane-based dehumidifier [14].

Utilizing thermally-driven sorption systems helps to alleviate the burden on the electricity generation sector, and can significantly reduce the emissions associated with ventilation and air conditioning systems, particularly, when waste-heat (or renewable energy source) is used. Waste-heat (temperature <100 ºC) is abundant energy that can be harvested from various sources, such as industrial facilities, data centers, fuel cells, to name a few. Typical solid desiccant dehumidifiers use zeolite as an adsorbent material because it has a higher sorption capacity than silica gel. These systems require a relatively high regeneration temperature in the range of 90-260 ºC. On the other hand, liquid desiccant hygroscopic salt absorbents, such as LiBr, LiCl, and $CaCl_2$ have a higher sorption capacity than solid adsorbents (see **Fig. 4**) and a low regeneration temperature (60-90 ºC). Another advantage of using an inorganic salt solution in dehumidification is that it can improve the indoor air quality as these salts act as disinfectants [15]. However, there exists several disadvantages with liquid desiccant dehumidification systems that curtail their commercialization, as explained in detail later in this chapter.

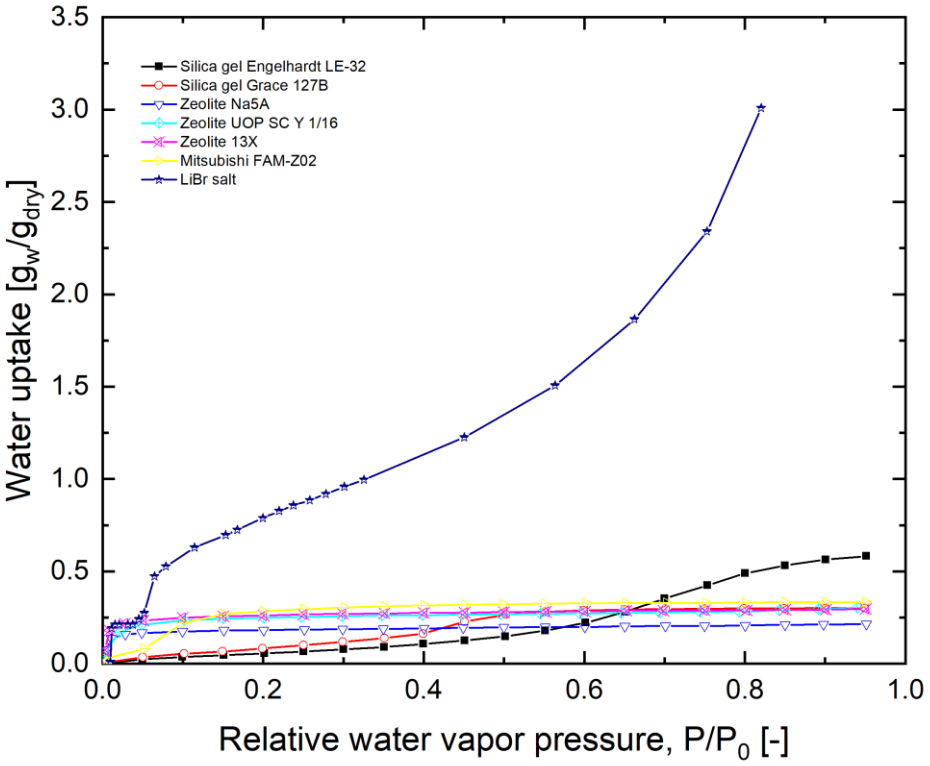

Fig. 4: A comparison between solid and liquid desiccants' (LiBr as an example) water sorption capacity [16,17].

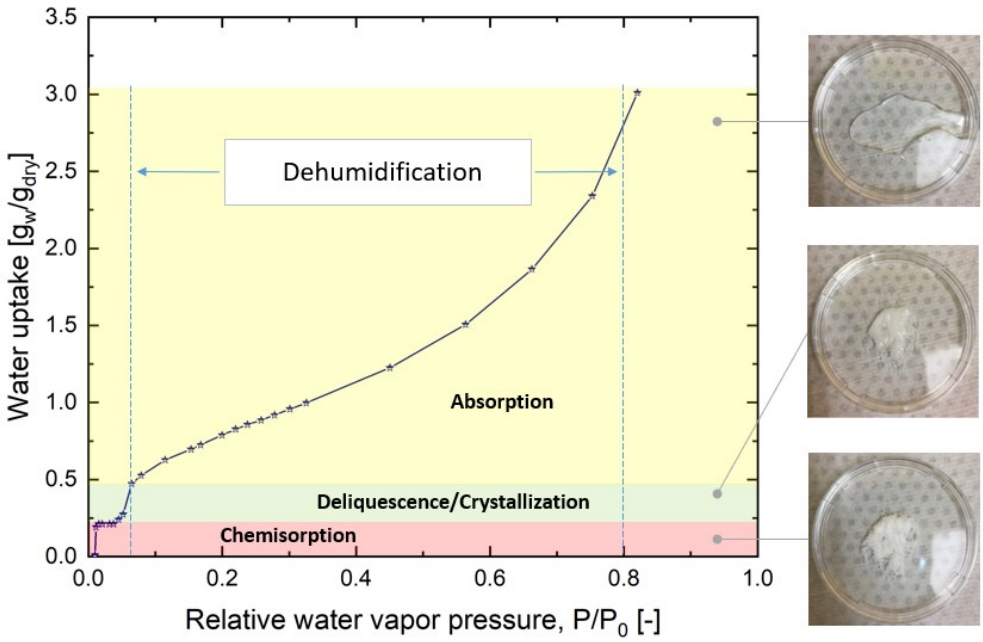

Fig. 5: A typical LiBr hygroscopic salt isotherm curve [18].

By studying the typical isotherm curve of the hygroscopic salts (see **Fig. 5**), it is clear that the hygroscopic salts are mostly working in the "liquid" absorption region (hence, the name "liquid desiccant"). Absorption is a phenomenon in which the atoms, molecules, or ions of one material penetrates the volume of a liquid material. Gas absorption into a liquid is the process in which the sorbate molecules (vapor or gas) enter the bulk phase of a liquid absorbent and gets absorbed [19].

Fig. 6 illustrates the working principle of a typical liquid desiccant dehumidification system [20]. During the absorption process, a stream of strong (highly concentred) salt solution is brought into "direct" contact with moist air (or pure water vapor) in the absorber. The water vapor is absorbed by the strong solution and exits the reactor with low moisture content. In the regeneration process, heat is added (Q_{in}) in the regenerator to the weak solution to remove the water vapor and restore the high concentration state of the solution. The same reactor used as an absorber can be used as a regenerator by passing a hot stream in the regeneration process. Alternatively, a separate conventional boiler/heat exchanger can be used as a regenerator.

Nevertheless, the research on a liquid salt solution dehumidifier is limited to laboratory-scale experiments rather than practical applications in buildings [15]. A packed-column absorber (**Fig. 7**) that operates in the falling-film mode is the most popular design used in liquid desiccant dehumidifiers due its high effectiveness and low pressure drop [21]. In this design, the humid air is brought into direct contact with a concentrated salt solution to absorb the moisture. Due to this, there is a high risk of solution carryover into the airstream. Inhaling air contaminated with salt particles can cause problems in the human respiratory system. Problems such as salt crystallization and corrosion should also be addressed for practical applications [15,22,23].

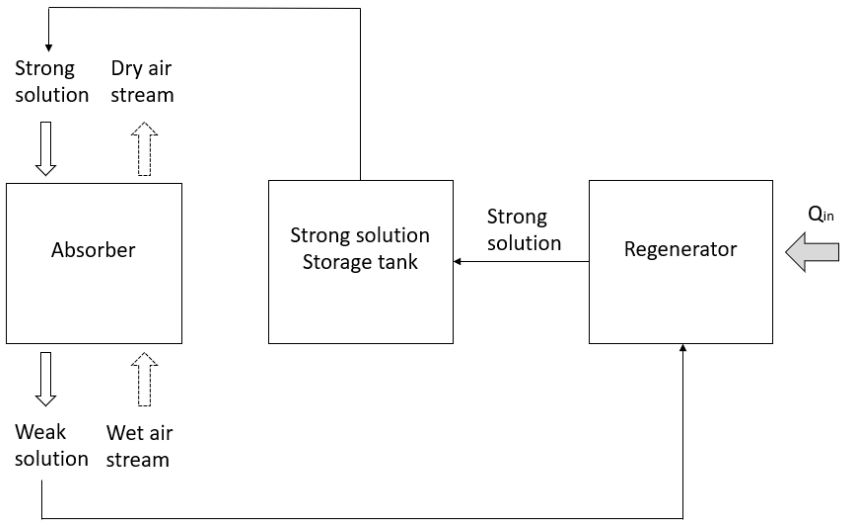

Fig. 6: A schematic of a typical liquid desiccant dehumidification system.

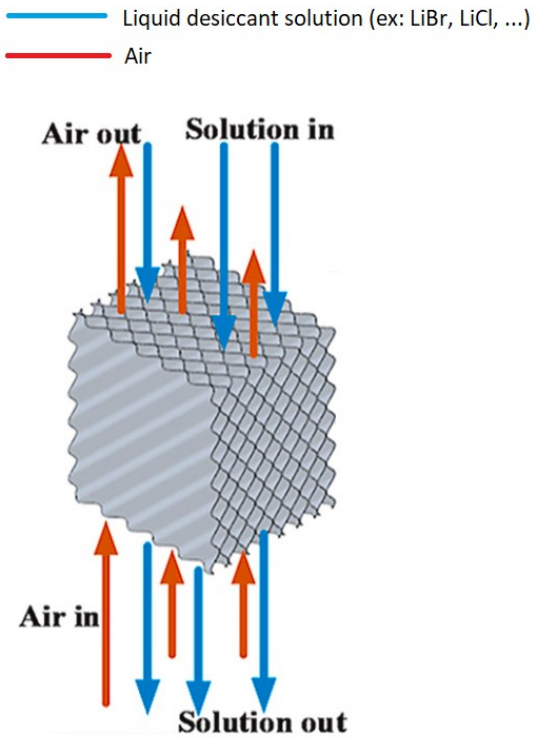

Fig. 7: A packed column absorber [24].

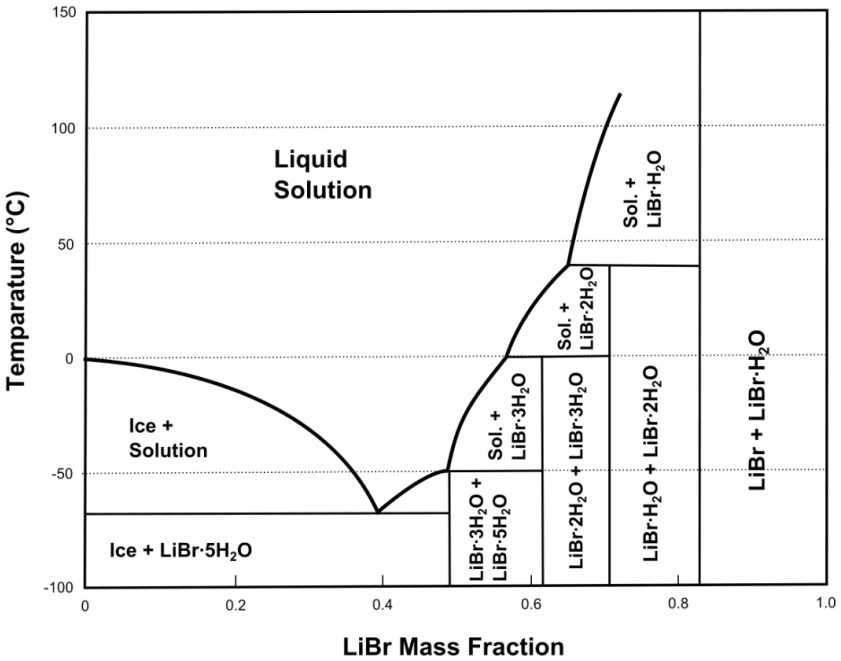

Fig. 8: A phase diagram of a lithium bromide (LiBr) salt [25].

Fig. 9: The crystallization of a LiBr salt [26].

Crystallization is considered to be a major issue in absorption systems. For hygroscopic salts, there is a specific minimum solution temperature at any given salt mass fraction below which the salt will begin to crystallize out of the solution (see **Fig. 5**). The mass fraction threshold after which crystallization happens varies between salts (60% for LiBr and 45% for LiCl and $CaCl_2$) at the standard 25 ^oC temperature. This threshold can be identified from the phase diagram of the salt. For example, the phase diagram for a LiBr salt is shown in **Fig. 8**, which shows the different phases of the salt at different temperatures and (salt) mass fraction values. **Fig. 9** is presented to show how the crystallized LiBr salt looks like in absorption systems. Crystallization should be avoided in liquid flowing systems because it leads to the formation of solids that can block the piping network and cause damage to the pumping system. Dissolving the crystallized salt to restore the absorber operation is a labor intensive and time consuming process [27,28]. Developing a reactor that can work in the crystallization region allows a significant increase in the reactor working capacity.

It is clear from the above discussion that the absorber is a vital component of any absorption system and has the most significant impact on the size, cost, and efficiency of that system. Therefore, there is a need for a new compact and efficient absorber design concept that eliminates the fundamental and technical restrictions. The new reactor concept should provide high sorption capacities and absorption rates, be able to work in the crystallization region, and solve the issues related to solution carryover.

1.2. Key Performance Indicators

The key performance indicator (KPI) used to measure and assess the performance of the absorption dehumidifiers is the moisture removal rate per internal volume of the absorber (*MRR*, g/s-m^3), defined as:

$$MRR = \frac{\text{Rate of moisture removal}}{\text{Volume}} = \frac{\dot{m}_a \left(\omega_{a,i} - \omega_{a,o} \right)}{\text{Volume}} \quad 1.1$$

where, $\dot{m}_a$ is the mass flow rate of the humid air, and ω_i and ω_o are the inlet and outlet humidity ratios of the air, respectively. The typical values for the moisture removal rates for the state-of-the-art packed-column absorbers that use LiBr hygroscopic salt are within the 20-35 g/s-m^3 range.

The dehumidification coefficient of performance (*DCOP*, -) is another KPI that can be used to measure the power consumed to achieve the required moisture removal rate (i.e., the ratio between the latent heat to energy input). Mathematically, the coefficient of performance is expressed as:

$$DCOP = \frac{\text{Latent heat removed}}{\text{Energy input}} = \frac{\dot{m}_a h_{fg} \left(\omega_{a,i} - \omega_{a,o} \right)}{\text{Energy input}} \quad 1.2$$

1.3. Research Objectives

The main objective of this research is to develop a new concept for compact absorbers and provide fundamental understanding of the heat and mass transfer inside the proposed absorber design. The milestones of the present work are summarized as follows:

- to develop a novel design concept for efficient and compact absorption reactors with a surface-to-volume ratio (up to 12,000 m^2/m^3) to achieve high moisture removal rates (up to 135 g/s-m^3);

- to eliminate the practical challenges, such as solution carryover, crystallization, and corrosion that are associated with the liquid absorption system and hinder its utilization in real dehumidification applications; and

- to build a bench-scale demonstration as a proof-of-concept and evaluate its performance for dehumidification applications under typical working conditions.

2. Literature Review

2.1. Introduction

The absorber (or the reactor) is the most critical component of the absorption systems, and it has a significant impact on the size, cost, and efficiency of the system. High absorption rates are vital for having efficient and compact absorber designs, and hence cost-effective systems.

This chapter is dedicated to a literature review on the common absorber designs to provide insight on their working principles, design, operational challenges, and limitations. The presented review only focuses on the absorber designs that can be used for water-hygroscopic salt solution pairs (ex: H_2O-LiBr), and designs that involve using other working pairs are out of the scope of this thesis. Due to the complex nature of the absorption process, none of the existing analytical or numerical models can used with confidence to predict the process accurately [29,30], therefore, the presented review herein is focused on experimental studies with significant impact. Further detailed information about absorber designs and mathematical modeling can be found in the published literature, e.g., Ref. [29,31–33].

2.2. Packed Column (falling-film) Absorbers

Absorption packed-bed column/towers are widely used in petrochemical, pharmaceutical, and carbon capture industries. The large specific surface area (per volume) available for the absorption process (200-600 m^2/m^3 [34–39]) and the long reactant contact time make the packed column one of the most compact and efficient reactors [23]. This type of absorber is also known for its simple design, low capital cost, low pressure drop, low operating and maintenance costs [40]. **Fig. 10** shows the layout of a typical packed-bed absorption column. It consists of a hollow column that is filled with small packing inserts that provide the surface area for the reaction. The inserts can have various shapes and they can be made out metal or corrosion-resistant materials like plastics and ceramics [41]. The liquid sorbent solution is distributed from the top of the column and flows down to the bottom due to the gravity. This reactor design does not require an internal component (i.e., a heat exchanger) to remove the heat of absorption (other than the sorbate steam), therefore, the liquid solution is subcooled before it is fed into reactor in order to enhance the absorption potential. The sorbate (gas or vapor) stream is often introduced from the bottom and flows in a counter flow to react with the sorbent. The reactants can also be introduced in cross-flow fashion.

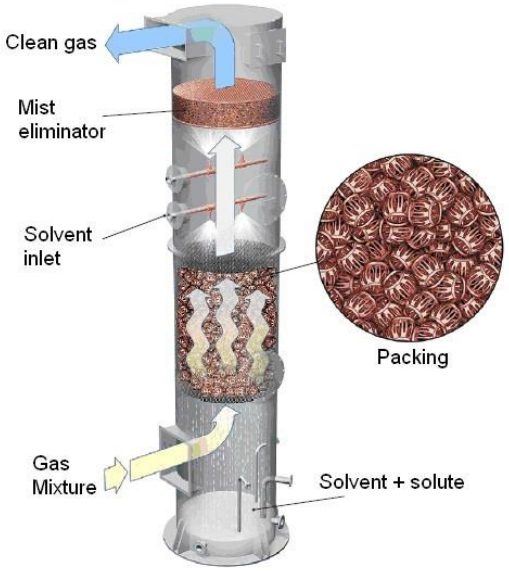

Fig. 10: The layout of a typical packed-bed absorber [42].

A packed-column absorber works on the falling-film mode in which the distributed liquid sorbent forms a liquid film to absorb the sorbent. The main mass transfer mechanism in this mode of operation is the diffusion, which is a rather slow process. The packing inserts create turbulence in the liquid flow and refresh/renew the interface of the reaction to improve the mass transfer [40]. However, it is the thickness of the formed film which mainly dictates the absorption rate, performance, and the size of the reactor [43]. The characteristic dimension of falling films is on the order of 1 *mm* [44]. Thinner films reduce the (diffusion) mass transfer resistance and result in faster absorption rates and more compact designs. The absorption rate in a packed-column absorber using hygroscopic salt solutions ranges between 0.2 to 3 *g/s* [34–36,39,45–47].

Although there have been some efforts to investigate the performance of the packed-column absorber in indoor applications such as dehumidification [34,48–52], the major concern in using this type of reactors in such applications is the risk of solution carryover by the forced sorbate stream [2,53]. Packed-column absorbers require high solution flow rates to achieve good wetting in order to avoid the decrease in efficiency due to the reduction in the reaction surface-to-volume ratio [23]. This requirement makes this type of absorber unsuitable to handle the low flow rates in indoor applications such as dehumidification. Higher flow rates increase the risk of solution carryover which can cause respiratory problems.

2.3. Spray Absorber

A spray absorber works on the principle of breaking the liquid absorbent solution into small droplets using nozzles. The working principle of a typical spray absorber is illustrated in **Fig. 11**. This reactor can have a different configuration in which the liquid solution is introduced as atomized drops [54], free-falling drops [55], liquid in the form of a flat (fan) [55,56] or conical sheets [57] as depicted in **Fig. 12**. The formation of small fine droplets reduces the mass transfer resistance and considerably enhances the reaction surface area. It is only the mass transfer that occurs inside the reactor, while the heat of absorption is transferred externally using a separate conventional single-phase heat exchanger. The separation of the heat and mass transfer process gives spray absorbers the advantage of being compact and cost-effective [23,58].

The early studies indicated that the absorption effectiveness of spray absorbers is not high [59,60]. Due to the small residence time, the slow diffusion process limits the mass transfer to the core of the formed droplets from the sprayed solution, therefore, equilibrium is not reached [40]. There are some studies that were conducted to understand the absorption process in spray absorbers. Warnakulasuriya and Worek [61] experimentally investigated the enhancement in absorption rate by increasing the reaction area using the atomization concept. In the experimental setup, a single nozzle was used in atomizing a salt solution for water vapor absorption. The size and velocity of the droplets were measured using a laser system. An analytical model, based on the "Newman absorption model" [62], was developed to predict the enhancement in the transfer rates. The experimentally measured droplet sizes were found to be 20% larger than expected from the analytical model, which was attributed to the effect of surface tension on reducing the surface area to form smaller drops. The results revealed that although increasing the sub-cooled levels (lowering the temperature) of the sprayed solution before the inlet of the reactor enhances the absorption rate, this enhancement is not tangible because lower temperatures result in higher viscosities which leads to shorter droplet residence time.

In another work, Warnakulasuriya and Worek [63] investigated the feasibility of forming droplets with a 300 μm diameter from a highly viscous LiBr solution using swirl-jet nozzles. A spray reactor working under the low-pressure of 1.23 kPa was built, and various swirl-jet nozzles were tested. The differential pressure across the nozzles was varied from 50 to 200 kPa to achieve flow rates between 0.018 to 0.043 kg/s. The tested nozzles were able to produce droplets with an average diameter of 375 μm - 425 μm. The experimental results showed that increasing the differential pressure across the nozzles decreases the drop sizes, but it also increases the velocity of the drops. The smaller drop size is favourable to increase the reaction surface area which enhances the absorption rates. On the other hand, higher velocities result in shorter residence time and lower absorption rates. Despite these counteracting effects, the authors [63]

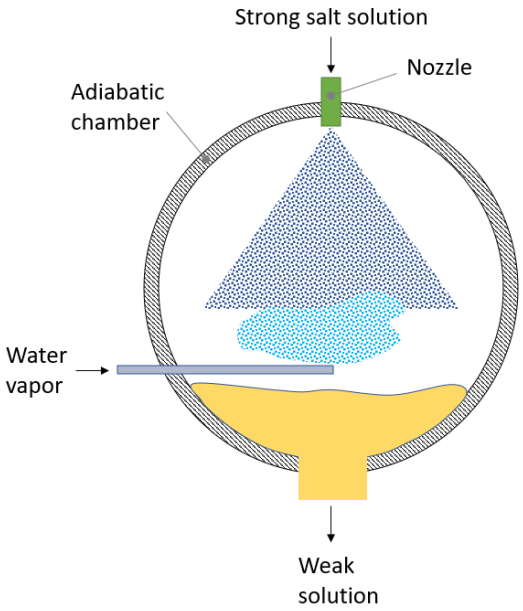

Fig. 11: The layout of a spray absorber (Recreated from [58]).

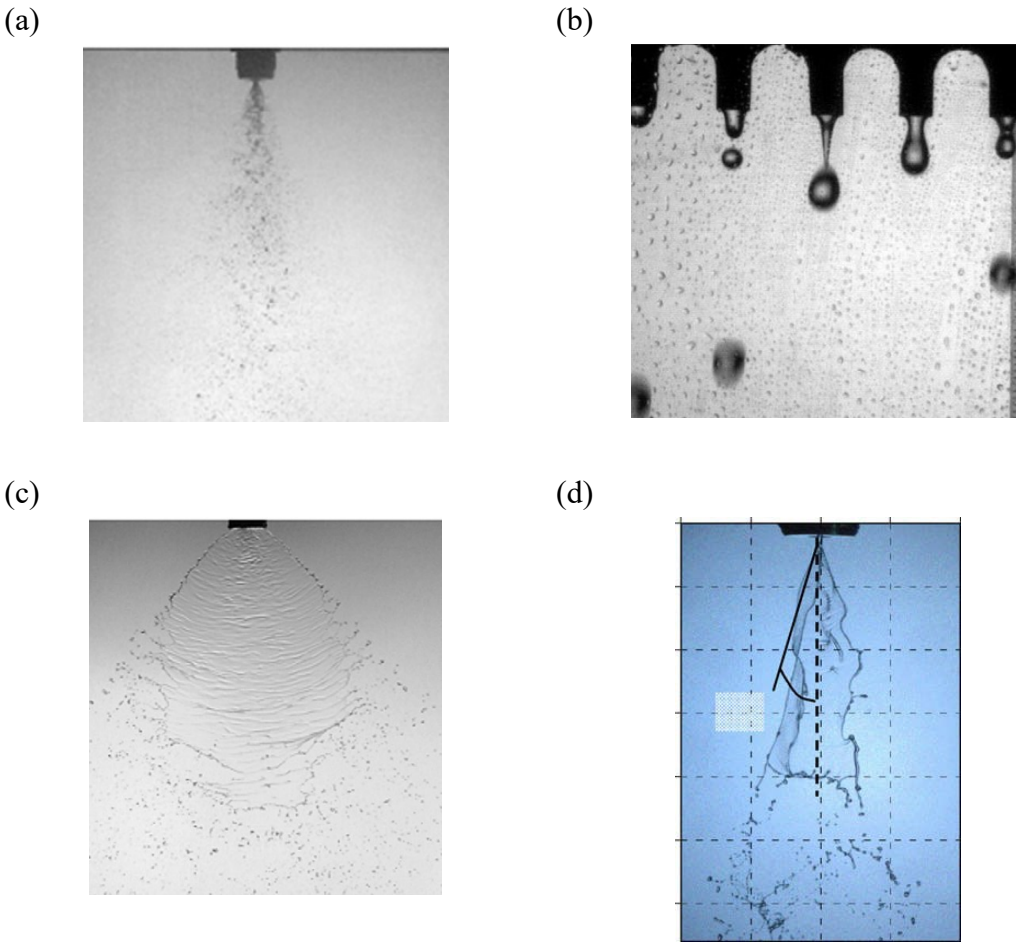

Fig. 12: Configurations in a spray absorber: (a) atomized droplets [54]; (b) free-falling drops [55]; (c) flat fan sheet [55]; and (d) a conical sheet [57].

concluded that the production of small droplets caused by increasing the differential pressure across the nozzles (thus, increasing the velocity of the drops) is still favourable for high viscous solutions with the tested nozzles. The results indicated that increasing the solution viscosity has no major effect on the droplet size, but it reduces the spray angle, hence, increases the droplets speed. It was also found that the nozzles that create higher swirl (angular velocity) form smaller droplets.

Gutiérrez et al. [55] tested two spray absorber configurations, namely, a free-falling droplets configuration (**Fig. 12b**) and a fan sheet configuration (**Fig. 12c**) for a LiBr-water chiller. The experimental results revealed that the fan-sheet configuration had a better performance than the free-falling droplets configuration, which can result in a 50% reduction in the size compared to the conventional tube-bundle absorber.

Palacios et al. [56] conducted an experiment to evaluate the absorption rate in a spray reactor with a flat-fan sheet configuration for LiBr-water absorption air-conditioning systems. The liquid solution flow rate was varied between 0.023 to 0.054 *kg/s* with a differential pressure drop in the 40-250 *kPa* range across the nozzles. The total surface area of the reaction (solution-vapor interface) was calculated by adding the interface area of the liquid sheet to the overall area of the droplets (generated during the disintegration), which were both measured by the analyzing the images of the back-illuminated spray. The experiment showed that absorption takes place primarily in the liquid sheet, and the contribution of the formed droplets after disintegration was secondary. It was also found that the flat sheet configuration was more favourable than the atomization configuration in terms of the solution residence time, reaction surface-to-volume ratio, and the differential pressure drop (energy consumption). For a 100 *mm* long absorption chamber, over 0.8 *g/s-l* (per chamber volume) of vapor were absorbed, which was an order of magnitude higher than the value for the conventional tube-bundle falling-film absorber. The study concluded that spray absorbers with a flat-fan sheet configuration exhibited a higher absorption rate compared to the conventional tube-bundle falling-film absorber and spray absorber with an atomization configuration. The authors [56] noted that the absorber can be designed to be five times smaller in size if a spray absorber with a flat-fan sheet was used instead of a tube-bundle falling-film absorber.

A spray absorber with an injected lithium bromide aqueous solution in the form of conical-sheet (**Fig. 12d**) using a hollow cone spray nozzle was studied by Palacios et al. [57]. The solution was sprayed at mass flow rates ranging from 0.0078 *kg/s* to 0.0116 *kg/s*. The corresponding pressure drop range in the injection nozzle was 90 *kPa*-250 *kPa*. The absorption rate was determined by energy balance calculation using the measured values of the flow rate of the injected solution and the temperature rise due to the absorbed heat. The total surface area of the reaction was calculated using the same methodology reported in Ref. [56]. The experiments showed that the absorption

was far from equilibrium before sheet disintegration, indicating that the generated droplets after liquid break-up plays a significant role in the abortion process. The authors [57] reported absorption rates that were orders of magnitude higher than the reported values for the conventional tube falling-film absorber and the spray absorber with atomization nozzles. They attributed this superior performance to the effect of fluid movement in the conical sheet formation enhancing the mass transport process. It was also noted that the power demand to overcome the pressure drop in the hollow conical nozzles was less than that of the atomization nozzles. The authors [57] recommended that the reactor length should not exceed 75 *mm* in order to achieve a minimum of 1 *g/s-l* vapor absorption rate per reactor volume.

Although spray absorbers provide high surface-to-volume ratios (10 times that of the conventional falling-film absorbers), they require additional work to inject the solutions. There is also restriction on the working capacities, as the flow rate that can be handled by the injectors is limited to some extent [64]. Another drawback of spray reactors is that there is a fair chance of solution carryover if there are used in dehumidification systems [60]. However, the major obstacle in using spray absorbers with the (high sorption capacity) hygroscopic salt solutions is the possibility of salt crystallization which would block the spray nozzles.

2.4. Tube-Bundle (falling-film) Absorber

The tubular absorber is mainly used in closed-cycle absorption systems. It is regarded as the key component in these systems that determines the overall efficiency and cost of the system. It is the largest component in the these systems occupying around 25% of the total system's volume [65], and its heat transfer area accounts for up to 40% of the entire heat transfer area [66]. Unlike packed-beds and spray reactors, the tubular falling-film reactor offers the possibility of transferring the heat of absorption out of the solution during the process through the wetted surfaces of the tubes [67]. The complex coupled heat and mass transfer in this component is not fully understood [29], and its design is based on empirical results [68]. This component is often oversized to ensure the proper operation of the system, resulting in heavy and costly equipment [68,69].

A tubular falling-film absorber consists of tubes that can be arranged in a horizontal (**Fig. 13a**) or vertical (**Fig. 13b**) orientation. In either configuration, the reactor is set to work in the falling-film mode. The tube-bundle horizontal absorber is the most widely used design in conventional absorption systems because it its stable operation [58], and because it is easy to install, better in dealing with liquid distribution, and has a lower manufacturing cost [70]. A schematic for the tubular reactor with a horizontal configuration is shown in **Fig. 13a**. In this configuration, the solution is introduced via a distributor at the top of the reactor. The solution falls due to gravity over the outer

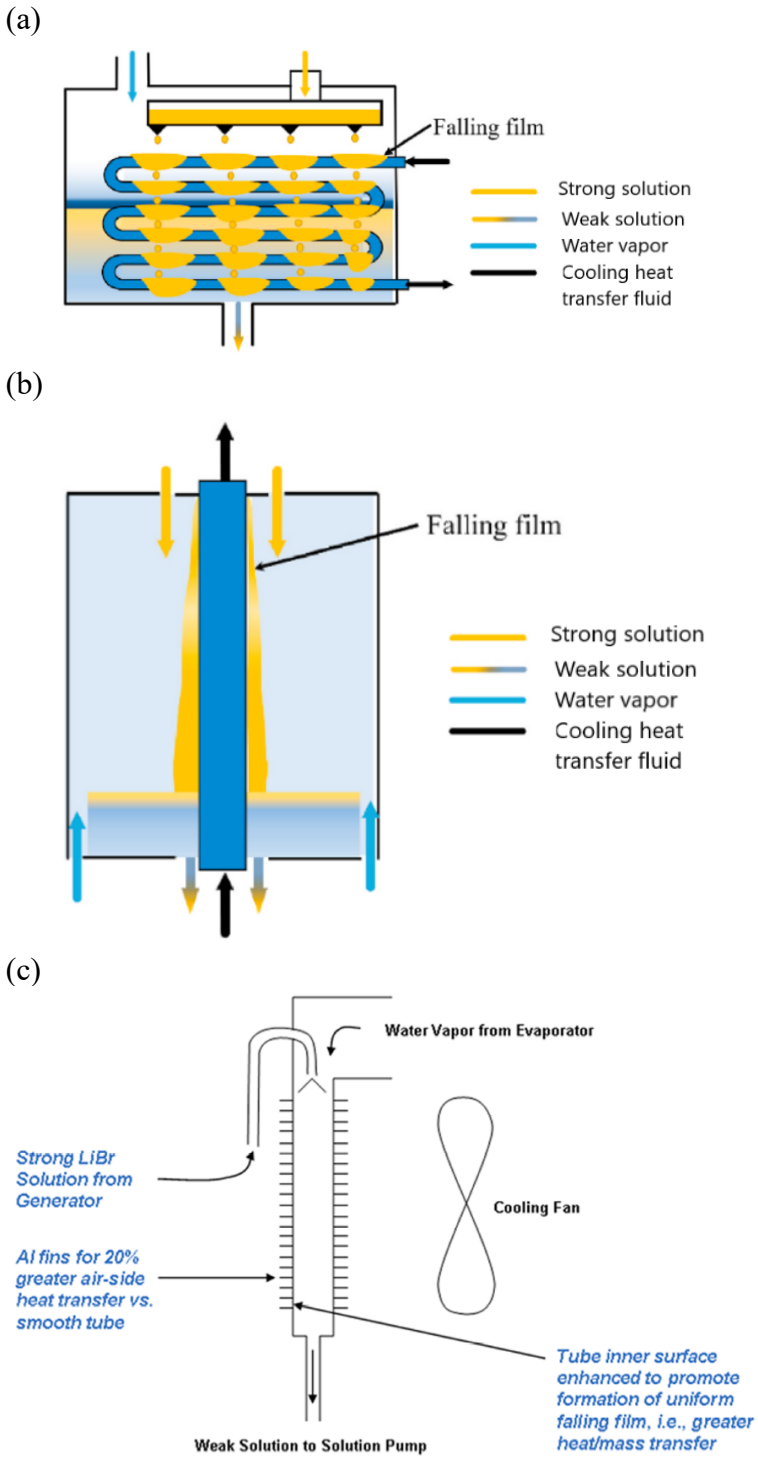

Fig. 13: A tubular falling-film absorber: (a) a horizontal configuration; (b) a vertical outer solution flow configuration; and (c) a vertical inner solution flow configuration [71].

surface of the horizontal tubes surrounded by a (stagnant) pool of water vapor. The absorption takes place as the solution falls from the top to the bottom of the reactor. Cooling heat transfer fluid is circulated inside the tubes (usually in serpentine form) to

remove the released heat of absorption at the liquid-gas interface that would otherwise impede the absorption process.

Despite the aforementioned advantages of reactors with a horizontal tubes arrangement, the uniform distribution and the complete surface wetting of the tubes is difficult to maintain in this configuration due to the flow instabilities [59,70]. As the solution flows downward, the wetted tube surface gradually decreases and some tubes might reach a 'dry-out' condition [70]. In some cases, only 50% of the total tubes' surface area participates actively in the absorption process to provide a contact area for the reactants [72]. The reduction in the reaction surface area greatly affects the absorption process and poor wettability results in poor reactor performance. The wettability problem is further exacerbated when a solution such as a lithium bromide solution is used in high concentrations [59]. The surface wettability can be improved by increasing the flow rates, but beyond a certain optimum value, this will result in a thicker solution film and increased heat and mass transfer resistances in the liquid side [32].

The schematics for vertical tubular falling-film absorbers with a liquid solution flowing on the outer and inner surface of the tubes are shown in **Fig. 13b** and **Fig. 13c**, respectively. In either arrangement, the tubes are oriented vertically, and the liquid solution flows downward due to the gravity and absorbs the ambient water vapor. The cooling medium (to remove the heat of absorption) flows inside the tubes in the arrangement shown in **Fig. 13b**, while cooling is done on the outside surface of the tubes in the arrangement depicted in **Fig. 13c**. The latter design offers the possibility of using air as a cooling medium which eliminates the need for the large cooling towers usually required in closed-cycle absorption systems [30,33,73]. Unlike the falling film in horizontal tubes in which the solution flow is laminar, in the vertical falling-film, the solution often flows in a wavy-flow regime which is known to significantly enhance the absorption rate [67,74]. The wavy motion caused by the hydrodynamic instabilities breaks the thermal and concentration boundary layers which considerably enhances the heat and mass transfer [75]. Although tubular vertical configurations provide surface-to-volume ratios, the formation of thin films to reduce the mass transfer resistance is difficult over long reactors [60].

For tubular reactors working with a lithium bromide solution in the falling-film mode, studies have shown that the non-dimensional Lewis number, defined as the ratio of thermal diffusivity to mass diffusivity, is on the order of 10^2. This relatively high Lewis number means that the solution concentration boundary layer is slowly developing compared to the thermal boundary layer. In another words, while the heat is transferred more rapidly across the film, the absorbed mass (water vapor) tends to remain at the gas-liquid interface inhibiting the absorption of additional vapor molecules [75,76]; suggesting that the focus should be on improving the mass transfer

to enhance the absorption rate and its performance. Research studies on the mass transfer resistance in both (salt) liquid solution and gas phases concluded that, the resistance in the solution side that was the dominant hurdle [33,44,77]. For reactors working on the falling-film mode, the formation of a relatively thick liquid solution film presents a significant resistance in both heat and mass transfer [43]. Thicker film results in higher interface temperature and solution vapor pressure, therefore, the mass transfer due to the reduced (pressure) driving force will be limited [76]. The thickness of the film in the falling-film mode, dedicated by the hydrodynamics of the film, was on the order of 1 *mm* [44]. The available surface area for the heat and mass per volume of the tube-bundle horizontal reactor was reported to be within the 70-500 m^2/m^3 range [78].

To enhance the heat and mass transfer in the tubular absorbers, three modifications have been suggested in the open literature as reported by Islam et al. [79]. The first suggested modification was to use modified surfaces (like fins or protrusions) to the external surface of the tubes to increase the wetted surface area (for reaction) and facilitate the formation of stable film. Yoon et al. [80] experimentally evaluated the performance of a LiBr-H_2O tubular horizonal absorber with various tube types, namely, bare tube, bumping bare tube, floral tube, and twisted floral tube. All tested tubes had the same length of 0.4 *m*. The experiments showed that absorption fluxes generally increased by increasing the solution flow rate. However, there was an optimum flow rate of 0.03 *kg/s-m* (per unit tube length) after which the performance started to decline, regardless of the tube type. That was attributed to the increased thermal resistance due to the thickened formed film. At the optimum flow rate, the twisted floral tube showed the best performance in terms of heat and mass transfer while the bare tube was reported to have the lowest performance. In another study, Zhang et al. [81] experimentally investigated the heat and mass transfer in LiBr-H_2O falling-film absorber with various horizontal tubes (bare tube, floral tube, and floral finned tube). The tested tubes had a 0.5 *m* length, with a surface area (per tube length) of 0.0502 m^2/m, 0.0511 m^2/m, and 0.0567 m^2/m for the bare tube, floral tube, and floral finned tube, respectively. The results from this study were in agreement with the previous study conducted by Yoon et al. [80] in terms of the existence of an optimum flow rate to achieve high heat and mass transfer.

Miller et al. [76] investigated the use of advanced surfaces to enhance the heat and mass transfer for a LiBr vertical absorber. The study compared the performance of tubes with pin fins, fluted tube, grooved tubes, twisted tubes, with the smooth tube as a benchmark. Experiments showed that the pin-fin tube with a 6.4 pitch exhibited the best performance in terms of absorption rate. At a liquid film Reynolds number (Re) of 150, the measured absorbed mass fluxes were 2.75×10^{-3} kg/m^2-*s* and 1.4×10^{-3} kg/m^2-*s* for the pin-fin tubes and smooth tubes, respectively. The second-best performance was

achieved using the grooved-tube absorber resulting in a 175% enhancement in the absorbed mass compared to the smooth tube.

An experimental study was conducted by Ma et al. [82] for a spiral tube vertical absorber that had the size of 3000 *mm* × 25 *mm* × 1.5 *mm* × 40 *mm* × 3 (length × outer diameter × thick × pitch × number of grooves). The experiments were conducted for solution Reynolds numbers within the 200-500 range, and for mass transfer fluxes in the $6x10^{-3}$ kg/m^2-s to $10x10^{-3}$ kg/m^2-s range.

Although enhanced tubes are commonly used in conventional heat exchangers, they are not used in absorption systems because of the large increase in the manufacturing cost associated with these tubes [68]. The second type of modification to enhance heat and mass transfer rates is achieved by creating hydrodynamic instabilities in the flow by adding surface-active agents (surfactants) [83,84]. Kashiwagi et al. [85] used the term "Marangoni convection" to describe the induced interfacial turbulences caused by the local variations in the surface tension when a small amount of surfactant is added to the liquid solution. The interfacial turbulence creates mixing within the liquid layers and refreshes/renews the interface of the reaction for improved heat and mass transfer rates. The experimental data presented by Kim et al. [86] showed that the mass transfer was enhanced by a factor of 2.5 using a 60% LiBr aqueous solution with a 100 ppm 2-ethyl-hexanol surfactant compared to the base solution without the addition of the surfactant. Kang et al. [87] investigated the addition of iron (Fe) nanoparticles and carbon nanotubes (CNT) with concentrations of 0.0, 0.01 and 0.1 wt % to a LiBr solution for heat and mass transfer enhancement. For both additives, the enhancement in the mass transfer was more significant than in the heat transfer. The study concluded that CNT is a better candidate additive than Fe nanoparticles as it resulted in a higher mass transfer enhancement.

Islam et al. [79] proposed the third type of modification to enhance the absorption rate in tubular absorbers by using the film-inversion concept. There are two distinct flow regimes for a flow over (horizontal) tube-bundle absorber; namely the falling-film flow regime and the inter-tube regime. The falling-film flow regime exists when the liquid film flows over the surface of horizontal tubes due to the gravity. After detaching from the tubes, the film falls down between the tubes in what is known as the inter-tube regime. The flow in the inter-tube regime can take on different forms such as droplet, jet, or sheet flow [70]. The concept of film-inversion is achieved by repeatedly inversing the surface of the falling-film in the inter-tube region by using guided vanes as illustrated in **Fig. 14**. The alternate surface inversion causes the relatively colder surface to come in contact with the vapor, which enhances the absorption rate. For a liquid solution at 26 ºC with a distribution density of 0.0595 *kg/m-s*, the absorbed vapor mass flux was 0.00213 kg/m^2-s for the film-inverting absorber, compared to the 0.00406

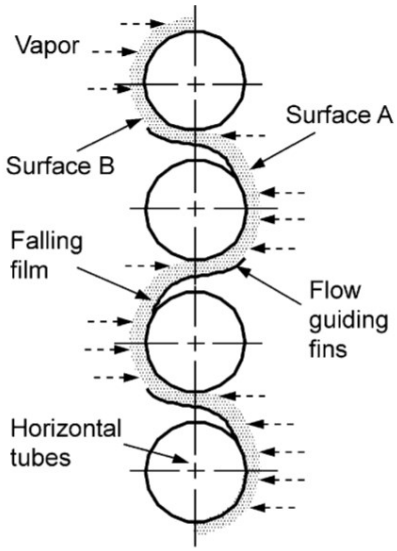

Fig. 14: A film-inverting falling film absorber [70].

kg/m²-s value for a conventional horizontal tube-bundle absorber, i.e., a 90% enhancement.

Although the proposed film-inverting concept can result in a 100% increase in the absorption rate compared to the conventional LiBr horizontal tube-bundle absorber configuration, nevertheless, the design of a practical film-inverting absorber needs further development as the design of the guide vanes and their location is tedious [70].

2.5. Rotating/Spinning Absorber

The rotary absorber relies on the concept of using centrifugal force to reduce the film thickness to reduce the heat and mass transfer resistance. In this approach, the rotary absorber replaces the gravitational acceleration in a falling-film absorber with centrifugal acceleration to achieve thinner films. The absorber can take on the form of a rotary drum (**Fig. 15a**), spinning disc (**Fig. 15b**), or rotary coil (**Fig. 15c**). Further information about the working principles of these absorbers can found in the cited references [88–90]. Although rotary absorbers have been considered for LiBr absorption systems [90–92], there is scarce information about the detailed performance data of these absorbers.

Aoune et al. [93] theoretically and experimentally investigated the heat and mass transfer characteristics of a brass spinning disc absorber with a 2.5 *cm* thickness and a 50 cm diameter rotating at 900 rpm. Although absorption fluxes can be achieved at modest rotational speeds, the tests showed that performance decreases significantly at high solution viscosities. The experimental mass fluxes were found to be higher than the predicted values by the penetration theory [94], and this was attributed to the enhancement due to the mixing within the film.

(a)

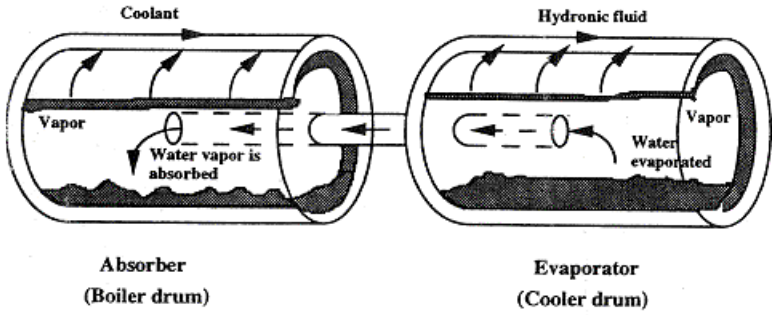

(b)

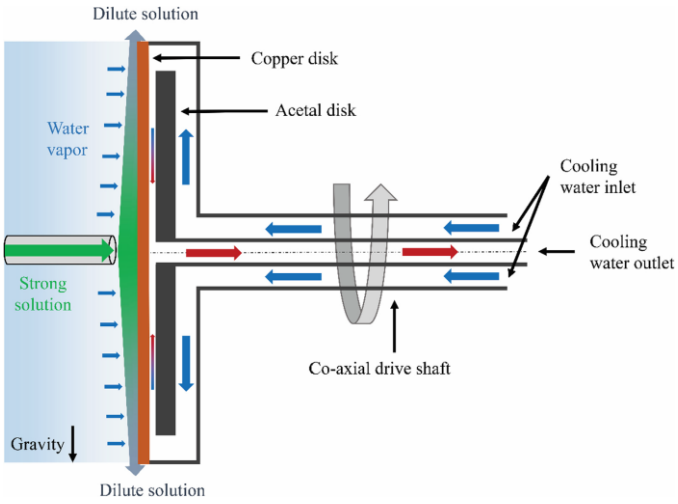

(c)

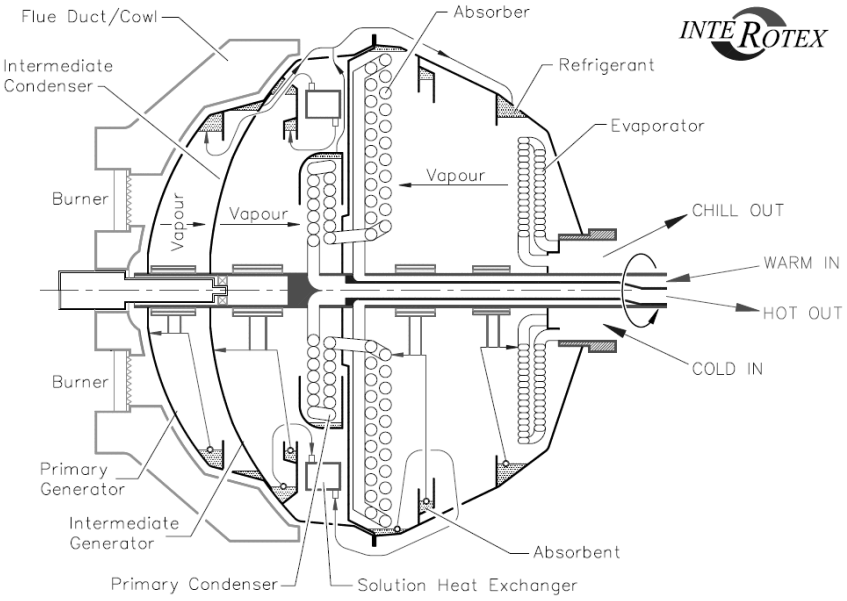

Fig. 15: Rotary absorber designs: (a) a rotary drum [89]; (b) a spinning disc [88]; and (c) an absorption machine with a rotary coil [90].

Bangerth et al. [88] conducted a detailed study on a 6.35 *mm* thick flat spinning disc absorber with a 30 *cm* diameter using an aqueous LiBr solution. The measured vapor absorption fluxes were 5.5 times higher when compared with that reported by Kyung and Herold [95] for a conventional horizontal tube-bundle absorber. The authors [88] noted that this enhancement was achieved at higher solution flow rates than those for a conventional tube-bundle absorber. The same authors examined the performance of the same spinning disc absorber but with an enhancement in the heat transfer of the coolant heat transfer fluid (water) side using manifold-microchannels [96]. The highest absorption rate reported in this study [96] for the tested spinning disc absorber was 0.016 kg/m^2-s, which is 5.3 times higher when compared to the average absorbed mass flux values for the conventional tubular absorber reported in the literature (0.001-0.003 kg/m^2-s).

Although, spinning disc absorbers can enhance heat and mass transfer rates, their performance can be strongly affected by solution flow rate and rotational speed [97]. In addition, the need for mechanical energy to rotate the absorber limits the design to small capacity systems [98].

2.6. Bubble Column Absorber

In this design, the absorbent solution flows inside a channel while the absorbate is bubbled through the absorbent stream using a vapor distributor. A set of orifices is often used as the vapor distributor. The heat of absorption is captured by circulating a coolant around the solution channel. The bubble dynamics, which are affected by surface tension, orifice diameter, orifice spacing, liquid concentration, and vapor flow rate play a significant role in the absorber's performance [98]. A schematic of a typical bubble absorber is depicted in **Fig. 16**.

The bubble absorber works in the bubble-mode, which is generally more efficient than the falling-film mode as it provides a very large liquid-vapor interfacial area and a good absorbent-absorbate mixing. The study conducted by Kang et al. [99] showed that the absorption rate in the bubble-mode is always higher than in the falling-film mode and can lead to a 50% smaller sized absorber design. The wettability problems associated with the falling-film mode does not exist in the bubble-mode because there is no need for liquid distribution. A bubble absorber is more suitable for applications that require low flow rates than the falling-film absorber, as the latter has poor wettability under such low flow rates which significantly reduces the absorption rates. The simple design of the bubble absorber means low capital and operating cost.

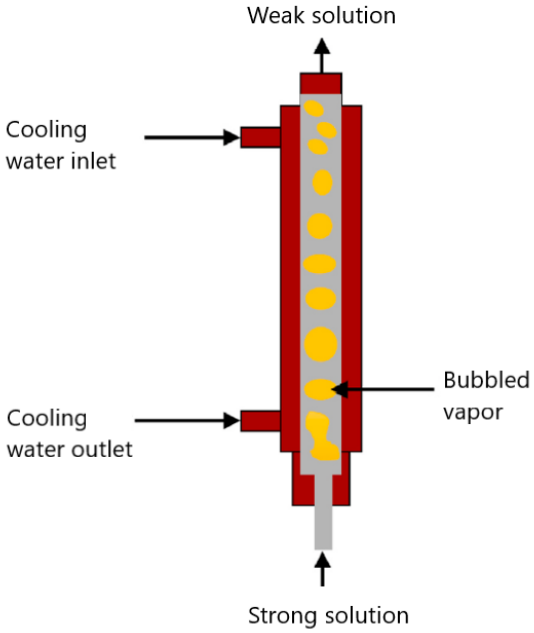

Fig. 16: A typical design of a bubble absorber [32].

Most of the studies in the open literature considered the bubble absorber for NH_3/H_2O absorption [100–107], R134a/Dimethylformamide [108,109], and R124/Dimethylformamide [110–113] systems, which is out of the scope of this research. The only experimental study that investigated the use of a bubble absorber for H_2O/LiBr systems is the study conducted by Donnellan et al. [114]. The authors [114] conducted an experiment using a bubble-column that was made of a glass cylinder that was 10 *cm* in diameter and 1 m in height. The cylinder contained a liquid solution of lithium bromide that filled 32 *cm* of the total cylinder length. The temperature of the solution was kept constant by circulating a coolant oil around the cylinder. Steam was injected in the bubble column via a needle valve. The generated bubbles were tracked using a high-speed camera.

Despite the aforementioned advantages, the bubble absorber is plagued with a high pressure drop in both the liquid and vapor phases. In addition, the hydrostatic pressure of the liquid column can have an adverse effect on absorption rates, which puts restrictions on the absorber's height and capacities. Moreover, the bulk flow of the liquid makes the absorption heat transfer to the surrounding coolant more difficult compared to the falling-film mode [98].

2.7. Membrane-based Absorber

In a membrane-based absorber, the absorbent solution is confined in a narrow channel between a membrane sheet and a heat transfer plate. The thickness of the confined liquid solution inside the channel is on the order of microns, therefore, the very thin solution layer has lower heat and mass transfer resistance compared to that of a falling-film absorber. The membrane sheet allows only the water vapor to pass through, while it prevents the absorbent solution transfer to the other (water-vapor) side of the membrane. The heat of absorption is transferred to a heat transfer fluid via the heat transfer plate. The membrane-based absorber has the ability to control the solution film thickness (which affects the mass transfer) and solution flow rate (for adjusting the capacity) independently [115]; a unique feature that other absorber designs do not offer. **Fig. 17** shows a schematic of a typical membrane-based absorber.

Ali and Schwerdt [116] investigated the characteristics and properties of microporous hydrophobic, both experimentally and analytically, to investigate their influence on the water vapor absorption rate into a thin layer of aqueous LiBr solution. The study considered various polytetrafluoroethylene (PTFE) hydrophobic membranes with various thicknesses and average pore sizes. The results indicated that the desired membrane characteristics were high permeability to water vapor, hydrophobicity to an aqueous solution to avoid wettability of membrane pores, and no capillary condensation to avoid the blocking of pores. The study concluded that for practical uses, the membrane should have a thickness smaller than 60 μm, a mean pore size about 0.45 μm, and 80% porosity. Based on this study [116], Ali [117] presented an analytical study for designing a compact plate-and-frame absorber using a hydrophobic microporous membrane for absorption chillers. The results indicated that the thickness of the solution channel was the most significant parameter that affected the compactness of the absorber. Smaller solution channels were favourable to achieve a higher surface-to-volume ratio.

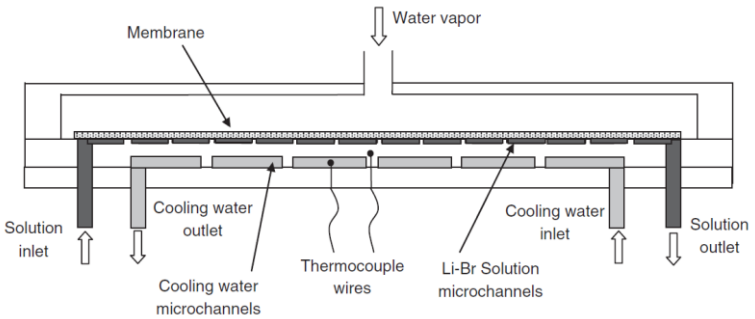

Fig. 17: A typical design of a membrane-based absorber [115].

Isfahani et al. [115,118] conducted an experimental study on absorption chiller systems that used highly porous nanofibrous membranes in the absorber. The authors noted that the experimental value for the absorption rate flux (0.006 kg/m^2-s) is 2.5 times higher than in a falling-film absorber. Isfahani et al. [119] also investigated the enhancement of the absorption rate by using microstructures to facilitate mixing in the LiBr solution channel. The study showed that higher absorption rates can be achieved with much wider channels compared to the absorber that did not include microstructures. The study recommended using microstructures in the solution channel for a membrane-based absorber to achieve lower pressure drops. Isfahani et al. [119] studied the water vapor absorption in an adiabatic (no heat removal) membrane-based absorber that had microchannels in the LiBr solution side. Various nanofibrous flat membranes with various pore diameters (0.45 μm and 1 μm) and thicknesses (25-175 μm) were tested. The study concluded that the solution mass transfer resistance dominated the process for a solution channel (film thickness) that was 150 μm long. The experimental study presented by Hernando et al. [120] for exactly the same absorber with microchannel studied by Isfahani et al. [119] showed that the absorption rate flux increased from 0.003 kg/m^2-s for the adiabatic mode to 0.005 kg/m^2-s when the heat of absorption was removed in the cooling-mode.

Studies have shown that membrane-based absorbers can enhance the absorption rates due to the thin solution (film) thickness and reduce heat and mass transfer resistance compared to the tubular falling-film absorbers. However, there are some challenges that should be overcome for their practical use. Membranes are usually prone to fouling and the risk for pore blocking increases with the use of salt solutions that can crystallize. Another reason that can result in the blocking of the pores is the condensation of water vapor. As the membrane thickness in these absorbers was thin (~100 μm), the design process should ensure that the mechanical strength requirements were fulfilled.

2.8. Summary of Literature Review

The presented literature review indicates that the research on liquid desiccant dehumidification systems is still limited to numerical simulations or laboratory-scale experiments rather than practical applications. The conventional liquid desiccant dehumidification systems have a major practical problem which is the risk of solution carryover by the forced sorbate stream [2,53]. Another key issue in working with absorption reactors is the crystallization of the salt solution that can block the piping network and damage the pumping system. The corrosive nature of the inorganic salt solutions also presents a limitation on the material that can be used to construct the reactor.

Although there are different absorber designs proposed in the literature, the ones that are used for dehumidification systems are the packed-column and membrane absorbers. **Table 1** provides a summary of the liquid desiccant absorbers used in dehumidification systems. One can conclude that packed-column absorbers offer more compact designs than the membrane absorbers as they tend to have higher moisture removal rates per volume (MRR, $g/s\text{-}m^3$). Also, the packed-column absorber is considered to be the most practical and mature design that can be used for dehumidification systems because of its simplicity and scalability. This design works in the falling-film mode in which a liquid film absorbs the water vapor as it falls from the top to the bottom due to the gravity. The main mechanism for the mass transfer in this type of reactor is the diffusion through the liquid solution film, which is a rather slow process and presents a fundamental limitation on maximum absorption rates (and realization of compact designs).

Based on the above observations, one can conclude that there is a need to develop a new reactor concept to address the abovementioned issues of the existing designs. The new design should:

- provide a high sorption capacities and absorption rates (i.e., high MRR values);
- be able to work in the crystallization region (to increase the working capacity);
- solve the issues related to solution carryover (to avoid respiratory health problems for indoor applications);
- provide flexibility in the design capacities (unlike the conventional absorbers); and
- have the ability to handle both low and high sorbate (water vapor) flow rates.

Table 1: A summary of liquid desiccant absorbers used in dehumidification systems.

Reference	Absorber Design	Liquid Desiccant	Specific Area [m^2/m^3]	Inlet air temperature [C]	Inlet air humidity [g/kg]	Moisture removal rate, MRR [$g/s\text{-}m^3$]
[35]	Packed-column absorber	LiBr	396	25.4-35.4	9.5-18.2	23.7-35
[35]		LiCl	396	26.9-35.1	9.8–20.4	20.9-48.95
[121]		LiCl	450	25-30	10.8-16.2	-
[53]		$CaCl_2$	608	30	18.873	-
[122]		LiBr	-	23.6-35.4	10.4-18.7	-
[47]		LiCl	210	30	18	7.6-17
[123]		LiBr	-	-	-	-
[124]		LiBr	-	23.6-35.7	11.2-22.8	-
[125]		LiCl	550	35	15	6.2-16
[39]		$CaCl_2$	390	31	18	8-24.2
[46]		$CaCl_2$	608	26.8-39.0	16-24	-
[60]		LiCl	-	26-31	10.5-17.9	-
[126]	Membrane absorber	LiBr	-	30	19	-
[127]		LiBr	-	35	19.4	-
[128]		LiBr	-	30	18	8.5-8.7
[129]		LiBr	-	35	17.8-25.26	2.5-5.6

2.9. Proposed Absorber Design

In this PhD program, a novel design concept for absorption reactors is proposed that can be used for dehumidification systems. The proposed reactor concept provides compactness (i.e., high moisture removal rates per volume), flexibility in the capacities, permits working in the crystallization region, and eliminates the metal corrosion associated with the corrosive hygroscopic salts. This is achieved by creating novel spherical microreactors by encapsulating an aqueous hygroscopic salt (like LiBr, LiCl, or $CaCl_2$) solution inside an elastic spherical semi-permeable membrane shell. This shell is highly permeable to sorbate but impermeable to the salt and its solution. The formed spherical microreactors (i.e., microcapsules) are highly uniform in size and can be designed to have a micro-scale size (500-1,000 μm diameter) and have an adjustable shell thickness. They provide high reaction surface-to-volume ratio that allows fast absorption rates, therefore, more compact reactor designs. As shown in **Fig. 18**, the proposed microcapsules offer surface-to-volume ratios between 6,000-12,000 m^2/m^3, which is up to two orders of magnitude higher than the conventional packed-column absorbers (200-600 m^2/m^3 [34–39]).

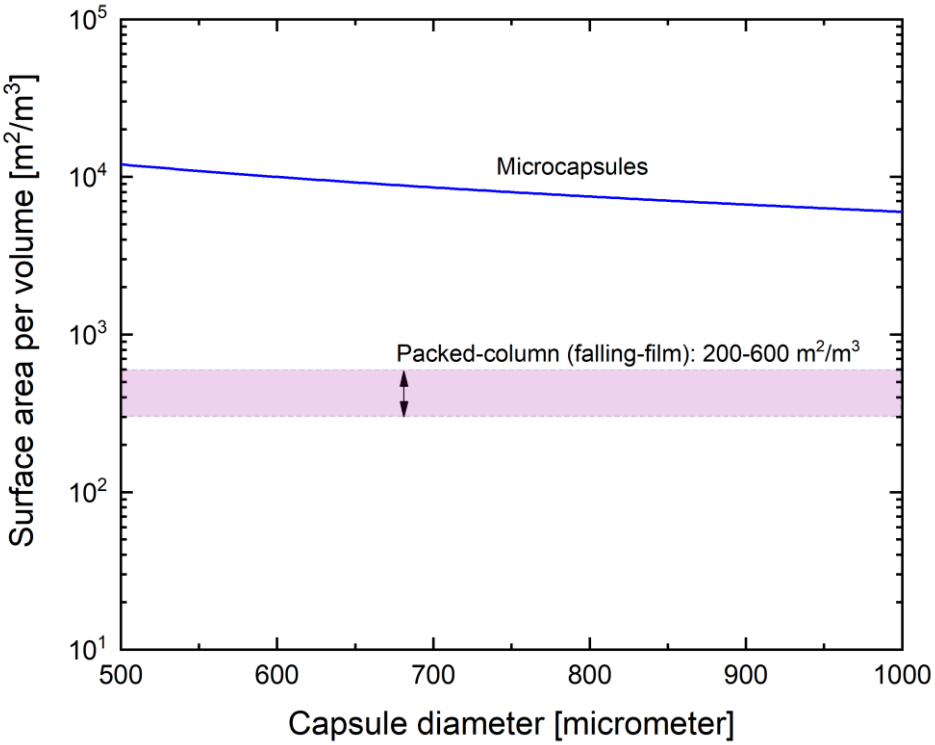

Fig. 18: The reaction surface area per volume for microcapsules and packed-column absorber [34–39].

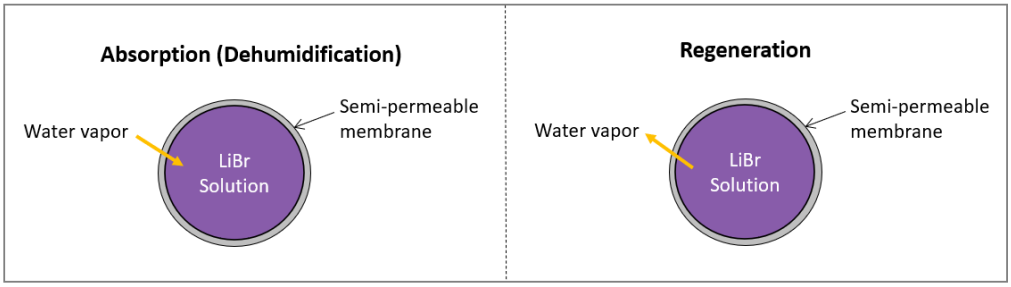

Fig. 19: Absorption and regeneration principles of the proposed spherical microreactor for dehumidification applications.

The working principles of the spherical microreactors during absorption (dehumidification) and regeneration processes is illustrated in **Fig. 19** . The sorbate (water vapor) diffuses through the shell and is absorbed by the absorbent (salt solution) in the absorption process. In the desorption process, heat is transferred to the capsule to desorb the water vapor in order to increase the salt concentration for the next absorption cycle.

3. Design, Synthesis, and Characterization of Spherical Microreactors

3.1. Introduction

In order to design a compact and efficient absorber based on the proposed spherical microreactors in Chapter 2, it is important to have control over the design parameters, namely, the diameter and shell thickness. These parameters play a key role in absorption rate and the mechanical requirements of the encapsulated spherical reactors [130]. Moreover, synthesizing microreactors with a uniform size enables performing fundamental studies focused on a single spherical particle to be extended and applied to the overall heat and mass transfer phenomena, thus, modeling and characterization of the reactor performance with high certainty.

The most conventional method to make encapsulated particles is the formation of emulsions by mixing; a process that involves the mechanical agitation of the immiscible fluids to create a shear force in order to break up the droplets. Although, this method was employed by some researchers [18,131], due to the non-uniform applied shear force of this method, the particles formed were highly polydisperse (non-uniform in size) and resulted in variable salt loading. These small particles (60–80 μm) with uncontrollable size cannot be used directly in dehumidification systems because they will result in a significant pressure drop. In addition, the formed shell using this method was rigid, and the experimental results have shown that the encapsulated liquid desiccant will start to leak when a certain humidity level is reached (as the fixed volume was overfilled), and this resulted in solution carryover. The experimental results also showed that the performance of the particles produced by this method would deteriorate because of the reduction in the sorption capacities and mass transfer due to particle agglomeration. Further, the formed particles prepared by this method had brittle walls which affected their mechanical properties and resulted in weak encapsulated particles [132].

Alternatively, a microfluidic technique enables the formation of encapsulated microspheres that are highly uniform in size. The encapsulation is achieved by designing and fabricating a custom-built microfluidic device to encapsulate the core aqueous salt solution inside a UV-curable resin that acts as the shell and becomes solid when exposed to a UV light source. A study on carbon dioxide (CO_2) capture using a similar encapsulation technique with an elastic shell has shown that the absorption rates for the encapsulated carbonate solutions were 10 folds higher than in a 1 mm thick film of a carbonate solution that usually forms in the conventional absorption reactors [133]. Therefore, in this study, this microfluidics method has been selected to fabricate the spherical microreactors to: i) enhance the moisture absorption rate (by significantly increasing the surface-to-volume ratio and reducing the diffusion length); and ii)

eliminate the challenges related to the solution carryover, crystallization and corrosion in the liquid absorption systems used in dehumidification applications.

3.2. Microfluidic Encapsulation

A microcapsule is a micrometer-scale particle, bubble, or liquid drop that is enclosed by a shell that acts as a barrier separating the core from the outer environment [130]. Microencapsulated aqueous liquid, which is the focus of this work, is created by making a water-in oil-in water (W/O/W) double emulsion. An emulsion is a colloid of two immiscible liquids, where one liquid contains a dispersion of the other liquid. It is a special type of mixture made by combining two liquids that normally do not mix. The single emulsion type includes water-in oil (W/O) and oil-in water (O/W) emulsions. Surface active agents (surfactants) are crucial for the long-term stability of the emulsions. The surfactant molecules migrate to the liquid-liquid interface and prevent droplet coalescence. High order emulsions, such as water-in oil-in water (W/O/W) or oil-in water-in oil (O/W/O), can be created using three fluids.

Microfluidic technology can be used to create emulsions with a controlled size and high precision. In such microfluidic devices, the liquids are introduced with precise specific flow rates to create one droplet at a time [134]. The droplet sizes are determined by the shear forces exerted by the precisely controlled flowing fluids; therefore, highly monodisperse drops are formed [130]. Based on channel geometries and fluid configurations, single-emulsion droplet formation in a traditional microfluidic device can be classified into three major categories, namely, cross-flow, co-flow, and flow-focusing.

In cross-flow (also know as the “T-junction”), the dispersed phase is injected perpendicularly to the continuous phase as illustrated by **Fig. 20a**. When these two immiscible fluids arrive at the T-junction, and as the dispersed fluid advances in the main channel, the continuous fluid creates a shear force that forces the dispersed phase to bend and form a narrow neck at the junction. Eventually, part of the dispersed fluid gets detached and forms a droplet that flows in the direction of the continuous liquid. The “T-junction” approach allows the control of droplet frequency and size, however, the frequency and size range remain limited by the chip design and properties of the fluids [135–137].

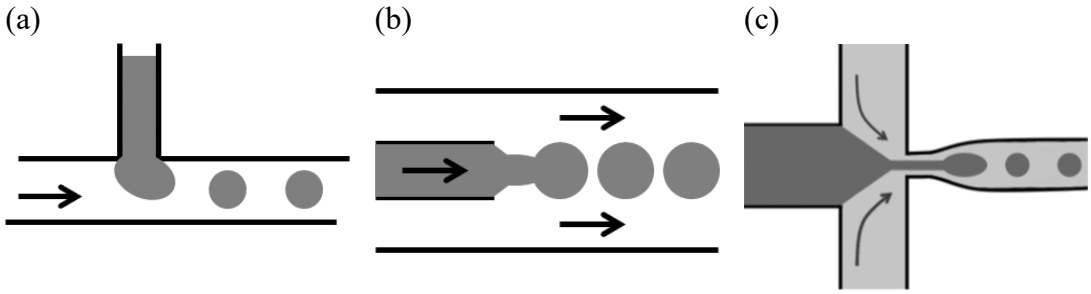

Fig. 20: Droplet generation principles: (a) cross-flow (T-junction); (b) planar co-flow; and (c) planar flow-focusing.

In the co-flow design (**Fig. 20b**), two concentric capillary tubes are used to introduce the fluids. The dispersed liquid is injected through the inner capillary, while the continuous liquid flows in the outer capillary and fully covers the inlet of the inner capillary to surround the dispersed phase. As the dispersed phase flows out of the inner capillary, the surface tension force acts in the opposite direction to pull it back, and a droplet starts to form. The continuous phase creates a drag force that eventually detaches the growing droplet. Despite being a simple design, the droplet size and frequency remain limited in the co-flow design [138–141].

An alternative design is the flow-focusing on which the dispersed phase is injected into the main channel while the continuous phase is introduced by two branches placed perpendicularly as depicted in **Fig. 20c**. Due to the competing action of the viscous force (that pinches the desired phase on both sides) and surface tension (that acts to minimize the surface energy of the dispersed phase), the dispersed phase breaks into droplets. This design provides more flexibility in terms of droplet size and frequency. Nevertheless, the knowledge and control of the droplet "Break up" phenomena remain limited [142,143].

The wetting properties of the microfluidic channel walls determines the type of emulsion that can be made [144]. In general, water-in-oil (W/O) emulsions can be produced in devices with hydrophobic walls, while oil-in-water (O/W) droplets can be generated in channels with hydrophilic walls [145,146]. Traditional (standard) microfluidic devices are fabricated by using soft-lithography to pattern channels in a silicone elastomer of polydimethylsiloxane (PDMS). Since PDMS is hydrophobic, these traditional devices can only be used to make water-in-oil (W/O) emulsions. Although, surface modification techniques such as oxygen plasma can be used to make the walls of the PDMS channels hydrophilic to enable the production of oil-in- water (O/W) emulsions, the treatment only lasts for few minutes or hours after which PDMS regains its hydrophobic properties [147].

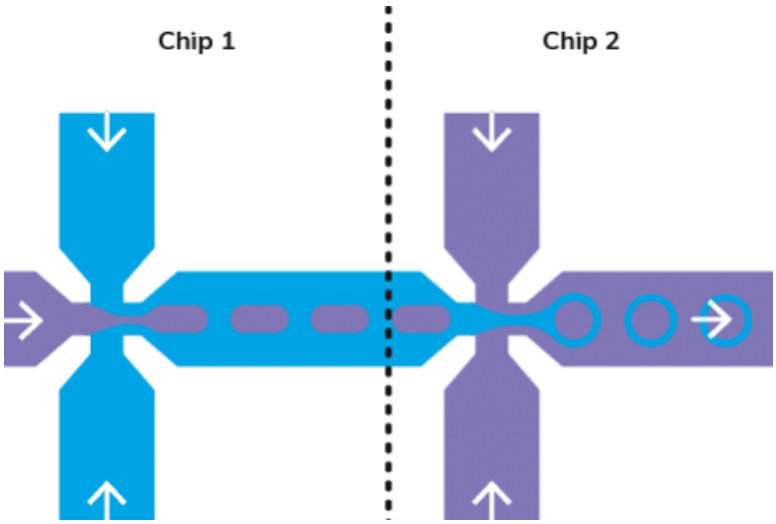

Fig. 21: A typical two-step process for double-emulsion production.

Creating a double emulsion (i.e., water-in oil-in water or oil-in water-in oil) is, however, not an easy task. A two-step process is usually followed to produce double emulsions by firstly forming the inner droplet, which is further encapsulated in a second emulsion step as illustrated in **Fig. 21**. This dictates a different wall wettability in every step. As discussed before, the standard PDMS devices are not reliable for creating oil-in-water emulsions.

Co-flow and flow-focusing can exist in a two-dimensional (2D) structure, as shown in **Fig. 20b** and **Fig. 20c**, respectively, or in a three-dimensional (3D) axisymmetric structure as shown in **Fig. 22a** and **Fig. 22b**. Utada et al. [144] invented an approach to produce double emulsions using a glass capillary device, which has since become the standard method for creating such emulsions. The device combines the 3D axisymmetric co-flow and flow-focusing approaches. An illustration for the invented device is shown in **Fig. 22c**. Two rounded glass capillary tubes are laid end to end within an outer square or circular glass tube. The inner fluid is pumped from the tapered end of the glass injection tube to the larger tip of the round capillary (collection tube). The middle fluid is pumped in the outer capillary in the same direction as the inner fluid to create a co-flow. At the same time, the outermost (continuous) fluid is pumped inside the outer tube in the opposite direction to hydrodynamically focus the co-flow. When all fluids enter the collection tube, a double emulsion is formed, consisting of an inner fluid droplet within a larger middle fluid droplet, contained in the continuous fluid [148].

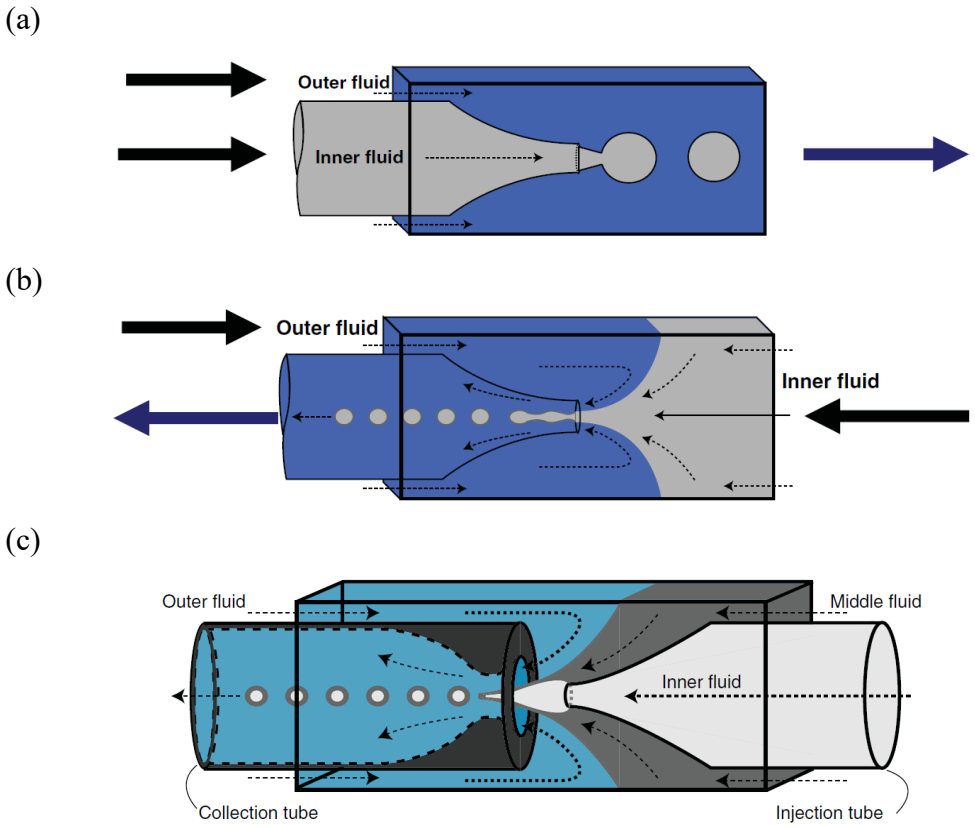

Fig. 22: A 3D axisymmetric structure of: (a) co-flow; (b) flow focusing; and (c) co-flow and flow focusing [148].

The device invented by Utada et al. [144] has the ability to create truly three-dimensional flows to completely shield the inner fluid from the outer one [134,144,148]. However, the combination of co-flow and flow focusing in the glass capillary device requires a perfect alignment of the glass capillaries [148]. The typical tip size of an injection tube is within the 10-50 μm range, while the range for the collection tube orifice range is between 20 to 200 μm, however, smaller or large sizes can be used [144]. As the device creates three-dimensional flows, theoretically, there is no requirement for a wall surface treatment as the middle fluid completely surrounds the inner fluid, and the outer fluid is always in contact with the collection tube. Nevertheless, as the tip sizes of the glass capillaries are very small, for practical uses, the tips are treated to ensure that there will be no cross flow between fluids. One major advantage of using glass is its ability to be easily (and almost permanently) treated using chemicals, such as octadecyltrimethoxysilane to make it hydrophobic or 2-[methoxy(polyethyleneoxy) propyl]trimethoxysilane to make the surface hydrophilic [134].

In this research, the microfluidic technique described by Utada et al. [144] was used as a platform to create a water-in-oil-in-water (W/O/W) double emulsion in order to encapsulate the aqueous liquid sorbent solutions (water-phase) inside a polymeric shell

material (oil-phase). The continuous fluid (water-phase) used was an aqueous solution composed of water, glycerol (to modify the viscosity), and a surfactant (to prevent the coalescence of droplets before shell polymerization). The liquid salt solution, shell material, and continuous fluid was referred to as the inner fluid, middle fluid, and outer fluid, respectively.

3.2.1. Material Screening and Compatibility

The first and most important criteria for selecting a shell material is its high permeability to water vapor. The shell material used in encapsulation is a liquid resin that is UV-curable. **Table 2** shows the water vapor permeability for some of the polymers and whether they can be formulated in a form of a UV curable liquid resin. Polydimethylsiloxane (PDMS), also known as silicone, is one of the most promising candidates, but it is highly viscous (> 5,000 *mPa-s*) which might prevent its encapsulation. TEGO Rad 2650 and SEMICOSIL 949 UV are two commercial acrylated silicone resins that are identified as good candidates for encapsulation due to their high permeability to water vapor, UV curability, and their relatively low viscosity (~150-300 *mPa-s*). A favorable property for SEMOCIL 949UV and TEGO Rad 2650 is that they form an elastic polymer upon UV curing (crosslinking). In this project, the company that manufactures SEMICOSIL was contacted to provide samples of their products, but unfortunately, no sample was provided. Samples for TEGO Rad 2650 were donated by Evonik Industries, therefore, this product was selected in this research for testing.

Table 2: Water vapor permeability for various polymers.

Polymer	H_2O permeability (Barrer)	UV-curability
$1000_{PEO}56_{PBT}44$ (PEO-PBT)	85,500	-
Sulfonated polyetheretherketon (SPEEK)	61,000	-
Polydimethylsiloxane (PDMS)	40,000	Yes
Ethyl cellulose (EC)	20,000	-
TEGO Rad 2650 Acrylated-PDMS	17,000	Yes
SEMICOSIL 949UV Acrylated-PDMS	17,000	Yes
Sulfonated polyethersulofon (SPES)	15,000	-
Cellulose acetate (CA)	6,000	Yes
Polyethersulfone (PES)	2,620	-
Natural rubber (NR)	2,600	-
Polyvinylchloride (PVC)	275	-
Polyvinylalcohol (PVA)	19	Yes

Before using microfluidic techniques, three tests were conducted to determine the possibility of achieving the encapsulation. These tests included an interfacial stability test, a crosslinking test, and a degradation test following Ref. [149]. The importance of each test and the testing procedure will be discussed in the following sections.

3.2.1.1. Interfacial Stability Test

The creation of an emulsion relies on the immiscible properties of the fluids. In order to determine whether the materials have the potential to maintain distinct phases in the process of creating microcapsules, it is necessary that the shell and core materials along with the outer and shell materials maintain distinct interfaces between them. To test this, the two pairs of materials were placed in a container and observed at beginning and finishing time points. If the two materials did not mix and a distinct barrier between materials is preserved, the interface is stable.

When the 60 wt% LiBr aqueous solution and TEGO Rad 2650 were first placed into one container, a clear interface was observed, as shown in **Fig. 23a**. After the 24hr time period had passed, the distinct barrier was still present, as depicted in **Fig. 23b**. The two materials did not mix or become homogenous. This indicated proper interfacial stability between the core and shell fluids.

The addition of a glycerol aqueous solution (70 wt% glycerol) and TEGO Rad 2650 into one container did not result in mixing of the two fluids as demonstrated in **Fig. 24a**. After the 24hr period, the fluids remained separate as illustrated in **Fig. 24b**, which indicated good interfacial stability.

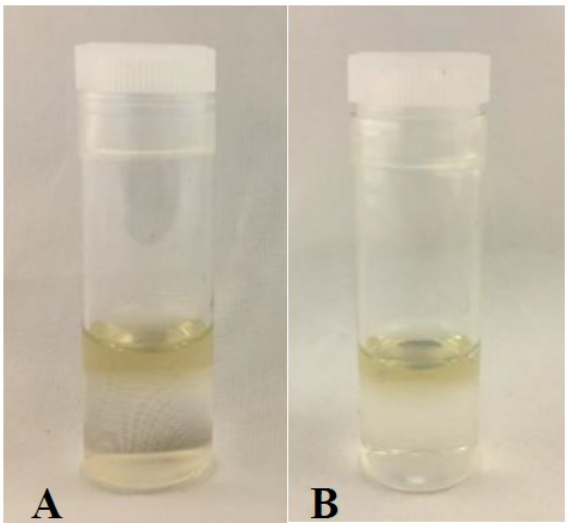

Fig. 23: A 60 wt% LiBr solution and TEGO Rad 2650: (a) the initial state; and (b) after 24 hours.

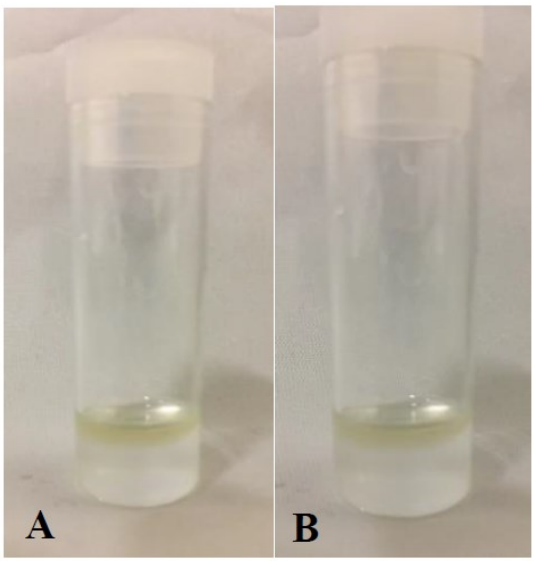

Fig. 24: A 70 wt% glycerol aqueous solution and TEGO Rad 2650: (a) the initial state; and (b) after 24 hours.

Since both the core-shell and shell-outer fluid interactions have proven to be stable and are immiscible, they possess the ability to successfully form microcapsules. It is not likely that the fluids will disperse into one another given the appropriate parameters.

3.2.1.2. Crosslinking Test

Crosslinking is a process that transforms a fluid into a stiffer, solid form. As a result, the middle material is often referred to as the shell. Before it is possible to determine the effects of the core fluid on crosslinking, an understanding of how the shell precursor alone crosslinks is necessary. Once this behaviour was characterized, a follow-up experiment was preformed to observe if the shell material would cure in the presence of the core.

For crosslinking experiments, a 365 *nm* wavelength emitting LED bulb was used with approximately 5.78 *W* power and with an intensity of 18 mW/cm^2. A square glass mould with the dimensions of 25 *mm* X 25 *mm* and a thickness of 0.18 *mm* was used to house the fluid during the crosslinking process. Once the material was placed in the mould, it was positioned under the bulb with a closed cover and exposed to the light for a set amount of time. For TEGO Rad 2650 to be able to cure under UV light, a photoinitiator was required to be added with a specific percentage (0.1-4%). A photoinitiator is a substance that initiates the crosslinking (polymerization) process of a material. Irgacure 1173 Darocur 2-hydroxy-2-methylpropiophenon (Sigma-Aldrich, Canada) was selected as the photoinitiator due to its greater solubility in an acylated-silicone such as TEGO Rad 2650.

The change in the photoinitiator concentration had a major impact on the crosslinking time of TEGO Rad 2650 as presented in **Fig. 25**. When a 0.1% concentration of the photoinitiator was added to TEGO Rad 2650, the sample was crosslinked in only 1 minute and 30 seconds. A 2% concentration of the photoinitiator led to a crosslinking time of 10 seconds. The remaining results are presented in **Fig. 25**. Due to the fast curing rate, "partial-crosslinking" as seen in the above results was not documented.

Once the crosslinking of TEGO Rad 2650 had been characterized, the next step was performed. A water-in-oil emulsion (by simple stirring) was created with the LiBr solution (water-phase) and the TEGO Rad 2650 (oil-phase) that already contained the photoinitiator. This emulsified fluid was then placed in the mould and exposed to UV for the same amount time performed on the non-emulsified sample. It was determined that because the emulsion sample successfully cured in the same amount of time as the sample without LiBr, it had no effect on the shell's ability to cure in its presence. This indicates that during capsule production, the shell should be able to cure around the core fluid without interference.

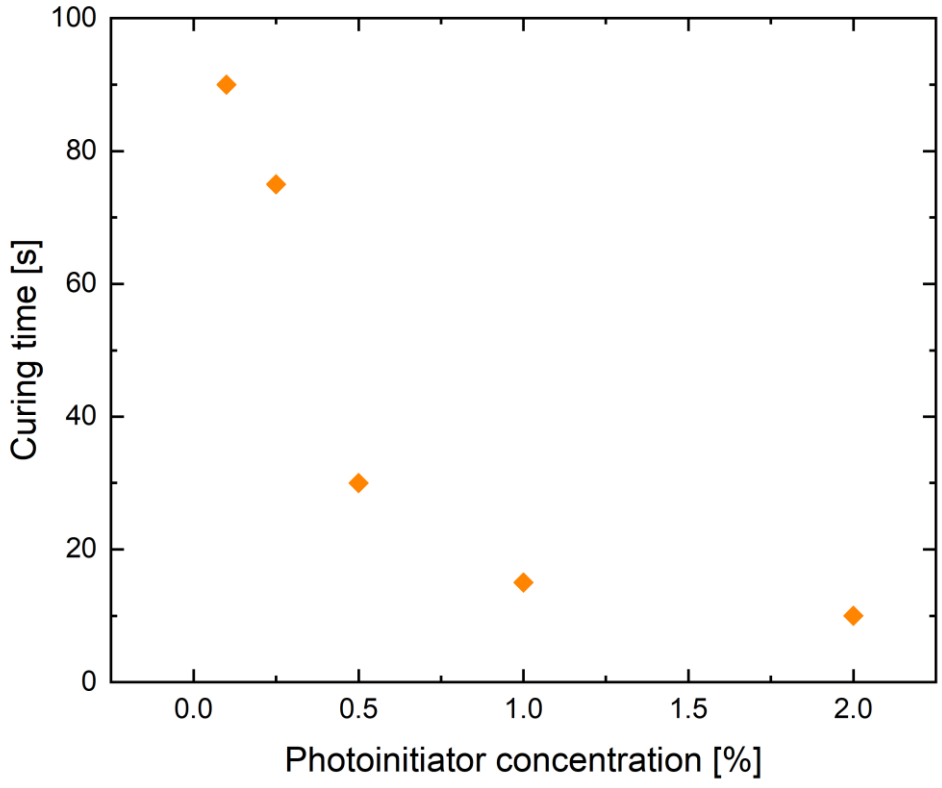

Fig. 25: A crosslinking study (25 *mm* X 25 *mm* X 0.18 *mm* samples).

3.2.1.3. Degradation Test

The final test was preformed to determine if the core causes the shell to degrade or dissolve. To evaluate this, a degradation study was carried out for seven days. Cured samples of TEGO Rad 2650 were cut into 4 pieces then were weighed using a precise electronic balance (OHAUS AX622 Adventurer). Half of these smaller samples were placed in 2 *ml* of water as controls and the remaining samples were placed in 2 *ml* of a 60 wt% LiBr solution. All eight sample pieces were weighed each consecutive day of the seven-day period. Each day, the samples were dried, weighed, and returned to the container after replacing the soaking fluid. The weight of the samples must be maintained without any signs of dissolving to indicate that the shell is resistant to the core fluid.

The change in weight of the control groups kept in water is presented in **Fig. 26.** Each point is a mean of 4 samples. There is no sign of degradation from the water, which is expected. Comparatively, **Fig. 26** shows the changes in weight for the LiBr solution-soaked samples. There are no significant changes in the weight of these samples. This demonstrated that the LiBr solution does not degrade or dissolve the shell material over time.

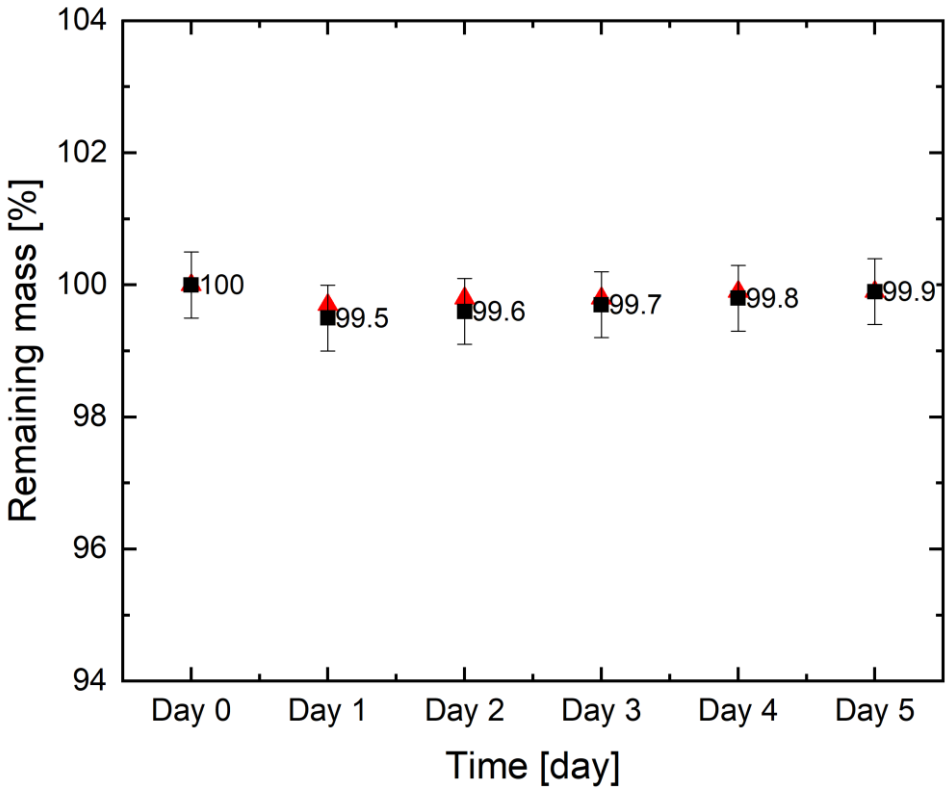

Fig. 26: The degradation of TEGO Rad 2650 over seven days: ■ control samples in water; and ▲ a 60 wt.% LiBr solution.

3.2.2. Custom-designed Microfluidic Device

To fabricate the microfluidic device described by Utada et al. [134], the round glass capillaries with an inside diameter (I.D.) and outside diameter (O.D.) of 0.75 and 1.0 *mm* (World Precision Instruments, USA), were pulled in a Flaming/Brown micropipette puller (P-1000, Sutter Instrument Co., Carl Zeiss Canada Ltd, Toronto, Canada) to produce the tapered tips for injection and collection capillaries. The tips were then polished to the desired orifice size using a 7,000 Grit abrasive paper as shown in **Fig. 27**. The tip size of the injection and collection glass tubes were 40 and 300 μm, respectively. The tip of injection tube was treated with n-Octadecyltrimethoxysilane (OTMS) (Gelest Inc., USA) to make its surface hydrophobic, while the collection tube tip was treated with 3-[methoxy(polyethyleneoxy)6-9]propyltrimethoxysilane, tech-90 (Gelest Inc., USA) to render its surface hydrophilic. The chemical treatment was conducted by soaking the capillaries in the appropriate chemical for 60 minutes then dried in an oven temperature of 120 ^{o}C for 1-2 hours. A glass round capillary tube with an I.D. and an O.D. of 1.12 and 1.5 *mm* (Gelest Inc., USA) was used to house the inner injection and collection tubes.

As discussed previously in Section 3.1, for the glass capillary device to function, a perfect alignment of the injection and collection tube is required. For this purpose, Martino et al. [150] presented a 3D printed assembly to mount glass capillaries to ensure a perfect alignment. The assembly relied on the fabrication of screws that hold the inner (injection and collection) glass tubes. A set of two nuts were glided onto a slider and were used to mount the outer tube. The screws (holding the injection and collection tubes) were gently guided through the nut.

Following the approach presented by Martino et al. [150], similar parts were designed and a 3D drawing for the assembly was prepared with the aid of SolidWorks software (Dassault Systèmes). The 3D drawings of the designed parts before and after the assembly are presented in **Fig. 28a** and **Fig. 28b**, respectively. The parts were printed using an Objet30 PolyJet 3D printer (Stratasys, Ltd.). The 3D printed microfluidic device after the assembly is shown in **Fig. 29a**. The perfect alignment was confirmed by the images taken with a digital microscope (Unitron MEC2, Miller Microscopes) as shown by **Fig. 29b**.

(a) (b)

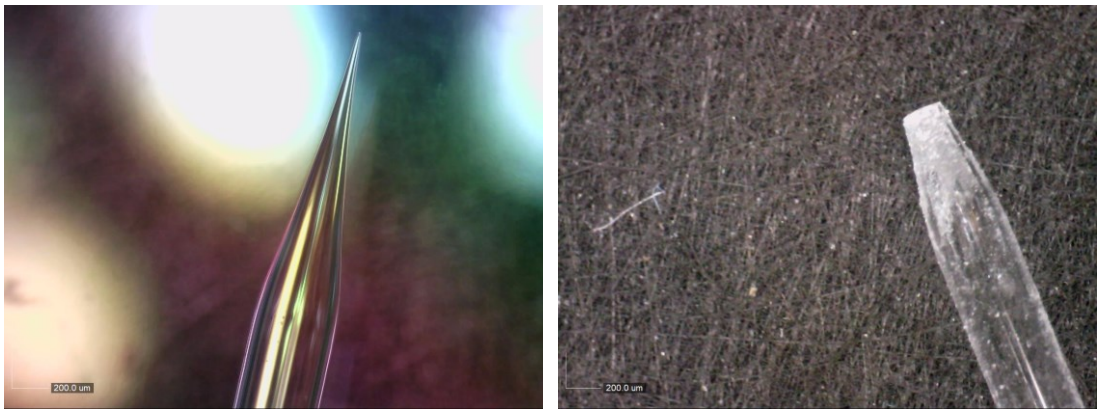

Fig. 27: Injection and collection glass capillary tubes.

(a)

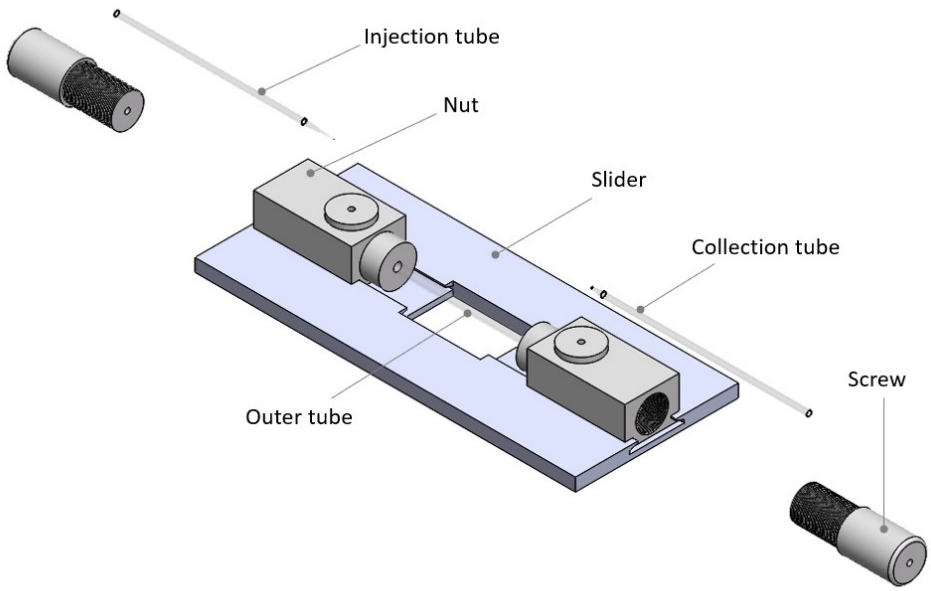

(b)

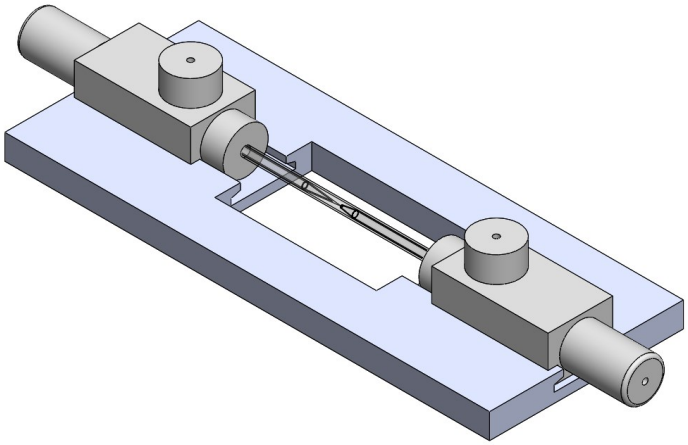

Fig. 28: A 3D CAD drawing of the microfluidic device: (a) before; and (b) after assembly.

(a) (b)

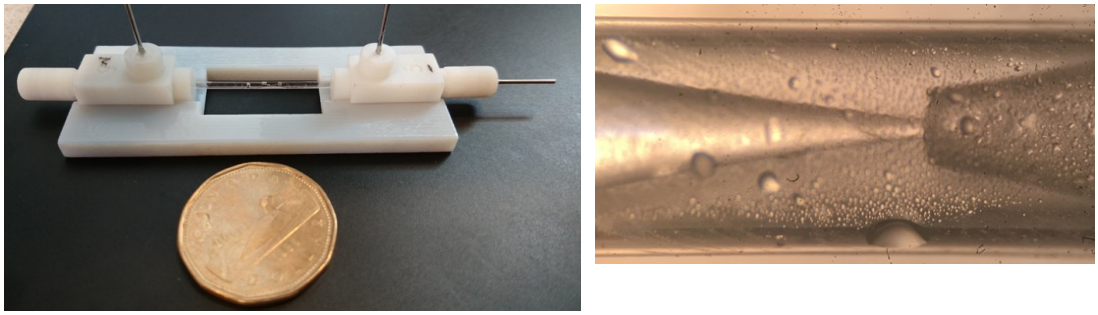

Fig. 29: (a) An assembled 3D printed microfluidic device; and (b) the alignment of the glass capillary tubes.

3.2.3. Microfluidic Experimental Setup

The inner fluid was an aqueous salt solution prepared by mixing a 60 wt% LiBr anhydrous salt (Sigma-Aldrich, Canada) and 40 wt% deionized water. Coloring dyes were added to the inner fluid mixture for better visualization. The middle phase was a mixture of 98 wt% TEGO Rad 2650 (Evonik Industries, USA) and 2 wt% Irgacure 1173 Darocur photoinitiator (Sigma-Aldrich, Canada). The outer phase was a mixture composed of 59 wt% deionized water, 40 wt% glycerol, and a 1 wt% Pluronic F-127 surfactant (Sigma-Aldrich, Canada).

A schematic of the microfluidic experimental setup is shown in **Fig. 30**. The microfluidic device was mounted on the slide of a digital microscope (Unitron MEC2, Miller Microscopes) equipped with a microscope camera to observe the double emulsion formation. One syringe pump (Model 11 Plus, Harvard Apparatus) was used to inject the inner fluid to the inlet of the microfluidic device at a rate of 5-10 *mL/h*. Another two syringe pumps (NE-300, New Era) were used to introduce the middle fluid and outer fluid at a rate of 5-10 *mL/h* and 50-60 *mL/h*, respectively. The microcapsules exited the microfluidic device via a polyethylene tubing (BD Intramedic) with an I.D. and O.D. of 1.19 and 1.70 *mm*, respectively. A commercial UV-LED with a 365 *nm* wavelength, 50 *W* power, and a 235 mW/cm^2 intensity was used for the in-line curing of the freshly produced microcapsules. The encapsulated liquid sorbent with the cured shell was collected in a vial.

The microfluidic setup used to conduct the experiment is shown in **Fig. 31**. The actual production of the microcapsules in the microfluidic device (before UV curing) is shown in **Fig. 32**. A microscopic image of the double emulsion creation inside the microfluidic device is shown in **Fig. 33**. The collected microcapsules were washed in deionized water multiple times to remove any carrier fluid residues, and they were finally stored in a glass vial as shown in **Fig. 34**. ImageJ software was used to analyze

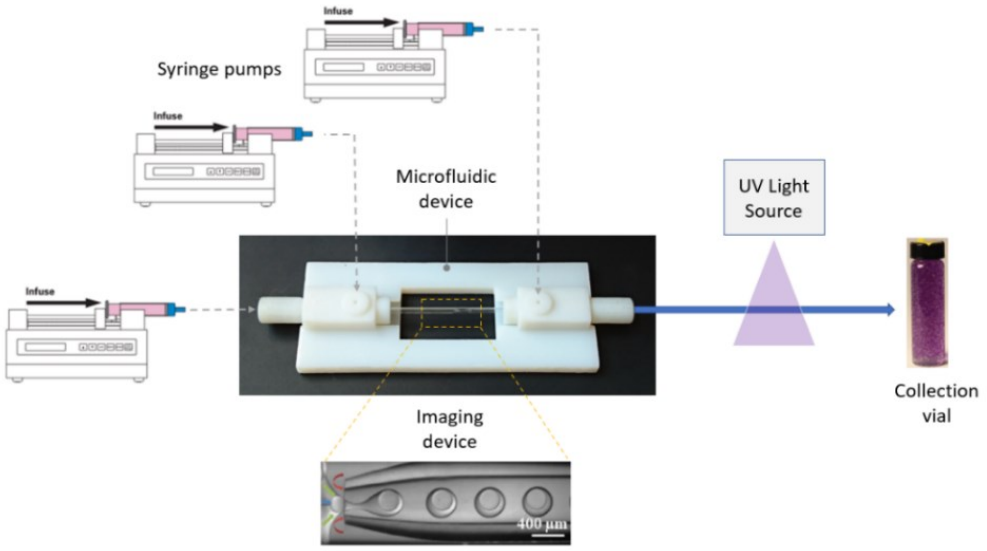

Fig. 30: A schematic of the microfluidic experimental setup.

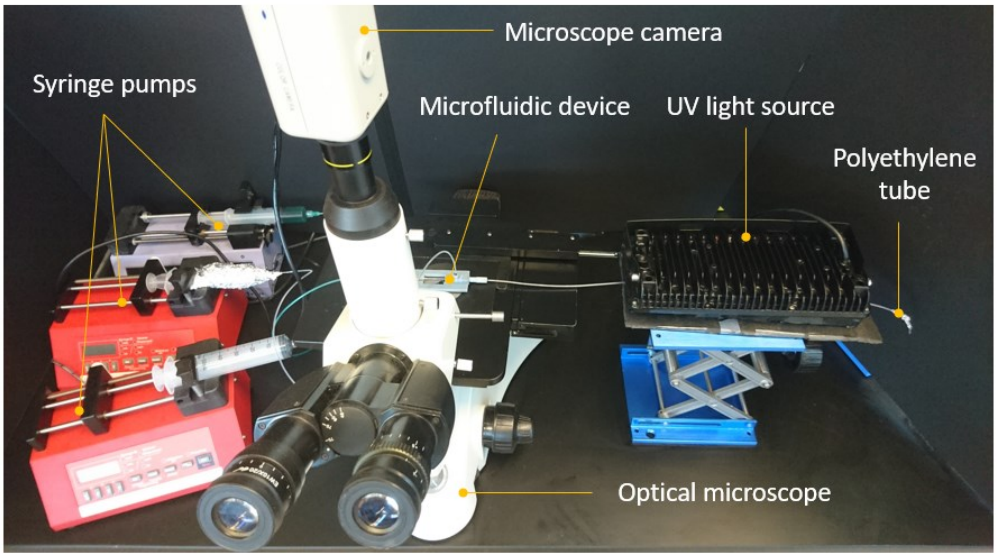

Fig. 31: The microfluidic experimental setup.

the circularity and measure the sizes of 50 microcapsules. The average outer and inner (core) diameters of the capsules were 700 and 570 μm, respectively, as presented in **Fig. 35**. The coefficient of variance (CV) for the outer and the inner diameter is 4.4% and 1.5%, respectively, which means the capsules are monodisperse (CV<5%).

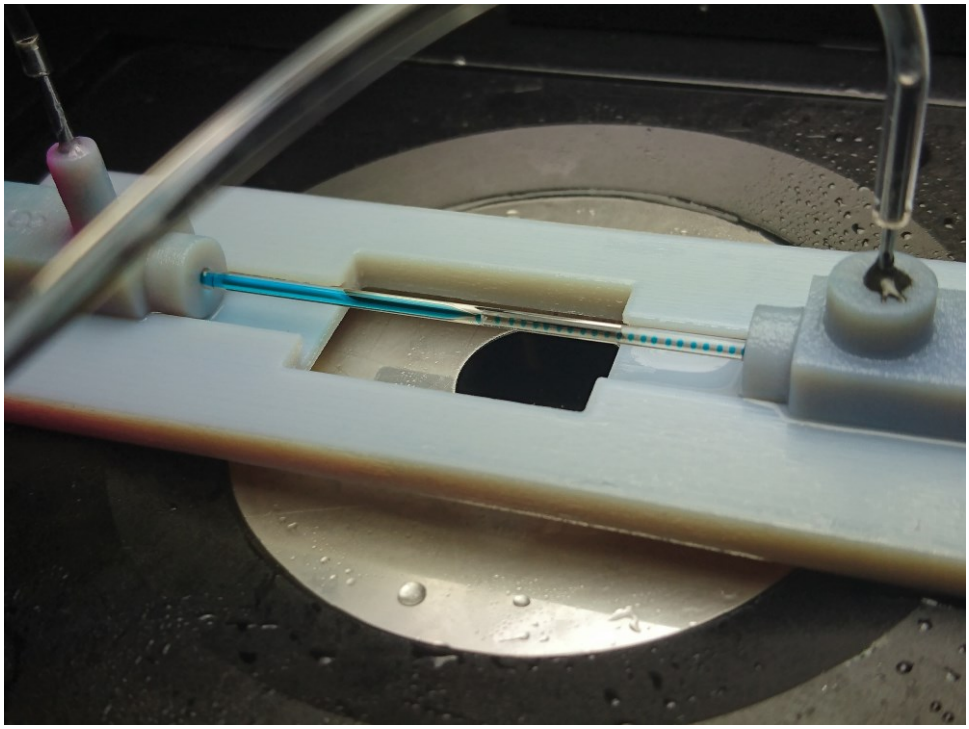

Fig. 32: The custom-built microfluidic device under operation.

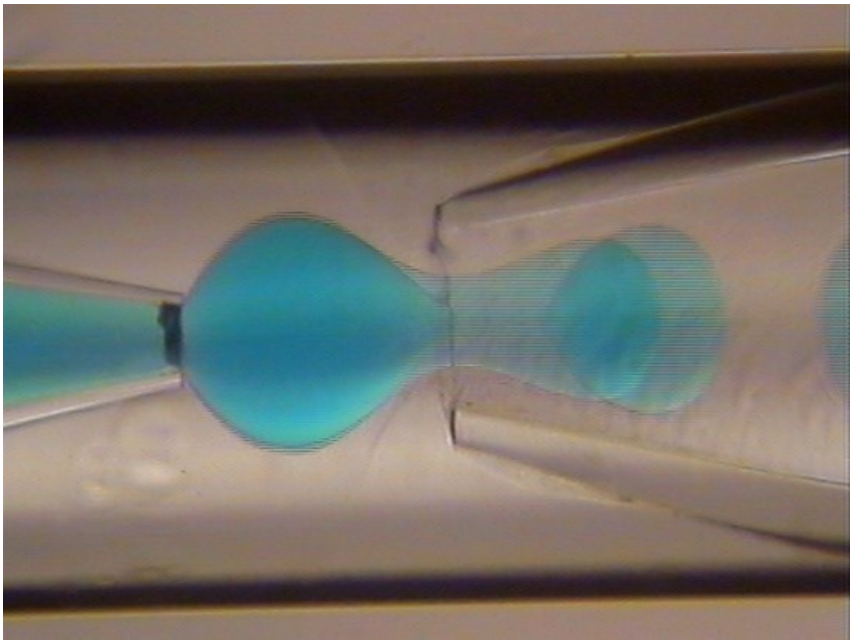

Fig. 33: A microscopic view of the microcapsule production process.

Fig. 34: Collected microcapsules (contain liquid desiccant: 60 wt% LiBr and 40 wt% deionized water).

To demonstrate that the size of the capsules can be adjusted by the changing the flow rates of the fluids, the mass flow rate of middle (Q_M) and outer fluids (Q_o) were fixed at 6.0 and 50 *mL/h*, respectively, while the flow rate of the middle fluid (Q_I) was varied between 3-7 *mL/h*. The produced capsules at the various ranges of Q_M/Q_I ratios are shown in **Fig. 36**. The variation of shell thickness, inner and outer diameters of the capsules as a function of the Q_M/Q_I ratio is shown in **Fig. 37**. One can observe from **Fig. 37** that the ratio has a little effect on the outer diameter, while the inner diameter increases by increasing the Q_I/Q_M ratio. It can be concluded that the shell thickness can be decreased by increasing the Q_I/Q_M ratio.

The outer diameter of the microcapsules can also be adjusted by adjusting the outer (carrier) fluid flow rates. A batch with smaller microcapsules was produced, the average outer and inner (core) diameters of the capsules were 378 and 343 μm, respectively, as presented in **Fig. 38**.

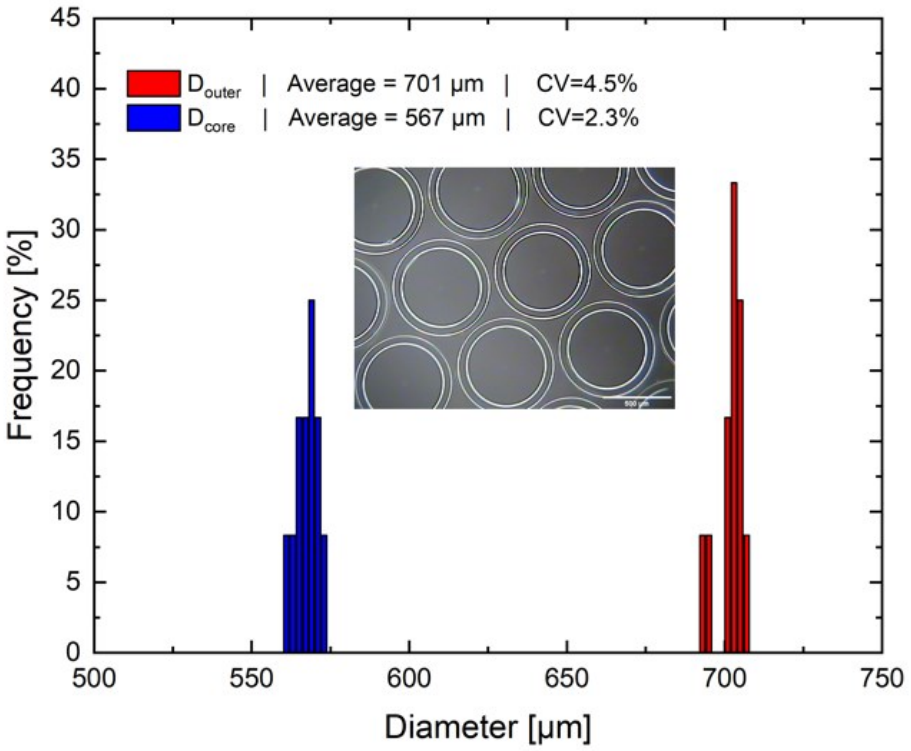

Fig. 35: The outer and inner diameter size distribution of microcapsules.

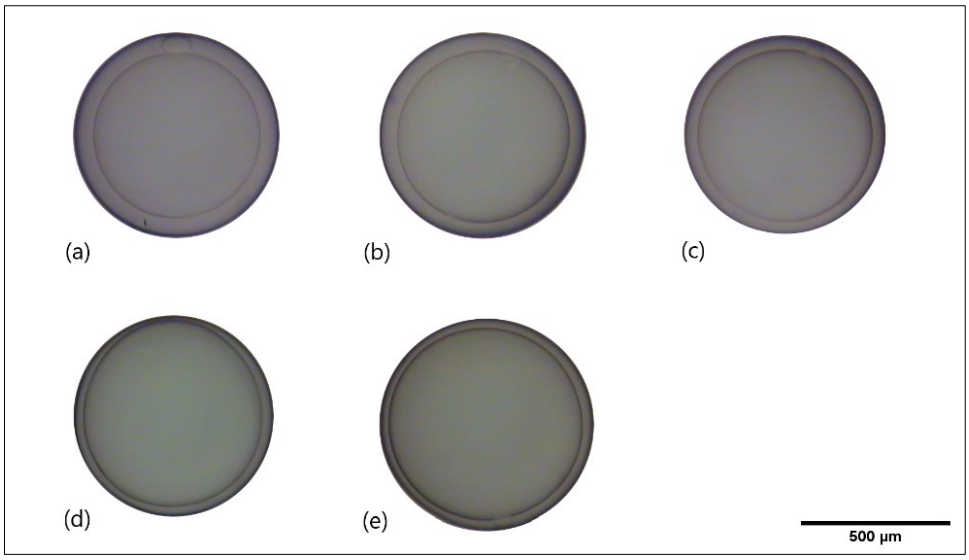

Fig. 36: The size of microcapsules with a LiBr 60 wt% at different Q_M/Q_I ratios: (a) 0.5; (b) 0.7; (c) 0.8; (d) 1.0; and (f) 1.2.

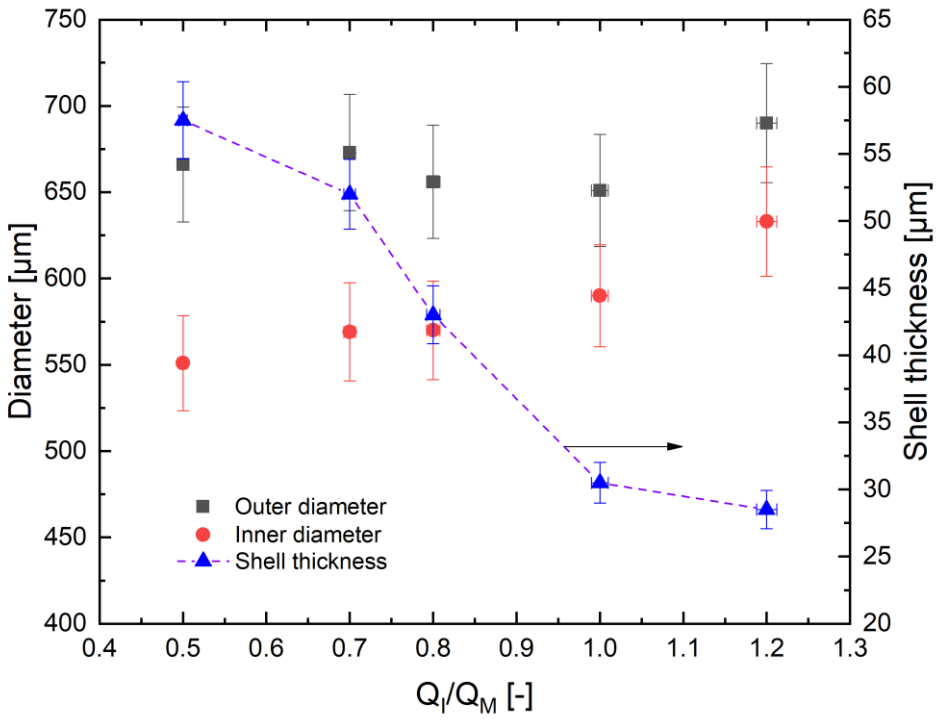

Fig. 37: The effect of flow rate ratios on inner diameter, outer diameter, and shell thickness.

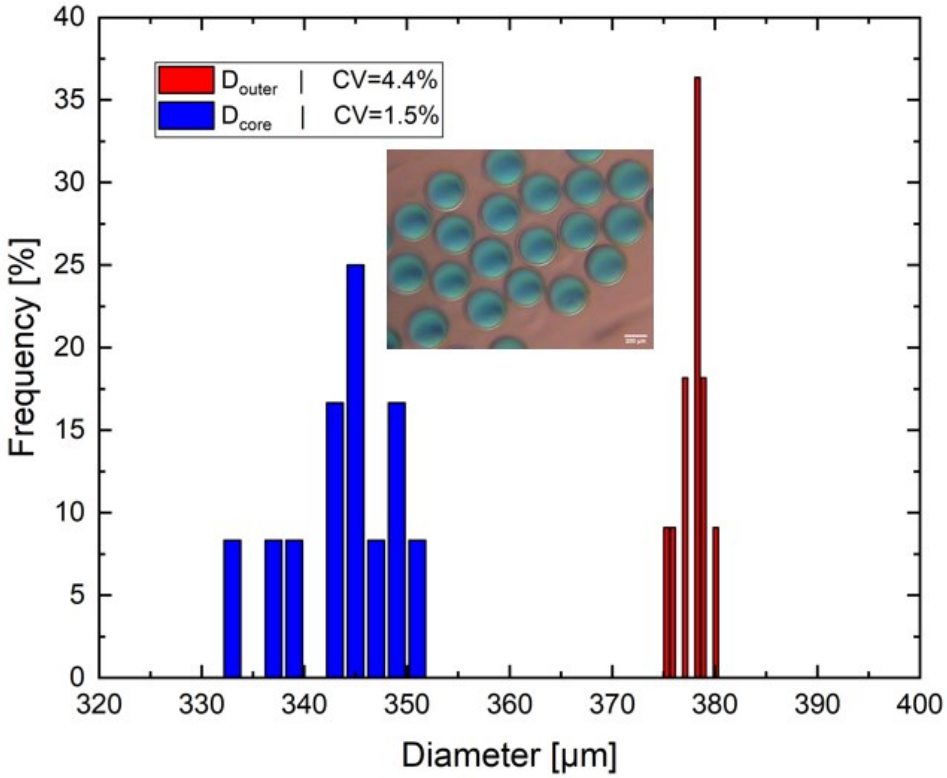

Fig. 38: The outer and inner diameter size distribution of microcapsules.

3.3. Material Characterization

3.3.1. Capsule Morphology During Dehydration and Rehydration

The morphology of the capsules during dehydration and rehydration is presented by the microscopic images in **Fig. 39**. The capsule was heated in the oven at 90 ºC for 3 hours to dehydrate the capsule (partially remove the water). Due to the elasticity of the shell, the capsule buckled as shown in **Fig. 39a**. The capsule then rehydrated by leaving the capsule in the room environment (~20 ºC and ~50% RH) for 3 hours. Interestingly, the capsule was able to regain its shape and the salt hydrates (formed during the dehydration) were detected as shown in **Fig. 39b**. This confirms that capsules can tolerate salt crystallization which is beneficial for increasing the sorption capacity. The capsule was then placed inside a water bath for 3 hours to completely hydrate it and dissolve the salt hydrates as shown in **Fig. 39c**.

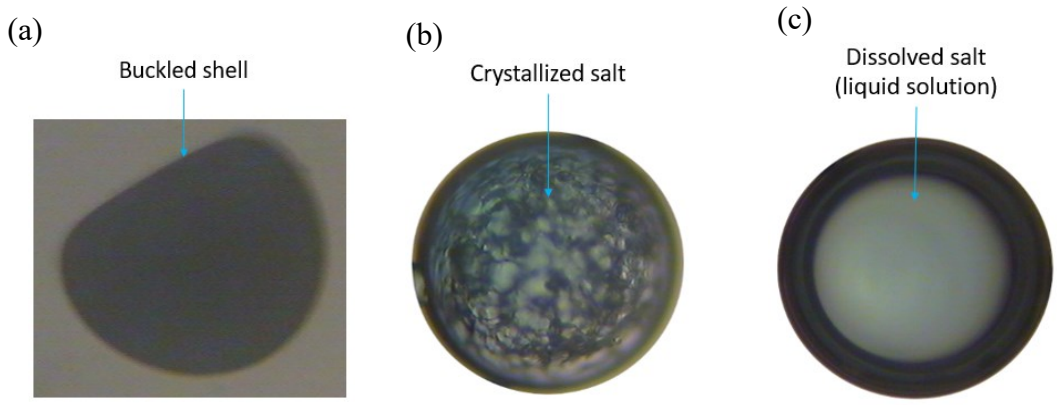

Fig. 39: (a) A collapsed shell after dehydration (desorption); (b) a collapsed shell after partial rehydration (absorption); and (c) complete rehydration in a water bath.

3.3.2. X-ray Diffraction Analysis

To confirm that the observed crystalline structure in the microscopic images of the microcapsules is indeed a LiBr salt, a small batch of microcapsules was packed into a quartz capillary. The bead-filled capillary was then placed in a vacuum oven at 48 °C for 1.5 days, after which clay was used to seal the open end, and the X-diffraction pattern was acquired immediately by using a D8 ADVANCE, Bruker diffractometer at 4D LABS, SFU. X-ray patterns were also acquired for the pure LiBr salt and the cured shell material sample as references, and the results are presented in **Fig. 40**. To analyze the results, the peaks in the X-ray pattern of the dried microcapsules were deconvoluted and compared with the reference patterns of the shell material and the pure LiBr salt. The peaks that centered at ~12 and 22 degrees are related to the shell material, and the peaks at ~27.5 and 31 degrees are assigned to the LiBr salt. The relative reduction of

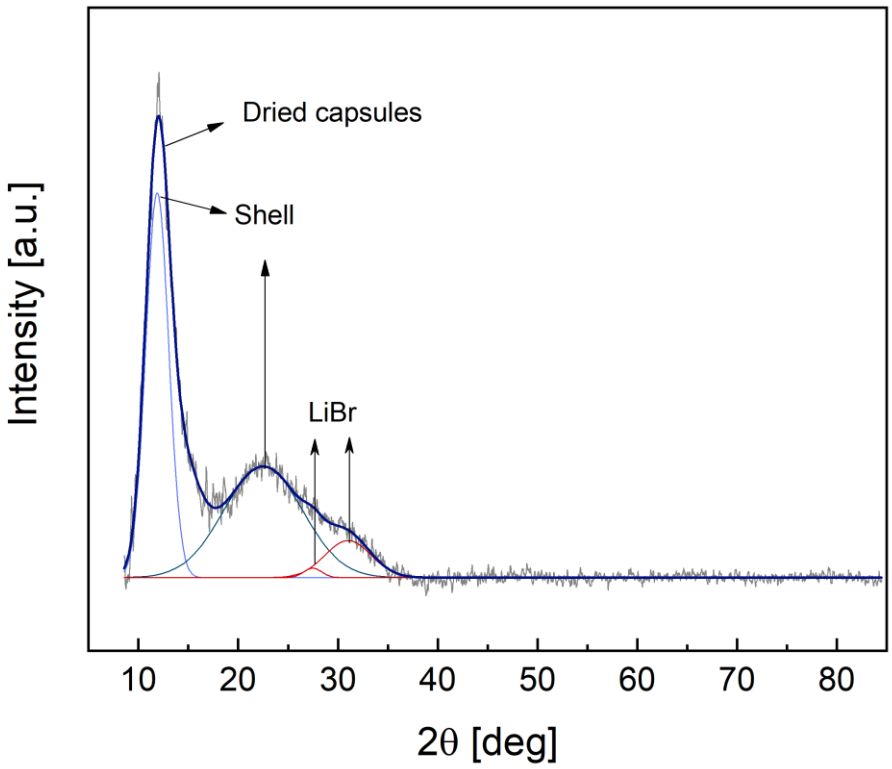

Fig. 40: X-ray diffraction patterns of the dried microcapsules (containing the LiBr salt), shell material, and pure LiBr salt.

the LiBr peak intensities relates to the coverage of shell material that affects the X-ray peak intensities and also peak positions.

3.3.3. Thermogravimetric Analysis

Water sorption isotherms (water vapor pressure: 0-2.1 *kPa*, corresponding to the relative humidity (RH) of 0-70%) for a ~18 *mg* sample that contained capsules (a 60 wt% LiBr solution) were measured using a thermogravimetric vapor sorption analyzer (IGA-002, Hiden Isochema) available in our lab (**see Fig. 41**). The temperature of the chamber that contained the sample was fixed at 30 °C. The pressure was increased with 4 *mbar* (40 *kPa*) steps, and in every step, the sample was given enough time to reach equilibrium as shown in **Fig. 42**. Isotherms curves were calculated by measuring the water uptake at the absorption and desorption process as shown in **Fig. 43** (the collected datapoints are presented in **Appendix A**). To measure dry weight, the sample was dried under vacuum for 6 hours at 80 °C at the end of the test. One can see from **Fig. 43** that the capsules did not show signs for hysteresis or salt/solution leakage as the absorption and desorption curves were almost identical. The linear water uptake in 10-70% RH indicates that the vapor is absorbed (or desorbed) by the sorbent in its liquid phase. The sharp drop in water uptake below 10% RH indicates the formation of solid hydrates (crystals).

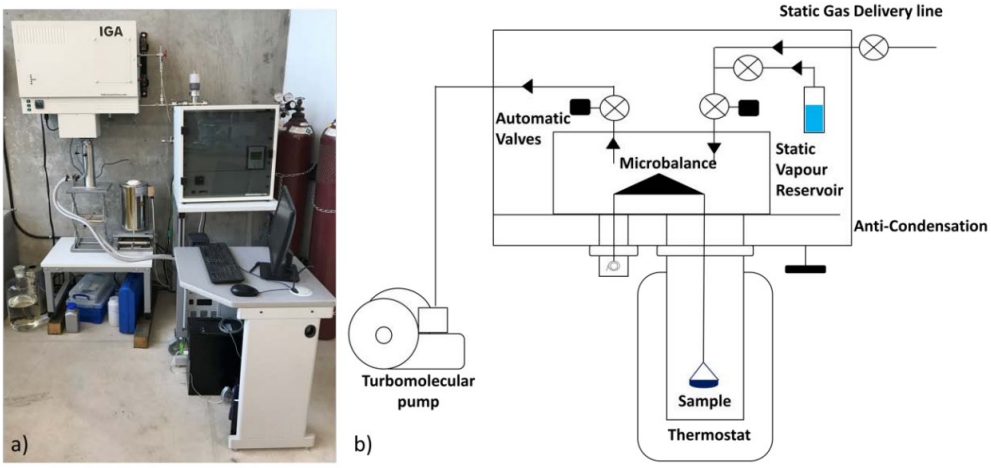

Fig. 41: (a) A thermogravimetric analyzer; and (b) a schematic of the thermogravimetric analyzer.

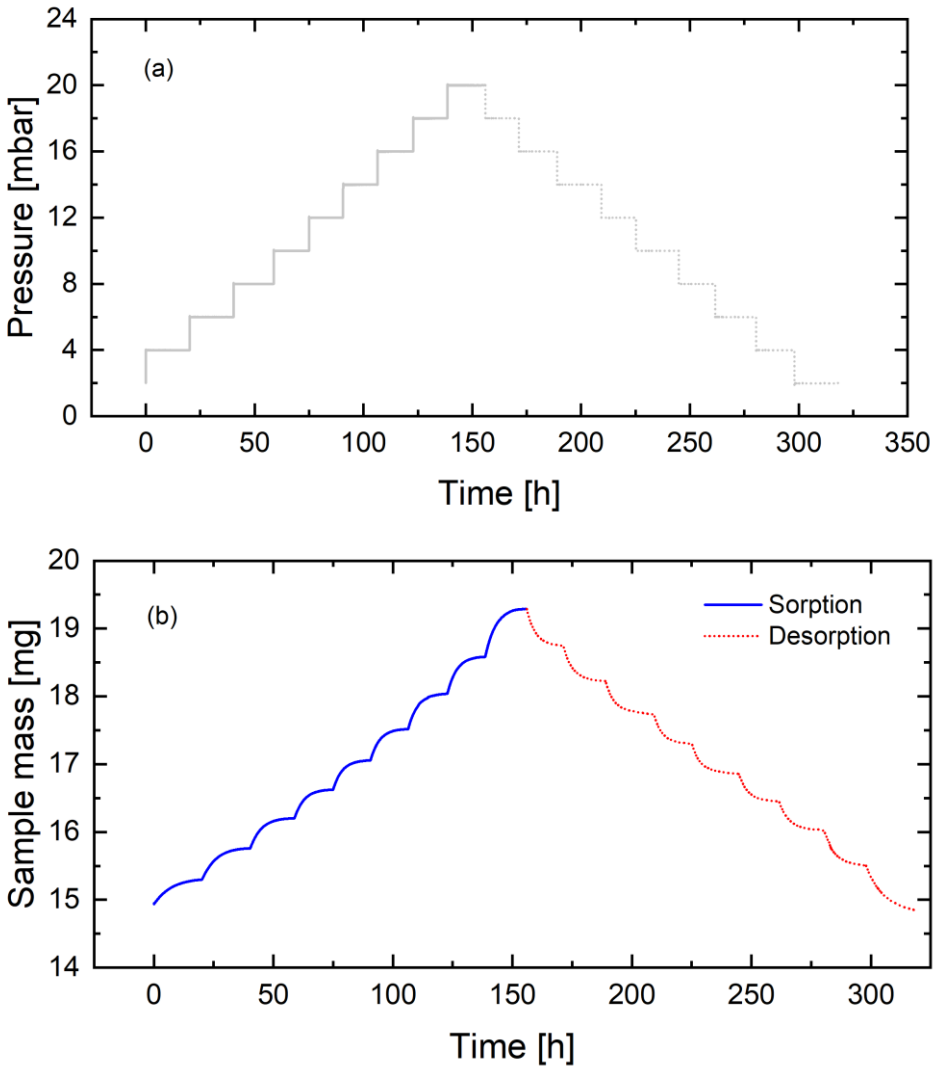

Fig. 42: The evolution of (a) pressure; and (b) the mass of the microcapsules with time during thermogravimetric testing.

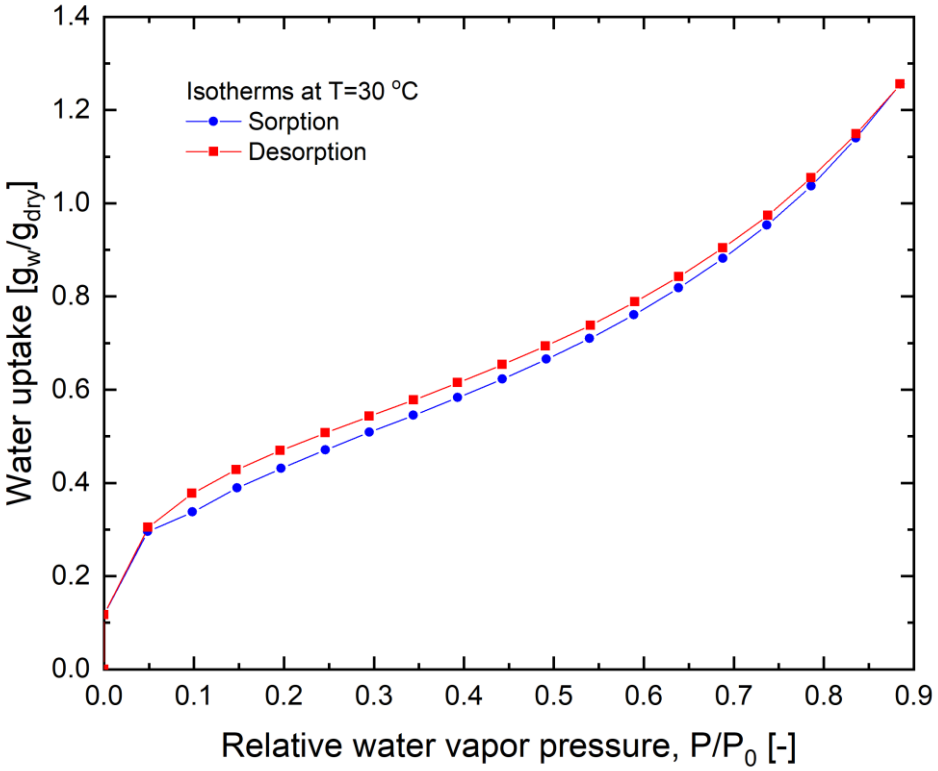

Fig. 43: The isotherm curve of the LiBr microcapsules.

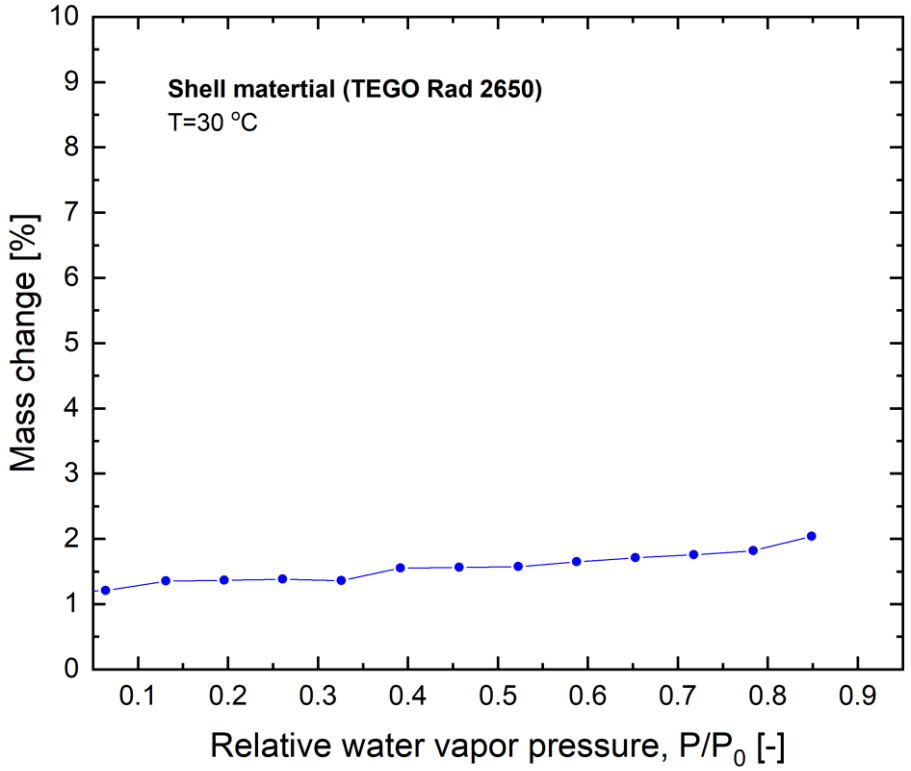

Fig. 44: The mass change of the shell material as a function of relative humidity.

As the shell is made of a membrane, a thermogravimetric test was also done for the (cured) shell sample to investigate its impact on the final sorption capacity of the microcapsules. The results, presented in **Fig. 44**, revealed that change in relative humidity does not result in any significant change in the mass of the shell material.

The comparison between the sorption capacity of the capsules and the common solid sorbent material in the literature shows that the capsules have a higher capacity, as presented in **Fig. 45**.

By having identical microcapsules with the same size, the isotherm curves can be predicted at any given size given the outer diameter, shell thickness, and reference isotherm curve of the pure salt. **Fig. 46** shows that the predicted isotherm curve is in good agreement with experimental data collected by the thermogravimetric vapor sorption analyzer for the produced LiBr microcapsules (outer diameter =700 μm, and shell thickness =70 μm). **Fig. 47** shows the predicted isotherm curves for 700 μm microcapsules with various shell thicknesses. From the graph, the actual salt loading (i.e., the ratio of the salt mass to the total dry weight of the microcapsules) can be estimated, and it was found that for the prepared microcapsules, the estimated salt loading is 54%.

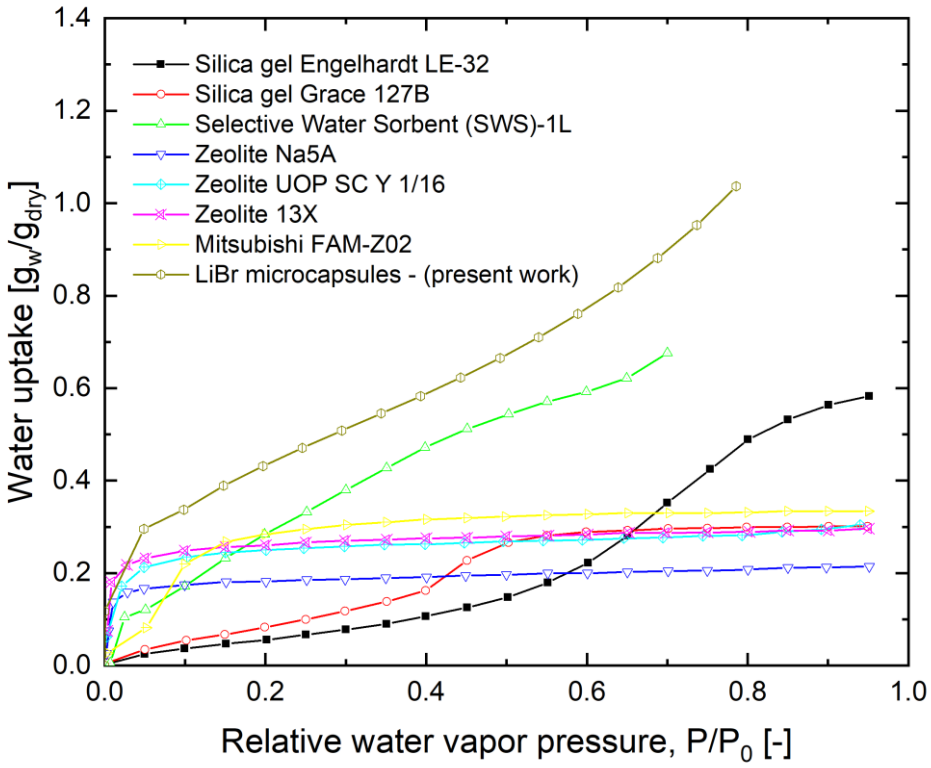

Fig. 45: The sorption capacity of capsules compared to common sorbent materials [17].

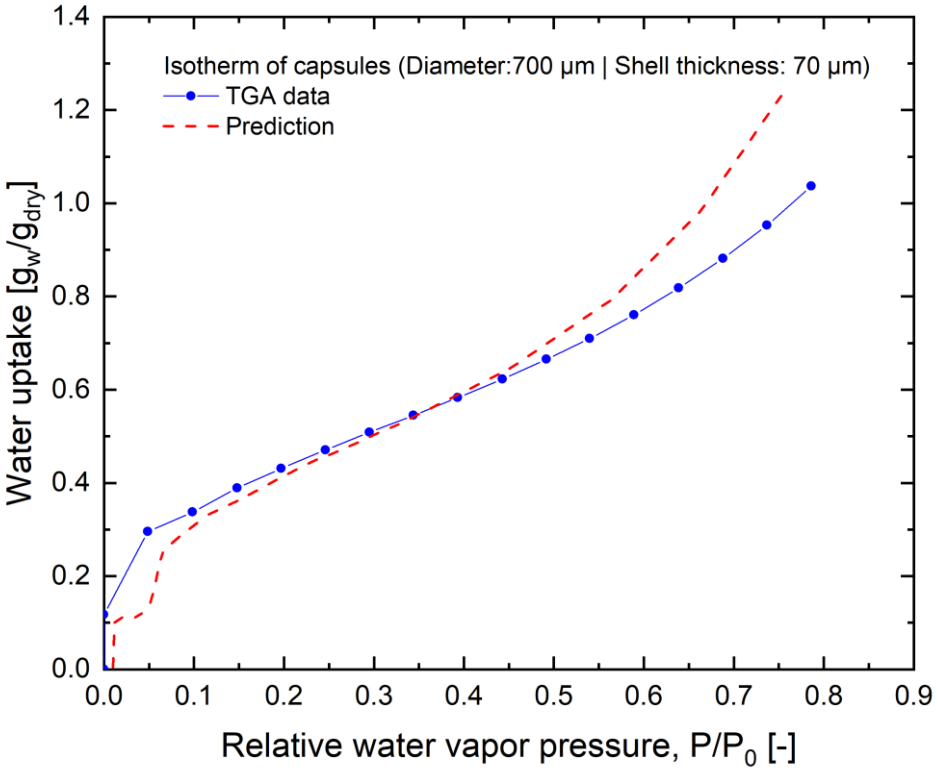

Fig. 46: The isotherm curve of the microcapsules: (a) the thermogravimetric analyzer (TGA) data; and (b) the prediction.

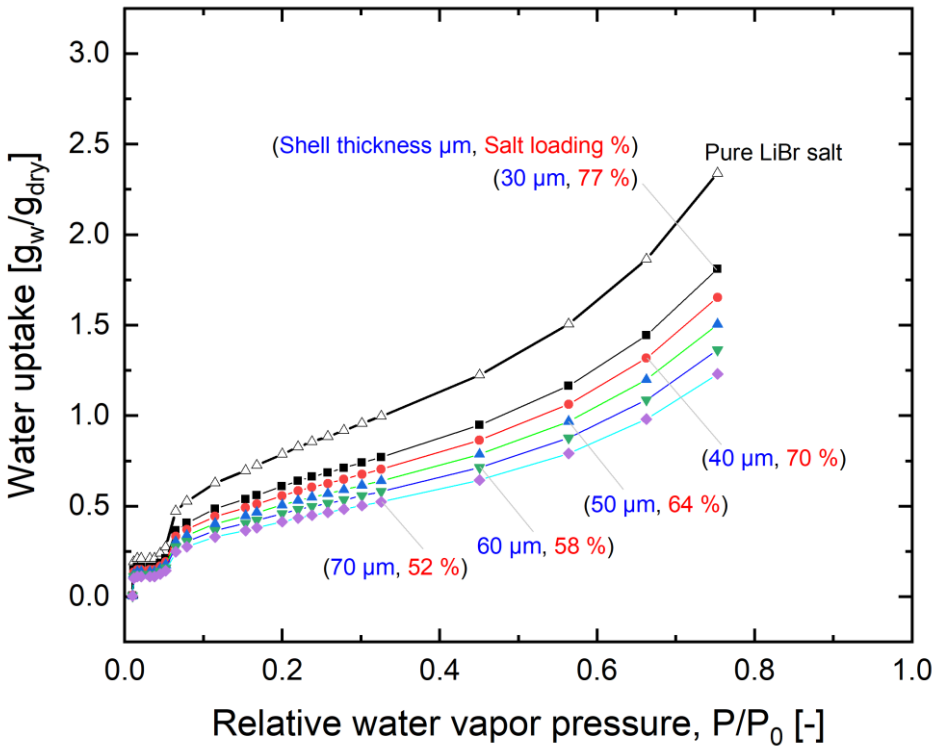

Fig. 47: The predicted isotherm curves of the microcapsules of various sizes.

3.3.4. Shell Morphology

A scanning electron microscope image of a sample was acquired using the microscope facility (Nova NanoSEM, FEI) at 4D LABS, SFU is shown in **Fig. 48**. The average size of the capsules is approximately ~700 μm. The shell that contains the liquid sorbent was perfectly spherical and no salt was observed on the outer surface of the shell which indicated that the shell was able to contain the salt and its solution without leakage issues.

A scanning electron microscope image is presented in **Fig. 49** for the cross-section of the shell after few microcapsules were cut into halves using a sharp razor blade. The average shell thickness of the capsules was around ~70 μm. The inner surface of the shell looks very smooth and free of any imperfections as shown in **Fig. 50a**. Scanning electron microscope images with high magnification (**Fig. 50b** and **Fig. 50c**) showed that there were dimples that were small in size (~few nanometers) on the surface of the shell. A higher magnification image (**Fig. 50d**) confirmed that the shell was made of a dense membrane, and that there would not be any leakages (salt particles or liquid solution) from the capsules.

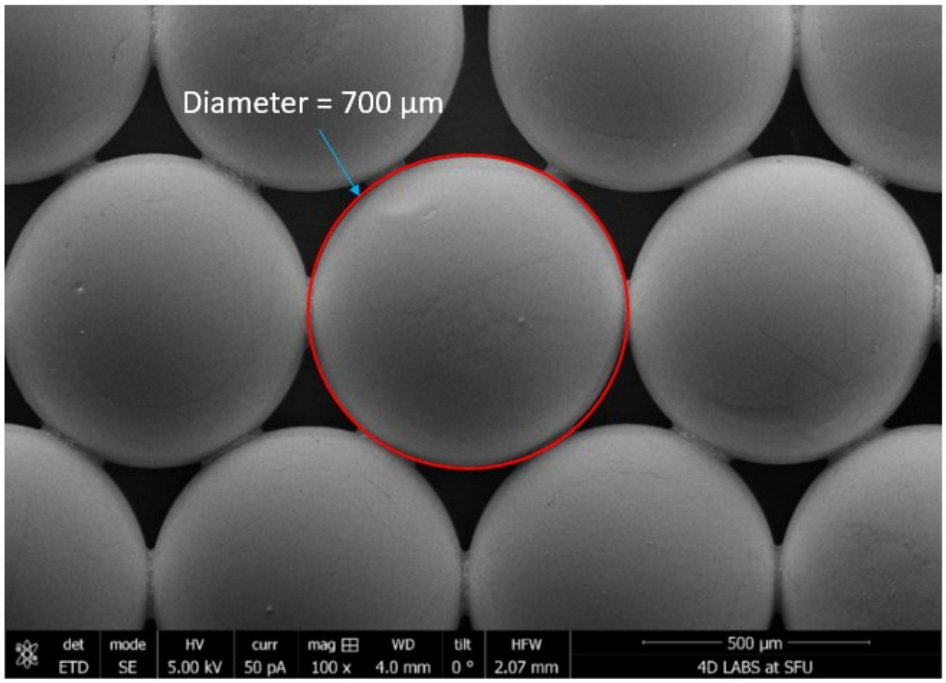

Fig. 48: A scanning electron microscope image of the shell's outer surface.

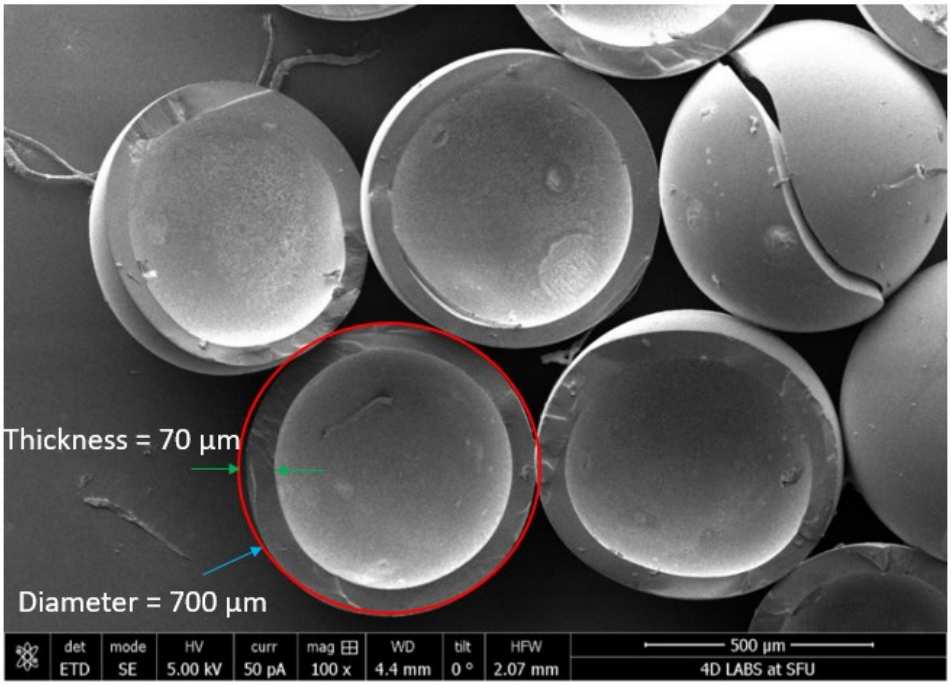

Fig. 49: A scanning electron microscope image of a shell's cross-section.

(a)

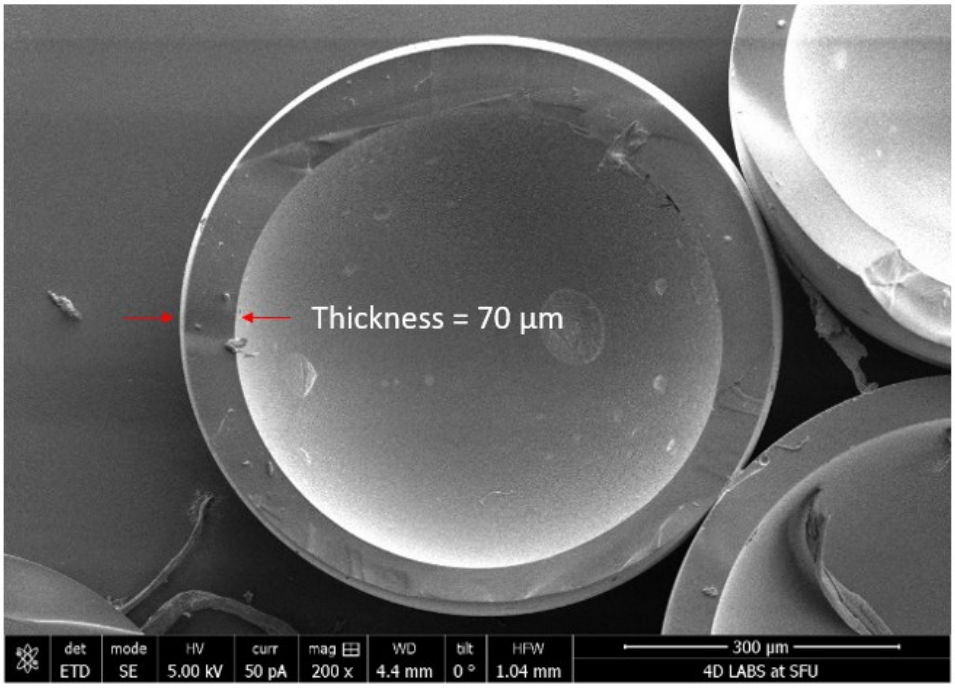

(b)

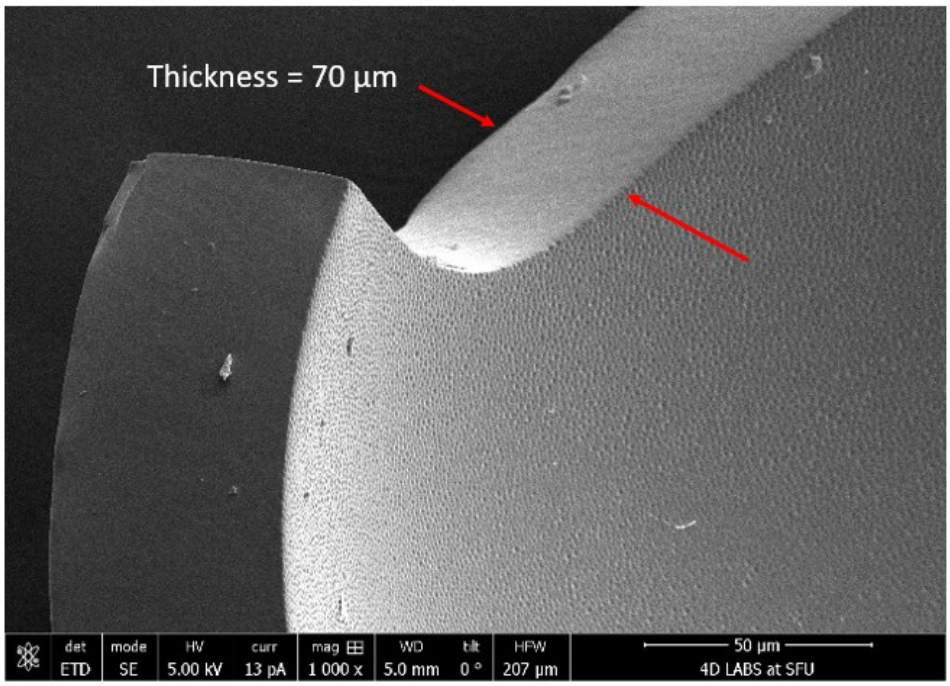
Thickness = 70 µm
det ETD
mode SE
HV 5.00 kV
curr 13 pA
mag 1 000 x
WD 5.0 mm
tilt 0 °
HFW 207 µm
50 µm
4D LABS at SFU

(c)

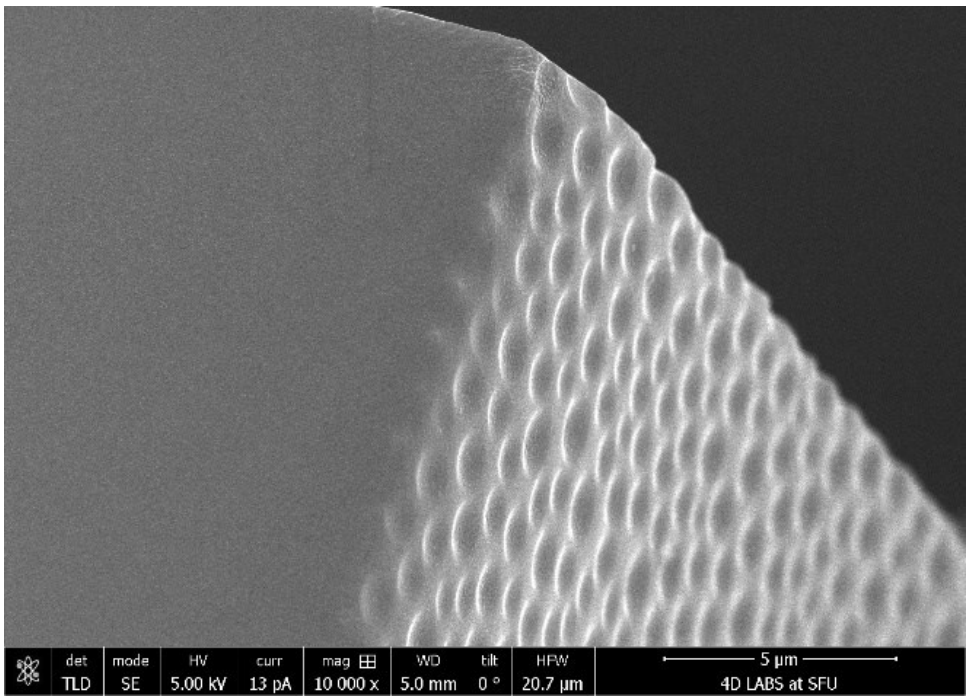
det TLD
mode SE
HV 5.00 kV
curr 13 pA
mag 10 000 x
WD 5.0 mm
tilt 0 °
HFW 20.7 µm
5 µm
4D LABS at SFU

(d)

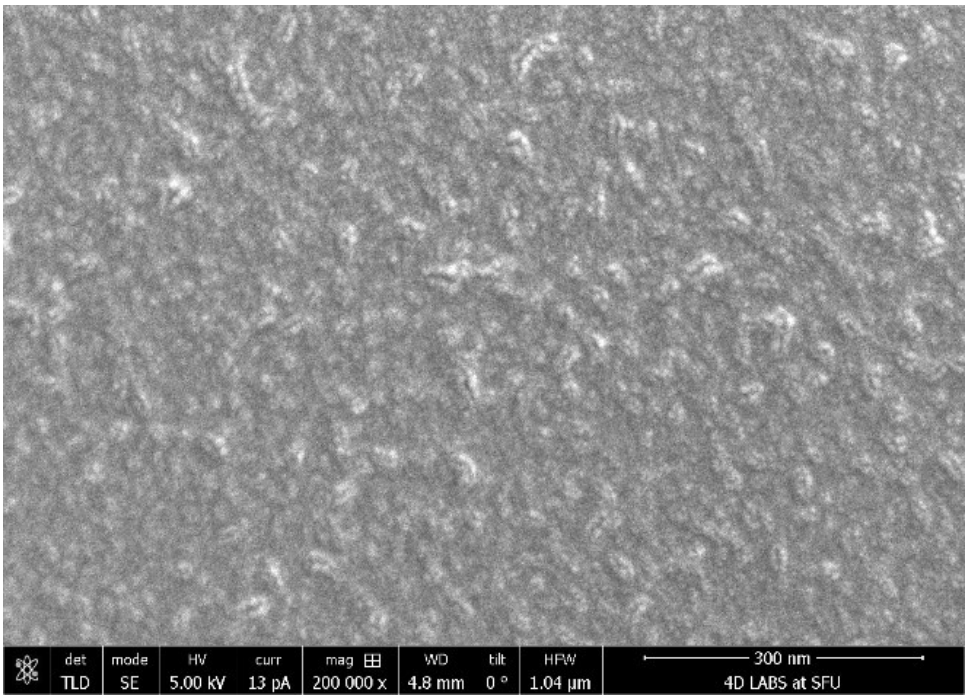

Fig. 50: High magnification (a) 200x; (b)1000x; (c)10,000x, and (d) 200,000x scanning electron microscope images of the shell cross-section.

3.3.5. Mechanical Strength Testing

3.3.5.1. Compression Test

To examine the mechanical integrity of the capsules, compression and expansion tests were performed. The compression test was performed using a thermomechanical analyzer (TMA) (Q400EM, TA instruments) available in our lab (see **Fig. 51**). The capsules were placed on the stage of the instrument, and a standard expansion probe with a 6.07 *mm* diameter contact area was used to apply a force of 0.05 *N* per minute ramp rate as shown in **Fig. 52**. The tests were conducted in a dry nitrogen environment at 20 ºC. The measured displacement as a function of applied load for capsules with various shell thicknesses to the outer diameter ratio (t_{shell}/D_o) is presented in **Fig. 53**. The results show that capsules can withstand up to a 1 Newton force (about 100 *g* mass) without breaking. The average measured mass of the capsules was 0.5 *mg*. This suggests that a capsule can withstand a force of up to 2 X 10^5 its weight. It is worth noting that by repeating the test multiple times, some capsules with a t_{shell}/D_o=0.045 ruptured. This is due to their thin shell. Therefore, it is recommended that the capsules be fabricated with a ratio of t_{shell}/D_o=0.047 or higher to ensure the mechanical integrity with acceptable shell mass transfer resistance.

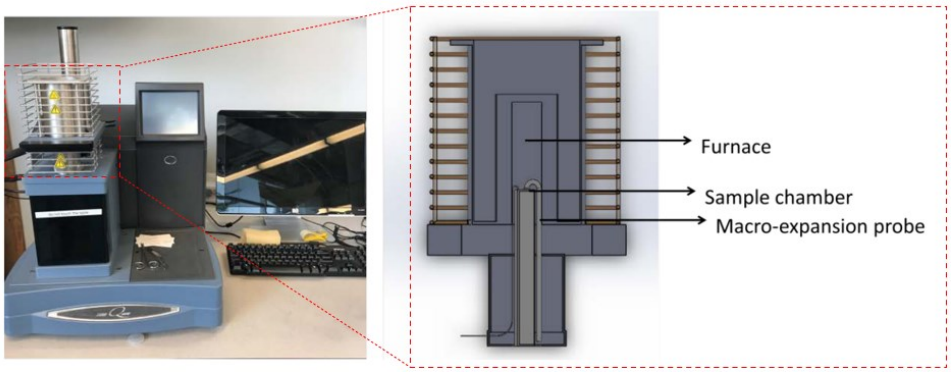

Fig. 51: The thermomechanical analyzer (Q400EM, TA instruments).

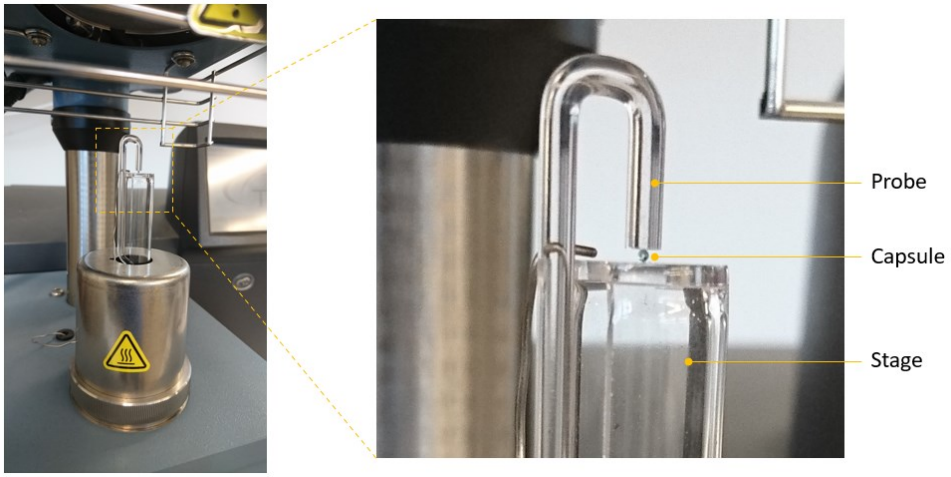

Fig. 52: Microcapsules under compression testing.

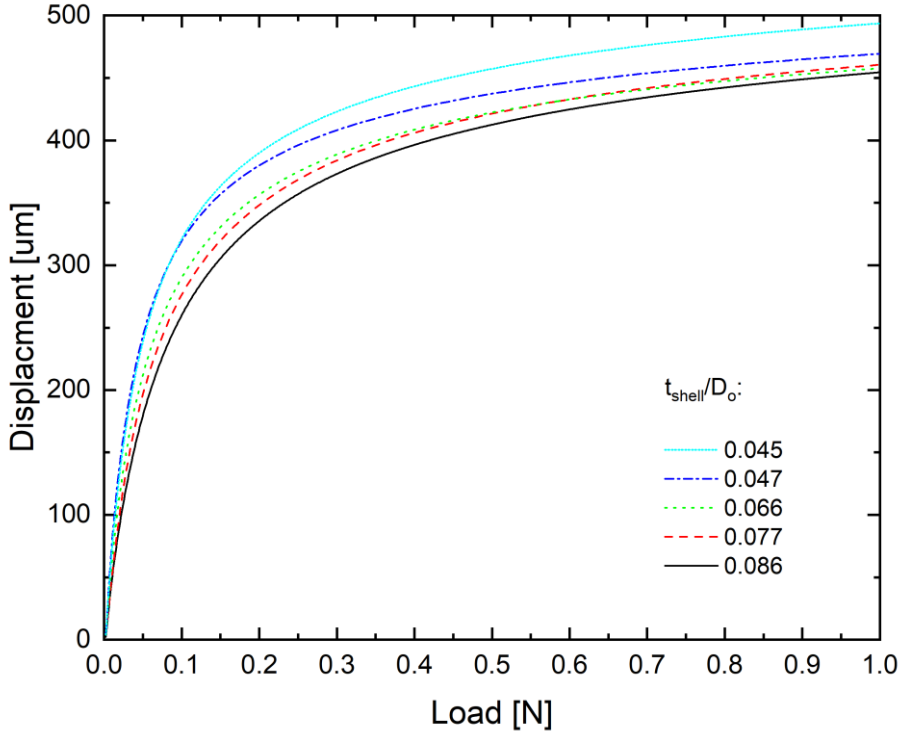

Fig. 53: Compression testing: displacement as a function of applied load.

3.3.5.2. Expansion Test

The elastic capsules will also be subjected to cyclic expansion pressure when they go through the absorption/desorption process. Therefore, a sample of the capsules was immersed in a water bath for 3 hours to promote the osmotic swelling due to the presence of the salt inside the capsules. A control sample which was used as a reference was soaked in a LiBr salt solution with the same concentration as that of the inner core (60 wt% LiBr) to reach osmotic equilibrium. Microscopic images of both samples (in a LiBr solution and a water bath) are shown in **Fig. 54**. By comparing the measured shell thickness in both samples, it appears that, due the to the osmotic swelling, the outer diameter of the capsules increased by 6% and the shell became ~28% thinner without affecting the integrity of the capsules.

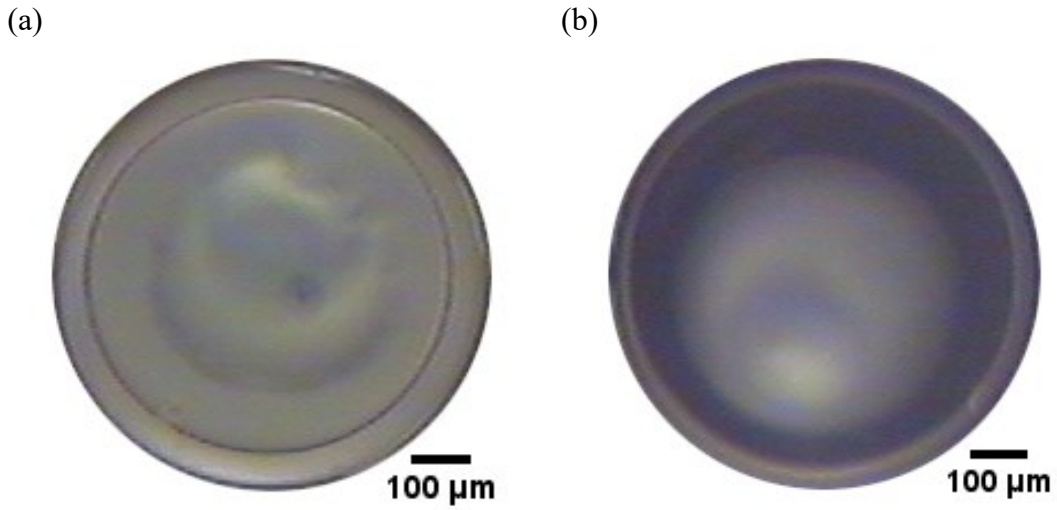

Fig. 54: The size of the microcapsule with 60 wt% LiBr (sol.) soaked in: (a) 60 wt% LiBr solution (D_o=686 *µm*, D_i=577 *µm*); and (b) deionized water (D_o=726 *µm*, D_i=648 *µm).*

3.3.5.3. Multi-cycle Performance Test

A small batch of microcapsules that contain the LiBr liquid desiccant was selected for muti-cycle performance testing using pressure swing sorption-desorption cycles. Pressure swings were done between 0 and 2.1 kPa at 30 °C as shown in **Fig. 55a**. It was found that the uptake capacity of the capsules did not change even after 200 cycles as presented in **Fig. 55b** and the capsules remained intact.

(a)

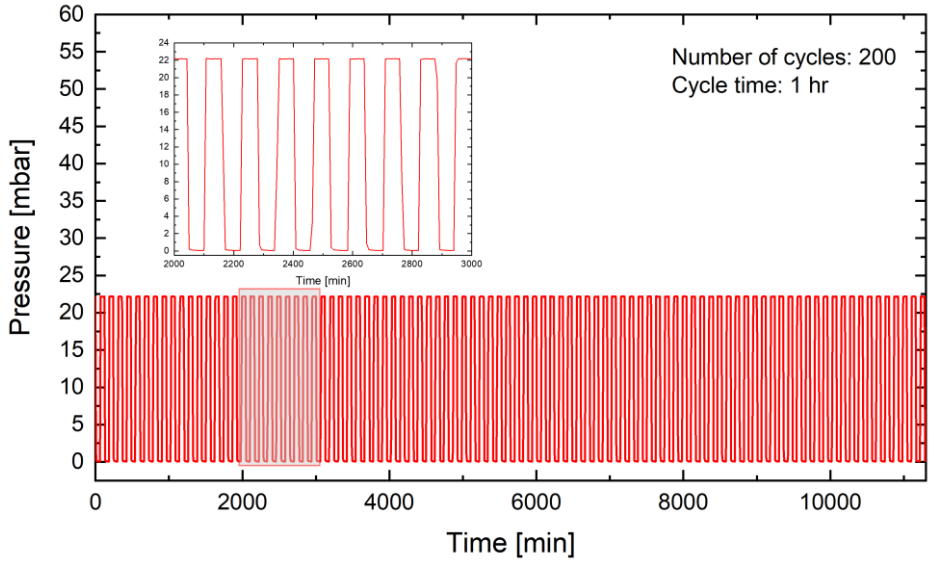

(b)

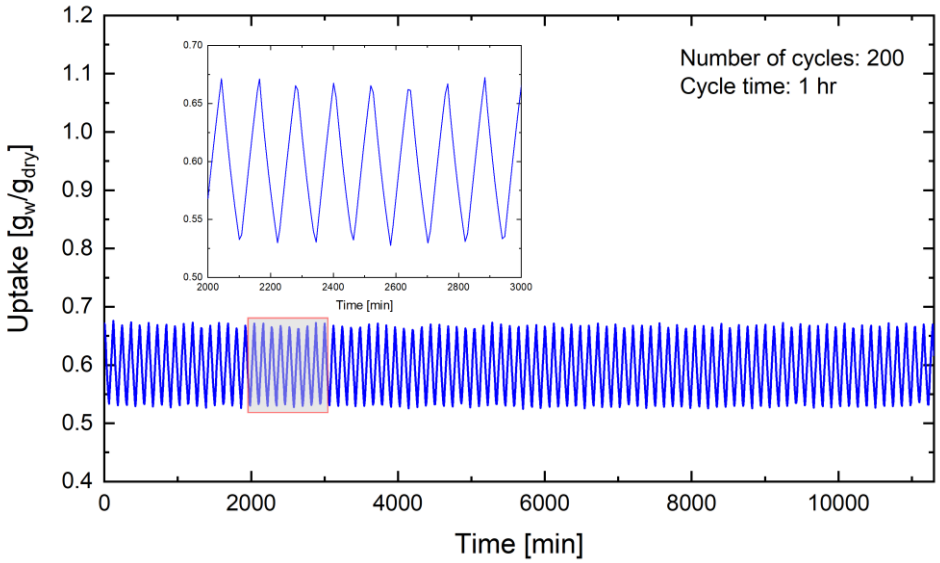

Fig. 55: (a) LiBr microcapsules (at 30 °C) uptake change; and (b) pressure swing (0-2.1 kPa) during sorption-desorption cycles.

3.4. Summary

Microfluidic technology enables synthesizing spherical particles with a uniform and controlled size with high precision. This enables fundamental studies on a single spherical particle and the opportunity to study the pertinent heat and mass transfer to predict the performance of a microreactor with high certainty. Nevertheless, the state-of-the-art approach for creating encapsulated particles using microfluidics techniques is still a "custom-made" glass capillary device.

In this PhD program, a microfluidic technique was used to produce spherical microreactors that contain a liquid LiBr desiccant. A custom-built microfluidic device was developed to create a double-emulsion, water-in oil-in water: an aqueous LiBr solution-in a liquid resin-in an aqueous carrier fluid. An experimental setup that included an optical microscope and a UV light source was utilized to monitor the microfluidic device under operation and to crosslink the resin to form a spherical shell that encapsulates the liquid desiccant.

Uniform-sized microcapsules were produced, and a thermogravimetric analysis was conducted to acquire isotherm curves to determine the sorption capacity. The collected sorption data showed that the produced microcapsules offered a higher sorption capacity (1 g_w/g_{dry} under 80% relative humidity) than the other commonly used solid desiccants. The amount of water adsorbed by the shell material was found to be insignificant and did not contribute to the microcapsule's overall sorption capacity. The microcapsules were able to contain the salt during crystallization, and X-ray diffraction analysis confirmed that the observed crystals in the microscopes images were indeed for the encapsulated (LiBr) salt.

The produced microreactors were proven to have excellent mechanical strength which was confirmed by the compression, expansion, and multi-cycle sorption-desorption tests. The microcapsules withstood a force of up to 2 X 10^5 their weight, expanded (elastically) during the absorption process without rupture, and did not leak or have a reduced capacity even after accelerated tests of 200 sorption-desorption cycles.

4. Fundamental Studies on Spherical Particles

4.1. Abstract

A new analytical solution, based on scale analysis and similarity transformation, is presented to solve a linearized form of the energy equation for the laminar forced convection over a sphere in a spherical coordinate system. Compact expressions for temperature, wall heat flux, and the Nusselt number are developed as a function of the Reynolds number (Re_D) and Prandtl number (Pr) for both isothermal and isoflux boundary conditions. A blending method is used to extend the range of the present analytical expression to cover $0 < \mathrm{Re}_D < 10^5$ and $0.7 < \mathrm{Pr} < \infty$. The present analysis reveals that the theoretical averaged-Nusselt numbers for the laminar forced convection over isoflux (constant wall heat flux) and isothermal (uniform wall temperature) spheres are identical. The proposed model is verified by comparing the analytical expression with the available experimental data over various Reynolds and Prandtl numbers. The derived expression for the averaged-Nusselt number was later used (in Chapter 6) in modeling the transient behaviour of the reactor. Another analytical model for estimating the thermal spreading resistance through a spherical particle is presented in **Appendix B**.

4.2. Introduction

Forced convection heat transfer from a solid sphere is an interesting problem that can be found in many applications. Many experimental studies were conducted to investigate the laminar forced convection heat transfer from an isothermal sphere. Drake and Backer [151] investigated the heat transfer from an isothermally heated sphere to a rarefied gas in a supersonic flow and proposed a correlation for air (Prandtl number, Pr=0.7). Their correlation was applicable for flows with a Reynolds number (Re_D) in the range of $0.1 < \mathrm{Re}_D < 2\times10^5$. Yuge [152] presented a correlation for the Nusselt number (Nu), for $10 < \mathrm{Re}_D < 1.5\times10^5$, to estimate the heat transfer from the isothermal spheres to an air flow. Raithby and Eckert [153] conducted a careful study to show the effect of turbulence intensity on the average heat transfer from an isothermal sphere to an air stream within the $3.6\times10^3 < \mathrm{Re}_D < 5.2\times10^4$ range. Whitaker [154] collected and analyzed experimental data from the literature and proposed an easy-to-use correlation for $3.5 < \mathrm{Re}_D < 7.6\times10^4$ and $0.7 < \mathrm{Pr} < 380$. Vliet and Leppert [155] experimentally studied the forced convection heat transfer from an isothermal sphere to liquid water flow. The authors [5] argued that in regions where there was a large temperature difference between the solid surface and water, the effect of the induced natural convection might be significant, and recommended an empirical correlation for calculating the average heat transfer coefficient from isothermal spheres to fluids with $2 < \mathrm{Pr} < 380$ for $1 < \mathrm{Re}_D < 3\times10^4$. Kramers [156] carried out the most

comprehensive study for the forced convention heat transfer from a solid sphere using air (Pr=0.71), water (Pr=7.3 and Pr=10.7), and oil (Pr=213 and Pr=380) as fluids to cover a wide range of Prandtl numbers. Will et al. [157] experimentally investigated the forced convection over isothermal spheres with the focus on fluid flows with higher Reynolds numbers ($>3.3\times10^5$) than those considered in previous studies. They [157] claimed that there was a critical Reynolds number beyond which there would be a sudden increase in the Nusselt number.

Developing an analytical model to study forced convection over a sphere is considered a complex task without neglecting the flow separation that occurs at $\mathrm{Re}_D > 20$. The analysis of the mass transport process from the surface of a sphere can be used to estimate the heat transfer, i.e., due to the analogy between the two processes. Lee and Barrow [158] used an approximate integral method to solve the integrated boundary-layer equations for axisymmetric flow over a sphere from the forward stagnation up to the point of separation by assuming quartics velocity and temperature profiles. An integral method was also used by Garner and Keey [159] to study the forced convection mass transfer from a sphere at low Reynolds numbers (2.3 to 255). An earlier modeling approach using an integral method was presented by Frössling [160], who estimated the mass transfer rate for a naphthalene droplet evaporating in air (Pr=2.53) by analytically analyzing a laminar boundary layer. Linton and Sutherland [161] compared the heat and mass transfer rates predicted by the theoretical work of Frössling [160] with the experimental data available in the literature for a flow over a sphere. Although, the theoretical local transfer rates were in fair agreement with the experimental data over the front half of the sphere, the results showed that the experimental local values at the front stagnation point were 44% lower than for the theory and differed considerably between studies in the literature.

Several studies were carried out to develop analytical solutions for the forced convection heat transfer from a sphere. Hsu [162] and Sideman [163] derived analytical expressions to estimate the Nusselt number for liquid metals ($\mathrm{Pr} \sim 0.01$) flowing past a single sphere by assuming a potential flow. Using the Laplace transform method, Drake and Backer [151] obtained an expression for the Nusselt number by solving a simplified energy equation for the forced convection over an isothermal sphere. Johnstone et al. [164] used a separation of variables method to provide a series solution for the laminar flow over an isothermal sphere by assuming a constant fluid velocity over the sphere. The separation of variables method was also used by Dennis et al. [165], who developed an analytical solution for the forced convection of viscous flows over an isothermal sphere at low values of Reynolds numbers. Ahmed et al. [166] developed an analytical solution for the laminar flow over a sphere by approximating the energy equation to a form of a transient heat conduction equation for which a solution was available. They [166] presented expressions for a surface averaged-

effective velocity at two asymptotes ($\mathrm{Pr} \ll 1$ and $\mathrm{Pr} \gg 1$) and used a blending technique to develop a general expression for the Nusselt number that was valid for $0 \le \mathrm{Re}_D \le 2\times10^4$ and all Prandtl numbers. The blending method was used earlier by Yovanovich [167] to provide a general expression for the heat transfer coefficient for isopotential spheroids. In another work, Ahmed et al. [168] included the influence of the turbulence level on the heat transfer characteristics in their modeling approach.

Our literature survey suggests that most of the experimental and theoretical studies were focused on forced convection over an isothermal sphere and that there is a scarcity of information about isoflux spheres (constant surface heat flux). To the best of our knowledge, there is no study that compared the theoretical heat transfer coefficients for isothermal and isoflux spheres. To this end, the objective of this study is to address this gap by developing new and compact expressions for temperature distribution and heat flux for the laminar forced convection heat transfer from a heated sphere, for both isothermal and isoflux boundary conditions. Both scale analysis and similarity transformation approaches are used to develop new compact models for the isothermal and isoflux cases. The developed models are compared and validated using experimental data available in the literature.

4.3. Mathematical Modeling

4.3.1. Similarity Solution for the Energy Equation

Fig. 56 schematically shows the temperature profiles in the thermal boundary layer (with a δ_T thickness) for a fluid with an approaching temperature T_∞ and velocity V_∞ flowing over a heated sphere with a radius a (or diameter D). The energy equation is:

$$\rho c_p \frac{\partial T}{\partial t} + \rho c_p \vec{V}\cdot\left(\vec{\nabla}T\right) = \vec{\nabla}\cdot\left(k\vec{\nabla}T\right) + \beta T\frac{Dp}{Dt} + \mu\Phi \qquad 4.1$$

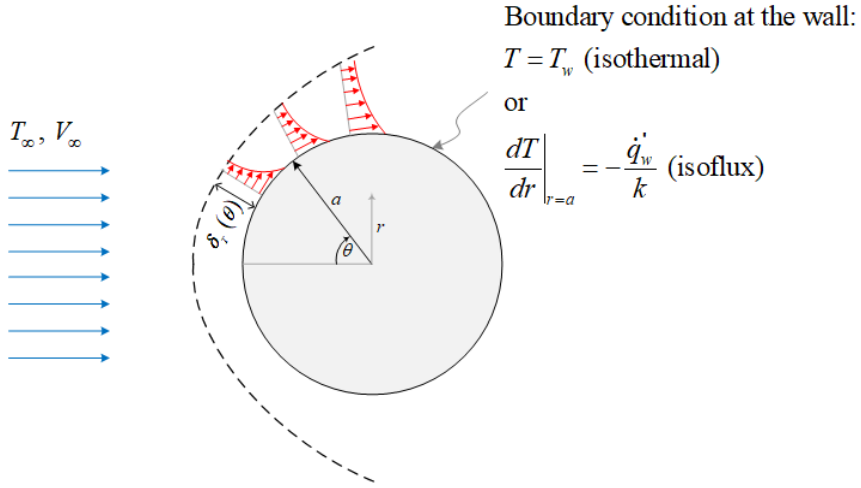

Fig. 56: A schematic diagram of the temperature profiles in the thermal boundary layer.

To simplify the problem, the following assumptions are made:

- Non-porous solid sphere;
- Steady-state heat transfer;
- Incompressible laminar flow ($\mathrm{Re} < 10^5$) with constant fluid properties;
- No flow separation;
- Symmetry around the azimuthal angle (2D problem in r and θ directions);
- Negligible pressure, gravity, and viscous dissipation terms;
- Negligible heat conduction in the θ-direction; and
- Oseen's approximation, i.e., to linearize the convective term (velocity of the fluid around the sphere is everywhere parallel to the surface and is constant) [169]:

$$\left[v_r \frac{\partial T}{\partial r} + \frac{v_\theta}{r} \frac{\partial T}{\partial \theta} \right] \rightarrow \frac{V}{r} \frac{\partial T}{\partial \theta} \tag{4.2}$$

Accordingly, the energy equation in spherical coordinates reduces to the following:

$$\frac{V}{\alpha} \frac{\partial T}{\partial \theta} = \frac{1}{r} \frac{\partial}{\partial r} \left(r^2 \frac{\partial T}{\partial r} \right) \qquad \begin{matrix} r \geq a \\ 0 \leq \theta \leq \pi \end{matrix} \tag{4.3}$$

The coordinate system is transformed to set the wall as the coordinate reference. By defining a new coordinate system in the radial direction as $r^* = r - a$, the energy equation becomes:

$$\frac{V}{\alpha} \frac{\partial T}{\partial \theta} = r \frac{\partial^2 T}{\partial r^2} + 2 \frac{\partial T}{\partial r} = r^* \frac{\partial^2 T}{\partial r^{*2}} + a \frac{\partial^2 T}{\partial r^{*2}} + 2 \frac{\partial T}{\partial r^*} \tag{4.4}$$

By performing a scale (order of magnitude) analysis and considering that $r^* \sim \delta_T$, the terms on the right-hand side of Eq. (4.4) scale at: $r^* \frac{\partial^2 T}{\partial r^{*2}} \sim \frac{T}{\delta_T}$, $a \frac{\partial^2 T}{\partial r^{*2}} \sim a \frac{T}{\delta_T{}^2}$, and $2 \frac{\partial T}{\partial r^*} \sim 2 \frac{T}{\delta_T}$. One can note that the second term is an order of magnitude larger than the first and third terms. Accordingly, Eq. (4.4) takes the following simpler form:

$$\frac{V}{\alpha} \frac{\partial T}{\partial \theta} = a \frac{\partial^2 T}{\partial r^{*2}} \qquad \begin{matrix} r^* \geq 0 \\ 0 \leq \theta \leq \pi \end{matrix} \tag{4.5}$$

By conducting a scale analysis, the scale of the thermal boundary layer thickness δ_T can be found:

$$\delta_T \sim \sqrt{\frac{\alpha a \theta}{V}} = \frac{\sqrt{2} a \sqrt{\theta}}{\sqrt{\mathrm{Re}_D \, \mathrm{Pr}}} \tag{4.6}$$

A non-dimensional similarity parameter η can be defined as:

$$\eta = \frac{r^*}{\delta_T} \tag{4.7}$$

Equation 4.5 is then reduced to an ordinary differential equation that has the following form:

$$\frac{d^2T}{d\eta^2} + \frac{\eta}{2}\frac{dT}{d\eta} = 0 \qquad 0 \le \eta \le \infty \tag{4.8}$$

A non-dimensional temperature can be defined as:

$$\Theta(\eta) = \frac{T(\eta) - T_\infty}{T_w(\eta) - T_\infty} \tag{4.9}$$

where, T_w is the sphere wall temperature ($T_w =$ const. for isothermal sphere, and $T_w = T_w(\eta)$ for isoflux sphere).

4.3.2. Isoflux Boundary Condition

For the case of a sphere with constant heat flux at the wall, the boundary conditions for Eq. (4.8) are:

$$r = a: \left.\frac{dT}{d\eta}\right|_{r=a} = -a\frac{\dot{q}''_w}{k} \tag{4.10}$$

$$r = \infty: \quad T = T_\infty \tag{4.11}$$

By solving Eq. (4.8) after applying the above boundary conditions, the following expression can be used to find the temperature distribution for the isoflux sphere case:

$$T(\eta) = T_\infty + \frac{\sqrt{\pi}}{k}\delta_T \dot{q}''_w \left[1 - erf\left(\frac{\eta}{2}\right)\right] \tag{4.12}$$

Or, in terms of r and θ :

$$T(r,\theta) = T_\infty + \frac{\sqrt{\pi}}{k}\frac{\sqrt{2}a}{\sqrt{\mathrm{Re}_D\,\mathrm{Pr}}}\dot{q}''_w \left[1 - erf\left(\left(\frac{r-a}{2\sqrt{2}a}\right)\frac{\sqrt{\mathrm{Re}_D\,\mathrm{Pr}}}{\sqrt{\theta}}\right)\right]\sqrt{\theta} \tag{4.13}$$

The local temperature at the wall, $\eta = 0$, can be determined by:

$$T_w = T_\infty + \frac{\sqrt{\pi}}{k}\delta_T \dot{q}''_w \tag{4.14}$$

4.3.3. Isothermal Boundary Condition

Considering the case in which the wall of the sphere is isothermal, the boundary conditions for Eq. (4.8) are:

$$r = a: \; T = T_w \tag{4.15}$$

$$r = \infty: \quad T = T_\infty \tag{4.16}$$

The temperature distribution for this case in terms of the similarity variable η can be found as:

$$T(\eta) = T_w + (T_w - T_\infty) erf\left(\frac{\eta}{2}\right) \tag{4.17}$$

The final form of the temperature distribution for the forced convection over an isothermal sphere as a function of r and θ is:

$$T(r,\theta) = T_w - (T_w - T_\infty) erf\left(\left(\frac{r-a}{2\sqrt{2}a}\right)\frac{\sqrt{\mathrm{Re}_D \,\mathrm{Pr}}}{\sqrt{\theta}}\right) \tag{4.18}$$

The local heat flux temperature at the wall can be evaluated by:

$$\dot{q}''_w = -k\left.\frac{dT}{dr}\right|_{r=a} = -k\left(\left.\frac{dT}{d\eta}\right|_{r=a}\right)\left(\frac{d\eta}{dr}\right) = \frac{1}{\pi}\frac{(T_w - T_\infty)}{\delta_T} \tag{4.19}$$

4.4. Results and Discussion

Fig. 57a and **Fig. 57b** show the temperature distribution for flow over a sphere with isoflux and isothermal boundary conditions at the wall, respectively, as evaluated using the expressions developed in this work, Eq. (4.13) and Eq. (4.18). For the purpose of showing the temperature variation inside the thermal boundary layer, the results are shown for a low value of Reynolds number ($\mathrm{Re}_D = 1000$) and a Prandtl number on the order of 1. For a sphere with a constant heat flux boundary condition, the wall temperature increases gradually in the angular direction θ and approaches its maximum at $\theta = \pi$ as illustrated by **Fig. 57a**.

The temperature profiles at various locations in the thermal boundary layer are shown in **Fig. 58a** and **Fig. 58b** for the isoflux and isothermal spheres, respectively.

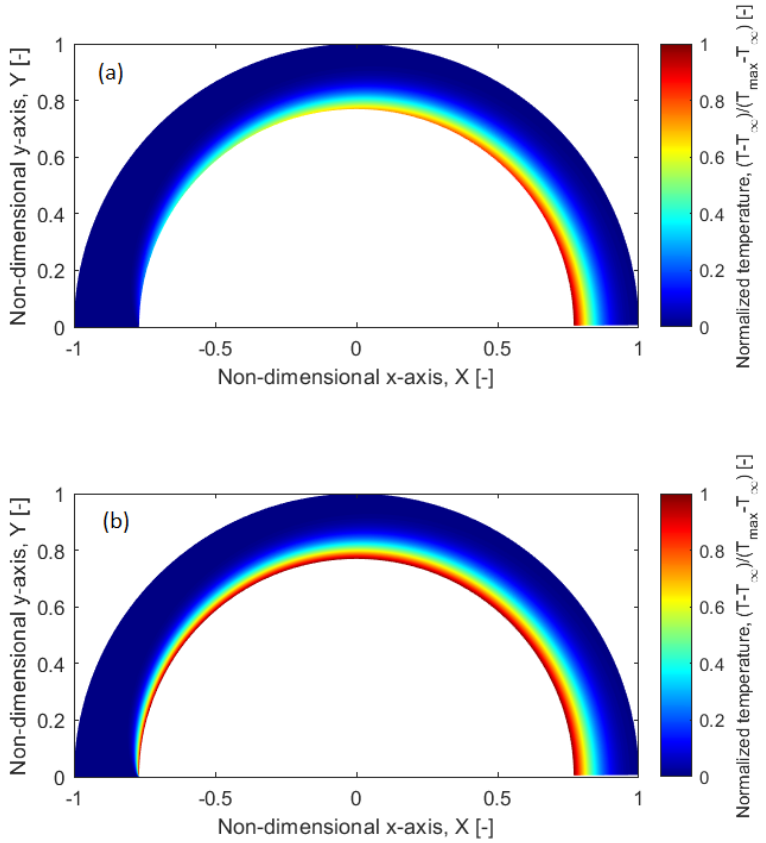

Fig. 57: The temperature distribution for forced convection ($\mathrm{Re}_D = 1000$, $\mathrm{Pr} = 1$) over a sphere with: (a) a constant heat flux of $\dot{q}_w'' = 100\ \mathrm{W/m^2}$; and (b) a uniform wall temperature of $T_w = 80^{\circ}\mathrm{C}$.

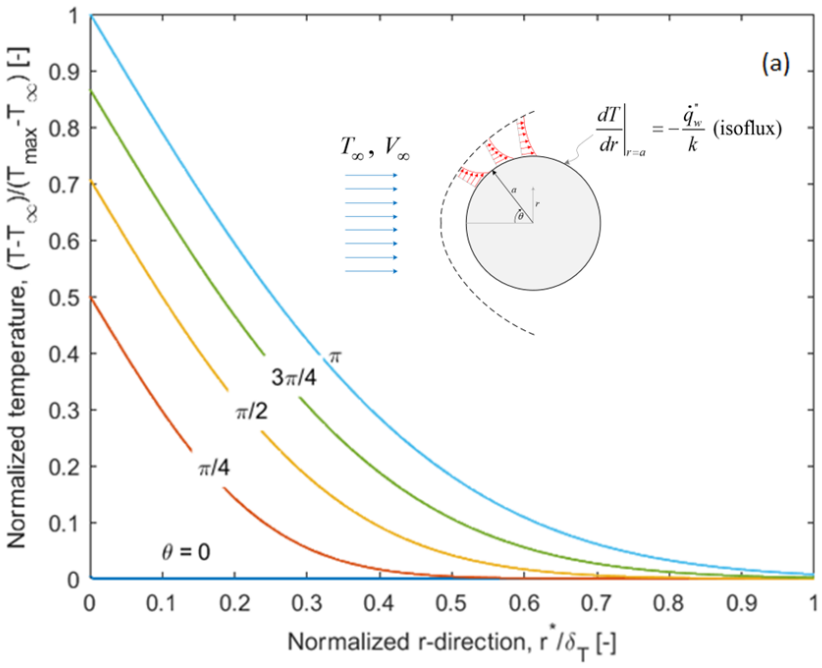

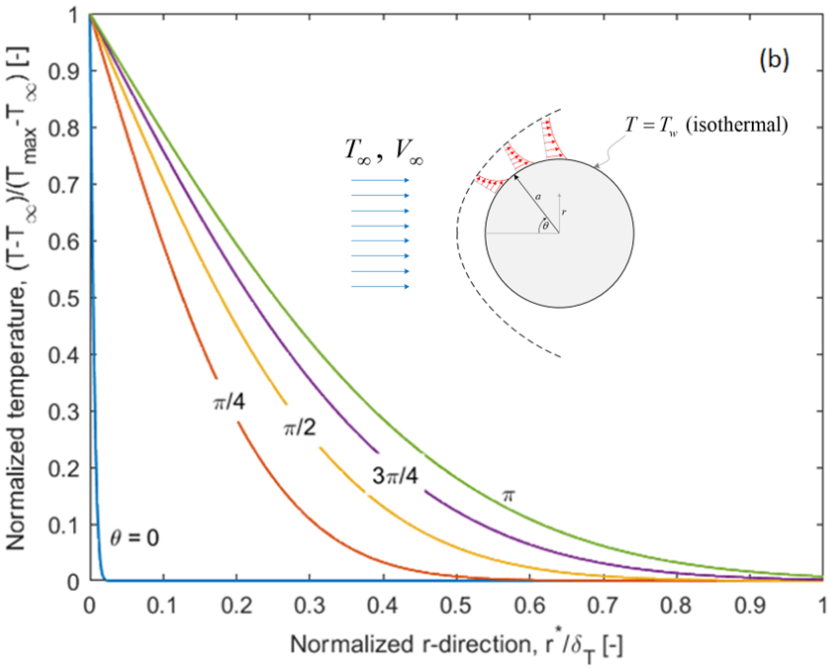

Fig. 58: Normalized temperature profiles at various locations in the thermal boundary layer for: (a) an isoflux; and (b) an isothermal sphere.

4.4.1. Nusselt Number Expressions (Isoflux and Isothermal Spheres)

The heat transfer coefficient can be expressed in terms of the Nusselt number, $Nu_D = \frac{hD}{k}$. In the analysis, two heat transfer asymptotes are considered: i) a conduction limit that represents the conduction heat transfer between the body and a surrounding stationary fluid; and ii) the other limit due to the advection (the bulk motion of the fluid) [166,170,171]. Accordingly, the total averaged Nusselt number is determined by:

$$\overline{Nu}_{\text{total}} = \overline{Nu}_{(\text{conduction})} + \overline{Nu}_{(\text{advection})} \tag{4.20}$$

The conduction limit can be determined by solving the conduction energy equation for a stationary thin fluid film that surrounds a heated sphere, as follows [172]:

$$\frac{\partial}{\partial r}\left(r^2 \frac{\partial T}{\partial r}\right) = 0 \tag{4.21}$$

For a flow with a constant wall heat flux, the boundary conditions are:

$$r = a : \left.\frac{\partial T}{\partial r}\right|_{r=a} = -\frac{\dot{q}''_w}{k} \tag{4.22}$$

$$r=\infty: \quad T=T_{\infty} \tag{4.23}$$

By applying the boundary conditions, the solution for Eq. (4.21) is:

$$T=\frac{\dot{q}_w^{"}a^2}{k}\frac{1}{r}+T_{\infty} \tag{4.24}$$

The temperature at the wall can be evaluated by:

$$T_w=T_{\infty}+\frac{\dot{q}_w^{"}a}{k} \tag{4.25}$$

It follows that the conduction limit for an isoflux sphere is:

$$\overline{Nu}_{\text{conduction}}=\frac{\dot{q}_w^{"}(2a)}{k(T_w-T_{\infty})}=2.0 \tag{4.26}$$

The solution for Eq. (4.21) for a sphere with an isothermal boundary condition results in the same value ($\overline{Nu}_{\text{conduction}}=2$).

The Nusselt number, due to the advection, can be obtained by studying the thermal boundary layer. The local value for the Nusselt number along the surface of a sphere is determined by:

$$Nu_{\text{advecion}}(\theta)=\frac{h(2a)}{k}=\frac{\dot{q}_w^{"}(2a)}{k(T_w-T_{\infty})} \tag{4.27}$$

By substitution, the expressions derived using the analysis presented herein for the temperature distribution, Eq. (4.14), for an isoflux sphere, it follows that:

$$Nu_{\text{advecion}}(\theta)=0.798\sqrt{\text{Re}_D\,\text{Pr}}\,(\theta)^{-1/2} \tag{4.28}$$

Performing the same analysis for the isothermal sphere, Eq. (4.19) - to find the local heat flux at the wall - results in the same above expression, Eq. (4.28). Accordingly, the averaged value $\overline{Nu}_D$ can be determined by:

$$\overline{Nu}_D=\frac{1}{A}\iint_A Nu\cdot dA=\frac{1}{2}\int_0^{\pi} Nu_D\cdot\sin(\theta)\,d\theta=0.714\sqrt{\text{Re}_D\,\text{Pr}} \tag{4.29}$$

Combining Eqs. (4.20), (4.26), and (4.29), the total averaged value for the Nusselt number for the laminar forced convection over a sphere with a uniform wall temperature or constant wall heat flux can determined by:

$$\overline{Nu}_{\text{D}}=2+0.714\sqrt{\text{Re}_D\,\text{Pr}} \tag{4.30}$$

Our analysis indicates that the theoretical Nusselt number for isoflux and isothermal cases are the same, i.e., one expression can be used for both cases. This result can be explained by substituting the expressions for T_w using Eqs. (4.12) and (4.14) in Eq. (4.9) at $\eta = 0$. For both isothermal and isoflux spheres, the non-dimensional temperature distribution, defined by Eq. (4.9), would be:

$$\Theta(\eta) = 1 - erf\left(\frac{\eta}{2}\right) \tag{4.31}$$

Interestingly, with this definition, the form of the Nusselt number and the non-dimensional temperature distribution over a sphere with a constant heat flux boundary condition at the wall would be identical to an isothermal sphere as shown in **Fig. 59**. The non-dimensional temperature profile as a function of the similarity variable η is plotted in **Fig. 60**. By comparing this figure with **Fig. 58a** and **Fig. 58b**, it can be observed that all curves collapse onto a single curve. It is worth noting that at $\eta \simeq 5$, there is no change in the temperature gradient, and that the scaling factor for the thermal boundary layer can be considered as 5. Accordingly, the thermal boundary layer thickness can be determined by:

$$\delta_T = 5\sqrt{\frac{\alpha a \theta}{V}} = 5\frac{\sqrt{2}a\sqrt{\theta}}{\sqrt{\mathrm{Re}_D\,\mathrm{Pr}}} \tag{4.32}$$

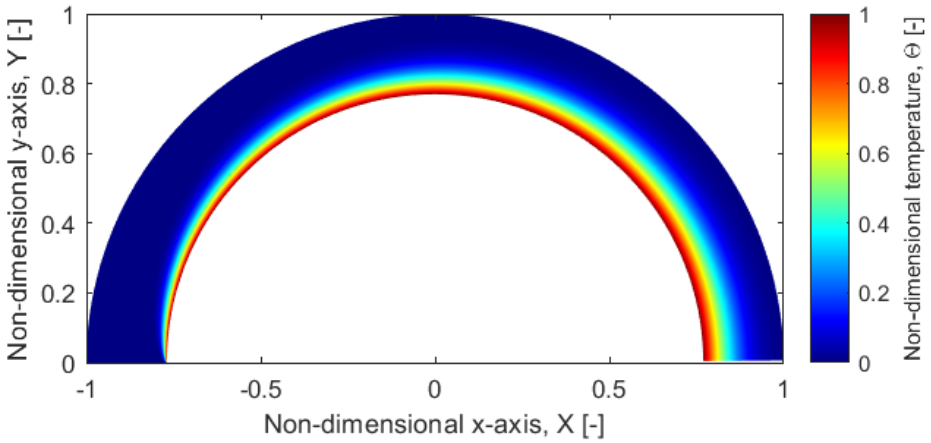

Fig. 59: The non-dimensional temperature distribution (see Eq. (28)) in the thermal boundary layer.

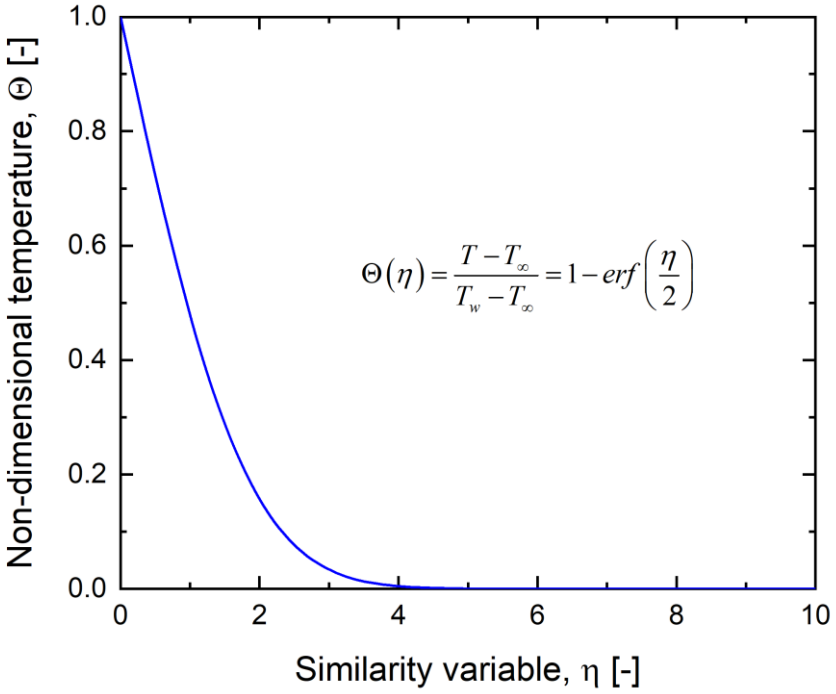

Fig. 60: The non-dimensional temperature distribution, Θ, as a function of the similarity variable η for laminar flow over isothermal and isoflux spheres.

4.4.2. Validation with Experimental Data

To assess the validity of the presented model for both isoflux and isothermal spheres, the Nusselt number values that were evaluated using Eq. (4.30) were compared with the data and empirical correlations available in the literature for both boundary conditions with $\mathrm{Pr}\sim 1$.

The experimental data collected by Kramers [156] (air, Pr=0.71) for forced convection over sphere is used to validate the isoflux case. In conducting the experiments, Kramers [156] used high frequency heating to induce volumetric heat generation from steel spheres, however; the temperature variation along the wall temperature was not reported. Due to the low thermal conductivity of steel and the low Reynolds numbers at which the experiments were conducted ($\mathrm{Re}_D = 10-2000$), the variation in the temperature along the surface of the spheres may be significant and the reported Nusselt number values are actually for a forced convection heat transfer from a sphere with constant heat flux boundary condition at the wall. **Fig. 61** shows that Eq. (4.30) represents a good agreement for Kramers' experimental data.

The empirical correlations developed by Drake and Backer [151], Yuge [152], Raithby and Eckert [153] for a forced convection (of air) over an isothermal sphere were used to assess the validity of Eq. (4.30) for this case. In these experiments, special

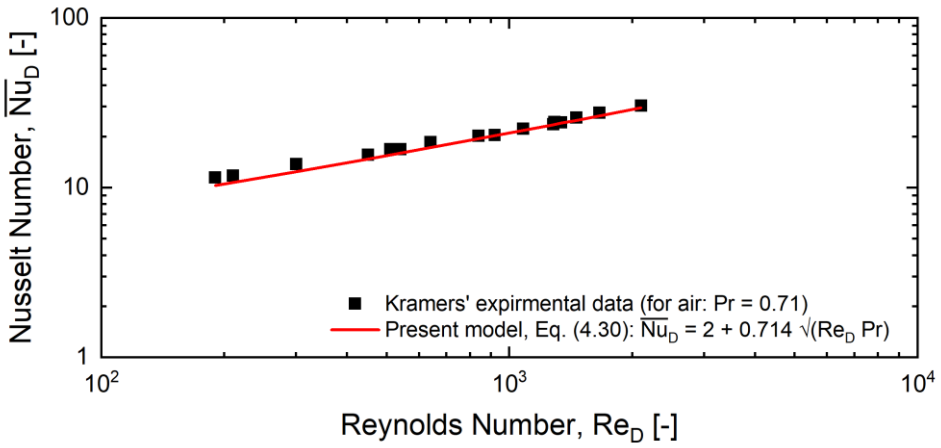

Fig. 61: Validation of Eq. (4.30) with air experimental data for a sphere with constant wall heat flux (Kramers [156]) .

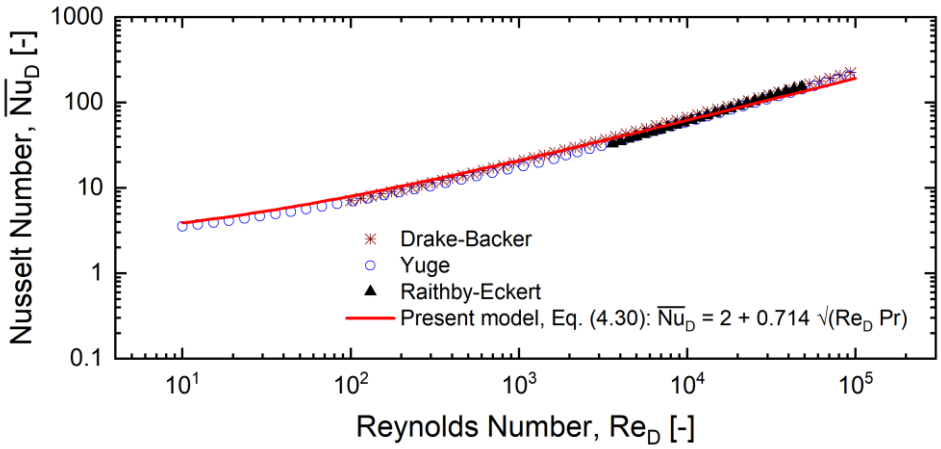

Fig. 62: Validation of Eq. (4.30) with the empirical correlations developed from the air data for an isothermal sphere (Drake and Backer [151], Yuge [152], and Raithby and Eckert [153]).

care was taken to ensure that there was no variation in the temperature along the surface of the sphere, i.e., the boundary condition at the wall was isothermal. One can observe from **Fig. 62** that the Nusselt number values calculated using Eq. (4.30) are in good agreement with the experimental data for the forced convection over isothermal spheres.

4.4.2.1. General Expression for the Nusselt Number

The thickness of the hydrodynamic boundary layer, δ_H, can be greater or less than that of the thermal boundary layer δ_T. The Prandtl number is a non-dimensional number that represents the ratio of the hydrodynamic boundary layer to the thermal boundary layer, and the heat transfer rate is a function of this number, see Eq. (4.30). The thickness of the hydrodynamic boundary layer is dictated by the velocity profile; therefore, it is important to define the velocity V in Eq. (4.3). This section is devoted to further verify that the theoretical heat transfer coefficients for both isothermal and isoflux spheres are the same by extending the analysis to cover a wide range of Prandtl numbers. To derive a general expression for the Nusselt number, we use the concept of the area-averaged effective velocity $\overline{V}_e$ discussed by Ahmed et al. [166]. Note that Ahmed et al. [166] transformed the energy equation in the spherical coordinates to a form of a transient heat conduction to derive an expression for the forced flow over an isothermal sphere and the analysis led to the same expression presented here using a similarity solution, Eq. (4.30). Ahmed et al. [166] assume that velocity is a power-law function of r-direction in order to have a general form for the velocity profiles at different Reynolds number. The use of power–law functions to approximate the velocity profiles throughout the boundary layer was found to be a good assumption as it was used for other geometries [173–175]. Ahmed et al. [166] derived expressions for an area-averaged effective velocity at two asymptotes, namely at $\mathrm{Pr} \to 0$ and $\mathrm{Pr} \to \infty$:

$$\overline{V}_e^0 = 1.178 V_\infty \qquad \text{at} \qquad \mathrm{Pr} \to 0 \tag{4.33}$$

$$\overline{V}_e^\infty = \frac{1.178 V_\infty}{(2\gamma+1)\mathrm{Pr}^{1/3}} \qquad \text{at} \qquad \mathrm{Pr} \to \infty \tag{4.34}$$

Ahmed et al. [166] used a blending technique to define the area-averaged effective velocity for the entire range of Pr as:

$$\overline{V}_e = \frac{\overline{V}_e^\infty}{\left[1+\left(\frac{\overline{V}_e^\infty}{\overline{V}_e^0}\right)^n\right]^{1/n}} \tag{4.35}$$

where, n is a fitting parameter determined by comparison against data. By substituting Eq. (4.33) and (4.34) into Eq. (4.35), it follows that:

$$\frac{\left(\overline{V}_e\right)^n}{V}=\frac{1.178/\left[\left(2\gamma+1\right)\mathrm{Pr}^{1/3}\right]}{\left(1+\left[1/2\left(2\gamma+1\right)\mathrm{Pr}^{1/3}\right]^n\right)^{1/n}} \qquad 0<\mathrm{Pr}<\infty \tag{4.36}$$

In the above equations, the parameter γ defines the form of the velocity profile for various Reynolds numbers. Ahmed et al. [166] suggested $\gamma=1/\mathrm{Re}^{0.25}$ for a sphere. By substituting Eq. (4.36) into Eq. (4.30), a general expression for the Nusselt number can be written as:

$$\overline{Nu}_D=2+\frac{0.779}{\left(2\gamma+1\right)}\mathrm{Re}_D^{1/2}\frac{\mathrm{Pr}^{1/3}}{\left[1+\left(\frac{1.0}{\left(2\gamma+1\right)^3\mathrm{Pr}}\right)\right]^{1/2n}} \tag{4.37}$$

It should be noted that, to find the exponent *n* that gives the best match for Eq. (4.37), Ahmed et al. [166] only considered a few correlations for air (Pr=0.7), namely, Yuge [152], Churchill [176], and Yovanovich [167] correlations, and proposed an exponent of *n*=3. In the present study, more data and empirical correlations for a wide range of Reynolds and Prandtl numbers were used to find the exponent in the aim to improve the accuracy and range of application of Eq. (34). It includes the data and correlations presented for liquid sodium with Pr=0.01 (Sideman [163]), air with Pr=0.7-2 (Drake and Backer [151], Yuge [152], Raithby and Eckert [153], and Clift et al. [177]), water with Pr=7-10 (Kramers [156], and Vliet-Leppert [155]), and oil with Pr=213 and Pr=380 (Kramers [156]). It was found that *n*=500 gives the best fit for the aforementioned data. It is worth noting that with *n*=500, the denominator $\left[1+\left(1/\left(2\gamma+1\right)^3\mathrm{Pr}\right)\right]^{1/2n}$ in Eq. (4.37) approaches 1.0. Therefore, the following general expression is proposed for evaluating the Nusselt number for the laminar forced convection over isothermal or isoflux spheres:

$$\overline{Nu}_D=2+\frac{0.779}{\left(2/\mathrm{Re}_D^{0.25}+1\right)}\mathrm{Re}_D^{1/2}\,\mathrm{Pr}^{1/3} \qquad \begin{matrix}0<\mathrm{Re}<10^5\\ 0<\mathrm{Pr}<\infty\end{matrix} \tag{4.38}$$

Fig. 63a to **Fig. 63e** compare the proposed general expression for the Nusselt number with Kramers' experimental data [156] at various Prandtl numbers for an isoflux sphere. The normalized root-mean-square-error (NRMSE, %) is used to estimate the average error between Eq. (4.38) and the Nusselt number data:

$$NRMSE\ [\%]=\frac{\sqrt{\sum_{i=1}^{n}\frac{\left(\hat{y}_i-y_i\right)^2}{N}}}{\sum_{i=1}^{n}\frac{y_i}{N}}\times 100\% \tag{4.39}$$

where, $\hat{y}_i$ and y_i are the predicted and experimental values, respectively, and N is the number of data points. For air data (Pr=0.7), the NRMSE is calculated as 5.9%.

Considering water data with the Prandtl numbers of Pr=7.3 and Pr=10.7, the general analytical expression predicts the Nusselt number values with a NRMSE of 11.7% and 4.5%, respectively. The errors of Eq. (4.38) from the oil data for Pr=213 and Pr=380 are 16.6% and 26.3%, respectively. The low values of NRMSE suggest that Eq. (4.38) is valid for the forced convention over a sphere with constant flux at the wall as a boundary condition.

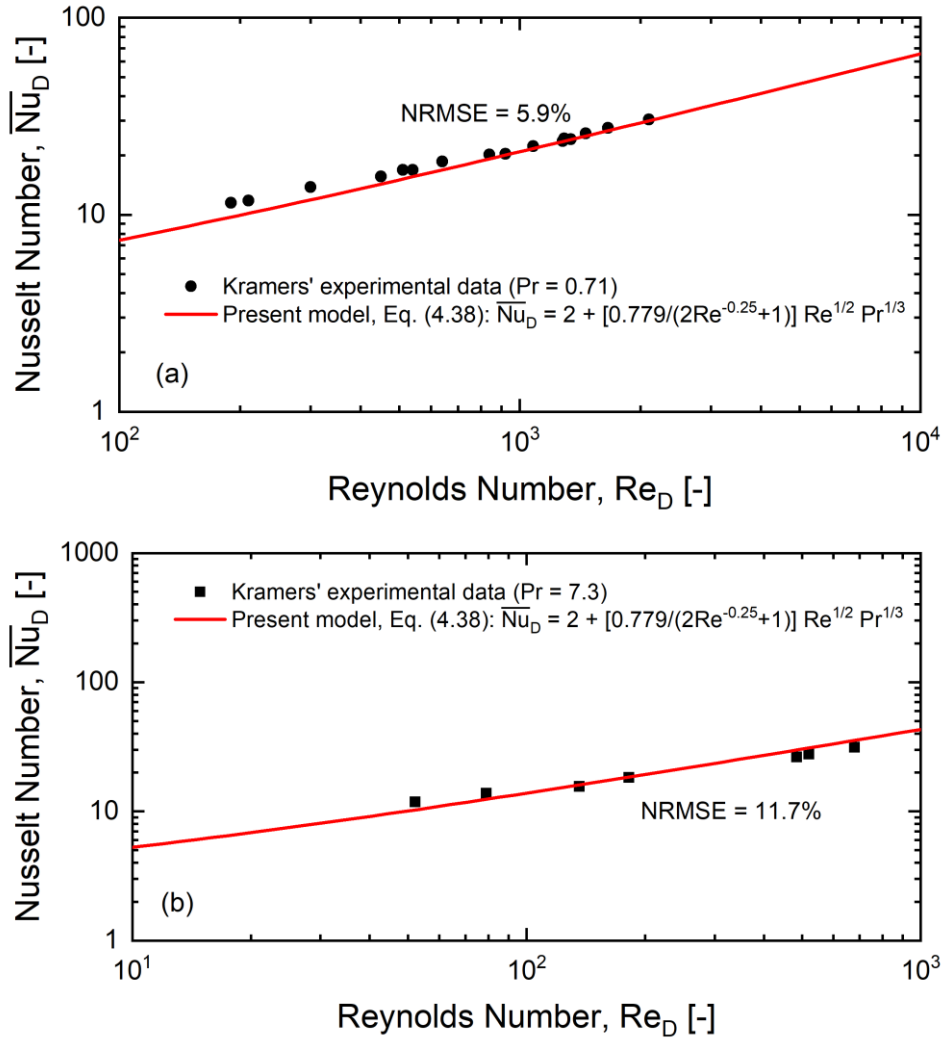

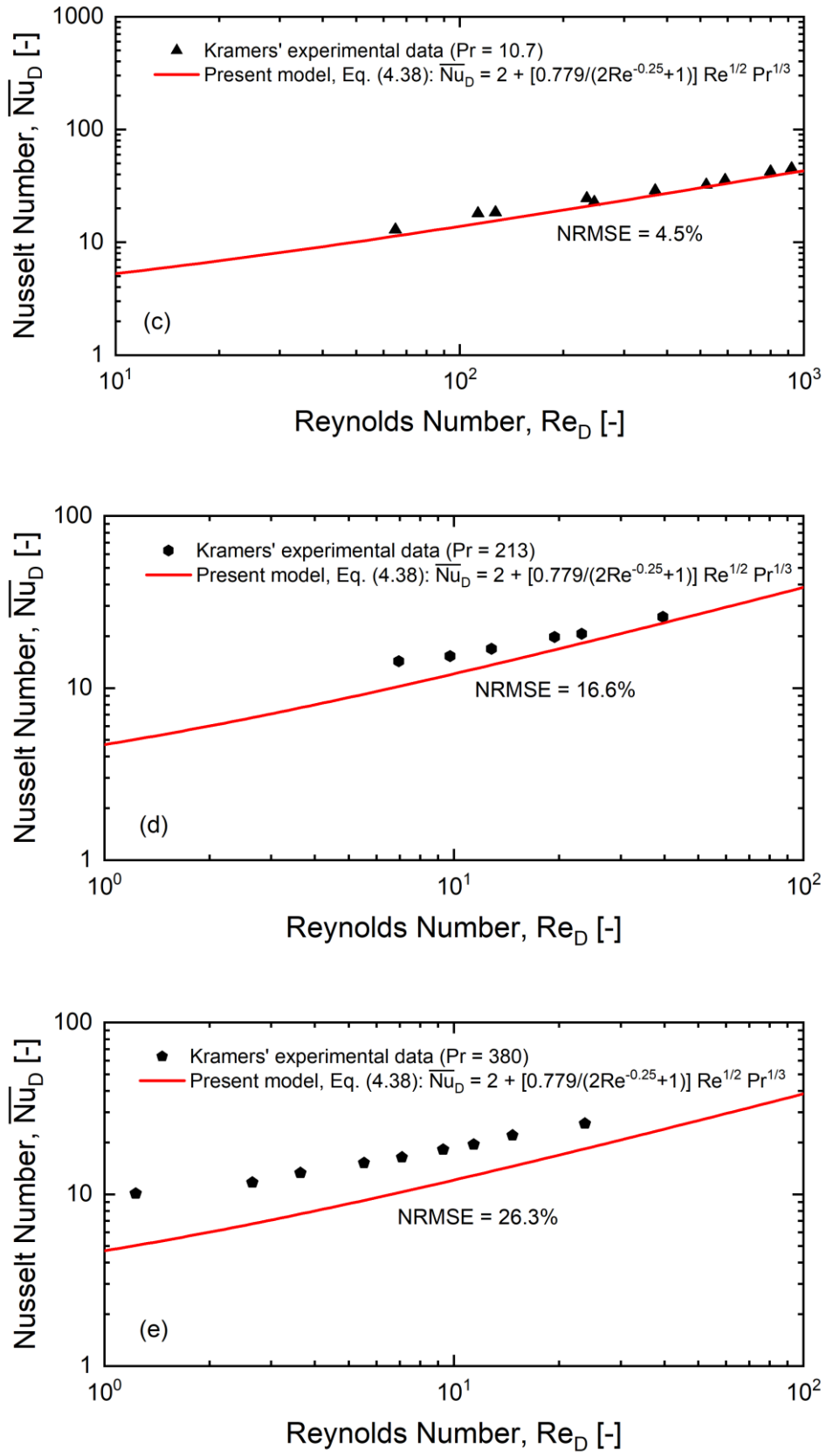

Fig. 63: Validation of the present model, Eq. (4.38), with the experimental data [156] for an isoflux sphere for: (a) Pr=0.71; (b) Pr=7.3; (c) Pr=10.7; (d) Pr=213; and (e) Pr=380.

Table 3 shows the NRMSE values for the proposed general expression in this work (Eq. (4.38)) and the Ahmed et al. [166] expression when they are compared with Kramers' data [156]. Both expressions almost have the same error when water and oil data are considered. However, for the air data, Eq. (4.38) has an error that is 50% lower than the value calculated for the Ahmed et al. expression [166].

Fig. 64a to **Fig. 64e** are presented to compare the Nusselt number values predicted by Eq. (4.38) and the Ahmed et al. [166] expression with the correlations presented by Witte [178], Yuge [152], Raithby- Eckert [153], Drake-Backer [151], and Vliet-Leppert [155] for the forced convection over an isothermal sphere. The errors of the expressions from the aforementioned correlations are summarized in **Table 3**. Considering Witte's data [178] for liquid sodium (Pr=0.01), both expressions tend to overestimate the Nusselt number values (NRMSE=83%), which is probably due to the difference in the velocity profile in Witte's experiments [178] compared to the one assumed in developing the abovementioned expressions. The relatively large errors that result in predicting the Nusselt numbers by using Eq. (4.38) suggests that perhaps more experimental data at low Prandtl numbers (Pr=0.01) are needed to develop a better fit. For air data (Pr=0.7), Eq. (4.38) has a smaller error than the expression proposed by Ahmed et al. [166]. In some cases, using the Ahmed et al. [166] expression results in errors that are 100% higher than that of Eq. (4.38) (see NRMSE values for Drake-Backer [151] and Yuge [152] correlations in Table 1). The results presented in **Fig. 64e** and **Table 3** show that both expressions have a relatively large error when compared with the correlation proposed by Vliet and Leppert [155] for water data (Pr=7). Nevertheless, the proposed expression in this work results in an 8% smaller error (NRMSE=24.6%) compared to that calculated for the Ahmed et al. [166] expression (NRMSE=26.7%). These high errors may be attributed to the fact that both expressions do not account for the natural convection in the experiments done by Vliet and Leppert [155] as discussed in the Introduction section. The results presented in **Table 3** indicate the validity of Eq. (4.38) for both isothermal and isoflux spheres and support the conclusion derived earlier about the similarity between the transfer coefficients for the laminar forced convection heat transfer from isoflux and isothermal spheres.

Table 3: The normalized root-mean-square-error (NRMSE) values for Eq. (4.38) and the Ahmed et al. expression.

Fluid	Boundary condition	Reference	Root-mean-square-error, NRMSE [%]	
			Ahmed et al. [166]	Present work, Eq. (4.38)
Liquid sodium: Pr=0.01	Isothermal	Witte [178]	83	83.1
	Isoflux	Kramers [156]	11.7	5.9
Air: Pr=0.7	Isothermal	Drake-Backer [151]	23.6	10
	Isothermal	Yuge [152]	14.5	7.9
	Isothermal	Raithby-Eckert [153]	12.4	11.3
Water: Pr=7	Isoflux	Kramers [156]	11.5	11.7
	Isothermal	Vliet-Leppert [155]	26.7	24.6
Water: Pr=10	Isoflux	Kramers [156]	4.4	4.5
Oil: Pr=213	Isoflux	Kramers [156]	17	16.6
Oil: Pr=380	Isoflux	Kramers [156]	26.8	26.3

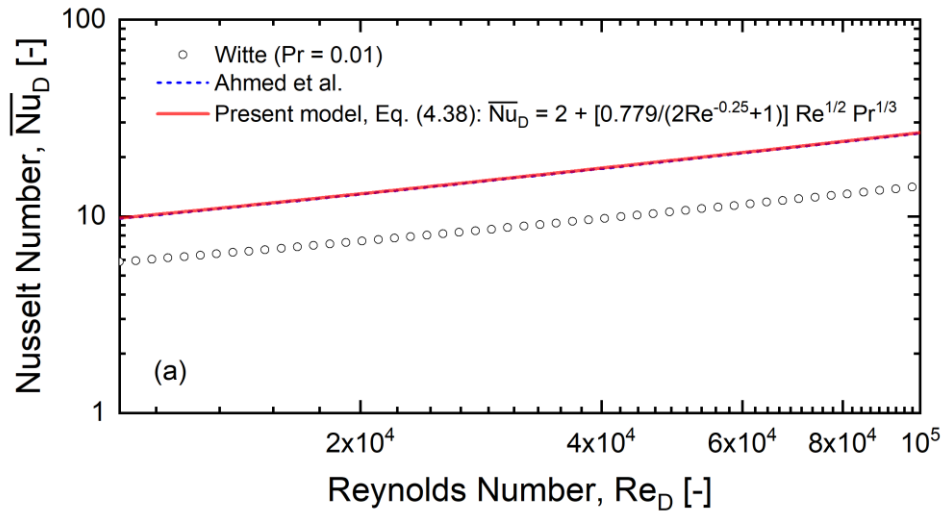
100
10
1
Nusselt Number, $\overline{Nu}_D$ [-]
Witte (Pr = 0.01)
Ahmed et al.
Present model, Eq. (4.38): $\overline{Nu}_D = 2 + [0.779/(2Re^{-0.25}+1)]\ Re^{1/2}\ Pr^{1/3}$
(a)
$2x10^4$
$4x10^4$
$6x10^4$
$8x10^4$
10^5
Reynolds Number, Re_D [-]

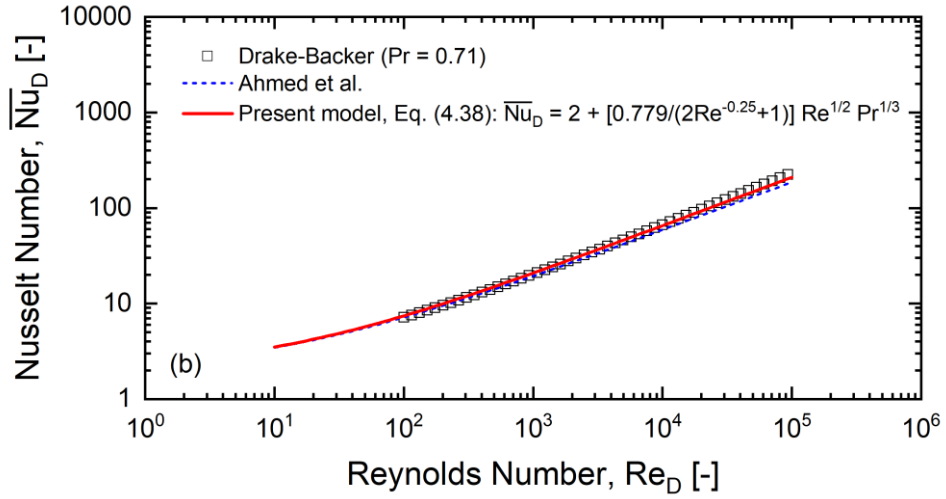
10000
1000
100
10
1
Nusselt Number, $\overline{Nu}_D$ [-]
Drake-Backer (Pr = 0.71)
Ahmed et al.
Present model, Eq. (4.38): $\overline{Nu}_D = 2 + [0.779/(2Re^{-0.25}+1)]\ Re^{1/2}\ Pr^{1/3}$
(b)
10^0
10^1
10^2
10^3
10^4
10^5
10^6
Reynolds Number, Re_D [-]

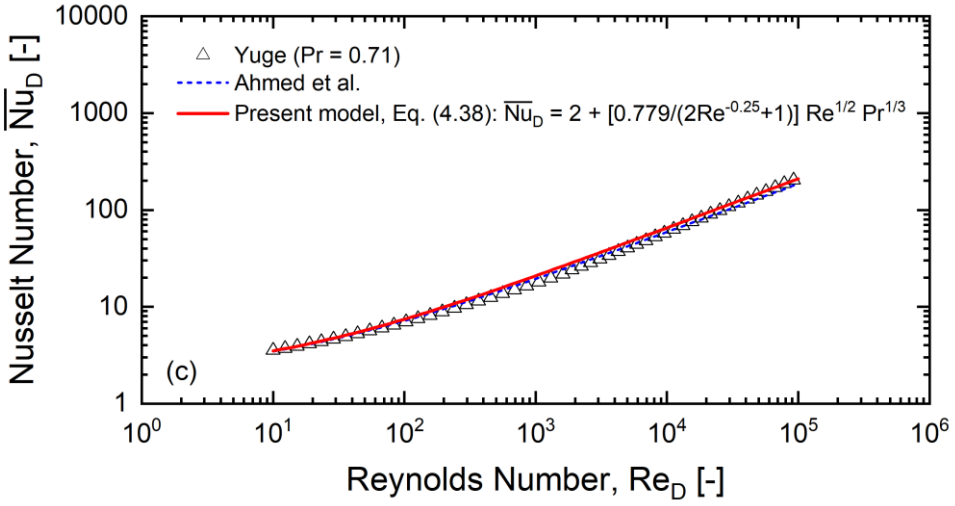
10000
1000
100
10
1
Nusselt Number, $\overline{Nu}_D$ [-]
Yuge (Pr = 0.71)
Ahmed et al.
Present model, Eq. (4.38): $\overline{Nu}_D = 2 + [0.779/(2Re^{-0.25}+1)]\ Re^{1/2}\ Pr^{1/3}$
(c)
10^0
10^1
10^2
10^3
10^4
10^5
10^6
Reynolds Number, Re_D [-]

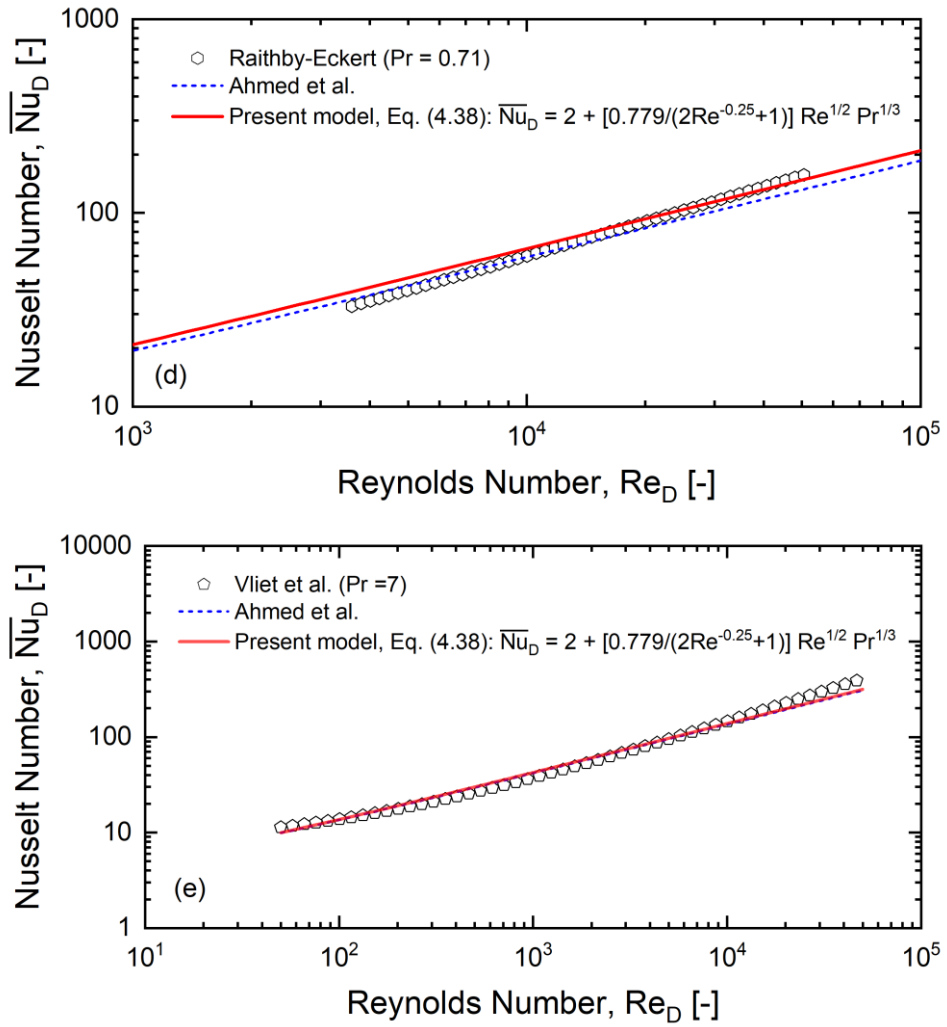

Fig. 64: Validation of the present model, Eq. (4.38), with the experimental data of: (a) Witte [178] ; (b) Drake-Backer [151] ; (c) Yuge [152]; (d) Raithby-Eckert [153] ; and (e) Vliet-Leppert [155] for an isothermal sphere.

4.5. Conclusions

The analysis presented in this study revealed that the averaged Nusselt number for the laminar forced convection heat transfer is identical for isothermal and isoflux spheres. This finding was verified by comparing the proposed model with the experimental data available in the literature. This result may be generalized for packed spheres, and the correlations developed for flow over isothermal spheres can be used to study the heat transfer in packed beds in which heat is generated at the surface of the spheres, as is the case with adsorption reactors, without any loss of accuracy. The analytical approach presented herein can be used to derive simple and compact expressions for Nusselt number for other geometries in their respective coordinate systems.

5. Reactor Design and Experimental Setup

5.1. Introduction

To assess the performance of the proposed novel microreactors, thousands of microcapsules should be fabricated and used in a setup to create enough moisture removal capacity to measure the absorbed humidity with proper certainty. Simple packing of these microreactors will reduce the mass transfer area (slower kinetics) and will result in high pressure drops due to the small size of the microreactors. To address this challenge, a custom-built bench-scale reactor was designed based on the "packed-sheet" concept to enable mimicking the simple packing arrangement. The initial prototype contained one packed-sheet that housed the microcapsules by means of two stainless steel meshes and was placed parallel to the direction of air flow. The system was tested over various (typical) operating conditions. Certain metrics were used to measure and assess the system's performance.

5.2. Reactor Design

About 8 grams of microcapsules were prepared based on to the procedure described in Chapter 3. The sheet-type sorption bed was comprised of two parallel stainless steel mesh layers, **Fig. 65a**, one at the bottom and the other at the top, supported by a 3D printed frame (ABS plastic) with dimensions of 180 *mm* x 30 *mm* x 2 *mm*, see **Fig. 65b** and **Fig. 65c**. The 425 μm nominal aperture of the stainless-steel mesh allowed the microcapsules, with a 700 μm outer diameter, to be accommodated and kept between the mesh layers without using any binder, see **Fig. 65d**. The voids in the mesh layers enabled direct contact between the microcapsules and air streams, which would result in a better heat and mass transfer, thus better dehumidification performance, due to the direct air flow around the microcapsules.

Two 3D printed (acrylate-like material) parts, top and bottom parts in **Fig. 66**, were used to house the packed-sheet, to provide an inlet and outlet for the air streams, and as a means to install the temperature, relative humidity, and pressure transducer sensors. The final assembly of the reactor is shown in **Fig. 67**. A 12 *mm* thick rubber insulation was used to minimize the heat loss from the bed.

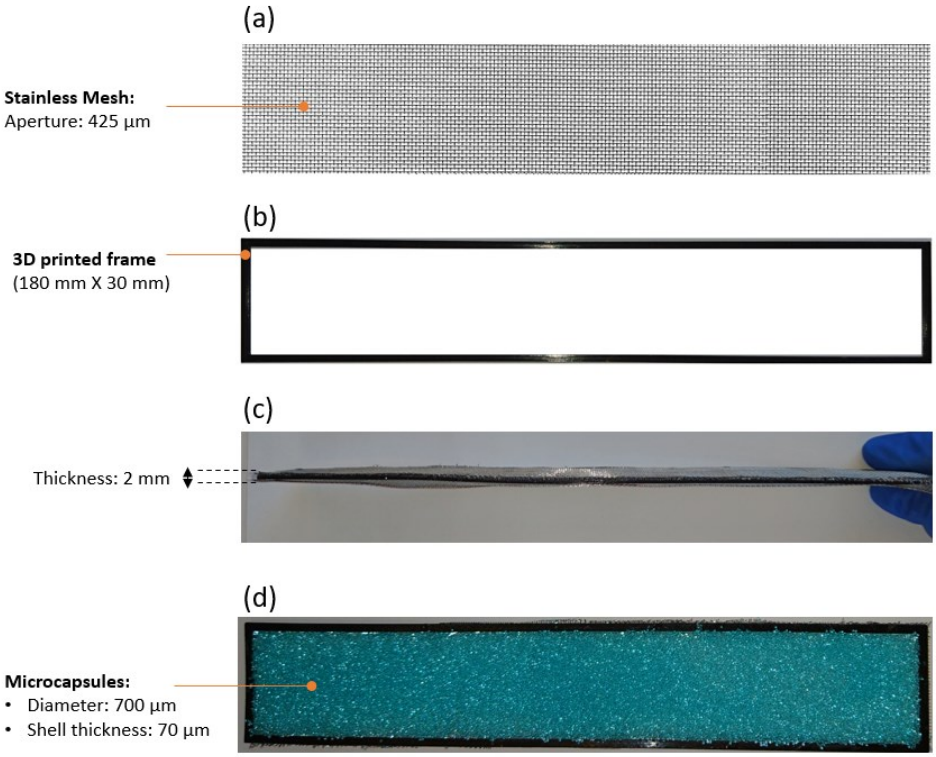

Fig. 65: The components of a single packed-sheet: (a) stainless mesh, (b) 3D printed frame, (c) meshes attached to the frame before packing, and (d) packed microcapsules.

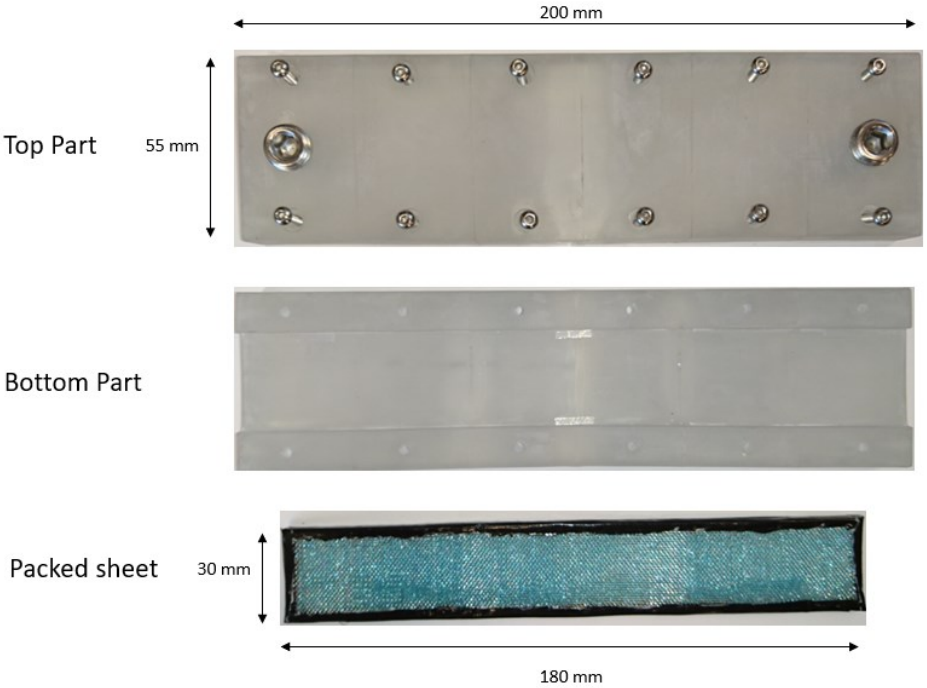

Fig. 66: The components of the sorption bed (before assembly).

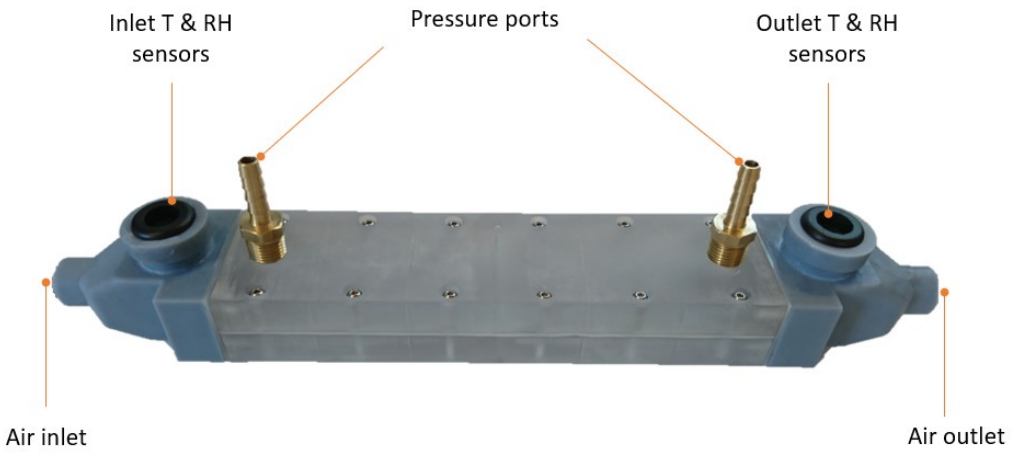

Fig. 67: The prototype of the sorption bed.

5.3. Experimental Setup

5.3.1. System Description

The working principle for the proposed dehumidification system is illustrated in **Fig. 68**. The process air stream represents the incoming air that should be dehumidified. During the dehumidification cycle, the process air is passed through the sorption bed (packed sheet) for the moisture to be absorbed by the liquid desiccant inside the microcapsules. During the regeneration cycle, the incoming air is heated to 60-80 ^{o}C to decrease the relative humidity of the air and make it dry to enable the moisture transfer from the microcapsules to the air (regenerating the microcapsules).

As shown in **Fig. 69**, the experimental setup consists of a compressed air supply, two environmental champers (C1 and C2), two three-way valves (V1 and V2), and a sorption bed. Two environmental champers (Cellkraft, P-10C) were used to control the temperature and humidity of the supplied air during the dehumidification and regeneration cycles. Three-way vales were used to direct the air flow, alternatively to the sorption bed and the exhaust line. The test bed was equipped with two relative humidity sensors (Vaisala HUMICAP® HMP110) and two T-type thermocouples (Omega Eng. Inc, Canada) installed at the inlet and outlet of the sorption bed to measure the relative humidity and temperature of the inlet and outlet air. The flow rate of the air supplied to the sorption bed was measured using a flow meter (ALICAT, M-50SLPM-D/SM). A differential pressure transducer (Model 267, Setra Systems, Inc.) was used measure the pressure drop across the bed.

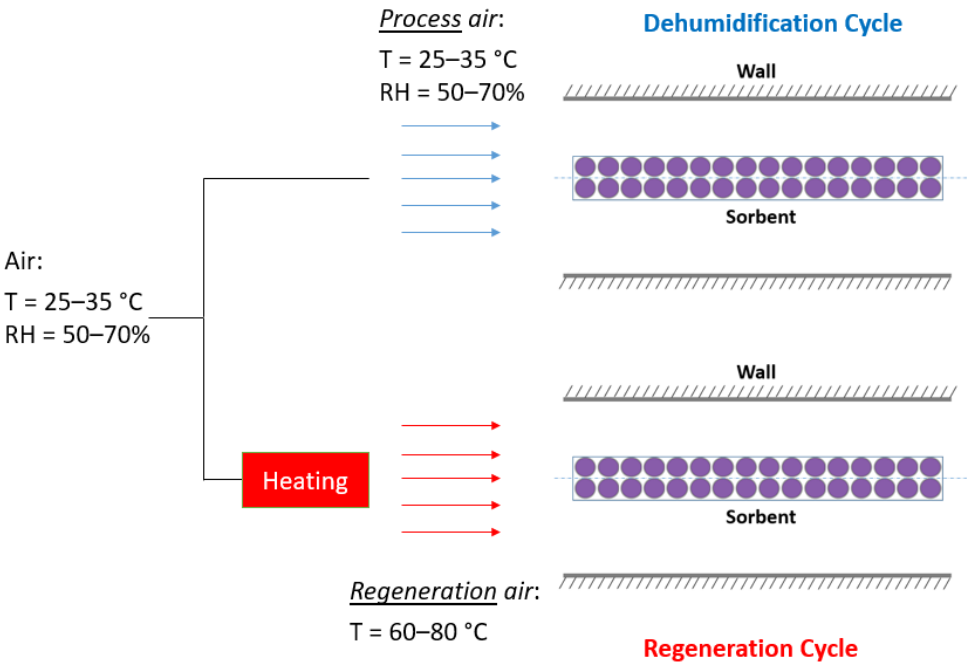

Fig. 68: An illustration of the working principle of the proposed reactor.

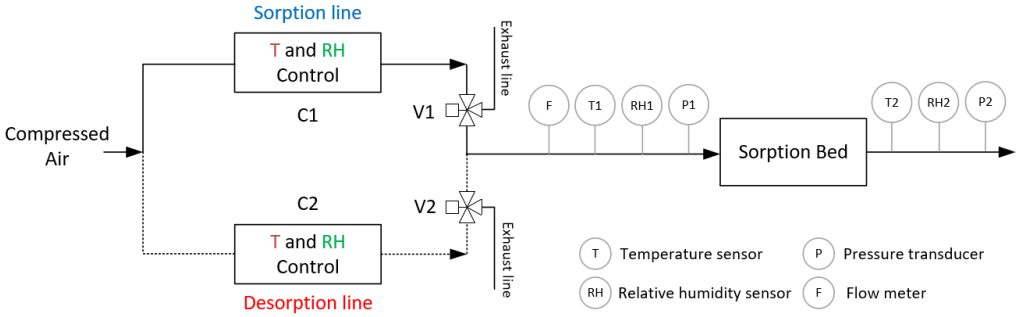

Fig. 69: A schematic of the custom-built experimental setup.

5.3.2. Test Procedure

With reference to **Fig. 69**, the following procedure was followed to perform the tests:

1. Before passing the air through the sorption bed, compressed air was directed through the environmental chambers (C1 and C2) to the control the temperature and relative humidity of the air and set them at the desired working conditions to mimic typical conditions during dehumidification and regeneration processes. Both control valves (V1 and V2) were connected to the exhaust lines during this step until the systems stabilized and the required working conditions were achieved. **Table 4** shows the operating conditions of the process and regeneration air during the conducted tests.
2. During the regeneration process, the three-way control valve (V1) was closed (connected to the exhaust line), and the other valve (V2) was opened to direct the hot and dry air (supplied from the environmental chamber C2). With the passage of time, the absorbed water was removed from the sorption bed and the microcapsules became regenerated. Once the required regeneration half-cycle time was achieved, the three-way vale (V2) was used to discharge the hot regeneration air to the surrounding environment through the exhaust line.
3. During the dehumidification process, the control valve (V1) was opened to allow the humid "process" air (supplied from the environmental chamber C1) to follow through the sorption bed. After the required half-cycle dehumidification time had passed, the process air was bypassed to the exhaust line connected to the surrounding environment by switching V1 to the other direction.
4. In order to prepare the sorption bed for the next dehumidification process, Step 1 was repeated to start the regeneration process.

Table 4: The operating conditions for the dehumidification system.

	Temperature [^{o}C]	Relative humidity [%]	Humidity ratio [g/kg]	Half-cycle time [min]	Flow rate [LPM]
Process air	25-35	50-70	8-15	30	3-10
Regeneration air	60-70	3-7	10-15	30	3-10

5.4. Key Performance Indicators

The key performance indicator (KPI) that was used to measure the performance of the proposed dehumidification system is the moisture removal rate (MRR, *g/s-m*^{3}), defined as:

$$MRR = \frac{\text{Rate of moisture removal}}{\text{Volume}} = \frac{\left[\int_0^{t_{\text{deh}}} \dot{m}_{\text{pro}} \left(\omega_{\text{pro,i}} - \omega_{\text{pro,o}}\right) \cdot dt\right] / t_{\text{deh}}}{\text{Volume}} \qquad 5.1$$

where, $\dot{m}_{\text{pro}}$ is the mass flow rate, $\omega_{\text{pro,i}}$ and $\omega_{\text{pro,o}}$ are the inlet humidity and the outlet humidity of the process air, respectively. The parameter t_{deh} is the time taken during dehumidification process (half-cycle time). The volume considered in Eq. (5.1) is the internal volume of the sorption bed. Typical values for moisture removal rates for the state-of-the-art packed-column absorbers that use LiBr hygroscopic salt are within the 20-35 *g/s-m*^{3} range.

Another performance indicator, the dehumidification coefficient of performance (*DCOP*,-), was used to measure the power consumed to achieve the required moisture removal rate (i.e., the ratio between the removed latent heat to energy input). Mathematically, the coefficient of performance is expressed as:

$$DCOP = \frac{\text{Latent heat removed}}{\text{Energy input}} = \frac{\int_0^{t_{\text{deh}}} \dot{m}_{\text{pro}} h_{fg} \left(\omega_{\text{pro,i}} - \omega_{\text{pro,o}}\right) \cdot dt}{\int_0^{t_{\text{reg}}} \dot{m}_{\text{reg}} c_p \left(\Delta T_{\text{reg}}\right) \cdot dt} \qquad 5.2$$

where, c_{p} is the specific heat of the air, and ΔT_{reg} represents the difference between the air inlet and outlet temperature during the heating of the regeneration air, the fan energy to overcome the pressure drop in the reactor is negligible compared to the air heater.

5.5. Uncertainty Analysis

The method proposed by Kline and McClintock [179] was used to compute the uncertainty of the present experimental data as follows:

$$Y = f\left(X_1, X_2, X_3, ...\right)$$
$$\partial Y = \sqrt{\left(\frac{\partial Y}{\partial X_1}\delta X_1\right)^2 + \left(\frac{\partial Y}{\partial X_2}\delta X_2\right)^2 + \left(\frac{\partial Y}{\partial X_3}\delta X_3\right)^2 + \ldots} \quad 5.3$$

where, ∂Y gives the overall uncertainty associated with parameter Y, and $\partial X_{1,2,3,...}$ are the uncertainties associated with measured parameters $X_{1,2,3,...}$. The uncertainty of the used devices used in the experiments are listed in **Table 5**.

Table 5: The uncertainty of the devices used in the experiments.

Parameter	Instrument	Range	Accuracy
Humidity	Vaisala HUMICAP® HMP110	0-100 % RH	± 1.5% RH for 0…+40°C ± 3.0% RH for -40 …0 °C
Temperature	Omega, T type thermocouple	0-200 °C	± 0.5 °C
Flow rate	ALICAT, M-50SLPM-D/SM	0-10 *lpm*	0.2%
Differential Pressure Transducer	Setra Model 267	0-5" *W.C.* (0-1244 *Pa*)	± 0.0125" *W.C.* (±3 *Pa*)

The analysis showed that the moisture removal rate (MRR) can be calculated with ±4.5% uncertainty, while the uncertainty in calculating the dehumidification coefficient of performance (DCOP) is ±5%.

5.6. Results and Discussion

The electric power consumption is directly related to the pressure drop across the bed. A high pressure drop is not favourable because it results in a high operating cost and high noise levels. For this reason, the variation of pressure drop across the sorption bed with respect to air inlet velocity presented was investigated and reported in **Fig. 70**. Considering the practical operating conditions, the maximum pressure drop (at 2 *m/s*) was 200 *Pa/m*. This value is two orders of magnitude lower than the reported values for simple packed beds (12,897 *Pa/m*) [180].

Temperature and humidity ratio profiles of the baseline test (Process air: T=30 °C and RH=60%) are reported in **Fig. 71a** and **Fig. 71b**, respectively. The experimental data at the various test conditions are presented in **Appendix C**. During the regeneration process (see **Fig. 68**), the heat is transferred from the hot and dry air to the microcapsules. As a result, the air exists from sorption bed relatively cooler, and water is released (from the microcapsules) to the air stream which results in an increase of its moisture content.

In the dehumidification process (see **Fig. 68**), the warm and humid process air cools down the bed, and the moisture is simultaneously absorbed by the liquid desiccant inside the microcapsules. At the beginning of the process, the air dehumidification is less effective because the microcapsules are still hot from the regeneration process. Once the bed is adequately cooled, the dehumidification process reaches its maximum value and then it gradually decreases due to the increasing water content in the microcapsules.

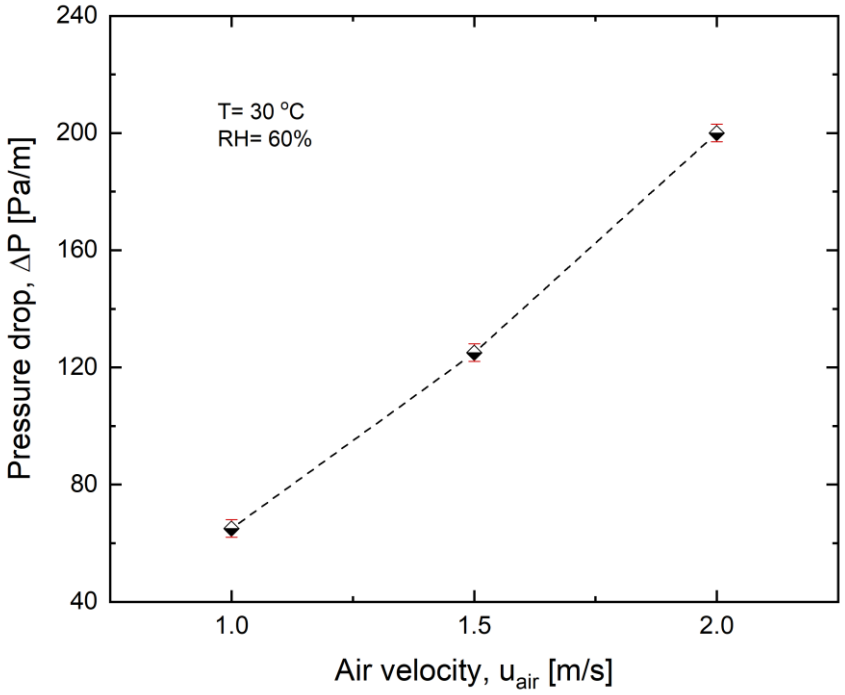

Fig. 70: The variation of pressure drop across the sorption bed with the air velocity.

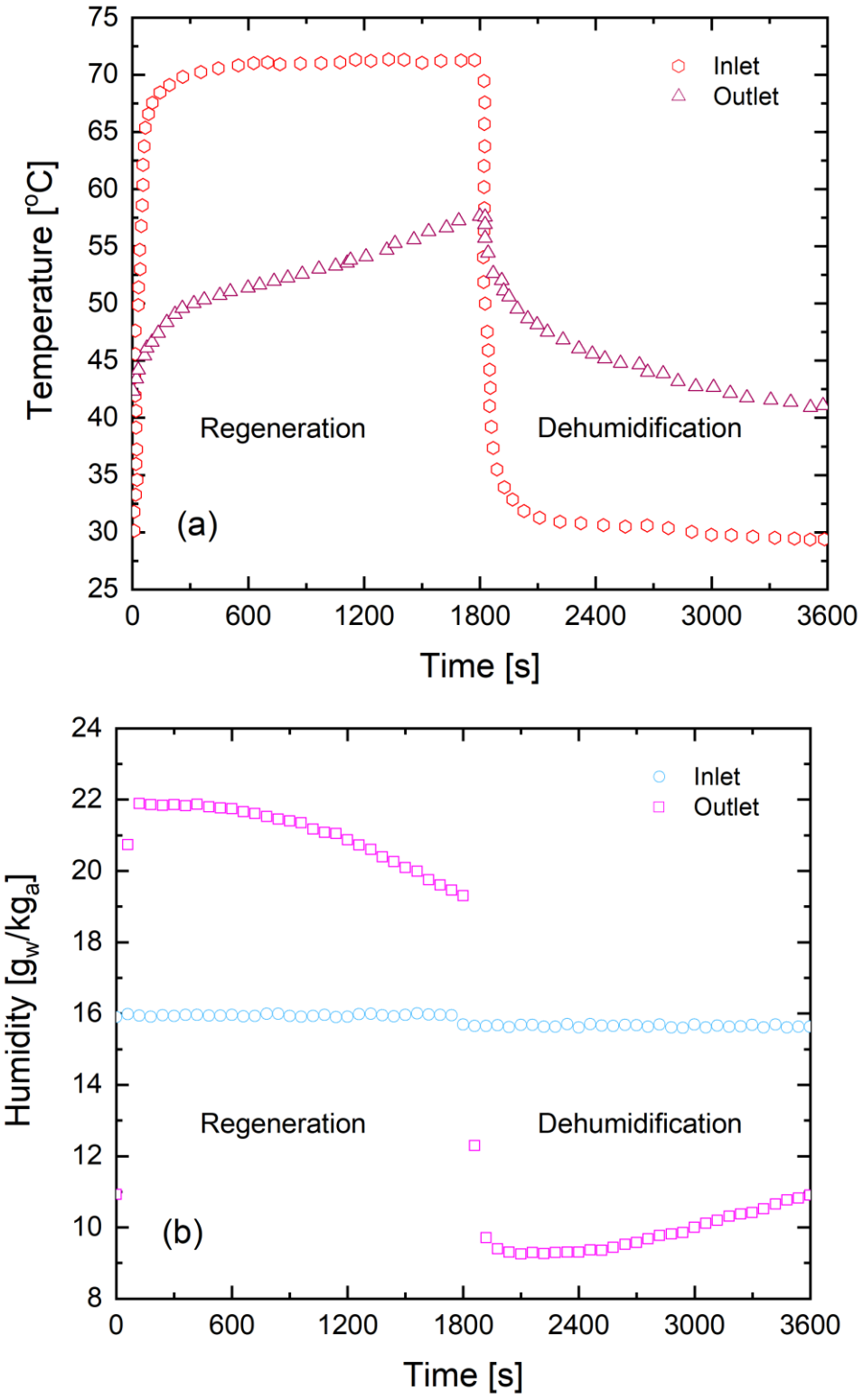

Fig. 71: (a) Temperature; and (b) humidity profiles during the regeneration ($T_{reg,i}$ = 60 °C and $RH_{reg,i}$ = 5%) and dehumidification processes ($T_{pro,i}$ = 30 °C and $RH_{pro,i}$ = 60%) in the base line experiment.

5.6.1. Effect of the Process Air Inlet Relative Humidity

The effect of supplied air inlet relative humidity on the moisture removal rate (MRR) is presented in **Fig. 72a**. As expected, the higher the relative humidity, the higher the driving force for the mass transfer from the humid air to the liquid desiccant inside the microcapsules, and consequently, the higher the moisture removal rate. As the relative humidity of the process air was increased from 50% to 70%, the moisture removal rate increased from 45 $g/s\text{-}m^3$ to 53 $g/s\text{-}m^3$ (+18%). The increase in the moisture content of the incoming air was also shown to have a positive impact on the dehumidification coefficient of performance (DCOP) as presented in **Fig. 72b**. This is because the rate of moisture removal increases while the energy input remains the same, see Eq. (5.2). This means that the system would be more energy efficient in applications with higher relative humidity levels, e.g., greenhouses.

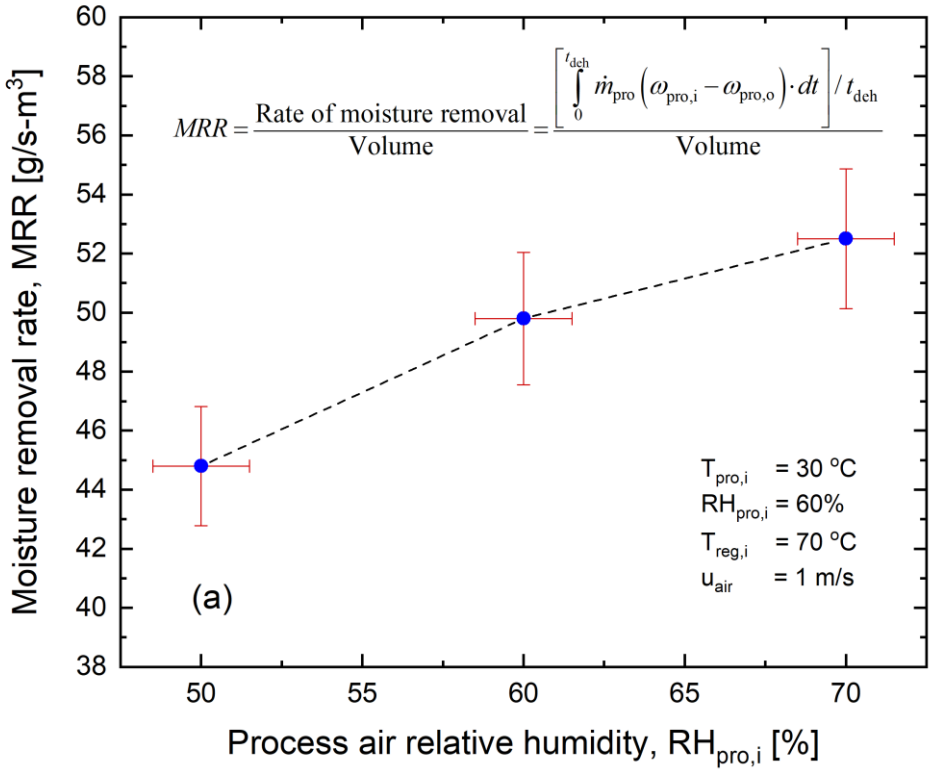

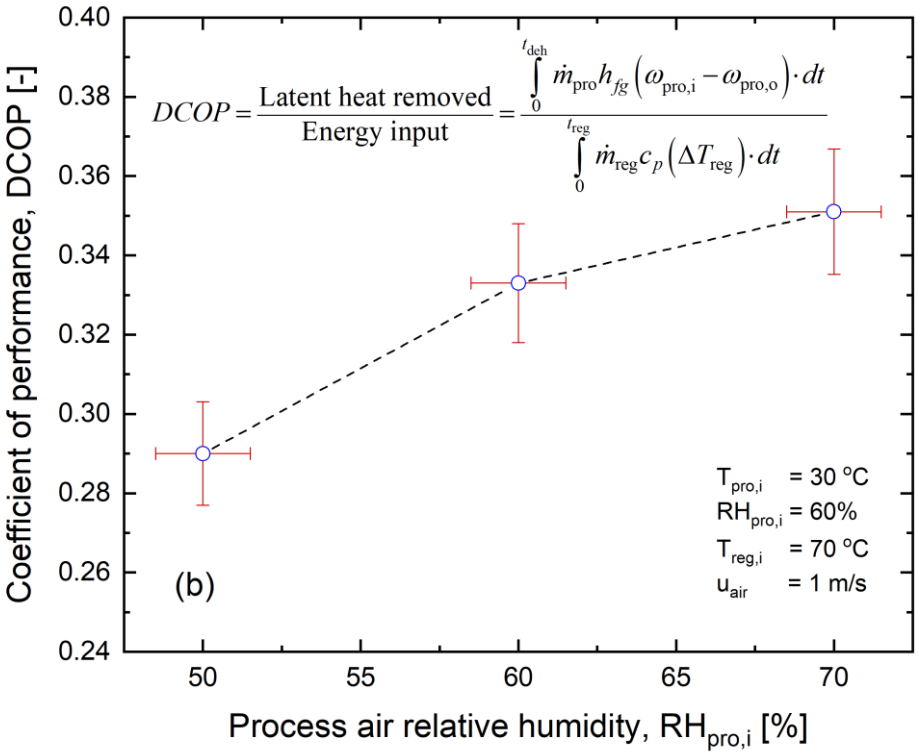

Fig. 72: The effect of process air inlet relative humidity on: (a) the moisture removal rate; and (b) the coefficient of performance ($T_{pro,i}$ = 30 °C, $T_{reg,i}$ = 70 °C, u_{air} = 1 m/*s*, and $t_{deh} = t_{reg}$ = 30 min).

5.6.2. Effect of the Process Air Inlet Temperature

The results showed that warmer process air would result in a lower system capacity to remove the moisture as presented in **Fig. 73**. At the same relative humidity, as the inlet temperature of the process air was increased from 25 °C to 35 °C, the removal rate decreased by 12% (from 51 to 45 *g/s-m*^{3}). On the other hand, the coefficient of performance increased by 10% (from 0.30 to 0.33). This can be explained by the fact that in warmer environments less energy is required to heat the air to the regeneration temperature, and the increase in energy consumption outweighs the reduction in the moisture removal rate.

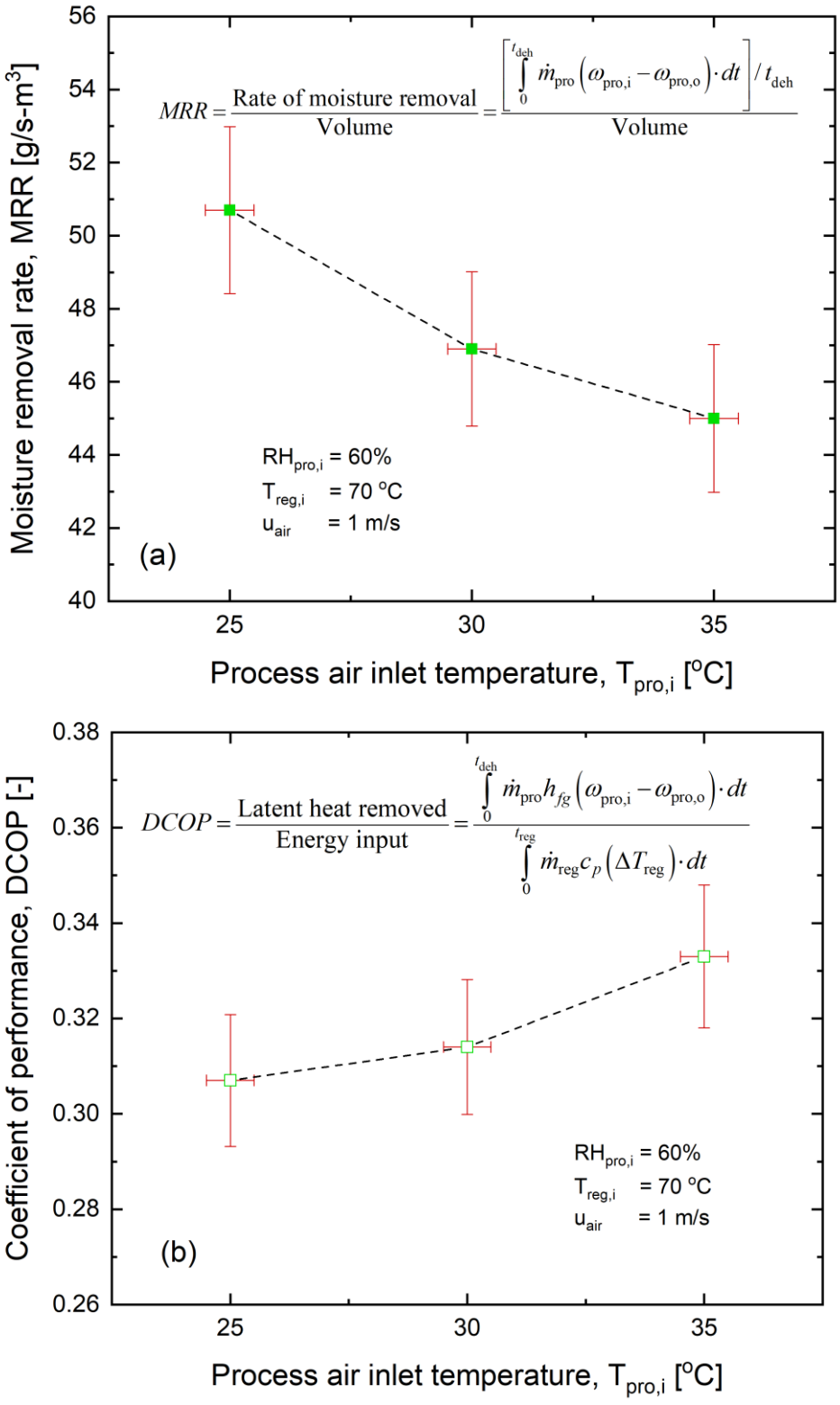

Fig. 73: The effect of process air inlet temperature on: (a) the moisture removal rate; and (b) the coefficient of performance ($RH_{pro,i}$ = 60%, $T_{reg,i}$ = 70 °C, u_{air} = 1 m/s, and t_{deh} = t_{reg} = 30 min).

5.6.3. Effect of Regeneration Air Temperature

The effect of regeneration temperature on the performance of the system is presented in **Fig. 74**. The results showed that the change in the moisture removal rate was directly proportional to the change in the regeneration temperature. Increasing the regeneration temperature from 60 °C to 70 °C resulted in a 43% increase in the moisture removal rate (see **Fig. 74a**). Higher regeneration temperatures resulted in higher supplied energy, which helps overcome the heat of absorption, which in turn, results in more water molecules to be desorbed from the liquid desiccant. Despite the increase in the energy input due to the increased regeneration temperature, the coefficient of performance remained almost constant, **Fig. 74b**. This indicates that the increase in the energy input can be compensated by the gain in the moisture removal rate (see Eq. (5.2)). Therefore, working with high regeneration temperatures will be favourable for a higher system performance.

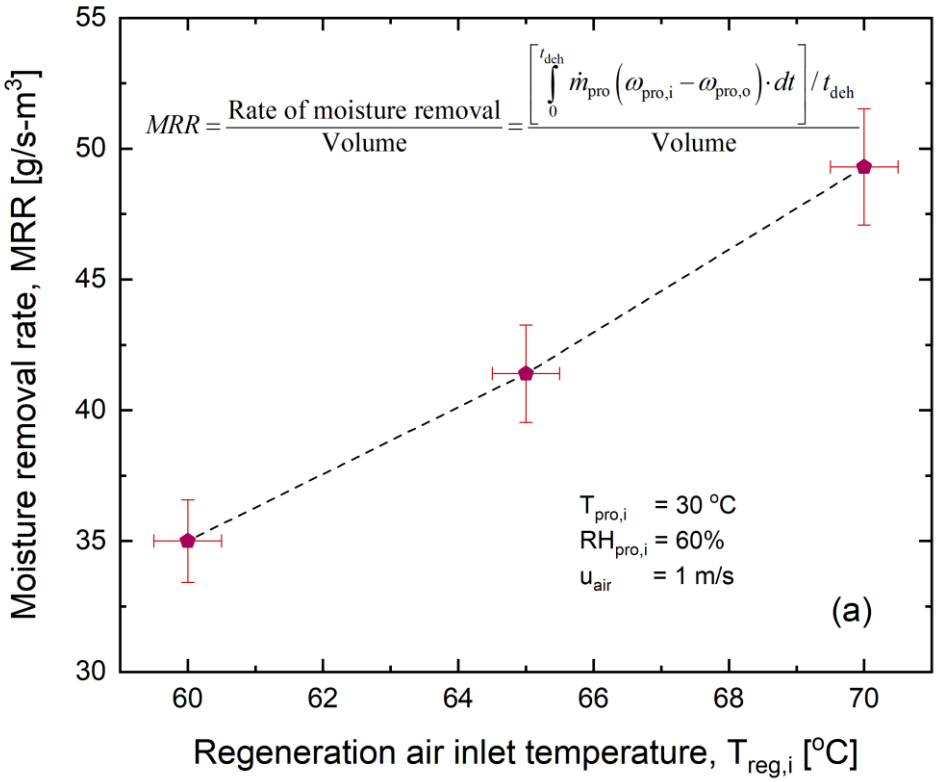

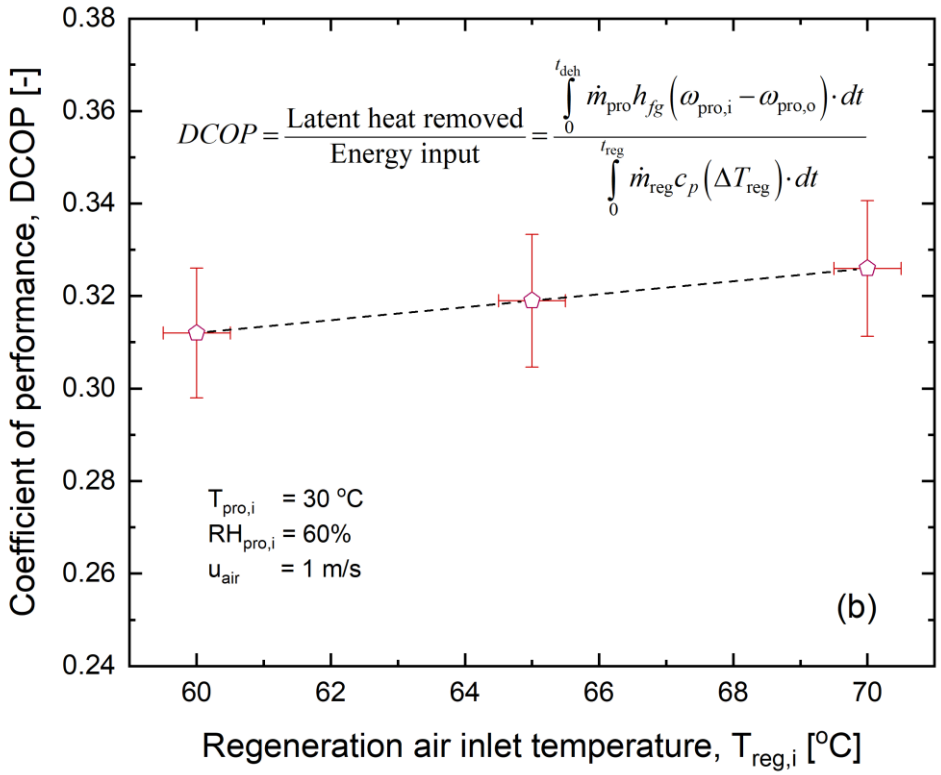

Fig. 74: The effect of regeneration air inlet temperature on: (a) moisture removal rate: and (b) the coefficient of performance ($T_{pro,i}$ = 30 °C, $RH_{pro,i}$ = 60%, u_{air} = 1 m/s, and $t_{deh} = t_{reg}$ = 30 min).

5.6.4. Effect of Air Velocity

Increasing the air velocity (i.e., flow rate) from 1 to 2 *m/s* resulted in a 47% increase in the moisture removal rate as shown in **Fig. 75a**. This is due to the increase in the number of water molecules in the air stream available for absorption, in addition to the enhancement in the convective heat and mass transfer coefficients. However, the improvement in the rate of moisture removal was accompanied by a 29% drop in the coefficient of performance **Fig. 75b**. This was because the thermal energy requirement also increased as the flow rates were increased. The maximum moisture removal rate (at 2 *m/s*) was 75 *g/s-m*^{3}, i.e., a two-fold higher than that reported for LiBr conventional packed towers (35 *g/s-m*^{3}) that were tested under typical dehumidification working conditions (Process air: inlet temperature=25-35 °C, and relative humidity=60-70%) [35].

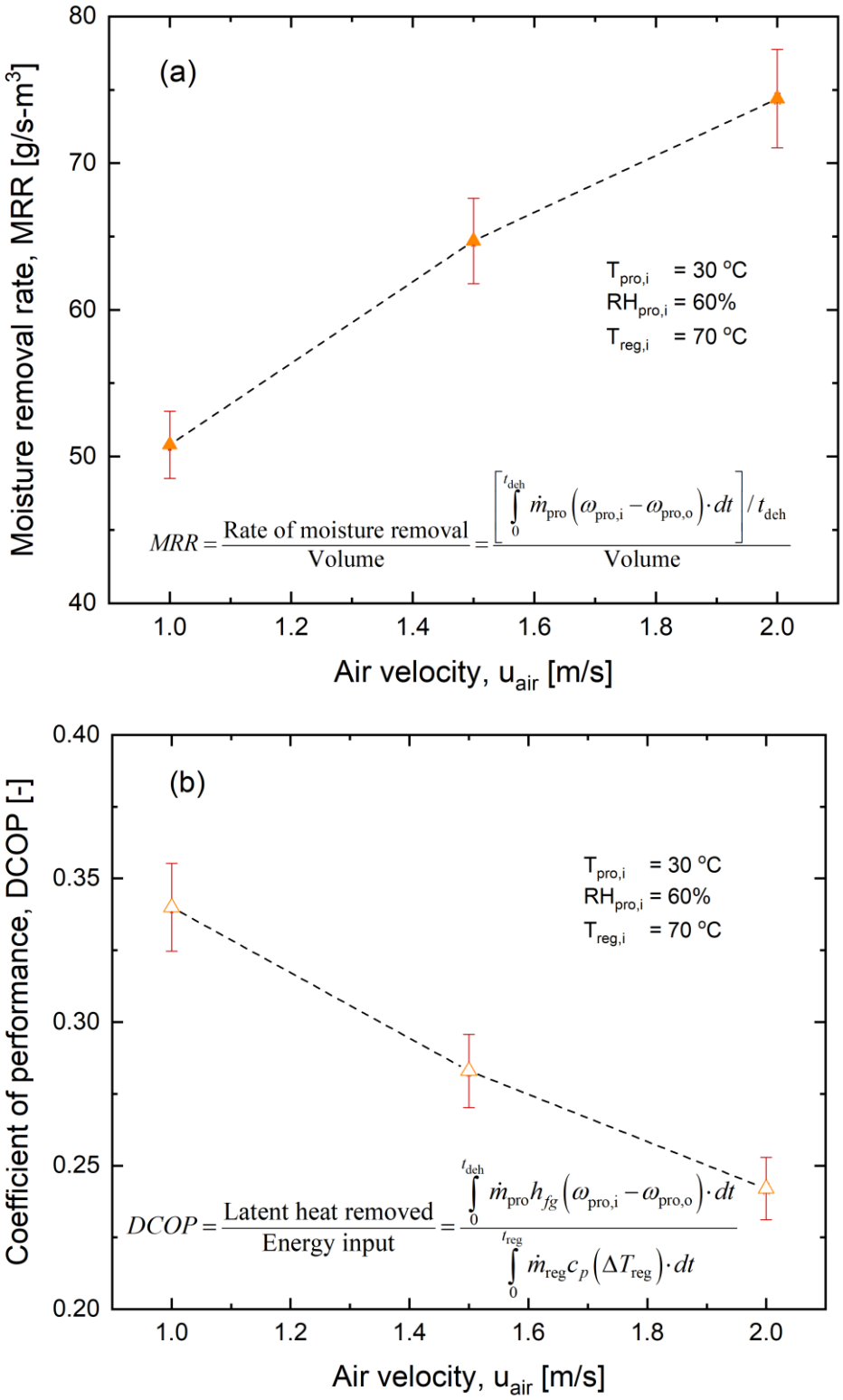

Fig. 75: The effect of air inlet velocity on: (a) the moisture removal rate; and (b) the coefficient of performance ($T_{pro,i}$ = 30 °C, $RH_{pro,i}$ = 60%, $T_{reg,i}$ = 70 °C, u_{air} = 1 m/s, and t_{deh} = t_{reg} = 30 min).

5.7. Conclusions

A novel custom-built sorption bed reactor was designed and tested for dehumidification applications. The "packed-sheet" reactor consisted of spherical microreactors (i.e., microcapsules that contain liquid desiccant) that were maintained by two stainless steel meshes in an air channel. The experimental results have shown the following:

- Both the moisture removal rate and the coefficient of performance will increase as the process air becomes more humid;
- In warmer environments, the moisture removal rate will decrease, but the coefficient of performance will be better because less thermal energy will be required to heat up the air to the required regeneration temperature;
- The change in the moisture removal rate is directly proportional to the change in the regeneration temperature. An increment of 10 °C in the regeneration temperature (from 60 °C to 70 °C, while maintaining a constant moisture content) resulted in a 40% increase in the moisture removal rate, while no noticeable change was observed in the coefficient of performance. Therefore, increasing the regeneration temperature in this range is favourable;
- Increasing the air velocity from 1 to 2 *m/s* resulted in a 47% increase in the moisture removal rate, at the expense of the coefficient of the performance dropping by 29%;
- The maximum moisture removal rate during the experiments was 75 $g/s\text{-}m^3$, i.e., a two-fold increase compared to the values reported for the conventional LiBr gas-liquid absorption packed towers (35 $g/s\text{-}m^3$); and
- The sorption bed has a low pressure drop of 200 *Pa/m* (two orders of magnitude lower than the simple packed beds), which is favourable for minimizing electric power consumption and reducing the noise levels.

6. Reactor Modeling and Optimization

6.1. Introduction

It is important to understand the effect of the key design and operating conditions on the performance of the proposed reactor in Chapter 5. To this end, a coupled heat and mass transfer model is developed and presented in this chapter to simulate the complex transient behaviour of the reactor and optimize its design.

6.2. Mathematical Modeling

A schematic for the proposed reactor is presented in **Fig. 76a**. The process/regeneration air is passed through the channel and is exposed to a packed-sheet filled with microcapsules that contain a LiBr liquid desiccant. The heat and mass transfer paths across the microcapsules is illustrated in **Fig. 76b**.

The main assumptions used to develop the mathematical model are [181–183]:

- 1-D flow in the Z-direction;
- Incompressible fully-developed laminar flow;
- Negligible heat conduction and mass diffusion along the length;
- Constant thermo-physical properties of the sorbent;
- The air flows past the spherical microreactors with a constant area-averaged effective velocity; and
- The Lewis number, *Le*, which reflects the ratio of the convective heat transfer coefficient to the convective mass transfer coefficient is equal to the unit for air [23].

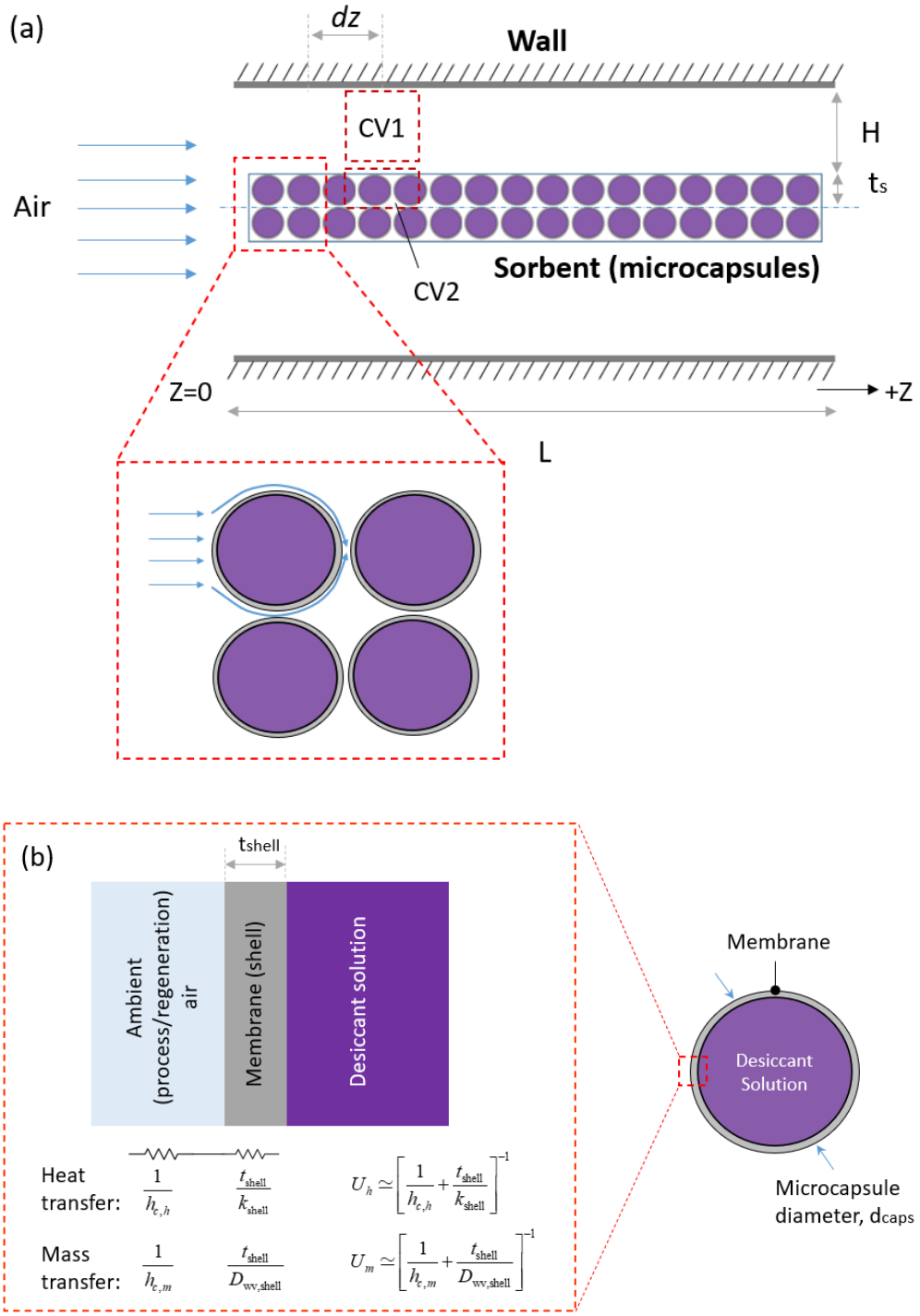

Fig. 76: (a) A schematic of the packed-sheet sorption reactor with encapsulated liquid sorption; and (b) heat and mass transfer across the microcapsules (i.e., microreactors).

The mass continuity and energy balance equations were applied to infinitesimal control volumes (with a *dz* length) in the air (CV1) and sorbent (CV2) domains, and are expressed as follows:

Air (CV1):

Mass Balance:

$$\frac{\partial \omega_a}{\partial t} = -u_a \frac{\partial \omega_a}{\partial z} - \frac{\rho_s A_{cs,s}}{\rho_a A_{cs,a}}(1-\varepsilon)\frac{\partial X_s}{\partial t} \tag{6.1}$$

Energy Balance:

$$\frac{\partial T_a}{\partial t} = -u_{\mathrm{a}} \frac{\partial T_a}{\partial z} - \frac{6U_h}{\rho_a d_{\mathrm{caps}} c_{p,a}} \frac{A_{cs,s}}{A_{cs,a}}(1-\varepsilon)(T_a - T_s) \tag{6.2}$$

Sorbent (CV2):

Mass Balance:

$$\frac{\partial X_s}{\partial t} = \frac{6U_m}{\rho_s d_{\mathrm{caps}}}(\omega_a - \omega_s) \tag{6.3}$$

Energy Balance:

$$\frac{\partial T_s}{\partial t} = \frac{\Delta H_s}{c_{p,s}} \frac{\partial X_s}{\partial t} + \frac{6U_h}{\rho_s c_{p,s} d_{\mathrm{caps}}}(T_a - T_s) \tag{6.4}$$

In the above equations, ω, T, refer X to the humidity and temperature, and water uptake, respectively. The subscripts a and s are related to the air and sorbent, respectively. The parameter u_a denotes the air velocity.

The active volume of the sorbent in the packed volume can be estimated by:

$$V_s = (1-\varepsilon)V_{s,\mathrm{tot}} = (1-\varepsilon)(A_{cs,s} \cdot dz) \tag{6.5}$$

where, $V_{\mathrm{s,tot}}$ is the total volume (includes the sorbent and voids), ε is the void fraction, and $A_{cs,s}$ is the cross-sectional area of the total volume. The total mass of the sorbent beads is determined by:

$$M_s = \rho_s V_{\mathrm{s}} = \rho_s (1-\varepsilon)(A_{cs,s} \cdot dz) \tag{6.6}$$

where, ρ_s is the density of the sorbent beads. The specific surface area of the packed microcapsules, a_s, inside the reactor is estimated by:

$$a_s = \frac{6}{d_{\text{caps}}}\left(1-\varepsilon\right) \tag{6.7}$$

where, d_{caps} is the diameter of the microcapsules. The available heat and mass transfer area is calculated by:

$$A_{h,m} = a_s V_{\text{tot}} = \frac{6}{d_{\text{caps}}}\left(1-\varepsilon\right)\left(A_{cs,s}\cdot dz\right) \tag{6.8}$$

The overall heat U_h and mass U_m transfer coefficients (neglecting the heat and mass resistance of the thin air layer, see assumption 5 and **Fig. 76b**) are determined by:

$$U_h = \left[\frac{1}{h_{c,h}} + \frac{t_{\text{shell}}}{k_{\text{shell}}}\right]^{-1} \tag{6.9}$$

$$U_m = \left[\frac{1}{h_{c,m}} + \frac{t_{\text{shell}}}{D_{\text{wv,shell}}}\right]^{-1} \tag{6.10}$$

The terms $1/h_{c,h}$ and $1/h_{c,m}$ in Eqs. (6.9) and (6.10) are the convective heat and mass transfer resistances, respectively. The terms $t_{\text{shell}}/k_{\text{shell}}$ and $t_{\text{shell}}/D_{\text{wv,shell}}$ represent the conductive heat and mass transfer resistances through the shell material, respectively. In the above equations, t_{shell}, k_{shell}, and $D_{\text{wv,shell}}$ are the thickness, thermal conductivity, and moisture mass diffusivity of the shell.

The convective heat transfer coefficient $h_{c,h}$ was estimated using the derived expression (Eq. 4.38) for spherical particles and presented in Chapter 4:

$$h_{c,h} = \frac{\overline{Nu}_D \cdot k_{air}}{d_{\text{caps}}} = \frac{k_{air}}{d_{\text{caps}}}\left[2 + \frac{0.779}{\left(2/\text{Re}_D^{0.25}+1\right)}\text{Re}_D^{1/2}\,\text{Pr}^{1/3}\right] \tag{6.11}$$

Due to the analogy between the heat and mass transfer, the convective mass transfer coefficient, $h_{c,m}$, can be estimated by (see also assumption 6: for air, $Le_a \simeq 1$) [184]:

$$h_{c,m} = \frac{h_{c,h}}{\rho_a c_{p,a}} Le_a^{-2/3} = \frac{h_{c,h}}{\rho_a c_{p,a}} \tag{6.12}$$

The humidity content of the air at the sorbent-air interface, ω_s, can be calculated using the psychometric relations as follows [185]:

$$\omega_s = \frac{0.622 RH_s}{\frac{P}{P_{vs}} - RH_s} \quad 6.13$$

$$P_{vs} = e^{\left(23.196 - 3816.44/(T_s - 46.13)\right)} \quad 6.14$$

where, P is the atmospheric pressure, and P_{vs} is the water saturation vapor pressure. The corresponding relative humidity of air at the sorbent-air interface can be estimated using the experimental isotherm curves. The experimental isotherm curve of the microcapsules measured using a thermogravimetric vapor sorption analyzer (IGA-002, Hiden Isochema) in our lab is shown in **Fig. 77**. The data were curve-fitted to find a polynomial that describes the relation between the relative humidity and water uptake, and is expressed as:

$$RH_s = 0.00198 - 0.0887 X_s - 0.747 X_s^2 + 9.07346 X_s^3 - 12.45188 X_s^4 + 4.97313 X_s^5 \quad 6.15$$

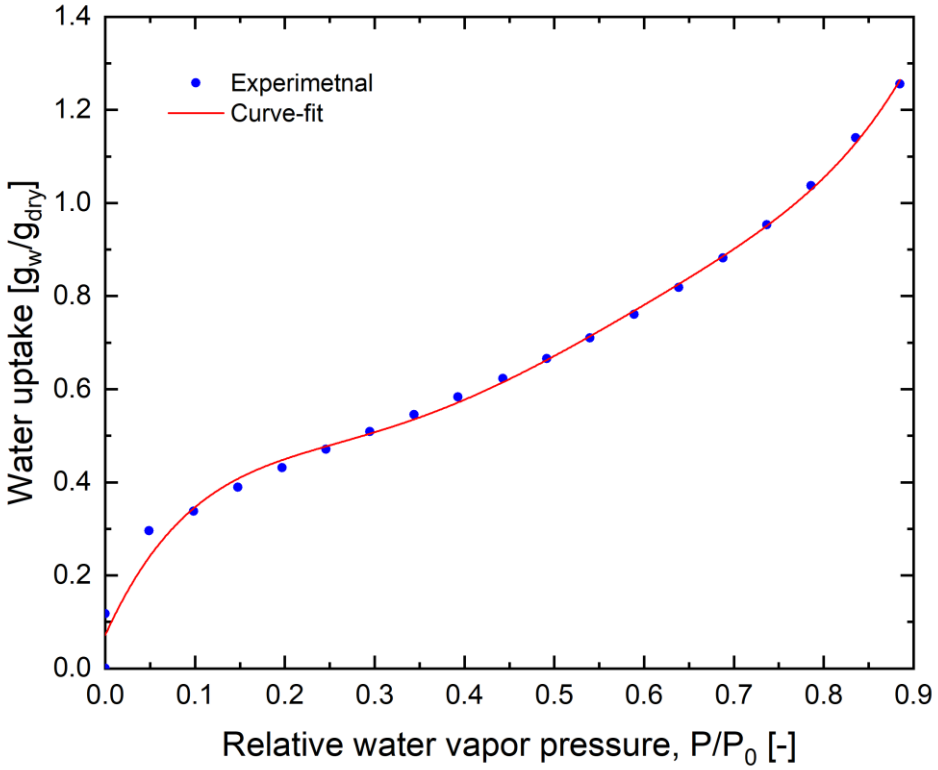

Fig. 77: The isotherm of the microcapsules: (a) experimental (thermogravimetric vapor sorption analyzer test); and (b) the proposed curve-fit, Eq. (6.15).

6.3. Model Validation

The coupled energy and mass balance equations (Eqs. (6.1) to (6.4)) were discretized along the reactor length using the finite element method, which resulted in a system of ordinary differential equations. A MATLAB code was written to solve the highly coupled heat and mass ordinary differential equations using the MATLAB ordinary differential equation solver [186]. The parameters used in the model validation are presented in **Table 6**. A comparison between the predicted temperature and humidity profiles and the experimental results for the baseline test are shown in **Fig. 78a** and **Fig. 78b**. The main deviations occur in the outlet air temperatures, as the model values are slightly higher than the measured ones. This might be attributed to the fact that the inlet temperatures were assumed to be constant in the model, whereas in real experiments, it takes few seconds for the inlet temperatures to reach the intended set values. The comparison between the predicted moisture removal rates and the coefficient of performance with the experimental data in terms of relative difference ((model - data)/model x 100) with various test conditions is presented in **Fig. 79**. The model was able predict all the experimental values with a ±10% relative difference.

Table 6: The parameters used in the model validation.

Parameter	Value
Reactor length, L	180 mm
Channel height, H	1.5 mm
Microcapsules' outer diameter, d_{caps}	700 μm
Shell thickness, t_{shell}	70 μm
Thermal conductivity of the shell, k_{shell}	0.2 W/m-K
Water vapor mass diffusivity, $D_{wv,shell}$	3.7×10^{-6} m^2/s
Heat of absorption, ΔH_s	2,600 kJ/kg

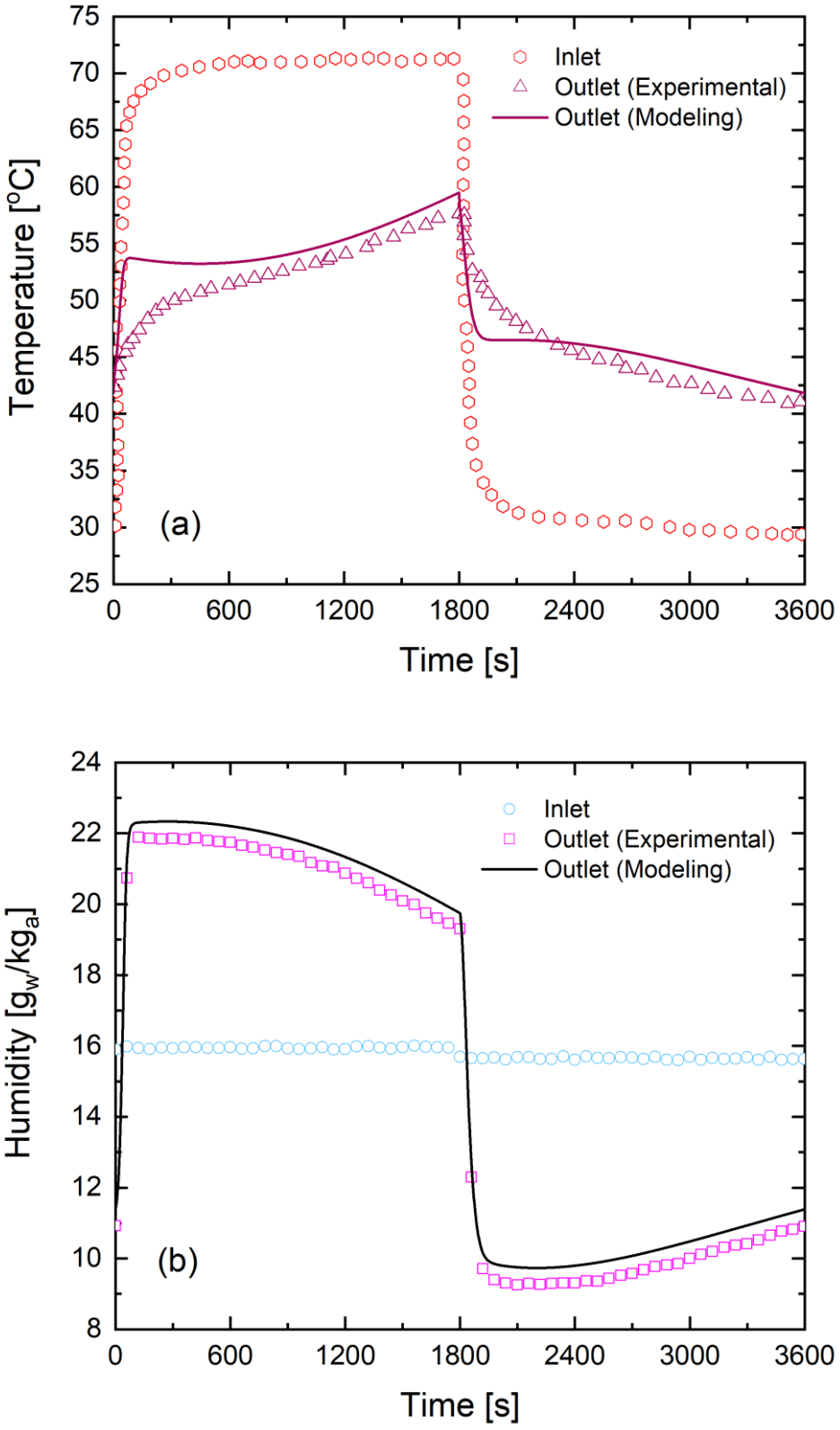

Fig. 78: Validation of the predicted (a) temperature; and (b) humidity profiles by the model with the experimental results of the baseline test ($T_{pro,i}$ = 30 °C, $RH_{pro,i}$ = 60% , $T_{reg,i}$ = 70 °C, u_{air}= 1 m/s, and t_{deh} = 30 min).

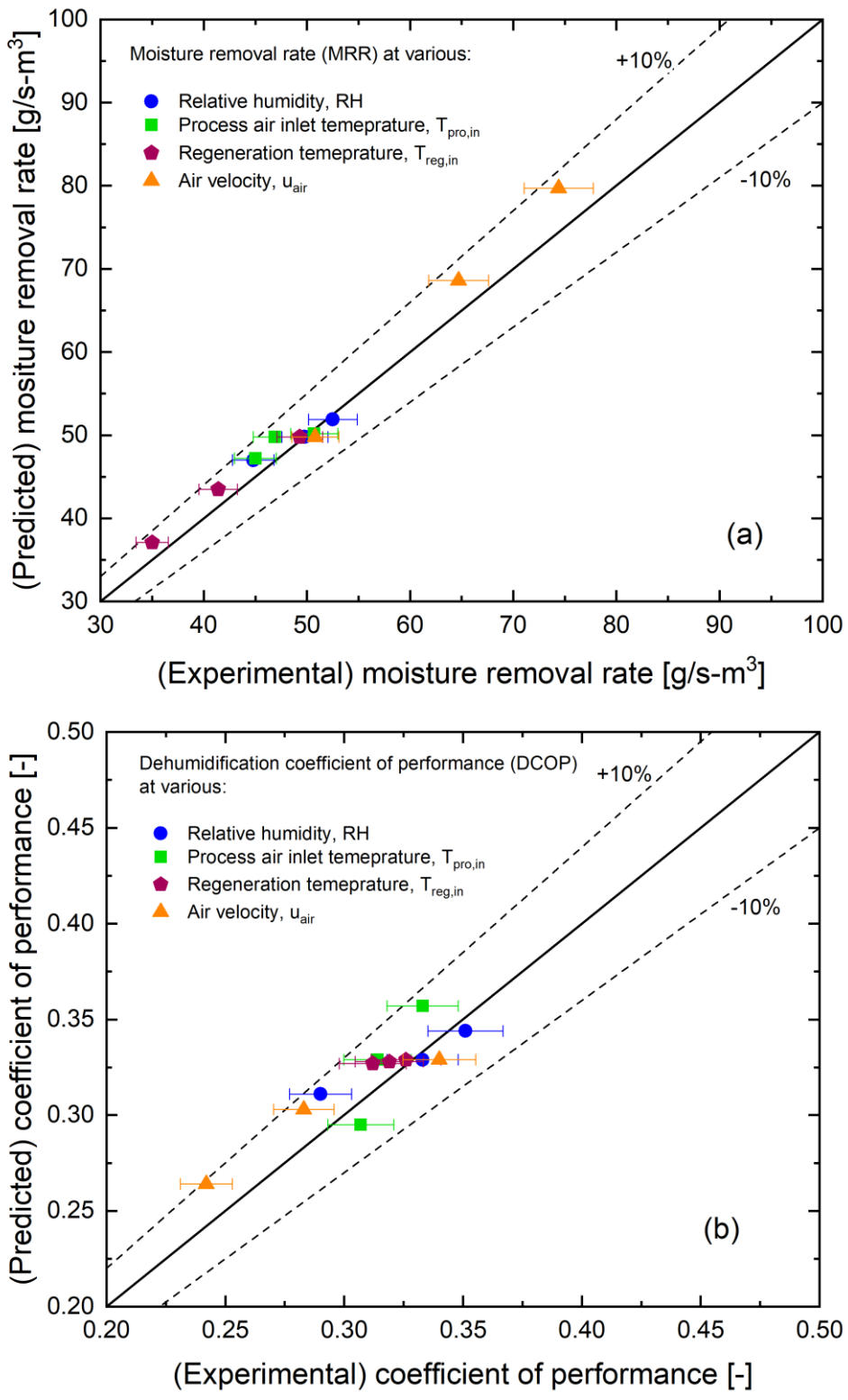

Fig. 79: Validation of the predicted (a) moisture removal rate; and (b) coefficient of performance by the model with the experimental results at the various test conditions.

6.4. Parametric Study

The validated model was used to carry out a parametric study to investigate the effect of the design and operating conditions on the performance of the dehumidification system. In doing so, only the considered parameter was varied, while the other parameters were fixed.

6.4.1. Effect of Sorption Bed Length

The impact of changing the sorption bed length on the moisture removal rates and the coefficient of performance is presented in **Fig. 80a** and **Fig. 80b**, respectively. As expected, the results suggest the change in removal rate is directly proportional to the reactor length, and that reactor designs with shorter lengths will result higher removal rates values. A reactor with a 100 *mm* length will have three times higher removal rate values than that with a 300 *mm* length (75 *g-s/m*^{3} and 25 *g-s/m*^{3}, respectively) as presented in **Fig. 80a**. Despite the fact that the increase in length means more liquid desiccant is used in the reactor (i.e., more moisture is absorbed), on the other hand, increasing the length would also mean a considerable increase in the reactor volume (see Eq. (5.1)). The results indicate that there is an optimum length that maximizes the dehumidification coefficient of performance as shown in **Fig. 80b**.

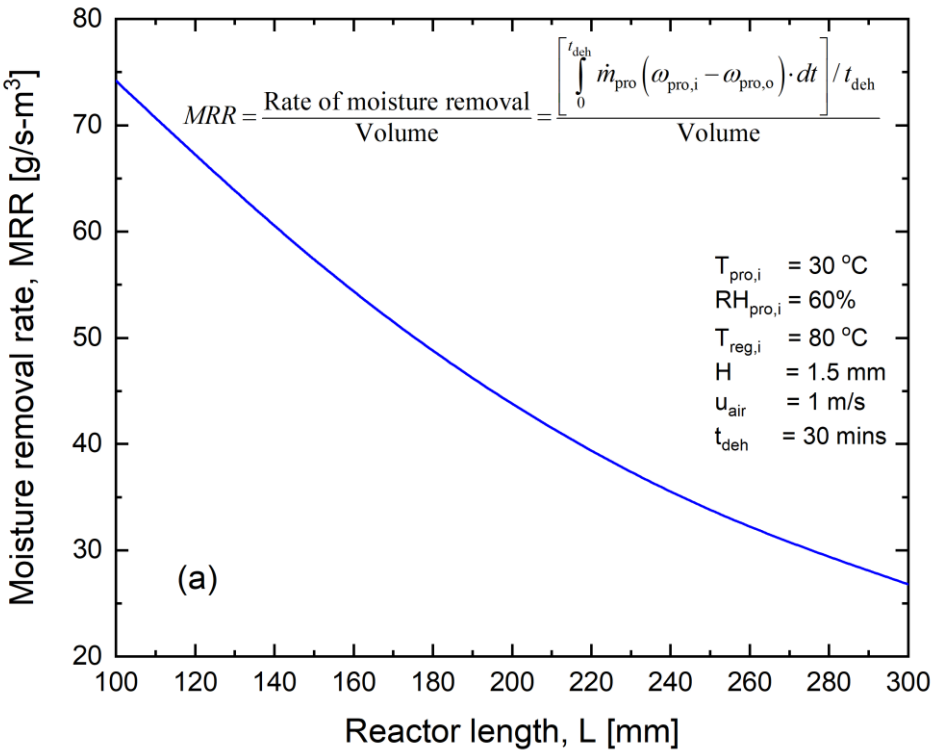

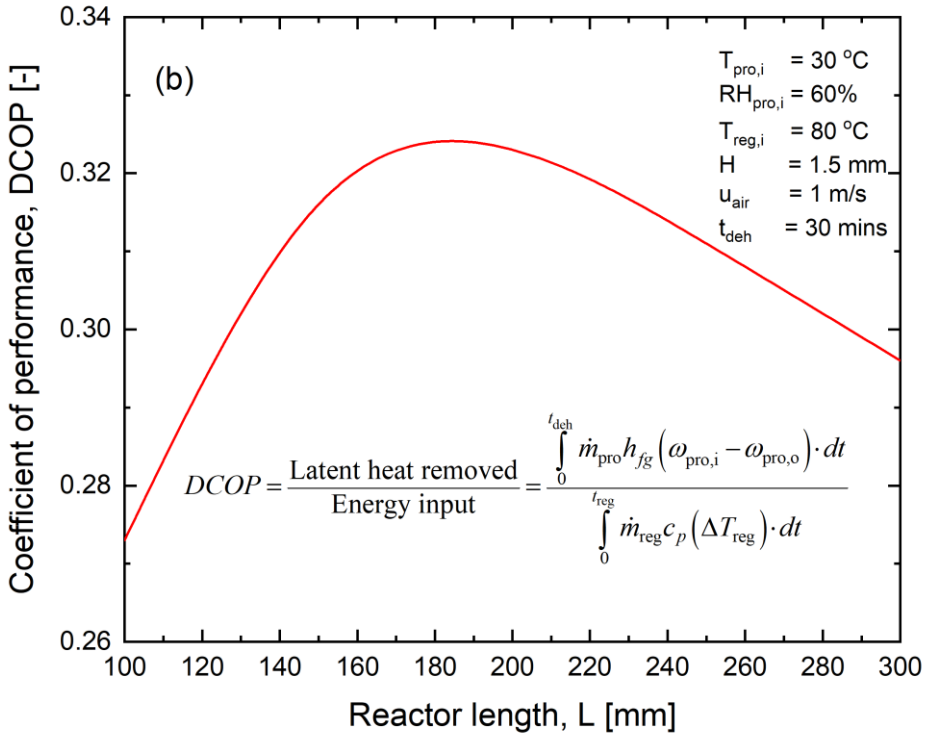

Fig. 80: The effect of the sorption bed length on: (a) the moisture removal rate; (b) the average humidity ratio; and (c) the dehumidification of performance.

6.4.2. Effect of Channel Height

The effect of changing the air channel height on the system performance was also investigated and presented in **Fig. 81**. For the same air velocity, increasing the channel height would mean an increase in the amount of moisture available for absorption (i.e., higher flow rates), but also larger reactor volumes. The model predicts that increasing the channel height within the practical design range would be favourable to increase the moisture removed per unit volume of the reactor. By increasing the channel height from 0.5 *mm* to 2.5 *mm*, it is expected that the removal rate can be enhanced by 100% (from 25 *g-s/m*^{3} to 50 *g-s/m*^{3}) as shown in **Fig. 81a**. It is also worth noting that channels with larger heights would result in lower pressure drops. On the other hand, the model predicts that there exists an optimal value (depends on the specific operating condition) for the channel height that maximizes the thermal energy usage (i.e., optimum coefficient of performance) as shown in **Fig. 81b**.

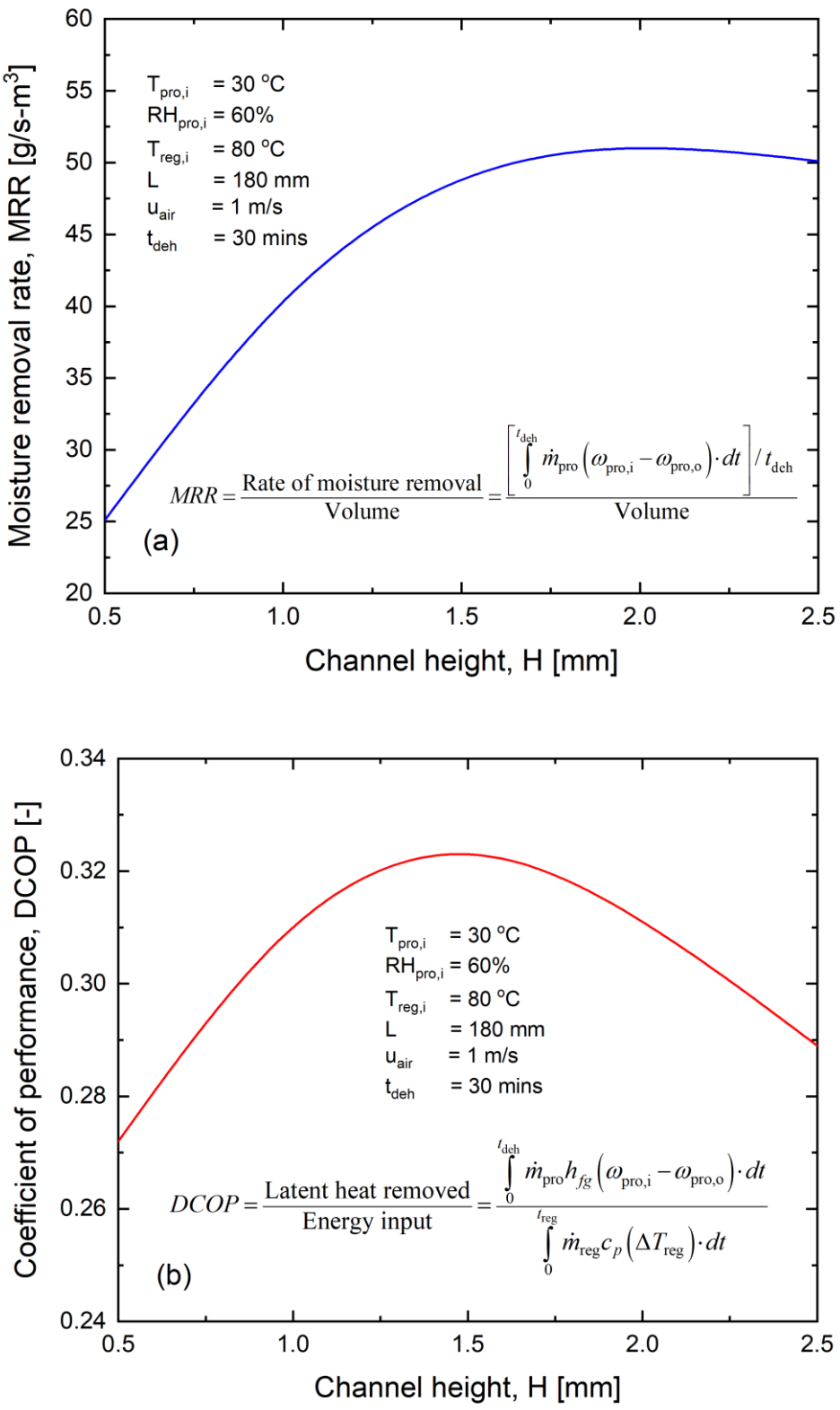

Fig. 81: The effect of the sorption channel height on: (a) the moisture removal rate; and (b) the coefficient of performance.

6.4.3. Effect of Process (Half-cycle) Time

The variation of the moisture removal rate and the coefficient of performance with the half-cycle time were also investigated, and the simulation results are presented in **Fig. 82a** and **Fig. 82b,** respectively. For any specific operating condition, there exists an optimal half-cycle time that results in the maximum removal rate and coefficient of performance. The results indicate that, for maximizing the performance, the system should be operated with half-cycle times in the 20-50 minute range.

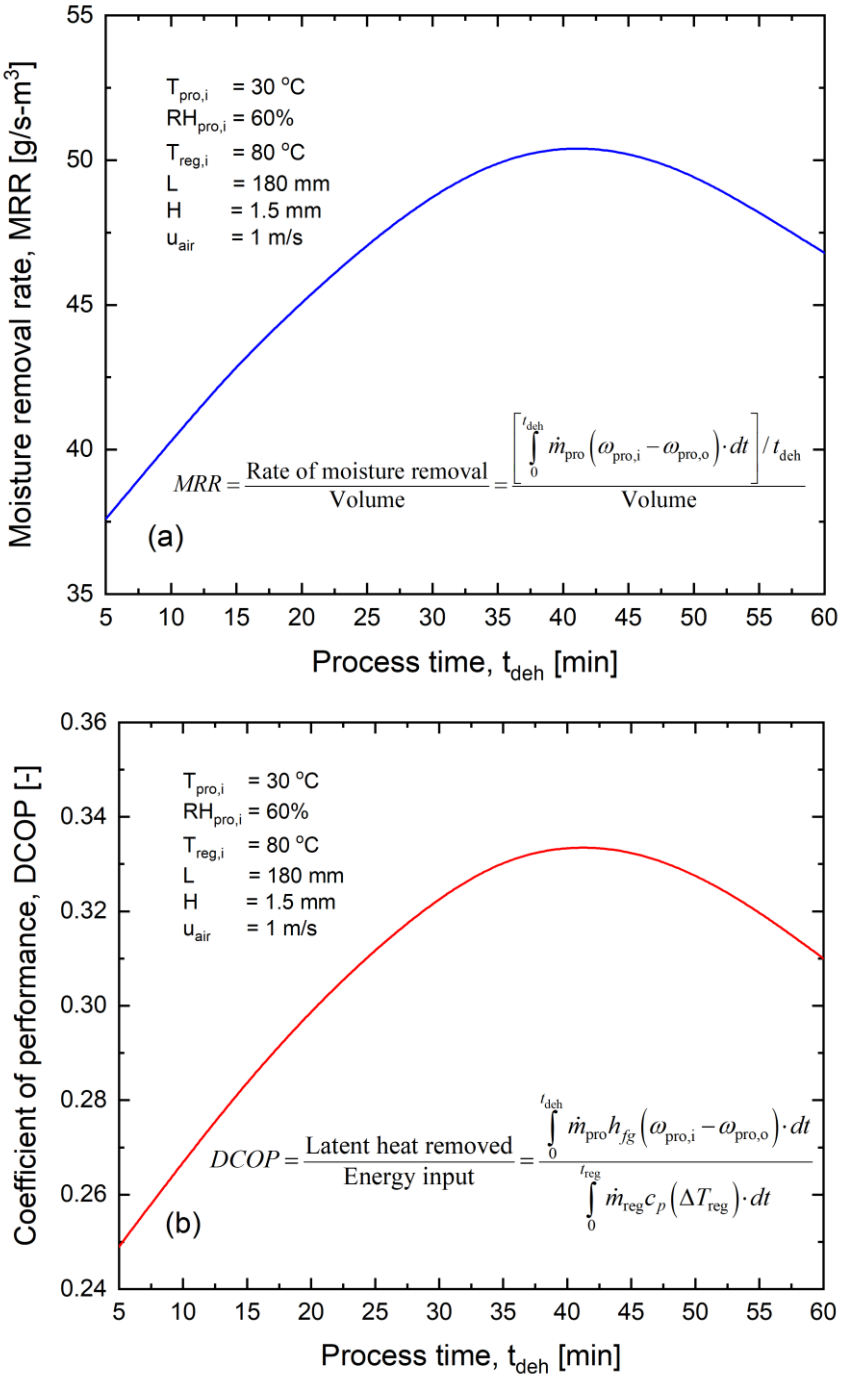

Fig. 82: The effect of the process time on: (a) the moisture removal rate; and (b) the coefficient of performance.

6.5. Optimization Study

The parametric study revealed that the various design and operating conditions would have different impacts on the system performance. Therefore, there is a need to conduct an optimization study. Parameters that include design variables (reactor length, channel height) and the "controllable" operating conditions (air velocity and half-cycle time) were selected to maximize both the moisture removal rate (MRR) and the dehumidification coefficient of performance (DCOP). The mathematical formulation of the multi-objective optimization problem is:

$$\textbf{Minimize: } -MRR,\ -DCOP \tag{6.16}$$

$$\textbf{Subject to:} \tag{6.17}$$

$100\ \text{mm} \le L \le 300\ \text{mm}$

$1.5\ \text{mm} \le H \le 3\ \text{mm}$

$0.5\ \text{m/s} \le u_{air} \le 2\ \text{m/s}$

$5\ \text{min} \le \text{Half-cycle time} \le 60\ \text{mins}$

The MATLAB code, described above (**Appendix D**), was linked to OASIS software [187], i.e., an optimization platform that is based on proprietary algorithms. OASIS algorithms integrate several approaches from metamodeling, machine learning, statistical analysis, and mathematical programming. The algorithms follow an iterative sampling, learning, resampling process that identifies the best solution in less time. The experimental results (Chapter 5) showed that high inlet temperatures and low relative humidity levels of the process air have adverse effects on the moisture removal rates (see Section 5.6.1 and 5.6.2). An optimization study was conducted to optimize the design for the worst-case scenario in an environment with the lowest relative humidity ($RH_{pro,i}$ = 50%) and the highest process inlet temperature ($T_{pro,i}$ = 35°C) in the typical working range ($T_{pro,i}$ = 25-35 °C, $RH_{pro,i}$ = 50-70%).

The pareto front that shows all the efficient solutions for the multi-objective (the moisture removal rate and coefficient of performance) problem is presented in **Fig. 83**. One can observe that there is a trade-off between the maximum removal rate and the coefficient of performance values that can be balanced. By considering that liquid desiccant dehumidifier systems are often powered by a free-energy source, such as solar thermal energy or waste-heat, perhaps achieving the highest moisture removal rates should be prioritized. In cases where the energy efficiency is of the same importance, other feasible solution(s) in the Pareto frontier that represent the best trade-off removal rate and coefficient of performance may be selected. The result from the optimization study shows that the reactor design can be optimized to realize removal rates value of ~130 *g-s/m*^{3} with a coefficient of performance of 0.25, which is 270% higher than the

highest value (35 *g/s-m*^{3}) reported for the conventional packed towers that use LiBr liquid desiccant [35]. The result of the optimization study is summarized in **Table 7**.

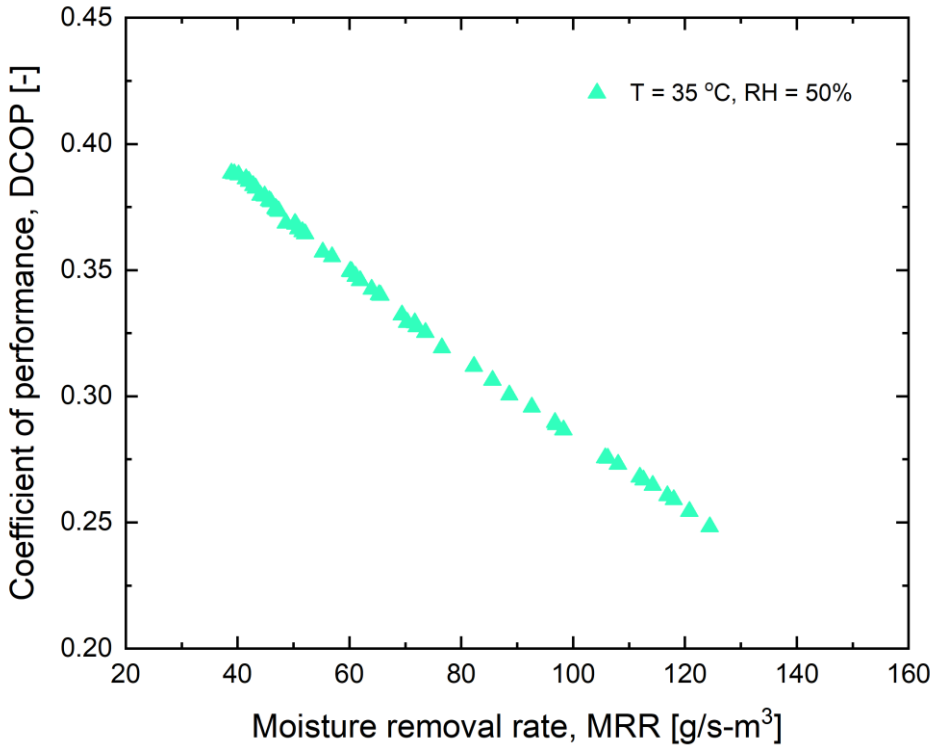

Fig. 83: The pareto front curve of the multi-objective (moisture removal rate and coefficient of performance) optimization.

Table 7: The optimal solution for (the moisture removal rate and the coefficient of performance) multi-objective optimization problem.

Optimal Parameter	Value
Reactor length, L	120 mm
Channel height, H	1.0 mm
Air velocity, u_{air}	2 m/s
Process (half-cycle) time, t_{deh}	15 min
Moisture removal rate, MRR	130 g/s-m^3
Dehumidification of performance, $DCOP$	0.25

6.6. Conclusions

In this chapter, a one-dimensional model that considers the coupled heat and mass transfer has been developed to simulate the transient behaviour of the proposed packed-sheet reactor. The model was validated with the collected experimental data over various operating conditions. A parametric study was conducted to investigate the impact of key design and operating conditions, as well as to serve as a guideline for designing future prototypes. In addition, the developed model was used in conducting an optimization study to maximize the performance of reactor. The main conclusions are:

- There is an optimal reactor length beyond which the coefficient of performance will drop;

- Increasing the channel height within the practical design range (0.5 *mm* to 2.5 *mm*) would be favourable to have more compact designs. By increasing the channel height from 0.5 *mm* to 2.5 *mm*, it is expected that the moisture removal rates can be enhanced by 100% (from 25 $g\text{-}s/m^3$ to 50 $g\text{-}s/m^3$);

- For any specific operating condition, there exists an optimal half-cycle that maximizes both the moisture removal rate (i.e., compact design) or the coefficient of performance (i.e., maximum energy efficiency) values; and

- Based on the optimization study, the design variables and controllable operating conditions can be optimized to maximize the performance and achieve moisture removal rate values of up to 135 $g/s\text{-}m^3$ (270% higher than the conventional liquid desiccant systems) with a coefficient of performance of 0.25.

7. Summary and Future Work

7.1. Summary

Chapter 1 provides an introduction to highlight the motivation behind the research and how is it important to develop efficient and compact dehumidification systems to control the humidity levels in buildings and greenhouses in order to reduce the energy consumption and greenhouse gas (GHG) emissions. Despite the advantages of thermally-driven liquid desiccant absorption systems over conventional dehumidification systems, the research on absorption dehumidification systems is still limited to laboratory-scale experiments rather than practical applications. The need for new absorber designs that eliminate the fundamental limitation (slow absorption process) and practical challenges of the conventional designs (solution carryover, crystallization, and corrosion) that hinder its utilization in real dehumidification applications has been highlighted.

Chapter 2 provides a critical literature review for various absorber designs, discussing their limitations and assessing their suitability in real dehumidification systems. Based on the conducted literature survey, a new design concept with spherical microreactors was proposed that has the potential to overcome the aforementioned practical challenges of liquid absorption systems and to achieve high absorption rates.

In Chapter 3, for the first time, microcapsules (i.e., microreactors) with a highly uniform size that encapsulate liquid desiccants (i.e., a LiBr solution) were produced using a custom-built microfluidic device. The produced microcapsules had a high sorption capacity (1 g_w/g_{dry}), and were proven to have excellent mechanical strength that was confirmed by the compression, expansion, multi-cycling (sorption-desorption) tests. The microcapsules were able to withstand a force of up to 2 X 10^5 their weight, expanded (elastically) during the absorption process without rupture, and did not leak or have reduced capacity even after an accelerated test of 200 sorption-desorption cycles.

In Chapter 4, a fundamental study was presented to study the heat transfer from/to spherical particles with specified boundary conditions mimicking the proposed microcapsules. An expression for the convective heat transfer coefficient was derived using analytical modeling, and the proposed analytical-based closed-form model was later used (in Chapter 6) for modeling the transient behaviour of the dehumidification reactor prototype.

In Chapter 5, a novel custom-built sorption bed reactor was designed, built, and tested for dehumidification applications. The concept of a “packed sheet” was introduced for the core of the modular dehumidifier. The packed-sheet reactor consisted

of microcapsules (containing liquid desiccant) that were suspended by two stainless steel meshes in the air channels. The experimental results showed that the proposed design had up to a two-fold higher moisture removal rate per volume (MRR=75 *g/s-m^3*) than a conventional LiBr gas-liquid absorption packed tower (MRR=35 *g/s-m^3*).

In Chapter 6, a one-dimensional coupled heat and mass transfer was developed to simulate the transient behaviour of the proposed packed-sheet reactor. The model was validated with the collected experimental data under various operating conditions. A parametric study was conducted to show the impact of design and controllable operating conditions, as well as to serve as a guideline for designing future prototypes. An optimization study was conducted. The results revealed that the performance of the proposed design can be maximized to realize moisture removal rates of up to 135 g/s-m^3 (270% higher than the conventional liquid desiccant systems) with a coefficient of performance of 0.25.

7.2. Future Work

The recommendations for future research are as follows:

- Investigate the encapsulation of other liquid desiccants, such as $CaCl_2$ and LiCl and evaluate the sorption capacity of the produced microcapsules.

- Investigate the possibility of increasing the salt loading inside the microcapsules to increase the sorption capacity.

- Search for other highly permeable shell materials that provide flexibility with minimal buckling.

- Design, build, and test an optimized pilot-scale absorber with “multiple” packed sheets under real-life testing conditions.

References

[1] Agency IE. Energy Technology Perspectives 2017. 2017. https://doi.org/https://doi.org/https://doi.org/10.1787/energy_tech-2017-en.

[2] Rafique MM, Gandhidasan P, Bahaidarah HMS. Liquid desiccant materials and dehumidifiers--A review. *Renew Sustain Energy Rev* 2016;56:179–95.

[3] Guieysse B, Hort C, Platel V, Munoz R, Ondarts M, Revah S. Biological treatment of indoor air for VOC removal: Potential and challenges. *Biotechnol Adv* 2008;26:398–410.

[4] Farooq M, Wahid A, Kobayashi N, Fujita D, Basra SMA. Plant drought stress: effects, mechanisms and management. Sustain. Agric., Springer; 2009, p. 153–88.

[5] https://www.statcan.gc.ca 2010.

[6] Wong B, McClung L, Snijders A, McClenahan D, Thornton J. The application of aquifer thermal energy storage in the Canadian greenhouse industry. Int. Symp. High Technol. Greenh. Syst. GreenSys2009 893, 2009, p. 437–44.

[7] Zühlsdorf B. High-performance heat pump systems. PhD Thesis, Technical University of Denmark, 2019.

[8] Han J, Gao Z, Guo H, Brad R, Waterer D. Comparison of greenhouse dehumidification strategies in cold regions. *Appl Eng Agric* 2015;31:133–42.

[9] Murphy J. Dehumidification performance of HVAC systems. *ASHRAE J* 2002;44:23.

[10] Nizovtsev MI, Borodulin VY, Letushko VN, Zakharov AA. Analysis of the efficiency of air-to-air heat exchanger with a periodic change in the flow direction. *Appl Therm Eng* 2016;93:113–21.

[11] Fernández-Seara J, Diz R, Uh\'\ia FJ, Dopazo A, Ferro JM. Experimental analysis of an air-to-air heat recovery unit for balanced ventilation systems in residential buildings. *Energy Convers Manag* 2011;52:635–40.

[12] Han J, Guo H, Brad R, Gao Z, Waterer D. Dehumidification Requirement for aGreenhouse Located in a Cold Region. *Appl Eng Agric* 2015;31:291–300.

[13] Chantoiseau E, Migeon C, Chasseriaux G, Bournet P-E. Heat-pump dehumidifier as an efficient device to prevent condensation in horticultural greenhouses. *Biosyst Eng* 2016;142:27–41.

[14] Huizing R, Chen H, Wong F. Contaminant transport in membrane based energy recovery ventilators. *Sci Technol Built Environ* 2015;21:54–66.

[15] Qi R, Dong C, Zhang L-Z. A review of liquid desiccant air dehumidification: From system to material manipulations. *Energy Build* 2020;215:109897.

[16] Gordeeva LG, Restuccia G, Freni A, Aristov YI. Water sorption on composites "LiBr in a porous carbon." *Fuel Process Technol* 2002;79:225–31.

[17] Bales C, Gantenbein P, Hauer A, Henning H-M, Jaenig D, Kerskes H, et al. Thermal properties of materials for thermo-chemical storage of solar heat. *Rep B2-IEA SHC Task* 2005;32.

[18] Yang K, Shi Y, Wu M, Wang W, Jin Y, Li R, et al. Hollow spherical SiO 2 micro-container encapsulation of LiCl for high-performance simultaneous heat reallocation and seawater desalination. *J Mater Chem A* 2020;8:1887–95.

[19] Lewis WK, Whitman WG. Principles of gas absorption. *Ind \& Eng Chem* 1924;16:1215–20.

[20] Dong C, Hibiki T, Zhang L, Lu L. Falling film liquid desiccant air dehumidification. *Exp Comput Multiph Flow* 2020;2:187–98.

[21] Elsarrag E, M. Ali EE, Jain S. Design guidelines and performance study on a

structured packed liquid desiccant air-conditioning system. *HVAC\&R Res* 2005;11:319–37.
[22] Chugh D, Gluesenkamp K, Abdelaziz O, Moghaddam S. Ionic liquid-based hybrid absorption cycle for water heating, dehumidification, and cooling. *Appl Energy* 2017;202:746–54.
[23] Jain S, Bansal PK. Performance analysis of liquid desiccant dehumidification systems. *Int J Refrig* 2007;30:861–72.
[24] Bhowmik M, Muthukumar P, Anandalakshmi R. Experimental based multi-objective optimisation for structured packed bed liquid desiccant dehumidification systems. *J Build Eng* 2020;32:101813.
[25] https://en.wikipedia.org/wiki/Lithium_bromide 2022.
[26] https://www.youtube.com/watch?v=boli4ecJuZs 2020.
[27] Liao X, Radermacher R. Absorption chiller crystallization control strategies for integrated cooling heating and power systems. *Int J Refrig* 2007;30:904–11.
[28] Wang K, Abdelaziz O, Kisari P, Vineyard EA. State-of-the-art review on crystallization control technologies for water/LiBr absorption heat pumps. *Int J Refrig* 2011;34:1325–37.
[29] Killion JD, Garimella S. A critical review of models of coupled heat and mass transfer in falling-film absorption. *Int J Refrig* 2001;24:755–97.
[30] Zogg RA, Westphalen D. Developing air-cooled LiBr absorption for light commercial combined heat and power applications. *HVAC&R Res* 2006;12:731–47.
[31] Zhai C, Wu W. Heat and mass transfer performance comparison of various absorbers/desorbers towards compact and efficient absorption heat pumps. *Int J Refrig* 2021;127:203–20.
[32] Sehgal S, Alvarado JL, Hassan IG, Kadam ST. A comprehensive review of recent developments in falling-film, spray, bubble and microchannel absorbers for absorption systems. *Renew Sustain Energy Rev* 2021;142:110807.
[33] Amaris C, Vallès M, Bourouis M. Vapour absorption enhancement using passive techniques for absorption cooling/heating technologies: A review. *Appl Energy* 2018;231:826–53.
[34] Bhowmik M, Muthukumar P, Anandalakshmi R. Experimental investigation on structured packed bed liquid desiccant dehumidifier: An optimal mixture design of experiments strategy. *Int J Refrig* 2021;122:232–44.
[35] Liu XH, Yi XQ, Jiang Y. Mass transfer performance comparison of two commonly used liquid desiccants: LiBr and LiCl aqueous solutions. *Energy Convers Manag* 2011;52:180–90.
[36] Chen T, Dai Z, Yin Y, Zhang X. Experimental investigation on the mass transfer performance of a novel packing used for liquid desiccant systems. *Sci Technol Built Environ* 2017;23:46–59.
[37] Tan LS, Shariff AM, Lau KK, Bustam MA. Factors affecting CO2 absorption efficiency in packed column: A review. *J Ind Eng Chem* 2012;18:1874–83.
[38] Longo GA, Gasparella A. Experimental analysis on chemical dehumidification of air in a packed column by hygroscopic salt solution: Comparison between structured and random packings. *HVAC&R Res* 2006;12:713–29.
[39] Bassuoni MM. An experimental study of structured packing dehumidifier/regenerator operating with liquid desiccant. *Energy* 2011;36:2628–38.
[40] Westerlund L, Dahl J. Absorbers in the open absorption system. *Appl Energy* 1994;48:33–49.

[41] Ludwig EE, editor. Chapter 9 Packed Towers. vol. 2, Gulf Professional Publishing; 1997, p. 230–415. https://doi.org/https://doi.org/10.1016/S1874-8635(97)80005-2.
[42] Benitez J. Principles and modern applications of mass transfer operations. John Wiley & Sons; 2016.
[43] Yu D, Chung J, Moghaddam S. Parametric study of water vapor absorption into a constrained thin film of lithium bromide solution. *Int J Heat Mass Transf* 2012;55:5687–95.
[44] Drost K, Liburdy J, Paul B, Peterson R. Enhancement of Heat and Mass Transfer in Mechanically Contstrained Ultra Thin Films. 2005.
[45] Liu XH, Zhang Y, Qu KY, Jiang Y. Experimental study on mass transfer performances of cross flow dehumidifier using liquid desiccant. *Energy Convers Manag* 2006;47:2682–92.
[46] Moon CG, Bansal PK, Jain S. New mass transfer performance data of a cross-flow liquid desiccant dehumidification system. *Int J Refrig* 2009;32:524–33.
[47] Fumo N, Goswami DY. Study of an aqueous lithium chloride desiccant system: air dehumidification and desiccant regeneration. *Sol Energy* 2002;72:351–61.
[48] Martin V, Goswami DY. Effectiveness of heat and mass transfer processes in a packed bed liquid desiccant dehumidifier/regenerator. *Hvac&R Res* 2000;6:21–39.
[49] Kim M-H, Park J-Y, Jeong J-W. Simplified model for packed-bed tower regenerator in a liquid desiccant system. *Appl Therm Eng* 2015;89:717–26.
[50] Chung T-W, Ghosh TK, Hines AL. Comparison between random and structured packings for dehumidification of air by lithium chloride solutions in a packed column and their heat and mass transfer correlations. *Ind Eng Chem Res* 1996;35:192–8.
[51] Chung T-W. Predictions of moisture removal efficiencies for packed-bed dehumidification systems. *Gas Sep Purif* 1994;8:265–8.
[52] Factor HM, Grossman G. A packed bed dehumidifier/regenerator for solar air conditioning with liquid desiccants. *Sol Energy* 1980;24:541–50.
[53] Bansal P, Jain S, Moon C. Performance comparison of an adiabatic and an internally cooled structured packed-bed dehumidifier. *Appl Therm Eng* 2011;31:14–9.
[54] Ventas R, Vereda C, Lecuona A, Venegas M, del Carmen Rodriguez-Hidalgo M. Effect of the NH3--LiNO3 concentration and pressure in a fog-jet spray adiabatic absorber. *Appl Therm Eng* 2012;37:430–7.
[55] Gutiérrez-Urueta G, Rodriguez P, Venegas M, Ziegler F, Rodriguez-Hidalgo MC. Experimental performances of a LiBr-water absorption facility equipped with adiabatic absorber. *Int J Refrig* 2011;34:1749–59.
[56] Palacios E, Izquierdo M, Marcos JD, Lizarte R. Evaluation of mass absorption in LiBr flat-fan sheets. *Appl Energy* 2009;86:2574–82.
[57] Palacios E, Izquierdo M, Lizarte R, Marcos JD. Lithium bromide absorption machines: Pressure drop and mass transfer in solutions conical sheets. *Energy Convers Manag* 2009;50:1802–9.
[58] Ibarra-Bahena J, Romero R. Performance of different experimental absorber designs in absorption heat pump cycle technologies: a review. *Energies* 2014;7:751–66.
[59] Stolk AL, Waszenaar RH. Heat and mass transfer phenomena in an absorber with drop-wise falling film on horizontal tubes 1986.
[60] Jain S, Tripathi S, Das RS. Experimental performance of a liquid desiccant

dehumidification system under tropical climates. *Energy Convers Manag* 2011;52:2461–6.
[61] Warnakulasuriya FSK, Worek WM. Adiabatic water absorption properties of an aqueous absorbent at very low pressures in a spray absorber. *Int J Heat Mass Transf* 2006;49:1592–602.
[62] Newman AB. The drying of porous solids: diffusion and surface emission equations. *AIChE Trans* 1931;27:203–20.
[63] Warnakulasuriya FSK, Worek WM. Drop formation of swirl-jet nozzles with high viscous solution in vacuum-new absorbent in spray absorption refrigeration. *Int J Heat Mass Transf* 2008;51:3362–8.
[64] Arzoz D, Rodriguez P, Izquierdo M. Experimental study on the adiabatic absorption of water vapor into LiBr--H2O solutions. *Appl Therm Eng* 2005;25:797–811.
[65] Jeong S, Garimella S. Optimal design of compact horizontal tube LiBr/water absorbers. *HVAC&R Res* 2005;11:27–44.
[66] Deng SM, Ma WB. Experimental studies on the characteristics of an absorber using LiBr/H2O solution as working fluid. *Int J Refrig* 1999;22:293–301.
[67] Kim BJ, Kang IS. Absorption of water vapor into wavy-laminar falling film of aqueous lithium-bromide. *KSME J* 1995;9:115–22.
[68] Miller WA. The synergism between heat and mass transfer additive and advanced surfaces in aqueous LiBr horizontal tube absorbers. 1999.
[69] Olbricht M, Luke A. Experimental investigation of the heat and mass transfer in a tube bundle absorber of an absorption chiller. *Heat Mass Transf* 2019;55:81–93.
[70] Sultana P. Study of thermal performances of falling film absorbers with and without film-inversion 2007.
[71] Tongu S, Makino Y, Ohnishi K, Nakatsugawa S. Practical operating of small-sized air-cooled double-effect absorption chiller-heater by using lithium bromide and aqueous. Int. Heat Pump Conf, 1993.
[72] Nomura T, Nishimura N, Wei S, Yamaguchi S, Kawakami R. Heat and mass transfer mechanism in the absorber of water/LiBr conventional absorption refrigerator: experimental examination by visualized model. Int. Absorpt. Heat Pump Conf., vol. 31, 1993, p. 203–8.
[73] Medrano M, Bourouis M, Coronas A. Absorption of water vapour in the falling film of water--lithium bromide inside a vertical tube at air-cooling thermal conditions. *Int J Therm Sci* 2002;41:891–8.
[74] Garcia-Rivera E, Castro J, Farnos J, Oliva A. Numerical and experimental investigation of a vertical LiBr falling film absorber considering wave regimes and in presence of mist flow. *Int J Therm Sci* 2016;109:342–61.
[75] Kim KJ, Berman NS, Chau DSC, Wood BD. Absorption of water vapour into falling films of aqueous lithium bromide. *Int J Refrig* 1995;18:486–94.
[76] Miller WA, Perez-Blanco H. Vertical-tube aqueous LiBr falling film absorption using advanced surfaces. 1993.
[77] Kulankara S, Herold KE. Theory of heat and mass transfer additives in absorption chillers. *HVAC&R Res* 2000;6:369–80.
[78] Zohuri B. Compact heat exchangers. Springer; 2017.
[79] Islam MR, Wijeysundera NE, Ho JC. Performance study of a falling-film absorber with a film-inverting configuration. *Int J Refrig* 2003;26:909–17.
[80] Yoon J-I, Kwon O-K, Moon C-G. Experimental investigation of heat and mass transfer in absorber with enhanced tubes. *KSME Int J* 1999;13:640–6.

[81] Zhang H, Yin D, You S, Zheng W, Wei S. Experimental investigation of heat and mass transfer in a LiBr-H2O solution falling film absorber on horizontal tubes: Comprehensive effects of tube types and surfactants. *Appl Therm Eng* 2019;146:203–11.
[82] Ma X-H, Lan Z, Hao Z, Wang Q-C, Bo S, Bai T. Heat transfer and thermodynamic performance of LiBr/H2O absorption heat transformer with vapor absorption inside vertical spiral tubes. *Heat Transf Eng* 2014;35:1130–6.
[83] Kim KJ, Berman NS, Wood BD. Surface tension of aqueous lithium bromide+ 2-ethyl-1-hexanol. *J Chem Eng Data* 1994;39:122–4.
[84] Yao W, Bjurstroem H, Setterwall F. Surface tension of lithium bromide solutions with heat-transfer additives. *J Chem Eng Data* 1991;36:96–8.
[85] Kashiwagi T. Basic mechanism of absorption heat and mass transfer enhancement by the Marangoni effect. *Newsl IEA Heat Pupm Cent* 1988;6:2–6.
[86] Kim KJ, Berman NS, Wood BD. Absorption of water vapor into LiBr solutions with 2-ethyl-1-hexanol. *AIChE J* 1996;42.
[87] Kang YT, Kim HJ, Lee K Il. Heat and mass transfer enhancement of binary nanofluids for H2O/LiBr falling film absorption process. *Int J Refrig* 2008;31:850–6.
[88] Bangerth S, Tiwari R, Shooshtari A, Ohadi M. Heat/mass transfer enhancement of an exothermic absorption utilizing a spinning disk reactor. *Int J Heat Mass Transf* 2019;129:326–41.
[89] Kang YT, Christensen RN. Transient analysis and design model of a LiBr-H2O absorber with rotating drums. *ASHRAE Trans* 1995:1163–74.
[90] Gilchrist K, Lorton R, Green RJ. Process intensification applied to an aqueous LiBr rotating absorption chiller with dry heat rejection. *Appl Therm Eng* 2002;22:847–54.
[91] Zaltash A, Petrov A, Linkous R, Vineyard E, Goodnack D, Egilegor B. Performance evaluation of a 4.5 kW (1.3 refrigeration tons) air-cooled lithium bromide/water hot-water-fired absorption unit. ASME Int. Mech. Eng. Congr. Expo., vol. 43092, 2007, p. 197–210.
[92] Izquierdo M, Lizarte R, Marcos JD, Gutiérrez G. Air conditioning using an air-cooled single effect lithium bromide absorption chiller: Results of a trial conducted in Madrid in August 2005. *Appl Therm Eng* 2008;28:1074–81.
[93] Aoune A, Ramshaw C. Process intensification: heat and mass transfer characteristics of liquid films on rotating discs. *Int J Heat Mass Transf* 1999;42:2543–56.
[94] Datta R, Rinker RG. Penetration theory solution for gas absorption and chemical reaction in cocurrent and countercurrent flow wetted-wall columns. *Can J Chem Eng* 1984;62:78–84.
[95] Kyung I-S, Herold KE. Performance of horizontal smooth tube absorber with and without 2-ethyl-hexanol. *J Heat Transf* 2002;124:177–83.
[96] Bangerth S, Tiwari R, Shooshtari A, Ohadi M. Process intensification in a spinning disk absorber for absorption heat pumps. *Appl Therm Eng* 2019;162:114179.
[97] Pathanjali C, Rahman MM. Numerical simulation of gas absorption to a thin liquid film over a rotating disk in the presence of simultaneous chemical reaction. IECEC 96. Proc. 31st Intersoc. Energy Convers. Eng. Conf., vol. 2, 1996, p. 1055–60.
[98] Goel N. Theoretical and experimental analysis of absorption-condensation in a combined power and cooling cycle. University of Florida; 2005.

[99] Kang YT, Akisawa A, Kashiwagi T. Analytical investigation of two different absorption modes: falling film and bubble types. *Int J Refrig* 2000;23:430–43.
[100] Kim HY, Saha BB, Koyama S. Development of a slug flow absorber working with ammonia-water mixture: part I—flow characterization and experimental investigation. *Int J Refrig* 2003;26:508–15.
[101] Lee J-C, Lee K-B, Chun B-H, Lee CH, Ha JJ, Kim SH. A study on numerical simulations and experiments for mass transfer in bubble mode absorber of ammonia and water. *Int J Refrig* 2003;26:551–8.
[102] Issa M, Ishida K, Monde M. Mass and heat transfers during absorption of ammonia into ammonia water mixture. *Int Commun Heat Mass Transf* 2002;29:773–86.
[103] Kang YT, Nagano T, Kashiwagi T. Visualization of bubble behavior and bubble diameter correlation for NH3--H2O bubble absorption. *Int J Refrig* 2002;25:127–35.
[104] Kang YT, Nagano T, Kashiwagi T. Mass transfer correlation of NH3--H2O bubble absorption. *Int J Refrig* 2002;25:878–86.
[105] Terasaka K, Oka J, Tsuge H. Ammonia absorption from a bubble expanding at a submerged orifice into water. *Chem Eng Sci* 2002;57:3757–65.
[106] Staicovici MD. A non-Equilibrium phenomenological theory of the mass and heat transfer in physical and chemical interactions: Part II—Modeling of the NH3/H2O bubble absorption, analytical study of absorption and experiments. *Int J Heat Mass Transf* 2000;43:4175–88.
[107] Ferreira CAI, Keizer C, Machielsen CHM. Heat and mass transfer in vertical tubular bubble absorbers for ammonia-water absorption refrigeration systems. *Int J Refrig* 1984;7:348–57.
[108] Suresh M, Mani A. Experimental studies on bubble characteristics for R134a--DMF bubble absorber. *Exp Therm Fluid Sci* 2012;39:79–89.
[109] Suresh M, Mani A. Experimental studies on heat and mass transfer characteristics for R134a--DMF bubble absorber. *Int J Refrig* 2012;35:1104–14.
[110] Jiang M, Xu S, Wu X. Experimental investigation for heat and mass transfer characteristics of R124-DMAC bubble absorption in a vertical tubular absorber. *Int J Heat Mass Transf* 2017;108:2198–210.
[111] Jiang M, Xu S, Wu X, Wang W. Heat and mass transfer characteristics of R124-DMAC bubble absorption in a vertical tube absorber. *Exp Therm Fluid Sci* 2017;81:466–74.
[112] Jiang M, Xu S, Wu X, Hu J, Wang W. Visual experimental research on the effect of nozzle orifice structure on R124--DMAC absorption process in a vertical bubble tube. *Int J Refrig* 2016;68:107–17.
[113] Xu S, Jiang M, Hu J, Wu X, Wang W. Visual experimental research on bubble absorption in a vertical tube with R124--DMAC working pair. *Exp Therm Fluid Sci* 2016;74:1–10.
[114] Donnellan P, Cronin K, Lee W, Duggan S, Byrne E. Absorption of steam bubbles in lithium bromide solution. *Chem Eng Sci* 2014;119:10–21.
[115] Isfahani RN, Moghaddam S. Absorption characteristics of lithium bromide (LiBr) solution constrained by superhydrophobic nanofibrous structures. *Int J Heat Mass Transf* 2013;63:82–90.
[116] Ali AHH, Schwerdt P. Characteristics of the membrane utilized in a compact absorber for lithium bromide--water absorption chillers. *Int J Refrig* 2009;32:1886–96.
[117] Ali AHH. Design of a compact absorber with a hydrophobic membrane contactor

at the liquid--vapor interface for lithium bromide--water absorption chillers. *Appl Energy* 2010;87:1112–21.
[118] Isfahani RN, Sampath K, Moghaddam S. Nanofibrous membrane-based absorption refrigeration system. *Int J Refrig* 2013;36:2297–307.
[119] Isfahani RN, Bigham S, Mortazavi M, Wei X, Moghaddam S. Impact of micromixing on performance of a membrane-based absorber. *Energy* 2015;90:997–1004.
[120] Garcia-Hernando N, Venegas M, De Vega M. Experimental performance comparison of three flat sheet membranes operating in an adiabatic microchannel absorber. *Appl Therm Eng* 2019;152:835–43.
[121] Chen Y, Zhang X, Yin Y. Experimental and theoretical analysis of liquid desiccant dehumidification process based on an advanced hybrid air-conditioning system. *Appl Therm Eng* 2016;98:387–99.
[122] Lazzarin RM, Gasparella A, Longo GA. Chemical dehumidification by liquid desiccants: theory and experiment. *Int J Refrig* 1999;22:334–47.
[123] Jain S, Dhar PL, Kaushik SC. Experimental studies on the dehumidifier and regenerator of a liquid desiccant cooling system. *Appl Therm Eng* 2000;20:253–67.
[124] Longo GA, Gasparella A. Experimental and theoretical analysis of heat and mass transfer in a packed column dehumidifier/regenerator with liquid desiccant. *Int J Heat Mass Transf* 2005;48:5240–54.
[125] Zhang L, Hihara E, Matsuoka F, Dang C. Experimental analysis of mass transfer in adiabatic structured packing dehumidifier/regenerator with liquid desiccant. *Int J Heat Mass Transf* 2010;53:2856–63.
[126] Huang S-M, Yang M, Yang X. Performance analysis of a quasi-counter flow parallel-plate membrane contactor used for liquid desiccant air dehumidification. *Appl Therm Eng* 2014;63:323–32.
[127] Moghaddam DG, LePoudre P, Ge G, Besant RW, Simonson CJ. Small-scale single-panel liquid-to-air membrane energy exchanger (LAMEE) test facility development, commissioning and evaluating the steady-state performance. *Energy Build* 2013;66:424–36.
[128] Bai H, Zhu J, Chen Z, Ma L, Wang R, Li T. Performance testing of a cross-flow membrane-based liquid desiccant dehumidification system. *Appl Therm Eng* 2017;119:119–31.
[129] Chen Z, Zhu J, Bai H, Yan Y, Zhang L. Experimental study of a membrane-based dehumidification cooling system. *Appl Therm Eng* 2017;115:1315–21.
[130] Datta SS, Abbaspourrad A, Amstad E, Fan J, Kim S-H, Romanowsky M, et al. 25th anniversary article: Double emulsion templated solid microcapsules: Mechanics and controlled release. *Adv Mater* 2014;26:2205–18.
[131] Askalany A, Olkis C, Bramanti E, Lapshin D, Calabrese L, Proverbio E, et al. Silica-supported ionic liquids for heat-powered sorption desalination. *ACS Appl Mater Interfaces* 2019;11:36497–505.
[132] Iqbal P, Lu T, Zhang Z, Li Y. Preparation of multilayer microcapsules encapsulating aqueous lithium bromide and their mechanical stability. *Ind Eng Chem Res* 2019;58:6364–74.
[133] Vericella JJ, Baker SE, Stolaroff JK, Duoss EB, Hardin JO, Lewicki J, et al. Encapsulated liquid sorbents for carbon dioxide capture. *Nat Commun* 2015;6:1–7.
[134] Shah RK, Shum HC, Rowat AC, Lee D, Agresti JJ, Utada AS, et al. Designer emulsions using microfluidics. *Mater Today* 2008;11:18–27.

[135] Piccin E, Ferraro D, Sartori P, Chiarello E, Pierno M, Mistura G. Generation of water-in-oil and oil-in-water microdroplets in polyester-toner microfluidic devices. *Sensors Actuators B Chem* 2014;196:525–31.
[136] Liao Q, Li S, Chen R, Wang H, Zhu X, Zhang W, et al. Coalescence with droplets caused acceleration of the liquid movement in microchannels. *Ind Eng Chem Res* 2015;54:1161–9.
[137] Glawdel T, Ren CL. Global network design for robust operation of microfluidic droplet generators with pressure-driven flow. *Microfluid Nanofluidics* 2012;13:469–80.
[138] Hong Y, Wang F. Flow rate effect on droplet control in a co-flowing microfluidic device. *Microfluid Nanofluidics* 2007;3:341–6.
[139] Cramer C, Fischer P, Windhab EJ. Drop formation in a co-flowing ambient fluid. *Chem Eng Sci* 2004;59:3045–58.
[140] Zhu P, Tang X, Wang L. Droplet generation in co-flow microfluidic channels with vibration. *Microfluid Nanofluidics* 2016;20:47.
[141] Glawdel T, Elbuken C, Ren CL. Droplet generation in microfluidics. *Encycl Microfluid Nanofluidics* 2013:1–12.
[142] Anna SL, Bontoux N, Stone HA. Formation of dispersions using "flow focusing" in microchannels. *Appl Phys Lett* 2003;82:364–6.
[143] Ganán-Calvo AM, Gordillo JM. Perfectly monodisperse microbubbling by capillary flow focusing. *Phys Rev Lett* 2001;87:274501.
[144] Utada AS, Lorenceau E, Link DR, Kaplan PD, Stone HA, Weitz DA. Monodisperse double emulsions generated from a microcapillary device. *Science (80-)* 2005;308:537–41.
[145] Barbier V, Tatoulian M, Li H, Arefi-Khonsari F, Ajdari A, Tabeling P. Stable modification of PDMS surface properties by plasma polymerization: application to the formation of double emulsions in microfluidic systems. *Langmuir* 2006;22:5230–2.
[146] Okushima S, Nisisako T, Torii T, Higuchi T. Controlled production of monodisperse double emulsions by two-step droplet breakup in microfluidic devices. *Langmuir* 2004;20:9905–8.
[147] Zhao C-X. Multiphase flow microfluidics for the production of single or multiple emulsions for drug delivery. *Adv Drug Deliv Rev* 2013;65:1420–46.
[148] Utada AS, Chu L-Y, Fernandez-Nieves A, Link DR, Holtze C, Weitz DA. Dripping, jetting, drops, and wetting: The magic of microfluidics. *Mrs Bull* 2007;32:702–8.
[149] Stolaroff JK, Ye C, Oakdale JS, Baker SE, Smith WL, Nguyen DT, et al. Microencapsulation of advanced solvents for carbon capture. *Faraday Discuss* 2016;192:271–81.
[150] Martino C, Berger S, Wootton RCR, deMello AJ. A 3D-printed microcapillary assembly for facile double emulsion generation. *Lab Chip* 2014;14:4178–82.
[151] Drake RM, Backer GH. Heat transfer from spheres to a rarefied gas in supersonic flow. *Trans ASME* 1952;74:1241–9.
[152] Yuge T. Experiments on heat transfer from spheres including combined natural and forced convection. *J Heat Transf* 1960;82.
[153] Raithby GD, Eckert ERG. The effect of turbulence parameters and support position on the heat transfer from spheres. *Int J Heat Mass Transf* 1968;11:1233–52.
[154] Whitaker S. Forced convection heat transfer correlations for flow in pipes, past flat plates, single cylinders, single spheres, and for flow in packed beds and tube

bundles. *AIChE J* 1972;18:361–71.
[155] Vliet GC, Leppert G. Forced convection heat transfer from an isothermal sphere to water 1961.
[156] Kramers H. Heat transfer from spheres to flowing media. *Physica* 1946;12:61–80.
[157] Will JB, Kruyt NP, Venner CH. An experimental study of forced convective heat transfer from smooth, solid spheres. *Int J Heat Mass Transf* 2017;109:1059–67.
[158] Lee K, Barrow H. Transport processes in flow around a sphere with particular reference to the transfer of mass. *Int J Heat Mass Transf* 1968;11:1013–26.
[159] Garner FH, Keey RB. Mass-transfer from single solid spheres—I: Transfer at low Reynolds numbers. *Chem Eng Sci* 1958;9:119–29.
[160] Frössling N. The Evaporation of Falling Drops. *Gerlands Beitr Geophys* 1938;52:170–216.
[161] Linton M, Sutherland KL. Transfer from a sphere into a fluid in laminar flow. *Chem Eng Sci* 1960;12:214–29.
[162] Hsu C-J. Heat transfer to liquid metals flowing past spheres and elliptical-rod bundles. *Int J Heat Mass Transf* 1965;8:303–15.
[163] Sideman S. The equivalence of the penetration and potential flow theories. *Ind \& Eng Chem* 1966;58:54–8.
[164] Johnstone HF, Pigford RL, Chapin JH. Heat transfer to clouds of falling particles. 1941.
[165] Dennis SCR, Walker JDA, Hudson JD. Heat transfer from a sphere at low Reynolds numbers. *J Fluid Mech* 1973;60:273–83.
[166] Ahmed GR, Yovanovich MM. Approximate analytical solution of forced convection heat transfer from isothermal spheres for all Prandtl numbers 1994.
[167] Yovanovich M. General expression for forced convection heat and mass transfer fromisopotential spheroids. 26th Aerosp. Sci. Meet., 1988, p. 743.
[168] Ahmed GR, Yovanovich MM, Culham JR. Experimental and approximate analytical modeling of forced convection from isothermal spheres. *J Thermophys Heat Transf* 1997;11:223–31.
[169] Happel J, Brenner H. Low Reynolds number hydrodynamics: with special applications to particulate media. vol. 1. Springer Science \& Business Media; 2012.
[170] Hadad Y, Jafarpur K. Laminar forced convection heat transfer from isothermal bodies with unity aspect ratio in coaxial air flow. *Heat Transf Eng* 2012;33:245–54.
[171] Baptista PN, Oliveira FAR, Oliveira JC, Sastry SK. Dimensionless analysis of fluid-to-particle heat transfer coefficients. *J Food Eng* 1997;31:199–218.
[172] Ozisik MN. Heat conduction. John Wiley & Sons; 1993.
[173] Shevchuk I V. Turbulent heat and mass transfer over a rotating disk for the Prandtl or Schmidt numbers much larger than unity: an integral method. *Heat Mass Transf* 2009;45:1313–21.
[174] Shevchuk I V. A new evaluation method for Nusselt numbers in naphthalene sublimation experiments in rotating-disk systems. *Heat Mass Transf* 2008;44:1409–15.
[175] Shevchuk I V. Modelling of convective heat and mass transfer in rotating flows. Springer; 2016.
[176] Churchill SW. A comprehensive correlating equation for laminar, assisting, forced and free convection. *AIChE J* 1977;23:10–6.
[177] Clift R, Grace JR, Weber ME. Bubbles, drops, and particles 2005.

[178] Witte LC. An experimental study of forced-convection heat transfer from a sphere to liquid sodium 1968.
[179] Kline SJ. Describing uncertainty in single sample experiments. *Mech Eng* 1953;75:3–8.
[180] Chiang Y-C, Chen C-H, Chiang Y-C, Chen S-L. Circulating inclined fluidized beds with application for desiccant dehumidification systems. *Appl Energy* 2016;175:199–211.
[181] Narayanan R, Saman WY, White SD, Goldsworthy M. Comparative study of different desiccant wheel designs. *Appl Therm Eng* 2011;31:1613–20.
[182] De Antonellis S, Joppolo CM, Molinaroli L. Simulation, performance analysis and optimization of desiccant wheels. *Energy Build* 2010;42:1386–93.
[183] Zhang XJ, Dai YJ, Wang RZ. A simulation study of heat and mass transfer in a honeycombed rotary desiccant dehumidifier. *Appl Therm Eng* 2003;23:989–1003.
[184] Bergman TL, Bergman TL, Incropera FP, Dewitt DP, Lavine AS. Fundamentals of heat and mass transfer. John Wiley & Sons; 2011.
[185] Moran MJ, Shapiro HN, Boettner DD, Bailey MB. Fundamentals of engineering thermodynamics. John Wiley & Sons; 2010.
[186] MathWorks MATLAB software, https://www.mathworks.com 2020.
[187] OASIS optimization software, www.empowerops.com 2022.
[188] Ong KS, Tan CF, Lai KC, Tan KH. Heat spreading and heat transfer coefficient with fin heat sink. *Appl Therm Eng* 2017;112:1638–47.
[189] Hao X, Peng B, Chen Y, Xie G. Transient thermal model of a permanent magnet synchronous planar motor considering spreading thermal resistance. *Appl Therm Eng* 2015;81:1–9.
[190] Okereke MI, Ling Y. A computational investigation of the effect of three-dimensional void morphology on the thermal resistance of solder thermal interface materials. *Appl Therm Eng* 2018;142:346–60.
[191] Wang M, Cui W, Hou Y. Thermal spreading resistance of grooved vapor chamber heat spreader. *Appl Therm Eng* 2019;153:361–8.
[192] Yang K-S, Chung C-H, Tu C-W, Wong C-C, Yang T-Y, Lee M-T. Thermal spreading resistance characteristics of a high power light emitting diode module. *Appl Therm Eng* 2014;70:361–8.
[193] Chen D-L, Chen T-C, Yang P-F, Lai Y-S. Thermal resistance of side by side multi-chip package: Thermal mode analysis. *Microelectron Reliab* 2015;55:822–31.
[194] Jaworski M. Thermal performance of heat spreader for electronics cooling with incorporated phase change material. *Appl Therm Eng* 2012;35:212–9.
[195] Luzi CD, Keegan SD, Mariani NJ, Barreto GF. Evaluation of the spreading thermal resistance for rough spheres. *Int J Heat Mass Transf* 2015;86:826–31.
[196] Kennedy DP. Spreading resistance in cylindrical semiconductor devices. *J Appl Phys* 1960;31:1490–7.
[197] Muzychka YS, Culham JR, Yovanovich MM. Thermal spreading resistance of eccentric heat sources on rectangular flux channels. *J Electron Packag* 2003;125:178–85.
[198] Yovanovich MM, Muzychka YS, Culham JR. Spreading resistance of isoflux rectangles and strips on compound flux channels. *J Thermophys Heat Transf* 1999;13:495–500.
[199] Feng TQ, Xu JL. An analytical solution of thermal resistance of cubic heat spreaders for electronic cooling. *Appl Therm Eng* 2004;24:323–37.

[200] Yovanovich MM. Thermal resistances of circular source on finite circular cylinder with side and end cooling. *J Electron Packag* 2003;125:169–77.
[201] Yovanovich M, Schneider G, Tien C. Thermal resistance of hollow spheres subjected to arbitrary flux over their poles. 2nd Thermophys. Heat Transf. Conf., 1978, p. 872.
[202] Rahmani Y, Ganji DD, Bandpy MG. Analytical study of thermal spreading resistance in curved-edge heat spreader. *Appl Therm Eng* 2016;104:527–33.
[203] Huang M-J, Shaw Y-R, Chien H-C. Thermal spreading resistance of heat sources on rectangular flux channel under non-uniform convective cooling. *Int J Therm Sci* 2019;145:105979.
[204] Hsieh S-S, Lee R-Y, Shyu J-C, Chen S-W. Analytical solution of thermal resistance of vapor chamber heat sink with and without pillar. *Energy Convers Manag* 2007;48:2708–17.
[205] Muzychka YS, Yovanovich MM, Culham JR. Thermal spreading resistance in compound and orthotropic systems. *J Thermophys Heat Transf* 2004;18:45–51.
[206] Yovanovich MM, Culham JR, Teertstra P. Analytical modeling of spreading resistance in flux tubes, half spaces, and compound disks. *IEEE Trans Components, Packag Manuf Technol Part A* 1998;21:168–76.
[207] Razavi SM. Advanced thermal analysis of microelectronics using spreading resistance models. Memorial University of Newfoundland, 2016.
[208] Delouei AA, Emamian A, Karimnejad S, Sajjadi H, Jing D. Two-dimensional analytical solution for temperature distribution in FG hollow spheres: General thermal boundary conditions. *Int Commun Heat Mass Transf* 2020;113:104531.
[209] Ã-zisik MN, Özicsik MN, Özisik MN. Heat conduction. John Wiley & Sons; 1993.
[210] Bejan A, Kraus AD. Heat transfer handbook. vol. 1. John Wiley & Sons; 2003.
[211] multiphysics software v5.4 C. Comsol multiphysics software v5.4 2018.

Appendix A: Thermogravimetric Vapor Analyzer (TGA) Data

Table A1: TGA data of the microcapsules during the sorption cycle at 30 ºC.

Relative water vapor pressure, -	Water uptake, g/g
5.85E-5	0
3.13E-5	0.11706
0.0488	0.29564
0.0985	0.3373
0.148	0.38895
0.197	0.4313
0.246	0.47063
0.295	0.50838
0.344	0.54539
0.393	0.58266
0.443	0.6227
0.492	0.6652
0.54	0.71009
0.589	0.76056
0.639	0.81783
0.688	0.88138
0.737	0.95258
0.786	1.03666
0.836	1.14004
0.885	1.25535

Table A2: TGA data of the microcapsules during the desorption cycle at 30 ºC.

Relative water vapor pressure, -	Water uptake, g/g
3.13E-5	0.11706
0.049	0.30437
0.098	0.37749
0.147	0.4283
0.196	0.46935
0.246	0.50709
0.295	0.54284
0.344	0.57761
0.393	0.61485
0.443	0.6538
0.491	0.69375
0.541	0.73809
0.59	0.78845
0.639	0.8422
0.688	0.90381
0.738	0.97404
0.786	1.05483
0.836	1.14849
0.885	1.25535

Table A3: TGA data of the microcapsules during sorption at 30 ºC.

Relative water vapor pressure, -	Water uptake, g/g
-3.42E-4	1.15547
0.0643	1.20692
0.131	1.3519
0.196	1.3654
0.261	1.37958
0.326	1.36033
0.392	1.55275
0.457	1.56488
0.523	1.57614
0.588	1.6495
0.653	1.71112
0.718	1.75512
0.784	1.81855
0.849	2.03786

Appendix B: Thermal Spreading Resistance of a Hollow Hemisphere with Internal Convective Cooling

One of the possible absorber designs that can be considered to utilize the microreactors is illustrated in **Fig. B1** in which a metal heat exchanger can be used to pack the microcapsules, and a heat transfer fluid can be used to heat/cool the microreactors during the regeneration/dehumidification processes. For example, in the regeneration process, the heat will be transferred from the hot fluid to the metal fins, and then to the spherical microreactors. The small heat transfer area due to the point-contact between the capsule and the heat exchanger might present a limitation on the heat transfer mechanism. Therefore, it is of great importance to be able to estimate the thermal spreading resistance through a spherical particle.

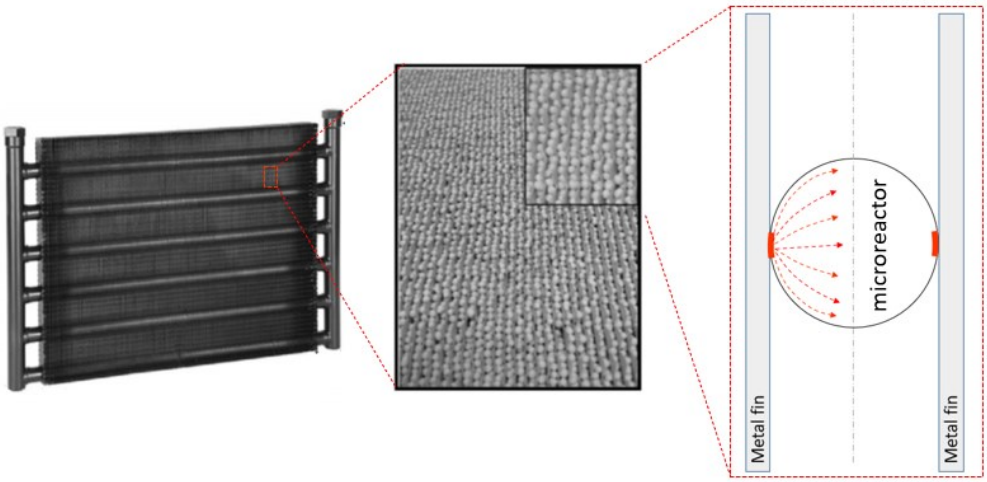

Fig. B1: Conduction heat transfer in packed heat exchanger.

B.1. Abstract

The 2D steady-state heat transfer in a hollow hemisphere subjected to an arbitrary heat flux applied on its poles, and convective cooling (or heating) at the inner surface, is studied analytically. Closed-form mathematical expressions for temperature distribution and non-dimensional thermal resistance as a function of radii ratio, contact angle, and the Biot number, are derived and presented for two cases that simulate the flux distribution from isoflux and isothermal heat sources. The analytical solution is verified by using a finite-element numerical solution, developed in a commercially-available software, and comparing the results. Moreover, it is demonstrated that the present fundamental analysis provides a general solution for other problems found in the literature, including spreading resistance in hollow spheres with insulated walls, as well as the heat source on a half-space and infinite disk with an isothermal end.

B.2. Introduction

In many applications, the estimation of thermal resistance plays a vital role in ensuring the proper design and operation of engineered devices. Mathematical expressions for thermal resistance are available in the literature for basic shapes in cartesian, cylindrical, and spherical coordinates. However, the problem of determining the spreading thermal resistance that occurs whenever heat leaves the heat source to a larger region cannot be evaluated by simple 1-D analytical models. This problem is encountered in different design areas, including heat sinks, cooling applications [188–194], and granular packed beds [195]. Exact solutions from analytical models are more favorable than approximate solutions from computational methods, as they offer compact expressions that can be easily and quickly evaluated. For this reason, there is notable interest in developing analytical, closed-form models to estimate thermal spreading resistance. Kennedy [196] investigated the heat conduction in semiconductor devices by considering the heat transfer within a homogeneous, finite, solid cylinder from a circular source fixed at one of its ends. Different combinations of boundary conditions at the other surfaces in the domain were considered, and equations that describe the spreading resistance and temperature distribution were presented graphically. Muzychka et al. [197] used the separation of variables method to provide a general solution for thermal spreading resistance of an eccentric heat source on a rectangular flux channel. It was shown that the presented solution can be used for single and multiple discrete heat sources on isotropic and compound flux channels by using superposition. Yovanovich et al. [198] presented a closed-form solution for the non-dimensional thermal resistance of a rectangular isoflux heat source on a compound two-layer body with convective or conductive cooling at one boundary. Using the Fourier expansion method, Feng and Xu [199] developed a three-dimensional analytical model to determine the resistance of a rectangular isoflux source fixed on the top of cubic heat spreaders used in electronic cooling. Yovanovich [200] developed a general model for spreading/constriction resistance for a circular source on a finite circular cylinder with side and end cooling. The validity of the model for special cases was discussed. Yovanovich et al. [201] presented an analytical solution to estimate the thermal resistance of hollow spheres subjected to heat flux on a finite area at their poles, with the spheres assumed to be insulated from the inner surface. The authors [201]compared their results with a half-space and two-zone models. Using the Maxwell coordinate system, Rahmani et al. [202] developed a model for spreading resistance in a curved-edge heat spreader. Huang et al. [203] presented a general solution for spreading resistance of multiple heat sources on a rectangular flux channel under non-uniform convective cooling. Using the separation of variables method, Hsieh et al. [204] presented a 3D analytical solution for the spreading resistance of centrally-positioned heat sources of a vapor chamber heat sink. Analytical solutions for spreading resistance in compound and orthotropic systems, with and without cooling, have been reviewed by Muzychka et al. [205] for cylindrical and rectangular geometries. Yovanovich et al. [206] also reviewed

analytical models to calculate thermal spreading resistance for compound disks, heat flux tubes and infinite layers in perfect contact with half-space. Razavi [207] presented a series of analytical solutions of the thermal spreading resistance for circular flux tubes and rectangular flux channels. Different boundary conditions were considered along the walls, source plane, and sink plane. The author [207] investigated the effect of the size of the heat source, thickness of the channels, and Biot number on the thermal resistance. Recently, Delouei et al. [208] investigated the steady-state heat conduction in thick hollow spheres by presenting an analytical solution that covers two boundary conditions, namely, variable heat flux and variable temperature.

One geometry that has not been investigated in the literature, is the thermal spreading resistance of a hollow hemi-sphere subjected to a heat flux on its pole and convective cooling at the inner surface. This problem becomes important, for example, in petroleum and cryogenic industries when heat leaks through the storage tanks to the stored fluids. These tanks often have a spherical shape to provide even distribution of stresses on the surfaces, and they are well-insulated. Heat may leak through spots with imperfect insulation, and that results in elevated temperatures and pressure, and in extreme cases, possible explosions. As the stored fluid inside the tank absorbs heat, natural convection inside the tank will occur. The aim of this study is to develop an analytical closed-form solution to determine the thermal spreading resistance for arbitrary isoflux and isothermal heat sources in a hollow hemi-sphere with convective heat transfer from the inner surface, and the associated temperature distribution.

B.3. Mathematical Modeling

Consider an insulated hollow hemi-sphere subjected to arbitrary heat flux from a heat source on a finite area at the outer radius with 2α contact angle, and convective cooling at the inner surface, as shown in **Fig. B2**. The 2D steady-state governing energy equation in the spherical coordinates is:

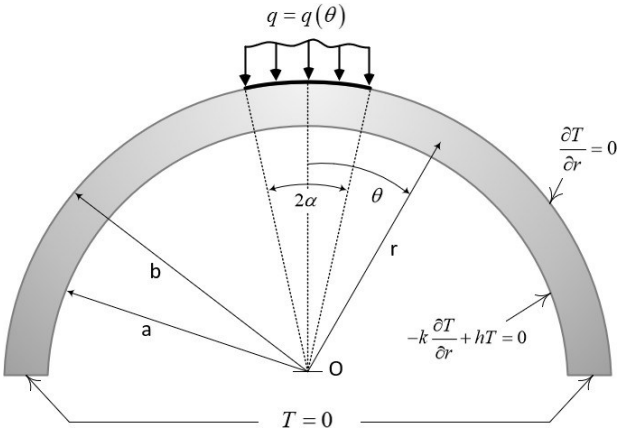

Fig. B2: A model for an insulated hollow hemi-sphere subjected to an arbitrary general heat flux on its pole, and convective cooling at the inner surface.

$$\frac{1}{r^2}\frac{\partial}{\partial r}\left(r^2\frac{\partial T}{\partial r}\right)+\frac{1}{r^2\sin(\theta)}\frac{\partial}{\partial\theta}\left(\sin(\theta)\frac{\partial T}{\partial\theta}\right)=0 \quad \text{B.1}$$

where, r and θ are spherical coordinates. Introducing new independent variable $\mu = \cos(\theta)$, the above equation can be written:

$$\frac{1}{r^2}\frac{\partial}{\partial r}\left(r^2\frac{\partial T}{\partial r}\right)+\frac{1}{r^2}\frac{\partial}{\partial\mu}\left[\left(1-\mu^2\right)\frac{\partial T}{\partial\mu}\right]=0 \quad \text{B.2}$$

Assuming isothermal conditions that are far away from the source contact area, the boundary conditions for the equivalent analytical model depicted in **Fig. B2** are:

$$\mu=0,\ a\leqslant r\leqslant b,\ T=0 \quad \text{B.3}$$

$$r=a,\ 0\leqslant\mu\leqslant 1,\ -k\frac{\partial T}{\partial r}+\frac{h}{k}T=0 \quad \text{B.4}$$

$$r=b,\ \frac{\partial T}{\partial r}=\begin{cases}0\leqslant\mu\leqslant\cos(\alpha), & \dfrac{q(\mu)}{k}\\ \cos(\alpha)\leqslant\mu\leqslant 1, & 0\end{cases} \quad \text{B.5}$$

Using the separation of variables, the general form of temperature distribution is assumed to be as follows:

$$T(r,\mu)=J(r)\cdot M(\mu) \quad \text{B.6}$$

where:

$$J(r)=\sum_{n}^{\infty}\left[C_{1n}r^n+C_{2n}r^{-(n+1)}\right] \quad \text{B.7}$$

$$M(\mu)=D_{1n}P_n(\mu)+D_{2n}Q_n(\mu) \quad \text{B.8}$$

The Legendre polynomials of the second kind $Q_n(\mu)$ become infinite at $\mu = \pm 1$, therefore, they are excluded from the solution on the physical grounds. Because of the boundary condition of the first kind at $\mu=0$ (Eq. (B.3)), Legendre polynomials of even degree must be excluded, and only polynomials with odd degree should be considered (n = 1, 3, 5, ...) [209]. Accordingly, the solution can be given as:

$$T(r,\mu)=\sum_{n,odd}^{\infty}\left[A_nr^n+B_nr^{-(n+1)}\right]P_n(\mu) \quad \text{B.9}$$

Applying the second boundary condition (Eq. (B.4)) in Eq. (B.9) gives:

$$B_n = \frac{na^{(n-1)} - \frac{h}{k}a^n}{(n+1)a^{-(n+2)} + \frac{h}{k}a^{-(n+1)}} A_n \qquad \text{B.10}$$

By defining the radii ratio $\varepsilon = a/b$, the coefficient $\varphi_n = B_n/A_n$, and introducing the non-dimensional Biot number $Bi = ha/k$, Eq. (B.9) becomes:

$$T(r,\mu) = \sum_{n,odd}^{\infty} A_n \left[r^n + \phi_n r^{-(n+1)} \right] P_n(\mu) \qquad \text{B.11}$$

where:

$$\phi_n = b^{2n+1}\varepsilon^{2n+1}\mathrm{Y}_n \qquad \text{B.12}$$

$$\mathrm{Y}_n = \frac{n - Bi}{(n+1) + Bi} \qquad \text{B.13}$$

To find the coefficient A_n, we apply the third boundary condition by substituting Eq. (B.5) in Eq. (B.11):

$$\frac{q(\mu)}{k} = \sum_{n,odd}^{\infty} A_n \left[nb^{n-1} - (n+1)\phi_n b^{-(n+2)} \right] P_n(\mu) \qquad \text{B.14}$$

Utilizing the orthogonality property of Legendre function, the following equation can be obtained:

$$\int_0^1 \frac{q(\mu)}{k} P_n(\mu)\, d\mu = \sum_{n,odd}^{\infty} A_n \left[nb^{n-1} - (n+1)\phi_n b^{-(n+2)} \right] \int_0^1 P_n^2(\mu) d\mu \qquad \text{B.15}$$

Recalling that $q(\mu) = 0$ in $0 \leqslant \mu \leqslant \cos(\alpha)$ range , and that $\int_0^1 P_n^2(\mu) d\mu = \frac{1}{2n+1}$ [209] , the coefficient A_n is determined as:

$$A_n = \frac{b^{(1-n)}}{k} \frac{(2n+1)}{\left[n - (n+1)\varepsilon^{2n+1}\mathrm{Y}_n \right]} \int_{\cos(\alpha)}^1 q(\mu) P_n(\mu) d\mu \qquad \text{B.16}$$

After substituting Eq. (B.12) and Eq. (B.16) in Eq. (B.11), the expression for the temperature distribution can be written in the following form:

$$T(r,\mu) = \frac{b}{k} \sum_{n,odd}^{\infty} \frac{2n+1}{\left[n - (n+1)\varepsilon^{2n+1}\mathrm{Y}_n \right]} \times \int_{\cos(\alpha)}^1 q(\mu) P_n(\mu) d\mu \times \left[\left(\frac{r}{b} \right)^n + \varepsilon^{2n+1}\mathrm{Y}_n \left(\frac{r}{b} \right)^{-(n+1)} \right] P_n(\mu) \qquad \text{B.17}$$

The thermal resistance can be defined as:

$$R = \frac{\bar{T}_{\text{source}} - \bar{T}_{\text{sink}}}{Q} \tag{B.18}$$

where, T_{source} and T_{sink} are the source and sink average temperatures, respectively. Here, we take T_{sink} as the bulk temperature of the fluid inside the hemi-sphere. For convenience, this temperature is taken as $T_{sink} = 0$. The source average temperature can be determined by:

$$\bar{T}_{\text{source}} = \frac{1}{A_c}\iint_{A_c} T(b,\mu)\, dA_c \tag{B.19}$$

The elemental contact area for the heat flux:

$$dA_c = 2\pi b^2 \sin(\theta)\, d\theta = 2\pi b^2 d\mu \tag{B.20}$$

The total contact area, therefore, is:

$$A_c = 2\pi b^2 \left[1 - \cos(\alpha)\right] \tag{B.21}$$

Eq. (B.19) can be written as:

$$\bar{T}_{\text{source}} = \frac{1}{\left[1 - \cos(\alpha)\right]}\int_{\cos(\alpha)}^{1} T(b,\mu)\, d\mu \tag{B.22}$$

The total heat flux is determined by:

$$Q = \iint_{A_c} q(\theta)\, dA_c = 2\pi b^2 \int_{\cos(\alpha)}^{1} q(\mu)\, d\mu \tag{B.23}$$

Substituting Eqs. (B.22) and (B.23) in Eq. (B.18):

$$R = \frac{1}{2\pi bk\left[1 - \cos(\alpha)\right]\int_{\cos(\alpha)}^{1} q(\mu)\, d\mu} \sum_{n,odd}^{\infty} \frac{(2n+1)\left(1 + \varepsilon^{2n+1} Y_n\right)}{\left[n - (n+1)\varepsilon^{2n+1} Y_n\right]} \tag{B.24}$$

$$\times \int_{\cos(\alpha)}^{1} q(\mu) P_n(\mu)\, d\mu \times \int_{\cos(\alpha)}^{1} P_n(\mu) d\mu$$

Taking the chord, $c = b \sin(\alpha)$, as a characteristic length, a non-dimensional thermal resistance can be defined as:

$$R^* = kcR \tag{B.25}$$

B.3.1. Special cases

The present analysis can be considered as a general solution for different problems found in the literature. These special cases will be discussed in the following sections. To extend the present analysis, we consider the cases with an isothermal heat source. However, this will result in a mixed boundary condition at the outer radius (see **Fig. B2** and Eq. (B.5)) and the problem will be difficult to solve in this form. To solve this, Yovanovich et al. [201] presented a general form for contact-area flux distribution:

$$q(\mu) = q_0 \left[\mu - \cos(\alpha)\right]^{\nu} \tag{B.26}$$

where, q_0 is a convenient heat flux level. In the above expressions, the case when $\nu = 0$ results in a uniform heat flux, while $\nu = -1/2$ gives a flux distribution that has its minimum at the center of the contact area, the latter has the same form as a flux distribution over an isothermal circular contact situated on the surface of an isolated half-space. This flux distribution can be taken as a good approximation for the mixed boundary condition in the spherical coordinates. When considering the isothermal source condition, it is useful to define a non-dimensional contact angle as $\vartheta = 2\alpha/\pi$.

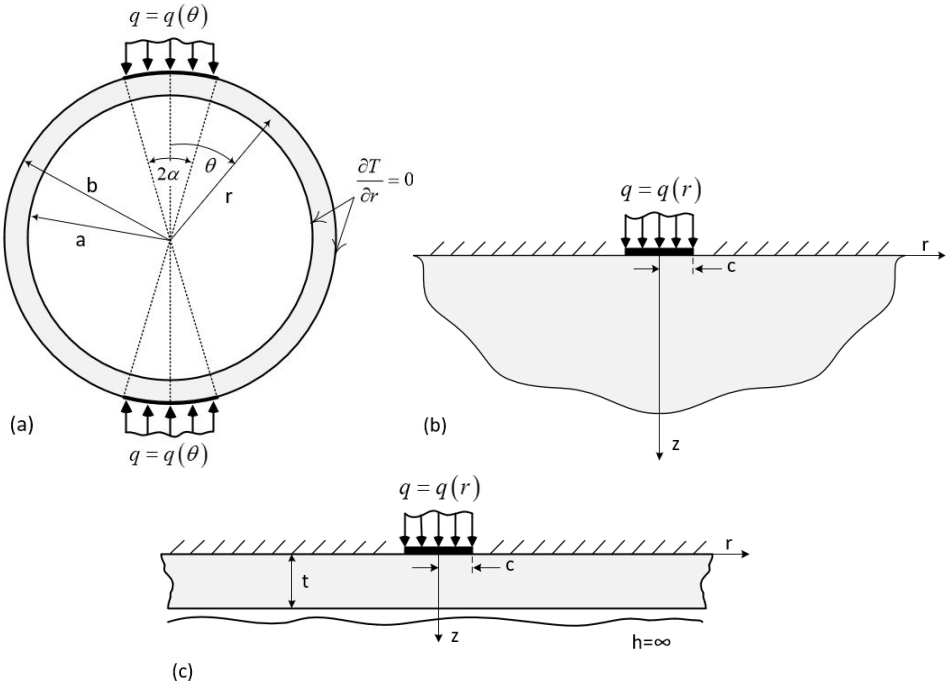

Fig. B3: Special cases: (a) A hollow sphere subjected to heat flux; (b) the spreading resistance in half-space (circular source); and (c) an isothermal circular source on a thin infinite disk.

B.3.1.1. Thermal Resistance of a Hollow Sphere

As mentioned in Section B.2, the work done by Yovanovich et al. [201] considered the thermal resistance of a full sphere subjected to an arbitrary flux over its poles with no heat transfer from the inner surface (insulated). For the case when the convective heat transfer coefficient h → 0 in Eq. (B.4), the generalized analysis presented herein can be used to provide a solution for the problem investigated by Yovanovich et al. [201], as illustrated in **Fig. B3a**. The non-dimensional thermal resistance of sphere is twice of that expressed by Eq. (B.25) ($R^* = 2kcR$).

B.3.1.2. Spreading Resistances in Half-Space

When the non-dimensional contact angle approaches zero, $\vartheta \to 0$ (corresponds to $c \to 0$), and $\varepsilon \to 0$, this case can be considered to be a good approximation for the thermal spreading resistance of a circular source, with a radius c, in a half-space (**Fig. B3b**). The spreading resistance in a half-space is taken as that defined by Eq. (B.25), $R^* = 2kcR$ [210].

B.3.1.3. Spreading Resistance of Isothermal Circular Source on a Thin Infinite Disk

The present model can also be used to estimate the thermal spreading resistance of a circular source, with a radius c, on a thin infinite disk that has t thickness (see **Fig. B3c**). This can be realized when $\vartheta \to 0$ and $h \to \infty$, and setting $v = -1/2$ in Eq. (B.26) to simulate the isothermal source condition. The definition of the resistance for this special case is $R^* = 4kcR$, as suggested by Yovanovich [200]. This resistance is a function of the relative disk thickness $\chi = t/c$. For the hemi-spherical geometry illustrated by **Fig. B3c**, it can be defined as $\chi = (b - a)/c = (1 - \varepsilon)/\sin(\alpha)$.

B.4. Results and Discussion

B.4.1. Hollow Hemi-Sphere

To evaluate the expressions for the temperature distribution and dimensionless thermal resistance, a computer code was written, and the solution was obtained using MATLAB software. As there is no available experimental data in the open literature to verify the analytical model and the code, the problem was solved by following a strict computational (finite-element) modeling approach using the COMSOL Multiphysics software package v5.4 (finite-element numerical method) [211]. A 3D hemi-sphere was modeled with boundary conditions, with extremely fine mesh (to avoid any uncertainties associated with mesh dependency), and a steady-state heat transfer study

was conducted by applying a constant and uniform heat flux ($\nu = 0$) at the pole, and a convective heat flux at the inner surface. The temperature distribution, normalized by the maximum temperature (at $\theta = 0$), from the analytical and numerical models is presented in **Fig. B4** for different half-contact angle values (α = 1°, 5°, 10°, and 15°). It is clear from **Fig. B4**, that the results from the 2D steady-state analytical model are in very good agreement with the 3D numerical solution.

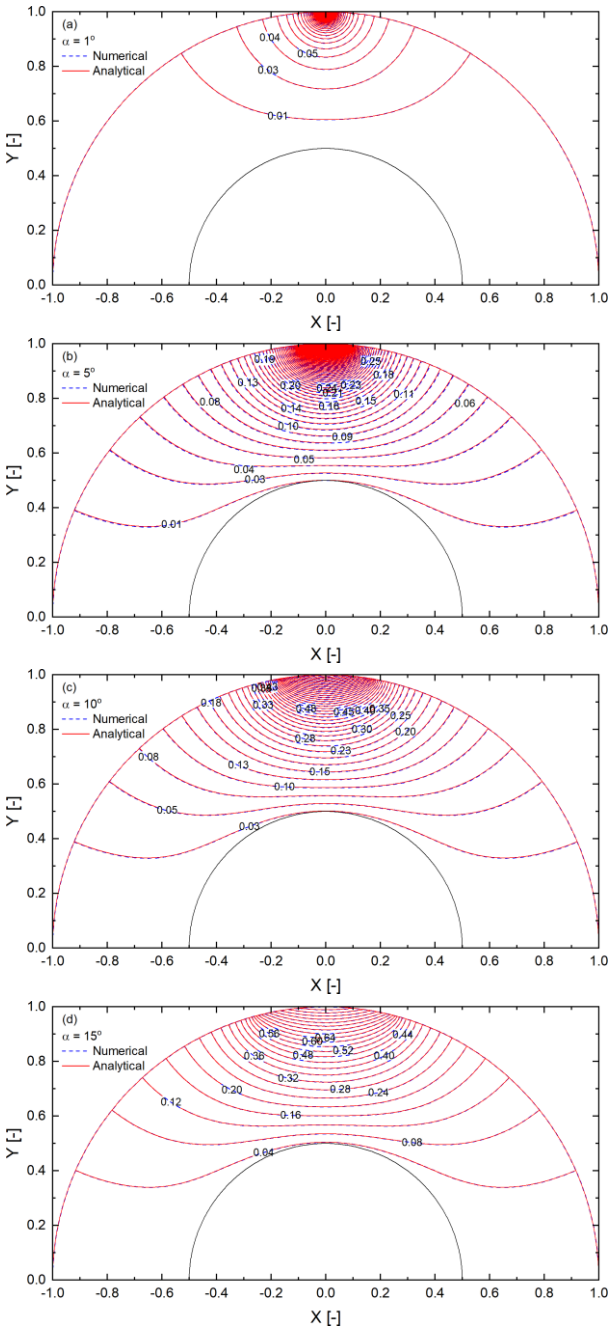

Fig. B4: The normalized temperature distribution (T/T_{max}) from the 2D analytical and 3D numerical models for: (a) α =1°; (b) 5°; (c) 10°; and (d) 15°. For all cases, $\varepsilon = 0.5$, $Bi = 20$, $\nu = 0$.

Fig. B5 depicts the variation of the non-dimensional thermal resistance with respect to ε and *Bi*, for different α values. Results shown in **Fig. B5a** to **Fig. B5d** indicate that, for low values of *Bi* (≤ 1), the thermal resistance increases rapidly with the increase in ε. This is because the inner wall of the hemi-sphere acts as an adiabatic surface $\left.\frac{\partial T}{\partial r}\right|_{r=a} \to 0$, and heat has to be spread through a restricted path in the angular direction of a thin wall (large values of ε). On the other hand, when *Bi* values are high enough (≥ 10), thinner walls facilitate the spreading of the heat to the inner surface, resulting in lower thermal resistances. It can also be observed that, for very small values of ε (≤ 0.2), i.e., thin spherical shells, the thermal resistance curves converge to a single value of 0.27–0.30 when α is within a 1–15° range. It is worth noting that it might be misleading to conclude from **Fig. B5** that the resistance is higher for large α values. In fact, although the average source temperature is lower for smaller α, hence the thermal resistance is lower, the Sine function in the definition of the non-dimensional resistance (Eq. (B.25)) is greater for larger α.

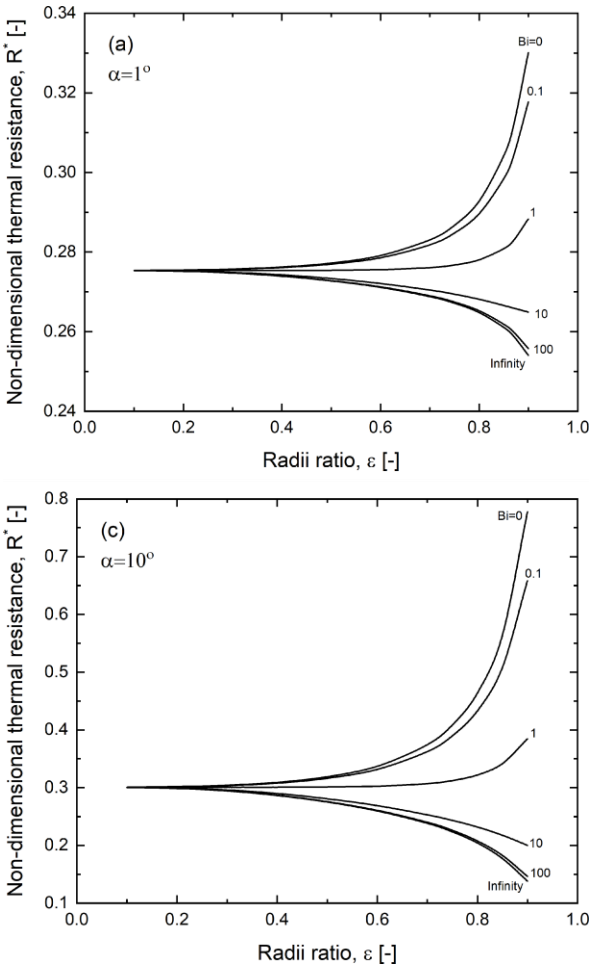

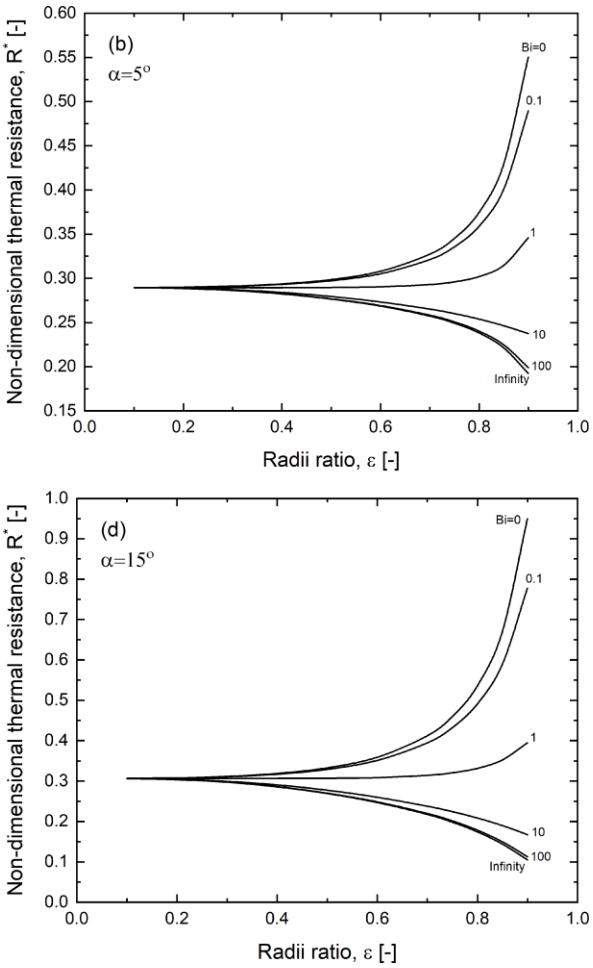

Fig. B5: The variation of non-dimensional thermal resistance with radii ratio ε, and Biot number *Bi*, for: (a) $\alpha = 1^{\circ}$; (b) $\alpha = 5^{\circ}$; (c) $\alpha = 10^{\circ}$; and (d) $\alpha = 15^{\circ}$.

Table B1: Non-dimensional spreading thermal resistance of a hollow sphere subjected to flux over its poles.

ε	$R^* = 2kcR$ ($\nu = 0$)			$R^* = 2kcR$ ($\nu = -1/2$)		
	Yovanovich et al. [201]	Present analysis	Difference [%]	Yovanovich et al. [201]	Present analysis	Difference [%]
0	0.5821	0.5776	-0.8	0.5404	0.5339	-1.2
0.2	0.5831	0.5785	-0.8	0.5415	0.5348	-1.2
0.4	0.5908	0.5862	-0.8	0.5492	0.5425	-1.2
0.6	0.6200	0.6152	-0.8	0.5784	0.5715	-1.2
0.8	0.7577	0.7519	-0.8	0.7157	0.7078	-1.1
0.9	1.1263	1.1175	-0.8	1.0813	1.0705	-1.0
0.92	1.3318	1.3212	-0.8	1.2842	1.2715	-1.0
0.94	1.6896	1.6754	-0.9	1.6364	1.6201	-1.0
0.96	2.4339	2.4108	-0.9	2.3662	2.3412	-1.0
0.98	4.7372	4.6752	-1.3	4.6171	4.5532	-1.4
0.99	9.4051	9.2116	-2.1	9.1720	8.9766	-2.1

B.4.2. Hollow Sphere

Table B1 compares the results from the present model and those presented by Yovanovich et al. [201] for thermal resistance of a hollow sphere with $\alpha = 5^{\circ}$, as discussed in Section B.3.1.1. By using the expression for the heat flux distribution given by Eq. (B.26), it can be concluded that the results are in very good agreement, for both isoflux ($v = 0$) and isothermal ($v = -1/2$) cases, with a maximum relative difference of $\simeq 2\%$.

B.4.3. Heat Spreading in a Half-Space from a Circular Source

The results from the present analysis, using spherical coordinates, are compared with that presented by Bejan and Kraus [210] (cylindrical coordinates) for heat spreading in a half-space, considering a circular heat source. This comparison is presented in **Table B2** for isoflux and isothermal heat sources. The relative difference between the two modeling approaches is less than 2%.

Table B2: Non-dimensional spreading thermal resistance of a circular isothermal source in a half-space.

Source type	Bejan and Kraus [210]	Present analysis	Difference [%]
Isoflux ($v = 0$)	$8/3\pi^2$	0.2726	0.9
Isothermal ($v = -1/2$)	1/4	0.2542	1.7

Table B3: Non-dimensional spreading thermal resistance of an isothermal circular source on a thin infinite disk.

χ	$R^* = 4kcR$ ($v = -1/2$)			χ	$R^* = 4kcR$ ($v = -1/2$)		
	Yovanovich [200]	Present analysis	Difference [%]		Yovanovich [200]	Present analysis	Difference [%]
0	0.0000	0.0011	0.0	2	0.7889	0.7907	0.2
0.1	0.1089	0.1014	-6.9	3	0.8559	0.8601	0.5
0.2	0.2015	0.1936	-3.9	4	0.8910	0.8970	0.7
0.3	0.2824	0.2750	-2.6	5	0.9124	0.9198	0.8
0.4	0.3532	0.3466	-1.9	6	0.9268	0.9354	0.9
0.5	0.4149	0.4090	-1.4	7	0.9372	0.9468	1.0
0.6	0.4684	0.4633	-1.1	8	0.9450	0.9555	1.1
0.7	0.5148	0.5105	-0.8	9	0.9511	0.9624	1.2
0.8	0.5551	0.5514	-0.7	10	0.9560	0.9680	1.3
0.9	0.5901	0.5871	-0.5	20	0.9779	0.9957	1.8
1.0	0.6206	0.6182	-0.4				

B.4.3. Isothermal Circular Source on an Infinite Disc

Table B3 shows the calculated non-dimensional resistance considering the approach discussed in Section B.3.1.3 for an isothermal circular source on an infinite disk. The results, shown for different relative thickness χ, are compared with the values presented by Yovanovich [200]. The relative difference between the results is less than ±2% for χ = 0.4–20 (Corresponds to ε = 0.65–0.99). However, when $0 < \chi \leq 0.3$, the absolute error can reach up to 7%. This discrepancy between the results within this range is because, for very small values of χ (very large values of ε), the flux distribution given by Eq. (B.26) cannot be considered as a good approximation for the isothermal condition. For example, for χ = 0.1 (ε > 0.99), the relative difference between the minimum and maximum temperature within the half-contact angle α is > 100%.

B.5. Conclusions

The analytical expressions presented in this study provide a quick and accurate way to determine the temperature distribution and thermal spreading resistance of a hollow hemi-sphere subjected to heat flux on its pole, with heat being dissipated from the inner surface by convection. The results show that in the case of a low Biot number ($Bi \leq 1$), the thermal resistance increases rapidly for large values of radii ratio. Nevertheless, thinner walls would be favourable to dissipate the heat to the inner surface when $Bi \geq 10$. The analysis also demonstrates that a smaller source contact-angle will result in higher thermal resistances.

The fundamental analysis presented herein can be used to assess the effect of heat leaks in spherical petroleum and cryogenic tanks. It has also been shown that the analytical model can be extended to include other solutions for spreading resistance in hollow spheres with insulated walls, half-space, and infinite disk with isothermal end.

Appendix C: Reactor Experimental Data

Table C1-Table C9 show the experimental data points of the reactor at the various testing conditions.

Table C1: Reactor experimental data at $T_{pro,i}$ = 30 °C, $RH_{pro,i}$ = 50%, , and $T_{reg,i}$ = 60 °C.

Time [s]	Air velocity	Inlet temperature	Inlet humidity	Outlet temperature [°C]	Outlet humidity
0	1	30	13.2	46.4	8.1
120	1	30	13.2	45.7	7.4
240	1	30	13.2	45.7	7.3
360	1	30	13.2	45.7	7.3
480	1	30	13.2	45.5	7.4
600	1	30	13.2	45.2	7.4
720	1	30	13.2	44.9	7.6
840	1	30	13.2	44.5	7.7
960	1	30	13.2	44	7.9
1080	1	30	13.2	43.6	8.1
1200	1	30	13.2	43	8.2
1320	1	30	13.2	42.6	8.4
1440	1	30	13.2	42	8.6
1560	1	30	13.2	41.6	8.8
1680	1	30	13.2	41	8.9
1800	1	70	13.2	54.3	19.3
1920	1	70	13.2	53.9	19.4
2040	1	70	13.2	53.7	19.4
2160	1	70	13.2	53.7	19.3
2280	1	70	13.2	53.8	19.3
2400	1	70	13.2	54	19.1
2520	1	70	13.2	54.3	19
2640	1	70	13.2	54.8	18.8
2760	1	70	13.2	55.4	18.6
2880	1	70	13.2	55	18
3000	1	70	13.2	56.8	18
3120	1	70	13.2	57.7	17.7
3240	1	70	13.2	58.6	17.3
3360	1	70	13.2	59.6	17
3480	1	70	13.2	60.6	16.6

Table C2: Reactor experimental data at $T_{pro,i}$ = 30 °C, $RH_{pro,i}$ = 60%, and $T_{reg,i}$ = 60 °C..

Time [s]	Air velocity	Inlet temperature	Inlet humidity	Outlet temperature [°C]	Outlet humidity
0	1	30	15.9	46.7	10.1
120	1	30	15.9	46.5	9.8
240	1	30	15.9	46.4	9.73
360	1	30	15.9	46.3	9.74
480	1	30	15.9	46.2	9.8
600	1	30	15.9	45.9	9.9
720	1	30	15.9	45.5	10
840	1	30	15.9	45.1	10.1
960	1	30	15.9	44.7	10.3
1080	1	30	15.9	44.2	10.5
1200	1	30	15.9	43.7	10.7
1320	1	30	15.9	43.3	10.8
1440	1	30	15.9	42.8	11.1
1560	1	30	15.9	42.3	11.2
1680	1	30	15.9	41.8	11.4
1800	1	70	15.9	53.6	22.3
1920	1	70	15.9	53.4	22.3
2040	1	70	15.9	53.2	22.3
2160	1	70	15.9	53.2	22.2
2280	1	70	15.9	53.3	22.2
2400	1	70	15.9	53.5	22
2520	1	70	15.9	53.8	21.9
2640	1	70	15.9	54.2	21.7
2760	1	70	15.9	54.7	21.5
2880	1	70	15.9	55.3	21.3
3000	1	70	15.9	56	21
3120	1	70	15.9	56.8	20.8
3240	1	70	15.9	57.6	20.4
3360	1	70	15.9	58.5	20.1
3480	1	70	15.9	59.5	19.8

Table C3: Reactor experimental data at $T_{pro,i}$ = 30 °C, $RH_{pro,i}$ = 70%, , and $T_{reg,i}$ = 60 °C..

Time [s]	Air velocity	Inlet temperature	Inlet humidity	Outlet temperature [ºC]	Outlet humidity
0	1	30	18.7	47.1	12.6
120	1	30	18.7	46.9	12.3
240	1	30	18.7	46.9	12.3
360	1	30	18.7	46.8	12.3
480	1	30	18.7	46.6	12.3
600	1	30	18.7	46.3	12.4
720	1	30	18.7	46	12.5
840	1	30	18.7	45.6	12.7
960	1	30	18.7	45.2	12.8
1080	1	30	18.7	44.8	13
1200	1	30	18.7	44.3	13.2
1320	1	30	18.7	43.8	13.3
1440	1	30	18.7	43.4	13.5
1560	1	30	18.7	42.9	13.7
1680	1	30	18.7	42.5	13.8
1800	1	70	18.7	53.3	25.2
1920	1	70	18.7	53	25.2
2040	1	70	18.7	52.9	25.2
2160	1	70	18.7	52.9	25.1
2280	1	70	18.7	53	25
2400	1	70	18.7	53.2	24.9
2520	1	70	18.7	53.4	24.8
2640	1	70	18.7	53.8	24.7
2760	1	70	18.7	54.3	24.5
2880	1	70	18.7	54.8	24.3
3000	1	70	18.7	55.4	24
3120	1	70	18.7	56.1	23.8
3240	1	70	18.7	56.8	23.5
3360	1	70	18.7	57.7	23.2
3480	1	70	18.7	58.5	22.8

Table C4: Reactor experimental data at $T_{pro,i}$ = 25 °C, $RH_{pro,i}$ = 60%, and $T_{reg,i}$ = 60 °C.

Time [s]	Air velocity	Inlet temperature	Inlet humidity	Outlet temperature [ºC]	Outlet humidity
0	1	25	11.8	42.8	6.7
120	1	25	11.8	41.2	5.7
240	1	25	11.8	41.2	5.6
360	1	25	11.8	41.3	5.6
480	1	25	11.8	41.1	5.6
600	1	25	11.8	41	5.7
720	1	25	11.8	40.7	5.7
840	1	25	11.8	40.4	5.8
960	1	25	11.8	40.1	5.9
1080	1	25	11.8	39.7	6.1
1200	1	25	11.8	39.3	6.3
1320	1	25	11.8	38.9	6.4
1440	1	25	11.8	38.4	6.6
1560	1	25	11.8	37.9	6.8
1680	1	25	11.8	37.5	7
1800	1	70	11.8	53.6	18.1
1920	1	70	11.8	53.2	18.2
2040	1	70	11.8	52.9	18.3
2160	1	70	11.8	52.7	18.3
2280	1	70	11.8	52.8	18.2
2400	1	70	11.8	52.9	18.1
2520	1	70	11.8	53.2	17.9
2640	1	70	11.8	53.7	17.8
2760	1	70	11.8	54.2	17.6
2880	1	70	11.8	54.8	17.3
3000	1	70	11.8	55.6	17
3120	1	70	11.8	56.4	16.7
3240	1	70	11.8	57.4	16.3
3360	1	70	11.8	58.4	15.9
3480	1	70	11.8	59.4	15.6

Table C5: Reactor experimental data at $T_{pro,i}$ = 35 °C, $RH_{pro,i}$ = 60% , and $T_{reg,i}$ = 70 °C.

Time [s]	Air velocity	Inlet temperature	Inlet humidity	Outlet temperature [°C]	Outlet humidity
0	1	35	21.3	50.7	15.6
120	1	35	21.3	50.7	15.4
240	1	35	21.3	50.6	15.4
360	1	35	21.3	50.5	15.4
480	1	35	21.3	50.3	15.5
600	1	35	21.3	49.9	15.6
720	1	35	21.3	49.6	15.8
840	1	35	21.3	49.2	15.9
960	1	35	21.3	48.8	16.1
1080	1	35	21.3	48.3	16.2
1200	1	35	21.3	47.8	16.4
1320	1	35	21.3	47.3	16.6
1440	1	35	21.3	46.9	16.8
1560	1	35	21.3	46.4	16.9
1680	1	35	21.3	46	17.1
1800	1	70	21.3	54.6	27.3
1920	1	70	21.3	54.4	27.3
2040	1	70	21.3	54.4	27.3
2160	1	70	21.3	54.4	27.2
2280	1	70	21.3	54.5	27.1
2400	1	70	21.3	54.7	27
2520	1	70	21.3	55	26.9
2640	1	70	21.3	55.3	26.7
2760	1	70	21.3	55.8	26.6
2880	1	70	21.3	56.3	26.4
3000	1	70	21.3	56.7	26.1
3120	1	70	21.3	57.6	25.9
3240	1	70	21.3	58.3	25.6
3360	1	70	21.3	59	25.3
3480	1	70	21.3	59.8	25

Table C6: Reactor experimental data at $T_{pro,i}$ = 30 °C, $RH_{pro,i}$ = 60%, and $T_{reg,i}$ = 60 °C.

Time [s]	Air velocity	Inlet temperature	Inlet humidity	Outlet temperature [°C]	Outlet humidity
0	1	30	15.9	41.7	11.7
120	1	30	15.9	41.6	11.5
240	1	30	15.9	41.7	11.5
360	1	30	15.9	41.6	11.5
480	1	30	15.9	41.6	11.5
600	1	30	15.9	41.5	11.5
720	1	30	15.9	41.3	11.6
840	1	30	15.9	41.1	11.6
960	1	30	15.9	40.9	11.7
1080	1	30	15.9	40.7	11.8
1200	1	30	15.9	40.5	11.9
1320	1	30	15.9	40.3	12
1440	1	30	15.9	39.9	12.1
1560	1	30	15.9	39.7	12.2
1680	1	30	15.9	39.4	12.3
1800	1	60	15.9	48.4	20.4
1920	1	60	15.9	48.3	20.4
2040	1	60	15.9	48.2	20.4
2160	1	60	15.9	48.1	20.4
2280	1	60	15.9	48.2	20.4
2400	1	60	15.9	48.3	20.3
2520	1	60	15.9	48.4	20.3
2640	1	60	15.9	48.6	20.2
2760	1	60	15.9	48.8	20.1
2880	1	60	15.9	49	20
3000	1	60	15.9	49.4	19.9
3120	1	60	15.9	49.7	19.8
3240	1	60	15.9	50.1	19.6
3360	1	60	15.9	50.5	19.4
3480	1	60	15.9	51	19.3

Table C7: Reactor experimental data at $T_{pro,i}$ = 30 °C, $RH_{pro,i}$ = 60%, and $T_{reg,i}$ = 65 °C.

Time [s]	Air velocity	Inlet temperature	Inlet humidity	Outlet temperature [°C]	Outlet humidity
0	1	30	15.9	44.1	10.9
120	1	30	15.9	44	10.7
240	1	30	15.9	44	10.6
360	1	30	15.9	43.9	10.6
480	1	30	15.9	43.8	10.6
600	1	30	15.9	43.7	10.7
720	1	30	15.9	43.4	10.8
840	1	30	15.9	43.2	10.9
960	1	30	15.9	42.8	11
1080	1	30	15.9	42.5	11.1
1200	1	30	15.9	42.1	11.2
1320	1	30	15.9	41.8	11.4
1440	1	30	15.9	41.4	11.5
1560	1	30	15.9	41	10.6
1680	1	30	15.9	40.7	11.8
1800	1	65	15.9	51.1	21.3
1920	1	65	15.9	50.9	21.3
2040	1	65	15.9	50.8	21.3
2160	1	65	15.9	50.7	21.3
2280	1	65	15.9	50.8	21.3
2400	1	65	15.9	50.9	21.2
2520	1	65	15.9	51.1	21.1
2640	1	65	15.9	51.4	21
2760	1	65	15.9	51.8	20.8
2880	1	65	15.9	52.1	20.7
3000	1	65	15.9	52.6	20.5
3120	1	65	15.9	53.2	20.3
3240	1	65	15.9	53.7	20.1
3360	1	65	15.9	54.4	19.8
3480	1	65	15.9	55	19.6

Table C8: Reactor experimental data at $T_{pro,i}$ = 30 °C, $RH_{pro,i}$ = 60%, $T_{reg,i}$ = 70 °C, and u_{air} = 1.5 m/s.

Time [s]	Air velocity	Inlet temperature	Inlet humidity	Outlet temperature [°C]	Outlet humidity
0	1	30	15.9	48.8	9.1
120	1	30	15.9	48	9.2
240	1	30	15.9	47.2	9.5
360	1	30	15.9	46.3	9.8
480	1	30	15.9	45.4	10.1
600	1	30	15.9	44.5	10.4
720	1	30	15.9	43.7	10.7
840	1	30	15.9	42.9	11
960	1	30	15.9	42	11.3
1080	1	30	15.9	41.3	11.6
1200	1	30	15.9	40.7	11.8
1320	1	30	15.9	40	12
1440	1	30	15.9	39.5	12.3
1560	1	30	15.9	38.9	12.5
1680	1	30	15.9	38.5	12.7
1800	1	70	15.9	51.1	23.2
1920	1	70	15.9	51.5	23
2040	1	70	15.9	52	22.7
2160	1	70	15.9	52.6	22.5
2280	1	70	15.9	53.3	22.2
2400	1	70	15.9	54.1	21.8
2520	1	70	15.9	55.1	21.4
2640	1	70	15.9	56.1	21
2760	1	70	15.9	57.3	20.6
2880	1	70	15.9	58.4	20.1
3000	1	70	15.9	59.6	19.7
3120	1	70	15.9	60.8	19.3
3240	1	70	15.9	62	18.8
3360	1	70	15.9	63.1	18.4
3480	1	70	15.9	64.1	18

Table C9: Reactor experimental data at $T_{pro,i}$ = 30 °C, $RH_{pro,i}$ = 60%, $T_{reg,i}$ = 70 °C, and u_{air} = 1.5 m/s.

Time [s]	Air velocity	Inlet temperature	Inlet humidity	Outlet temperature [°C]	Outlet humidity
0	2	30	15.9	48.9	9
120	2	30	15.9	47.3	9.5
240	2	30	15.9	45.9	9.9
360	2	30	15.9	44.6	10.4
480	2	30	15.9	43.4	10.8
600	2	30	15.9	42.3	11.2
720	2	30	15.9	41.3	11.6
840	2	30	15.9	40.5	11.9
960	2	30	15.9	39.7	12.2
1080	2	30	15.9	38.9	12.5
1200	2	30	15.9	38.3	12.7
1320	2	30	15.9	37.7	12.9
1440	2	30	15.9	37.2	13.1
1560	2	30	15.9	36.7	13.3
1680	2	30	15.9	36.3	13.5
1800	2	70	15.9	50.8	23.3
1920	2	70	15.9	51.6	22.9
2040	2	70	15.9	52.5	22.6
2160	2	70	15.9	53.6	22.1
2280	2	70	15.9	54.7	21.6
2400	2	70	15.9	55.9	21.1
2520	2	70	15.9	57.3	20.6
2640	2	70	15.9	58.7	20
2760	2	70	15.9	60	19.6
2880	2	70	15.9	61.3	19
3000	2	70	15.9	62.6	18.6
3120	2	70	15.9	63.8	18.1
3240	2	70	15.9	65	17.7
3360	2	70	15.9	65.8	17.4
3480	2	70	15.9	66.6	17.1

Appendix D: MATLAB code (Reactor Modeling)

```
clear
clc
close all

% --------------------------------
% Initial conditions

Ta_0 = 30;
Ts_0 = 30;

RH_0=0.60;
wa_0 =omega_RH_conv(Ta_0,RH_0);

RH_s_0=0.10;
Xs_0 =  Xs_RH_s_ini(RH_s_0);
% Xs_0 =  0.06;



% --------------------------------
% Operation parameters

u=1.0; % air velocity

RH_in_ads=0.60;
Ta_in_ads=30;
wa_in_ads=omega_RH_conv(Ta_in_ads,RH_in_ads);
% wa_in_ads=0.00877;

% RH_in_des=0.10;
Ta_in_des=70;
% wa_in_des=omega_RH_conv(Ta_in_des,RH_in_des);
% wa_in_des=0.00877;
wa_in_des=wa_in_ads;
% wa_in_des=0.0005;


No_half_cycles=9; % Number of half-cycles (one half-
cycle = adsorption or desorption)

% --------------------------------
% Design parameters

W_channel =30/1000; % Width of the channel
```

```
D_p=0.7/1000; % Diamamter of capsule
delta_shell= (70/1000000); % shell thickness[m]
thickness_s=0.7/1000; % Thickness of sorbent -- same
as capsule diamater
epsilon_s=0.3; % void fractin

H_channel = 1.5/1000; % Height of the channel

bedLength=180/1000;  % Length of testbed

% --------------------------------
% Discretization steps

N=100;   % number of nodes
t_HC=0.5*60*60; % cycle time in seconds
tSpan = [0:1:t_HC];

%
++++++++++++++++++++++++++++++++++++++++++++++++++++++++
++++++++++++++++++++++++++++++++++

% ------------------------------------Solution------
--------------------------------
date=datestr(now,'_yyyy_mm_dd');
timeNow=datestr(now,'_HH_MM_SS');

status=1;
% status=1: adsorption
% status=2: dsorption

for j=1:No_half_cycles

if j==1

t0=0;    %apply initial conditions
wa_ini(0*(N+1)+2 : 1*(N+1) , 1)=wa_0;
Xs_ini(1*(N+1)+2 : 2*(N+1) , 1)=Xs_0;
Ta_ini(2*(N+1)+2 : 3*(N+1) , 1)=Ta_0;
Ts_ini(3*(N+1)+2 : 4*(N+1) , 1)=Ts_0;

else

t0=tSol(length(tSol));

end


% check status: start with adsorption or desorption?
```

```
if status==1
    wa_in=wa_in_ads;
    Ta_in=Ta_in_ads;
else
    wa_in=wa_in_des;
    Ta_in=Ta_in_des;
end



y0(0*(N+1)+2 : 1*(N+1) , 1) = wa_ini(0*(N+1)+2 :
1*(N+1) , 1);
y0(1*(N+1)+2 : 2*(N+1) , 1) = Xs_ini(1*(N+1)+2 :
2*(N+1) , 1);
y0(2*(N+1)+2 : 3*(N+1) , 1) = Ta_ini(2*(N+1)+2 :
3*(N+1) , 1);
y0(3*(N+1)+2 : 4*(N+1) , 1) = Ts_ini(3*(N+1)+2 :
4*(N+1) , 1);

%--------------------------------

[tSol,ySol] = ode15s(@desicc_fun, tSpan,
y0,[],bedLength,W_channel,H_channel,thickness_s,D_p,d
elta_shell,epsilon_s,u,wa_in,Ta_in,N);

wa=ySol(:,  0*(N+1)+1 : 1*(N+1));
Xs=ySol(:,  1*(N+1)+1 : 2*(N+1));
Ta=ySol(:,  2*(N+1)+1 : 3*(N+1));
Ts=ySol(:,  3*(N+1)+1 : 4*(N+1));

%--------------------------------

% Recalculations

wa(:,1)=wa_in;
Ta(:,1)=Ta_in;
Ts(:,1)=Ta_in;
tSol_min=tSol/60;
wa_g_kg=wa*1000;
DELTA_wa_g_kg=(wa_in-wa)*1000;



%--------------------------------

% Reset initial conditions
```

```
wa_ini((0*(N+1)+2 :
1*(N+1)),1)=wa(length(wa),0*(N+1)+2 : 1*(N+1));
Xs_ini((1*(N+1)+2 :
2*(N+1)),1)=Xs(length(Xs),0*(N+1)+2 : 1*(N+1));
Ta_ini((2*(N+1)+2 :
3*(N+1)),1)=Ta(length(Ta),0*(N+1)+2 : 1*(N+1));
Ts_ini((3*(N+1)+2 :
4*(N+1)),1)=Ts(length(Ts),0*(N+1)+2 : 1*(N+1));


%---------------------------------
% Save data

t_HC_data=tSol+(t0*(j-1));
Data=[t_HC_data,Ta(:,N),wa(:,N)];

writematrix(Data,append('Sim',date,timeNow,'.xls'),'W
riteMode','append')


%---------------------------------

% Reset status from adsorption to desorption and vice
versa

if status==1
    status=2;
else
    status=1 ;
end

end

% ---------------------------------
%
% % Plot figures

% yyaxis left
% plot(tSol_min,wa_g_kg(:,N),'c','LineWidth',1);
% xlabel('Time [min]')
% ylabel('Air humidity ratio at z=L [g_w/kg_{dry
air}]')
% % ylabel('Air humidity ratio [g_w/kg_{dry air}]')
% % axis([0 60 0 14])
%
% hold on
% yyaxis right
```

```
%
plot(tSol_min,DELTA_wa_g_kg(:,N),'g','LineWidth',1);
% ylabel('Air humidity ratio difference at z=L
[g_w/kg_{dry air}]')
%
% legend('Air outlet humidity', 'Humidity
difference')
%
%
%
% figure
% plot(tSol_min,Xs(:,N),'m','LineWidth',1);
% xlabel('Time [min]')
% ylabel('Sorbent water uptake [g_w/g_{sorbent}]')
%
% figure
% plot(tSol_min,Ta(:,N),'b','LineWidth',1);
% xlabel('Time [min]')
% ylabel('Temperature [C]')
%
% hold on
%
% plot(tSol_min,Ts(:,N),'r','LineWidth',1);
% xlabel('Time [min]')
% legend('Air outlet temperature', 'Sorbent
temperature at z=L')


function dydt =
desicc_fun(t,y,bedLength,W_channel,H_channel,thicknes
s_s,D_p,delta_shell,epsilon_s,u,wa_in,Ta_in,N)


rho_a=1.186;
rho_s=1500;

cp_a=1009;
cp_s=2200;

nu_a=1.5e-5;

[U_h,U_m] =
H_M_coefficients(rho_a,cp_a,nu_a,D_p,delta_shell,u);


%--------------------------------
```

```
Acs_a=(H_channel * W_channel);  % cross-sectional
area of air "channel"
Acs_s=(W_channel * thickness_s); % cross-sectional
area of sorbent
Acs_a_mod=Acs_a+epsilon_s*Acs_s; % modified cross-
sectional area of air channel (to account for air
between the capsules)

%--------------------------------

B2= +1*(6*U_m)/(D_p*rho_s);

%--------------------------------

B1= -1*(rho_s/rho_a)*(Acs_s/Acs_a_mod)*(1-epsilon_s);

%--------------------------------

B3= -1*((6*U_h)/(D_p*rho_a*cp_a))*(1-
epsilon_s)*(Acs_s/Acs_a_mod);

%--------------------------------

B4= +1*(1/cp_s);

%--------------------------------

B5= +1*( (6*U_h)/(D_p*rho_s*cp_s));

%--------------------------------

delz=bedLength/N; % discretization of length

%--------------------------------

dydt=zeros(4*(N+1),1);

y(0*(N+1)+1)=wa_in;
y(2*(N+1)+1)=Ta_in;

%--------------------------------

for i=0*(N+1)+2 : 1*(N+1)
% Air mass balance

dydt(i)=  (-1)  * u*((y(i)-y(i-1))/delz) +  B1 * (B2
* (y(i)-hum_uptake(y,i,N)));
end
```

```
for i=1*(N+1)+2 : 2*(N+1)
% Sorbent mass balance
      dydt(i)= B2 * (y(i-(N+1))-hum_uptake(y,i,N));
end

for i=2*(N+1)+2 : 3*(N+1)
% Air energy balance
      dydt(i)=(-1)  * u*((y(i)-y(i-1))/delz) + B3 *
(y(i)-y(i+(N+1)));

end

for i=3*(N+1)+2 : 4*(N+1)
% Sorbent energy balance
      dydt(i)=(B4 * DELTAH_ads(y(i-2*(N+1))) * (B2 *
(y(i-3*(N+1))-hum_uptake(y,i,N))) + B5 * (y(i-(N+1))-
y(i));

end


end


function humUptak = hum_uptake(y,j,N)
if     ( j>= 0*(N+1)+2 )  &&  ( j <= 1*(N+1) )
          Ts=y(j+3*(N+1));
          Xs=y(j+(N+1));

elseif ( j>= 1*(N+1)+2 )  &&  ( j <= 2*(N+1))
              Ts=y(j+2*(N+1));
          Xs=y(j);

elseif ( j>= 3*(N+1)+2 )  &&  ( j <= 4*(N+1))
          Ts=y(j);
          Xs=y(j-2*(N+1));
end

%----------------------------------------

  % % % capsule isotherm New

Intercept = 0.00198;
B1 = -0.08873;
B2 = -0.747;
B3 = 9.07346;
B4 = -12.45188;
```

```
B5 = 4.97313;

RH = Intercept + B1*Xs + B2*Xs^2 + B3*Xs^3 + B4*Xs^4
+ B5*Xs^5;

%----------------------------------------


    P_vs = exp(23.196-3816.44/((Ts+273.15)-46.13));
    P=101325;
    humUptak = 0.622 * RH / ( (P/P_vs) -  RH  );



end


function X_s_ini = Xs_RH_s_ini(RH_s)

% % % capsule isotherm

Intercept = 0.06908;
B1 = 4.62427;
B2 = -23.41797;
B3 = 62.13456;
B4 = -74.83659;
B5 = 33.99652;
X_s_ini = Intercept + B1*RH_s + B2*RH_s^2 + B3*RH_s^3
+ B4*RH_s^4 + B5*RH_s^5;

%----------------------------------------


end
```